UNIVERSITY OF OKLAHOMA

GRADUATE COLLEGE

MULTIPLE CYCLIC TORNADO PRODUCTION MODES IN THE 5 MAY 2007 GREENSBURG, KANSAS SUPERCELL STORM

A DISSERTATION

SUBMITTED TO THE GRADUATE FACULTY

in partial fulfillment of the requirements for the

Degree of

DOCTOR OF PHILOSOPHY

By

ROBIN LYNN TANAMACHI
Norman, Oklahoma
2011

Downloaded from SHAREOK. Persistent Handle URL: https://hdl.handle.net/11244/319425

MULTIPLE CYCLIC TORNADO PRODUCTION MODES IN THE 5 MAY 2007 GREENSBURG, KANSAS SUPERCELL STORM

A DISSERTATION APPROVED FOR THE
SCHOOL OF METEOROLOGY

BY

_____
Dr. Howard Bluestein, Chair

_____
Dr. John Albert

_____
Dr. Robert Palmer

_____
Dr. Alan Shapiro

_____
Dr. Louis Wicker

_____
Dr. Ming Xue

© Copyright by ROBIN LYNN TANAMACHI 2011

All Rights Reserved.

DEDICATION

This work is dedicated to all of the victims of the 5 May 2007 Greensburg, Kansas tornadic storm, and in particular, to those whose lives were lost or irrevocably changed by the events of that evening. May their memories endure, and their experiences inspire.

ACKNOWLEDGMENTS

While this body of research is the product of many years' effort on my part, it would not have been possible without the generous assistance of a large number of individuals and organizations. Contributions ranged from the tangible (e.g., financial support, computing facilities, data storage, library resources) to the intangible (e.g., proofreading, administration, mentorship, and moral support). Herein, I attempt to highlight those who are the most deserving of my gratitude, but the order in which they appear does not necessarily imply that their contributions were any more or less crucial than anyone else's. If I have inadvertently omitted any person or any particular contribution, I can only humbly apologize.

My advisor, Dr. Howard Bluestein, has been my supervisor and chief research mentor since I arrived at the University of Oklahoma (OU) in the fall of 2002. His grants have supported my many projects (and some indulgences) during my years as a student. Under his tutelage, my radar data analysis, field data collection, and scientific writing abilities have flourished and matured. I am deeply indebted to him for supporting me as a graduate research assistant through numerous challenges, and for allowing me a change of dissertation topic midway through the doctoral process. Dr. Bluestein has always been a reliable advocate for my interests, introduced me to many interesting people, and kept me honest in my reasoning and writing. Undoubtedly, I am a better scientist (and storm chaser) now, thanks to him.

My entire committee has been unwaveringly supportive of my work. In particular, Dr. Louis Wicker of the National Severe Storms Laboratory (NSSL) provided an

enormous amount of voluntary assistance, securing for me supplemental funding, computing resources and support, and providing guidance on the practical implementation of numerical weather prediction (NWP) models and data assimilation (DA) using the ensemble Kalman filter (EnKF) technique. I could always count on him to provide honest feedback about the quality of my thinking, and to hit me with challenging questions when I was beginning to get complacent.

I firmly believe that fluid dynamics are a crucial component of an atmospheric scientist's knowledge inventory, and I've had the advantage of outstanding instruction in this area from two of my committee members, Dr. Alan Shapiro and Dr. Ming Xue. Dr. Shapiro, who gave superb and entertaining lessons in advanced atmospheric dynamics, also mentored me in some of the methods and pitfalls of radar data analysis and NWP models. Dr. Shapiro always seemed ready to discuss in detail any dynamics-related topic I that could spring on him, and could always be relied upon for intellectual and literary sustenance (as well as gastronomic sustenance – I'm certain that I have consumed several pounds of meat and mushrooms prepared by him at department "grillfests"). Dr. Xue provided me a solid knowledge base in computational fluid dynamics, both via his course of the same name and also his support and co-authorship of a 2008 publication that described my first foray into the use of NWP models for research purposes. I gained most of my basic understanding of DA, including radar DA, from his 2007 OU course "Objective Analysis and Data Assimilation."

Radar data is at the heart of this dissertation, and I feel very fortunate to have arrived at OU at the right time to experience capable instruction in weather radar

theory from Dr. Robert Palmer. From his 2006 course "Weather Radar Theory and Practice," I learned a great deal about how radar works from first principles, the uses and limitations of radar data, and the "cutting edge" radars from which I will likely analyze data in the not-too-distant future. As director of the Atmospheric Radar Research Center at OU, Dr. Palmer, sharing my *nikkei* affinity for all things Japanese, also generously supported my attendance at the first International Symposium on Radar and Modeling Studies of the Atmosphere at Kyoto University in 2009.

Numbers are the lifeblood of science, and mathematics undergirds all of meteorology. My mathematics courses came early and fast in my academic career, and so a discussion with Dr. John Albert (OU Department of Mathematics) about the underlying numerics of an NWP model, for instance, or the derivation of the EnKF, has always felt more natural to me when articulated in the language of mathematics. I am grateful to Dr. Albert for serving on my doctoral committee as my external member.

One additional individual, Dr. David Dowell, might as well have served on my doctoral committee for all his efforts helping me with this research. He secured funding from the National Center for Atmospheric Research (NCAR) for a two-week visit in late 2008, during which he gave me one-on-one instruction in the use of the Data Assimilation Research Testbed (DART) EnKF interface to the Weather Research and Forecasting (WRF) NWP model. These two computing tools feature prominently in the latter portion of this dissertation. (Sudie Kelly of NCAR administered and arranged my visit.) Dr. Dowell has also provided additional guidance to me during numerous subsequent face-to-face meetings and via e-mail.

My graduate research assistantship was funded via National Science Foundation grants ATM-0241037, ATM-0637148, and ATM-0934307 (administered by Stephen P. Nelson and Nancy Campbell), as well as NOAA NA08OAR4320904 (administered by Tracy Reinke of the Cooperative Institute for Meteorological Mesoscale Studies). I gratefully acknowledge Dr. David Stensrud of the NSSL for providing the latter support of my assistantship during the final six months. Dr. Frederick Carr served as my TA advisor during one semester in which I served as a course instructor.

A wealth of information about the Greensburg, Kansas tornadic storm, the warning process, and damage survey was provided by personnel of the National Weather Service (NWS) forecast office in Dodge City, Kansas. In particular, I thank Michael Umscheid, with whom I've had extended e-mail and in-person interaction since shortly after the Greensburg storm. Mike, who issued the "tornado emergency" declaration for Greensburg that undoubtedly minimized the death toll from the Greensburg tornado, has been more than generous with his time and information about the events of that evening. Jeffrey Hutton furnished the geographic shape files for the surveyed damage tracks that appear on maps throughout this dissertation.

My experiences fielding mobile Doppler radars have come largely as the result of a fruitful, multi-decadal collaboration between Dr. Bluestein and the Microwave Remote Sensing Laboratory (MIRSL) at the University of Massachusetts – Amherst (UMass). The data set that constitutes the nucleus of this dissertation was collected using the UMass mobile, X-band, polarimetric Doppler radar. I have thoroughly enjoyed working with the MIRSL engineers over the years, and have been impressed with their inventiveness and ingenuity. The MIRSL engineers and alumni who

contributed most to this dissertation include Kery Hardwick (who operated the radar on 5 May 2007), Dr. Stephen Frasier, Dr. Francesc Junyent, and Vijay Venkatesh.

I received computing and programming support from Dr. Mark Laufersweiler, Dr. Louis Wicker, Ryan May, Aaron Botnick, Jeremy Gibbs, Dr. Ted Mansell, Dr. Daniel Dawson, Nathan Snook, and the staff of OU Research Computing Services (RCS). Support for using WRF with DART was provided by Drs. Dave Gill and Michael Duda; support for the DART package in particular was provided by Drs. Jeffrey Anderson, Nancy Collins, Glen Romine, Chris Snyder, and Dustan Wheatley. Supercomputing resources and guidance were furnished by the Oklahoma Supercomputing Center for Education and Research (OSCER), under the directorship of Dr. Henry Neeman.

Conversations with the following people (in addition to those listed elsewhere) have helped to shape the content and focus of this dissertation research in a wide variety of ways (including which directions *not* to pursue): Les Lemon, Donald Guiliano, Dr. Conrad Ziegler, Dr. Jim Marquis, Donald Burgess, and Dr. George Bryan. Dr. Chuck Doswell also provided voluminous advice, encouragement, and wisdom throughout my dissertation process, often over wine on Friday evenings. He kindly reviewed the reading copy of this dissertation and alerted me to the existence of some publications that I missed during my literature search.

The WSR-88D and NWS automated surface observing station data used in this study were provided by the National Climatic Data Center (NCDC) and the National Oceanic and Atmospheric Adminstration (NOAA). Sharon Falk provided the Kansas

Groundwater Management District No. 5 (GMD5) automated observing station measurements.

The office environment in which I have spent my graduate student career has always been a delightful and intellectually stimulating one. I can always count on my officemates (Dr. Chris Weiss, Matthew Kramar, Michael French, Eric Holthaus, Jeffrey Snyder, and Jana Houser) for a healthy discussion of our respective work and world views. It has been my honor to engage in many seasons of field experiments with them (including the harrowing, cross-country trek of VORTEX2), sharing our mutual love of severe weather, and working together to coax supercells into giving up their secrets.

I hereby acknowledge 94 unwitting undergraduate students who took instruction from me in the Fall 2007 OU course "Meteorology 2603: Severe and Unusual Weather." Thanks to their (sometimes frank) feedback, I now solidly perceive myself as an instructor as well as a student of meteorology, and feel that my presentation and explanatory skills have improved by light years. The old instructors' adage is definitely true: You never learn a topic as well as when you have to teach it!

Along the same lines, I thank Dr. Kevin Kloesel for giving me the opportunity to serve as a volunteer tour guide for the National Weather Center. The experience of explaining meteorology to such widely varying audiences (from sixth-graders, to forecasters from the China Meteorological Administration, to television celebrities) helped me develop my skills as a communicator of science to the public and, in the process, made me much more comfortable in front of the camera.

The following people merit mention for providing me with counsel (in both professional and non-professional capacities) during the Ph.D. process: Dr. Stephanie Portersfield, Dr. Deann Gattis, Daphne LaDue, Orit Rabkin, and the authors of *The Woman's Guide to Navigating the Ph.D. in Engineering & Science* (B. B. Lazarus, L. M. Ritter, and S. A. Ambrose). The School of Meteorology office staff (Celia "Mom" Jones, Marcia Palutto, Nancy Campbell, Judy Henry, and Becky Steely) have given me invaluable administrative support (and innumerable hugs) over the years.

I debated at length whether or not to include a particular musical act in these acknowledgements, but finally decided to give a shout-out to the British electronic duo most widely known as The Future Sound of London. Whenever I found myself suffering from writer's block, their music was my "writer's laxative." Mocked by a blinking cursor, I had only to queue up the otherworldly, genre-resistant *Lifeforms*, and within a few minutes, the words began to flow again. They've earned one very grateful fan, if an unusual conduit for accolade.

I would not be nearly as productive and creative a scientist without a loving atmosphere at home. During my tenure as a doctoral student, a dear friend and colleague, Dr. Daniel Dawson, took the bold step of becoming my husband, and cheerfully took on the role of the sympathetic and supportive spouse as I focused on producing this body of research. He provided me with a sounding board for my ideas, often in the middle of the night, and helped to keep me honest when evaluating the underlying assumptions of my research. Dan, I would not have been able to see this endeavor through to the end without your steadfast love, patience, and

encouragement. Thank you, from the depths of my heart (and hearth), for welcoming me into your life, career, and family.

I am the product of the steadfast love, patience, and sacrifice of my immediate family. Mom, Dad, Amanda, Grandma Betty, Uncle Bob, Aunt Jeanne, and Aunt Kaoru never wavered in their support of my doctoral pursuits, despite how long and far it's taken me from them. They have always – *always* – believed in and capitalized on my strengths, rather than my frailties. I also enjoyed the blessings of several relatives who have passed on (Grandma Fumi, Grandpa Paul, and Grandpa Mas), who knew of my attraction to all things atmospheric from a very early age. I reserve my closing acknowledgements for my very deserving family: Thanks for all the good genes, good memories, and good cooking – I hope to pass on all three to future generations. I wonder, sometimes, what you think when you look on this wind-tousled child of yours, whose love for severe weather has catapulted her to minor fame and, on occasion, broken your windshield. Even if you don't read a single word of it, I hope this body of work helps you to understand my passion. My fondest wish is to have made you proud.

TABLE OF CONTENTS

MULTIPLE CYCLIC TORNADO PRODUCTION MODES IN THE 5 MAY 2007 GREENSBURG, KANSAS SUPERCELL STORM iv

DEDICATION vii

ACKNOWLEDGMENTS iv

TABLE OF CONTENTS xii

LIST OF TABLES xvii

LIST OF FIGURES xviii

ABSTRACT xxxiii

Chapter 1 Introduction 1

1.1 Motivation 1

1.2 Statement of hypothesis 5

1.3 Overview of dissertation 7

Chapter 2 Background 9

2.1 Cyclic tornadic supercells 9

2.2 Radar meteorology 14

2.2.1 Introduction 14

2.2.2 Radar data 15

2.2.3 Radars used in this study 22

2.3 The Great Plains nocturnal low-level jet 26

2.3.1 Past studies 26

2.3.2 Issues related to measurement of the LLJ winds 31

Chapter 3 The Greensburg storm 33

3.1 Meteorological overview 33

3.2 UMass X-Pol deployment 38

Chapter 4 Radar data 42

4.1 Description 42

4.1.1 KDDC data 42

4.1.2 UMass X-Pol data 43

4.2 Issues affecting UMass X-Pol data quality and usability 47

4.2.1 Reflectivity attenuation and calibration 47

4.2.2 Limitations of the polarimetric data 48

4.2.3 Radar orientation 49

Chapter 5 Radar data analysis 53

5.1 UMass X-Pol observations of tornadoes 53

5.1.1 UMass X-Pol vortex signatures and surveyed surface damage 53

5.1.2 Vortex tilt 57

5.1.3 Tornadoes originating from the same mid-level circulations 58

5.1.4 Cyclonic-anticyclonic satellite tornado pairs 59

5.2 Reflectivity features....60
5.2.1 Vertical cross-sections / pseudo-RHIs....61
5.2.2 Weak-echo holes and weak-echo columns....63
5.3 Comparison of tornado and updraft motion....71
5.4 Behavior of rear flank gust front(s)....75
5.5 Polarimetric observations....79
5.5.1 Z_{DR} arc....79
5.5.2 Tornadic debris signatures....80
5.6 Comment about clear-air velocity measurements....83
Chapter 6 Ensemble Kalman Filter (EnKF) experiments....85
6.1 Basic concepts of data assimilation....86
6.1.1 The Kalman filter (KF)....88
6.1.2 The extended Kalman filter (EKF)....91
6.1.3 The ensemble Kalman filter (EnKF)....92
6.1.4 The ensemble adjustment Kalman filter (EAKF)....95
6.1.5 Comparisons between EnKF and other DA schemes....96
6.2 Computing tools....97
6.2.1 Weather Research and Forecasting (WRF) model....97
6.2.2 Data Assimilation Research Testbed (DART)....99
6.2.3 Observation-space diagnostics....104

6.3 Experiment setup 105
6.3.1 Introduction and context 105
6.3.2 Experiment nomenclature 108
6.3.3 Base state environment 110
6.3.4 Radar data objective analysis 116
6.3.5 Experiment parameters 120
6.4 Results 124
6.4.1 Inclusion of UMass X-Pol Doppler velocities (kddc_only versus kddc+umass) 139
6.4.2 Variation of the initial low-level environmental velocity profile (0100vad versus 0230vad) 142
6.4.3 Pitch/roll sensitivity experiments 143
6.4.4 Closing comments 146
Chapter 7 Conclusions 148
7.1 Radar data analysis 149
7.2 EnKF experiments 151
References 155
Appendix A. Geographic information 177
Appendix B. Additional observations not used in this study 178
B.1 Haviland, Kansas wind profiler 178

B.2 Groundwater Management District No. 5 surface data 181

B.3 Lamont, Oklahoma rawinsonde 184

Appendix C. Caveat regarding the UMass X-Pol polarimetric fields 186

Appendix D. Azimuth adjustments to UMass X-Pol data 189

Appendix E. List of abbreviations 194

LIST OF TABLES

Table 1. A comparison of 2007 characteristics of the WSR-88D and UMass X-Pol radars.....23

Table 2. Chronology and damage survey information concerning the first ten tornadoes produced by the Greensburg storm, courtesy of M. Umscheid, NWS – Dodge City, Kansas office. An asterisk (*) denotes considerable uncertainty in measurements of path length and width owing to overlap with the damage path of the Greensburg tornado (Fig. 1).....37

Table 3. UMass X-Pol data collected in the Greensburg storm. Elevation angles are measured relative to the truck bed, while azimuth angles are measured clockwise from north (compass headings).....46

Table 4. EnKF experiment nomenclature used in this study.....109

Table 5. Experiment parameters.....122

Table 6. Latitudes, longitudes, and altitudes of some locations relevant to this study.....177

Table 7. GMD5 Station #1 (Greensburg) data from 4 May 2007 (local time), in the format in which they were received (S. Falk, personal communication). Data from the other nine stations are excluded for brevity.....183

Table 8. Azimuthal adjustments to UMass X-Pol volumes based upon clutter targets.....190

Table 9. Expansions of abbreviations, acronyms, and some variables used in this dissertation.....194

LIST OF FIGURES

Fig. 1. Objectively analyzed regions of KDDC reflectivity greater than or equal to 35 dBZ at 1.5 km AGL between 0029 and 0258 UTC on 5 May 2007. For clarity, contours for every sixth volume are shown, and shaded in alternating light and dark gray. Surveyed tornado damage tracks are plotted in heavy gray contours and numbered chronologically (following Lemon and Umscheid 2008). The locations of KDDC, UMass X-Pol, and Greensburg, Kansas are marked. Thin black lines denote county boundaries, and the heavy black line denotes the border between Kansas and Oklahoma. Tornado damage tracks are courtesy of J. Hutton of the NWS – Dodge City, Kansas forecast office. 4

Fig. 2. The Greensburg tornado, illuminated by lightning, as seen from 29 km southwest of Greensburg, Kansas at 0234 UTC. At this time, its damage path was at least 1.5 km wide. View is toward the north-northeast. Photograph courtesy of R. Fritchie. 5

Fig. 3. Conceptual models of (I) "series" and (II) "parallel" tornado damage tracks, and (III) combinations thereof. In this figure, Θ_{TD} (Θ_{LO}) is the angle between the storm and tornado motion vectors at tornado formation (decay). From Agee *et al.* (1976); adapted from Fujita *et al.* (1970). 9

Fig. 4. Schematic diagram of a mature, cyclonic supercell thunderstorm in the Northern Hemisphere as viewed from the south, with common features highlighted. Note the ambient vertical wind shear in the environment, and the locations of the mesocyclone, tornado, forward flank downdraft (FFD), rear flank downdraft (RFD), and surface gust fronts. Courtesy of National Severe Storms Laboratory (NSSL).....11

Fig. 5. Plan view diagram of the low-level (i.e., below 2 km AGL) air flow patterns in and around a mature supercell thunderstorm as depicted in Fig. 4. The locations of the FFD and RFD are shaded dark gray; the surface forward flank gust front (FFGF) and rear-flank gust front (RFGF) are denoted by stippled lines. The primary supercell updraft (UD) and smaller updrafts along the RFGF are shaded light gray. The southern "T" represents a favorable location for tornado development and the northern "T" a favorable location for tornado decay. Note that, in this depiction, the storm-relative motion of the tornado is to the left of the overall storm motion. Adapted from Lemon and Doswell (1979) and Davies-Jones (1986). 12

Fig. 6. Illustration of Rayleigh vs. Mie scattering regimes for incident electromagnetic radiation, courtesy Georgia State University. 16

Fig. 7. An example of Doppler velocity aliasing. In this case, a Doppler radar with a v_{max} of 30 m s^{-1} executes a full 360° azimuthal scan at a fixed elevation angle. The winds are westerly (from 270°) at 36 m s^{-1}; expected Doppler velocity measurements are given by the sinusoidal curve. Doppler velocities greater than v_{max} are aliased (solid black curve), resulting in discontinuities in the Doppler velocity measurements (vertical dashed lines). From Brown and Wood (2007). 18

Fig. 8. (a) Reflectivity (in dBZ) and (b) Doppler velocity (in kt) from KDDC at 0246 UTC on 5 May 2007, showing the Greensburg supercell as an EF-5 tornado was severely damaging the town of Greensburg. The elevation angle is 0.5°, the range rings are spaced 15 km apart, and the spokes are 30° apart. Thin brown lines on the map are Kansas county outlines. One knot (kt) is equal to 0.514 m s^{-1}. Note the "hook echo" reflectivity feature associated with the tornadic vortex signature just over 60

km east-southeast of KDDC, and the Doppler velocity aliasing in both the mesocyclone and the clear-air regions north and south of KDDC. 19

Fig. 9. Illustration of (left) a single, horizontally polarized signal being transmitted from a Doppler radar, compared with a dual (horizontally and vertically) polarized signal. Note that the orthogonally polarized pulses may not be transmitted simultaneously. Image courtesy of NOAA. 20

Fig. 10. Illustration of how standard atmospheric refraction modifies the path of a transmitted radar signal with increasing range from the radar, courtesy of NOAA. .. 24

Fig. 11. The UMass X-Pol radar truck (in 2008) and its attendant crew members (C. Baldi, H. Bluestein, and J. Snyder). Photograph © R. Tanamachi. 25

Fig. 12. VAD retrievals of wind speed (in m s^{-1}) vs. altitude (in m AGL) on 5 May 2007 from (a) KDDC and (b) KVNX radial velocity data. The LLJ is the developing "bulge" in wind speeds at 900 m AGL at KDDC and 700 m AGL at KVNX. Velocities aloft also increased, presumably as a result of synoptic-scale forcing, as a 500 mb trough approached from the west..... 30

Fig. 13. Surface map from 0100 UTC in western Oklahoma and Kansas. Temperatures and dewpoints are in °C. Full wind barbs are 5 m s^{-1}; half-barbs are 2.5 m s^{-1}. Base map from Plymouth State Weather Center; five Oklahoma Mesonet surface observations from the region upstream of the Greensburg storm have been added. The brown dashed line represents the 13 °C isodrosotherm, used as a proxy for the dryline, which was retreating westward through Dodge City. 34

Fig. 14. 500 mb analysis chart from 0000 UTC on 5 May 2007. Solid black contours are the geopotential height in dam; the interval between contours is 6 dam. Dashed

red contours and observations printed in red are the temperature in °C; the interval between contours is 2 °C. On the blue wind barbs, flags are 25 m s^{-1}, full wind barbs are 5 m s^{-1}; half-barbs are 2.5 m s^{-1}. From SPC archives (NOAA).....35

Fig. 15. Tornado 2 (22 km WNW) as seen by the UMass X-Pol radar crew at 0138 UTC. The town of Protection, Kansas is located by the grain elevator on the horizon. Note a second lowering (15 km W) in the foreground near the left edge of the frame; this lowering developed into tornado 3 at 0148 UTC. Photograph © R. Tanamachi; contrast enhanced. 39

Fig. 16. Video frames taken at (a) 0200 UTC and (b) 0204 UTC, showing tornadoes 4 and 5, as well as the remnants of tornado 3, which had dissipated several minutes earlier. Illumination of the scene comes from lightning. The bell-shaped updraft of the Greensburg storn can be seen in panel (b). View is toward the north-northwest in panel (a), and north in panel (b). Tree blockage along the horizon is apparent. For reference, the tree in front of tornado 5 in panel (a) also appears near the left edge of panel (b). Video © R. Tanamachi. 40

Fig. 17. Timeline of Greensburg storm, tornadoes, and radar data collection. KDDC operated continuously; start times of volume scans are given by tick marks. The life span of the Greensburg storm (starting from first detection by KDDC) is indicated by the orange arrow. Green bars indicate the life spans of tornadoes; numbering is as in Table 2. UMass X-Pol deployment times are indicated by red lines / bars. Dashed lines indicate times when single-elevation scans were collected; the solid red line indicates when “shallow” volume scans were collected, and the thick red bar indicates when “deep” volume scans were collected.....42

Fig. 18. UMass X-Pol (a) reflectivity (in dBZ_e) and (b) velocity (in m s^{-1}) data collected at 02:32:49 UTC, at an elevation angle of 2.9°. At this time, the damage track of the mature Greensburg tornado was 2.5 km wide. The UMass X-Pol radar is located at the origin (not shown). Panel (c) shows the Doppler velocity data after manual dealiasing and some editing. Range rings are 15 km apart; spokes are 30° apart. 45

Fig. 19. Comparison of (a) UMass X-Pol equivalent reflectivity factor (in dBZ_e) and (b) KDDC reflectivity (in dBZ) in the Greensburg supercell at about 0231 UTC. Zoom factor is the same in both panels, and elevation angles are chosen so that both radars sample the "core" of the Greensburg storm (with the highest reflectivity values) at an altitude of about 2 km. Range rings are every 15 km, and azimuth spokes every 30°. The radars are located at the origins of their respective polar grids. Note that the color scales differ between the two panels.....48

Fig. 20. The ENU coordinate system, showing how changes in pitch, roll, and yaw of the radar affect the orientation of data with respect to the coordinate axes. Note that the radar truck is depicted symbolically; it may have any orientation in space.....50

Fig. 21. Example of azimuthal (yaw) correction to UMass X-Pol data based upon location of nearby ground clutter targets. The top two panels are enlarged views of (a) unedited UMass X-Pol uncalibrated reflectivity (in dBZe) and (b) unedited, aliased Doppler velocity (in m s^{-1}) collected at 0152 UTC. Range rings are in km; azimuths are every 5 degrees. Panel (c) is a Google Earth satellite image showing the UMass X-Pol deployment site (red truck symbol) in relation to the town of Protection, Kansas. The Protection, Kansas grain elevator (circled in magenta) was easily

identifiable as a clutter target in UMass X-Pol data and was visible from the deployment site (Fig. 15). Based on the Google Earth depiction, the UMass X-Pol data in (a) and (b) were rotated clockwise 1.5 degrees. Two other clutter targets used to correct other UMass X-Pol sweeps are also circled in yellow on panel (c). 51

Fig. 22. UMass X-Pol uncalibrated equivalent reflectivity (Z, in dBZ_e, left column) and dealiased Doppler velocity (V_r, in m s^{-1}, right column) in the hook region of the Greensburg supercell at (a, b) 0139 UTC, 8.8°; (c, d) 0144 UTC, 7.7°; (e, f) 0158 UTC, 3.7°; (g, h) 0207 UTC, 4.0°; and (i, j) 0224 UTC, 9.3°. These images represent (a - d) the early tornado production stage with numerous small, short-lived vortices, (c, d) the transition to a single, long-track tornado production phase, (e, f) the developing phase of the Greensburg tornado, and (g – j) the mature Greensburg tornado with a two satellite tornadoes. Range rings are plotted every 5 km, azimuth spokes every 10°. Vortex signatures associated with tornadoes are numbered according to Fig. 1 and Table 2.....55

Fig. 23. UMass X-Pol-detected vortex signatures (dots, shaded by altitude in m AGL) associated with tornado damage tracks (Table 2). Times (in UTC) of the first and last vortex signatures for each track are indicated; the times for tornado 5 are in bold red text. A gap in the data from 0133 to 0138 UTC results in breaks in the vortex signature tracks for tornadoes 1 and 2. Data collection ceased at 0236 UTC; Greensburg was struck at 0245 UTC. Recall that "shallow" UMass X-Pol volumes were collected until 0216 UTC and "deep" volumes after, so there is more information about the vortex centers at altitudes above 5 km after that time.....57

Fig. 24. As in Fig. 22, but for UMass X-Pol data collected at 0219 UTC at an elevation angle of 4.6°. A possible, brief sub-vortex of tornado 5 is indicated; this feature did not appear in the preceding or succeeding volumes. 60

Fig. 25. UMass X-Pol uncalibrated equivalent reflectivity (Z, in dBZ_e, left column) and dealiased Doppler velocity (V_r, in m s^{-1}, right column) in the Greensburg supercell at 0223 UTC at (a, b) 3.4°; (c, d) 9.8°; and (e, f) 15.5°. At this time, the Greensburg tornado was approaching its peak intensity. Location of the weak-echo notch, BWER, and WEH associated with tornado 5 are indicated. 61

Fig. 26. A pseudo-RHI of UMass X-Pol (a) uncalibrated equivalent reflectivity (in dBZe) and (b) Doppler velocity (in m s^{-1}) at an azimuthal angle of 13.0 degrees (clockwise from north), slicing through the Greensburg tornado during its mature phase at 0228-0230 UTC. Note the northward tilt of the WEC with height, the horizontal vortex / reflectivity curl in the echo overhang (dashed circle), and relatively high reflectivity values near the surface on the far side of the vortex, where large hail was reported.....63

Fig. 27. Illustration from Sullivan (1959) of (a) one-celled and (b) two-celled vortices. The left panels show the flow as seen in a cross-section taken through the center of the vortices; the right panels show the flow as viewed from above. Note that the axial downdraft in the two-celled vortex (bounded by the dotted lines) is associated with divergence.....64

Fig. 28. Illustration from Trapp (2000) of vortex breakdown, in which a vortex (viewed here in cross-section) exhibits one-celled structure close to the surface and

two-celled structure aloft. Shading represents tangential motion with respect to the vortex core; darker shadings indicate faster winds.....65

Fig. 29. Schematic illustration of the superposition of (a) divergent flow or (b) convergent flow on a cyclonic vortex signature in Doppler velocity data. Red (blue) shading indicates flow away from (toward) the radar (which is assumed to be located well south of the features). A real Doppler velocity field generated by an axisymmetric vortex would exhibit some distortion from the geometry of the radar scan; see Brown and Wood (2007) for simulated Doppler velocity signatures of an idealized, convergent vortex. 65

Fig. 30. As in Fig. 22, but for but for UMass X-Pol data collected at (a) 0230 UTC at 12.2°, (b) 0232 UTC at 12.9°, and (c) 0228 UTC at 14.2°. The pairs of panels convey examples of (a, b) a convergent VS, (c, d) a neutral VS, and (e, f) a divergent VS. ..66

Fig. 31. As in Fig. 22, but for but for UMass X-Pol data collected at 0221 UTC at an elevation angle of 3.0°. Locations of a (a) WEH and (b) vortex signature are indicated by small black circles.....69

Fig. 32. Distance between UMass X-Pol-detected WEH and vortex signature (in km) as a function of range (of the vortex signature, in km) from the radar. Note that the distances are strongly discretized by the azimuthal spacing of the UMass X-Pol data (gray contours, every 0.8° starting at 0.4°). 70

Fig. 33. Scatterplot of WEH minus vortex signature range offset (in m) versus azimuthal offset (in deg). Histograms at the top (right) are for azimuthal (range) offset, with a bin width of 0.8° (420 m). 71

Fig. 34. Tracks of UMass X-Pol vortex signatures between 1.5 and 2.0 km AGL (blue dots) and the updraft of the Greensburg storm (green triangles) overlaid on top of tornado tracks. 73

Fig. 35. The (a) *u*- and (b) *v*-components of motion (in m s^{-1}) of the Greensburg storm updraft (solid blue with no markers) and tornadoes (marked lines) as depicted in Fig. 34. The magnitude of the velocity difference between the tornado and the updraft is shown in panel (c). There are no markers for tornadoes 7 and 9 because neither lasted longer than a full UMass X-Pol volume scan, so their velocities could not be computed. 74

Fig. 36. UMass X-Pol (a) uncalibrated equivalent reflectivity (in dBZ_e), (b) dealiased Doppler velocity (in m s^{-1}), and (c) cross-correlation coefficient (unitless) associated with tornado 3 in Greensburg supercell at 0151 UTC at an elevation angle of 3.8°. Tornado 3 is circled in solid black; the dashed black circle highlights a smaller circulation that was not associated with any surveyed surface damage. Red ovals encircle ground clutter targets; these velocity data have been edited out of panel (b). The dashed purple curve is the inferred leading edge of the rear flank gust front. Range rings are every 5 km; azimuth spokes are every 10°. 77

Fig. 37. The position of the RFGF, as inferred from UMass X-Pol equivalent reflectivity and velocity fields, relative to tornado 3 (black circle). Indicated times are UTC on 5 May 2007. 78

Fig. 38. (a, e) UMass X-Pol uncalibrated equivalent reflectivity (in dBZ_e), (b, f) dealiased Doppler velocity (in m s^{-1}), (c, g) Z_{DR} (in dB), and $\tilde{\rho}_{hv}$ (unitless) in the

Greensburg supercell at (a, b, c, d) 0149 UTC, 10.1°; (e, f, g, h) 0231 UTC, 4.1°. Range rings are every 5 km, azimuth spokes every 10°. 82

Fig. 39. As in Fig. 26, but for (a) Z_{DR} (in dB) and (b) $\tilde{\rho}_{hv}$ (unitless). 83

Fig. 40. As in Fig. 22, but for UMass X-Pol data collected at 0145 UTC at an elevation angle of 4.2°. Areas of ground clutter are circled in red on panel (a); associated velocities were edited out of panel (b). The inferred location of the RFGF is denoted by the purple dashed line. 84

Fig. 41. Conceptual illustration of the improvement in likelihood of $p(x_k^a)$ (blue) when observation(s) (red) are assimilated into the prior $p(x_k)$ (green). From Anderson (2005). 89

Fig. 42. As in Fig. 41, but conceptually illustrating one algorithmic approach to the EnKF. Each asterisk (*) represents an ensemble member element. Each perturbed observation (*) is associated with a sample randomly drawn from the prior distribution $p(x_k)$ (*), and each pair is then used to generate a new (posterior) value x_n^f (*). If we can assume the posterior distribution to be Gaussian (blue curve), then we can infer basic information about the true atmospheric state x_k^t. From Anderson (2005). 92

Fig. 43. Conceptual illustration of how assimilation of an observation (red) via EnKF can be used to update prior estimates of unobserved variables. From Anderson (2005), which provides a very clear series of illustrations of how these updates are performed. 94

Fig. 44. As in Fig. 41, but illustrating the EAKF concept. In this example, the EAKF preserves the bimodality of the prior distribution. From Anderson (2005). 96

Fig. 45. Horizontal and vertical grids of the WRF-ARW. From Skamarock *et al.* (2008).....98

Fig. 46. Vertical coordinate system of the WRF-ARW. From Skamarock et al. (2008).....98

Fig. 47. Geometry of a radar sweep at elevation angle θ_e collected by a ground-based radar at the origin. It can be seen that the radar beam sweeps out a conical surface. From Doviak and Zrnić (1993). 104

Fig. 48. Skew-T diagram of the 0000 UTC rawinsonde from Dodge City, Kansas (blue and black curves), showing the deep, dry layer below 700 mb following the dryline passage. Modifications to the sounding that were used in the generation of initial conditions for the EnKF experiments are highlighted in red. 113

Fig. 49. Hodographs of the model initial environmental wind profiles used in the EnKF experiments. The blue (red) curve represents the "vad0100" ("vad0230") wind profile. Altitude labels are in km AGL. The surface velocity components are from the KPTT observation at 0210 UTC on 5 May 2007, those in the 0.3 – 3.0 km layer are from KDDC VAD retrievals, and the upper-level wind profiles are from the DDC sounding taken at 0000 UTC.....115

Fig. 50. Observations used in the construction of the model initial environment. Heights and distances between observing platforms are not to scale. 115

Fig. 51. Objectively analyzed KDDC (a) reflectivity (in dBZ) and (b) Doppler velocity (in m s^{-1}) collected at 0229 UTC at an elevation angle of 0.5°. Observations associated with reflectivity values greater (less) than 20 dBZ were analyzed at (1 km) 2 km grid spacing. The purple dashed circle denotes the 30 km range ring around

KDDC; data inside this radius were discarded for the lowest three elevation angles (0.5°, 0.9°, and 1.3°) in each volume in order to avoid assimilation of data associated with ground clutter targets. 117

Fig. 52. (a) As in Fig. 18c, But after additional editing to remove noisy UMass X-Pol Doppler velocity data. Note that some gates clear UMass X-Pol are retained and dealiased. (b) Objectively analyzed Doppler velocity field produced from data in panel (a), displayed as a scatterplot. Only a portion of the larger objective analysis domain is shown. The values in the farthest ring of range gates from UMass X-Pol (60 km range) did not appear in the Solo II display (panel a) and could not be edited; their values carry over into the objective analysis (panel b). Range rings in panel (a) are in km; azimuth spokes are every 30°. 118

Fig. 53. Computational (blue) and objective analysis (cyan) domain boundaries. The purple box bounds thermal bubbles randomly placed in the initial environment. Tornado damage tracks are plotted in red and numbered according to Table 2. 120

Fig. 54. Prior ensemble mean reflectivity at 0.4 km AGL (in dBZ) at 0200 UTC for experiments (a) kddc_only_0100vad, (b) kddc_only_0230vad, (c) kddc+umass_0100vad, and (d) kddc+umass_0230vad. 128

Fig. 55. As in Fig. 54, but for analyses at 0230 UTC..... 129

Fig. 56. As in Fig. 54, but for ensemble mean vertical vorticity (in 10^{-3} s^{-1}) at 0.1 km AGL. 130

Fig. 57. As in Fig. 56, but for analyses at 0230 UTC..... 131

Fig. 58. As in Fig. 54, but for ensemble mean potential temperature (in K) at 0.1 km AGL (the scalar model level closest to the surface)..... 132

Fig. 59. As in Fig. 62, but for analyses at 0230 UTC..... 133

Fig. 60. As in Fig. 54, but for ensemble mean vertical velocity (in m s^{-1}) at 5.0 km AGL. Note that the color scales differ slightly between panels..... 134

Fig. 61. As in Fig. 60, but for analyses at 0230 UTC..... 135

Fig. 62. Time-height plot of ensemble mean maximum vertical vorticity for experiments (a) kddc_only_0100vad, (b) kddc_only_0230vad, (c) kddc+umass_0100vad, and (d) kddc+umass_0230vad. Times for which UMass X-Pol "shallow" and "deep" volumetric Doppler velocity were assimilated in addition to KDDC reflectivity and Doppler velocity data are delineated in purple. 136

Fig. 63. As in Fig. 62, but for ensemble mean maximum vertical velocity. 137

Fig. 64. (Top) Observation-space diagnostics for Doppler velocity, over 4-minute intervals, for kddc_only_0100vad (red curves), kddc_only_0230vad (blue curves), kddc+umass_0100vad (green curves) and kddc+umass_0230vad (black curves), for the 0 – 1 km AGL layer of the model. The quantities plotted are (solid curves) RMSI and (dashed curve) layer-averaged innovation (model minus observation). Both the prior and posterior diagnostic quantities are plotted; hence the "sawtooth" pattern. (Bottom) The number of objectively analyzed Doppler velocity observations, binned in 4-minute intervals. Thin lines indicate the number of available Doppler velocity observations; the thick lines indicate the number of observations that were actually assimilated into the model. Note that there are many more observations assimilated over this layer from 0115 to 0126 UTC, when UMass X-Pol was collecting single-elevation scans at 3.0° - 4.0°..... 138

Fig. 65. Same as Fig. 64, but for the 5 – 6 km AGL layer of the model. Note that there are many more observations assimilated over this layer between 0215 and 0236 UTC, when "deep" UMass X-Pol volumes were being collected..... 139

Fig. 66. Effects of pitch adjustments of +1° (blue) and -1° (green) on RMSI (solid curves) and layer-averaged-model innovations (dashed curves) for the 0 – 1 km AGL layer in the kddc+umass_0230vad experiments (red). 145

Fig. 67. As in Fig. 66, but for roll adjustments of +1° (blue) and -1° (green)..... 146

Fig. 68. 6-minute wind profiles from the HVLK1, from 2300 UTC on 4 May 2007 to 0300 UTC on 5 May 2007. The direction in which the barb points indicates wind direction, following meteorological convention. Flags are 50 m s^{-1}, full barbs are 10 m s^{-1}, and half-barbs are 5 m s^{-1}. White areas on this plot indicate data that did not pass continuity requirements for quality control. Note that winds below 2 km reach 30 m s^{-1}around 0200 UTC. Courtesy of NOAA. 179

Fig. 69. Velocity profiles from 500 m to 3000 m AGL as measured by HVLK1 at 0000 UTC 0100, and 0200 UTC. No data were reported at 0300 UTC. An LLJ appears to be developing at 0100 UTC; however, by 0200 UTC, the profiler data contain too many gaps in the vertical to infer the presence of the LLJ (Fig. 68). 180

Fig. 70. Signal power (in dB) corresponding to the velocity profiles in Fig. 68. Larger values typically indicate the presence of cloud or precipitation particles, but cannot be interpreted in the same way that "reflectivity" would be. The discontinuity at 8 km ASL results from the juxtaposition of profiler data collected in "low" and "high" mode. 181

Fig. 71. Map of GMD5 in south central Kansas (see inset at upper right). Locations of weather stations are marked in green; Station #1 (the southwesternmost station) is located just north of the city of Greensburg. 182

Fig. 72. Selected data from GMD5 Station #1 (located just north of Greensburg, Kansas) from 4-5 May 2007. Times are in UTC. Averages are calculated and reported at the *end* of each hour; thus the values shown at, e.g., data at 0300 UTC are averages for 0200 – 0300 UTC. Note that wind speeds are scaled by a factor of 10 for visibility. 184

Fig. 73. As in Fig. 48, but for the sounding taken at Lamont, Oklahoma at 0000 UTC on 5 May 2007 185

ABSTRACT

Long-track, violent tornadoes are rare events, but are responsible for a disproportionate majority of tornado fatalities, injuries, and property damage. It has been observed that such tornadoes are often generated as part of a series produced by one supercell, and preceded by one or more smaller tornadoes. At some point, a transition in the tornado production mode occurs, from short-track, cyclic tornado production (mode I), to long-track, single (plus satellite) tornado production (mode II). This transition has been documented only a few times at close range by Doppler weather radars.

A cyclic, tornadic supercell ("the Greensburg storm") generated at least 22 tornadoes in southwest Kansas on 5 May 2007. One of these was the first documented EF-5 tornado ("the Greensburg tornado"), which destroyed 95% of the buildings in Greensburg, Kansas and caused 11 fatalities. The University of Massachusetts X-band, polarimetric, mobile Doppler radar (UMass X-Pol), which was operating in the area as part of a severe storms research project, collected data in the Greensburg storm for over an hour, including its transition from tornado production mode I to mode II. The first 10 tornadoes produced by the Greensburg storm can be seen in this UMass X-Pol data set.

In this study, the UMass X-Pol data (as well as contemporaneous data from the WSR-88D at Dodge City, Kansas, or KDDC) are analyzed with the aim of diagnosing whether this transition occurred as a result of changes in the environmental wind profile, interaction of tornadoes with the storm's cold pool, or a combination of the two. These efforts met with limited success, largely because of the

relative scarcity of observations of low-level flow in the inflow sector of the Greensburg storm. However, in the process, features of the Greensburg storm related to tornado production (such as vortices, updrafts, and polarimetric signatures) are documented, and relationships among them before, during, and after this transition are diagnosed. In particular, it is found that:

- The horizontal motions of the earlier tornadoes (mode I) tracked to the left with respect to the updraft motion, while the motion of the Greensburg tornado and its satellites (mode II) more closely matched that of the updraft.
- The vortex signatures in the UMass X-Pol data matched with the surveyed damage tracks. In addition, several non-tornadic circulations were documented.
- A forward surge and retreat of a RFGF was documented a few minutes before the development of the Greensburg tornado.
- At least two cyclonic-anticyclonic pairs of satellite tornadoes (of the Greensburg tornado) occurred, possibly indicating the upward arching of low-level horizontal vortex lines over bulges in the RFGF.
- Weak-echo holes are documented in several tornadoes, and found to be consistently collocated with corresponding vortex signatures in azimuth but biased slightly far from the radar in range.
- A polarimetric tornadic debris signature is found near the surface in the mature Greensburg tornado. In addition, a Z_{DR} arc is documented whose presence corroborates increasing low-level vertical wind shear in the inflow

sector. Other polarimetric supercell features are consistent with those found in previous studies.

In an attempt to retrieve in-storm variables not observed by radar, KDDC and UMass X-Pol radar data were assimilated into a numerical weather prediction model using the ensemble Kalman filter (EnKF) technique. Two sets of experiments were performed, one in which UMass X-Pol data were either included or withheld from assimilation with KDDC data, and another in which the 0 – 3 km AGL initial environmental wind profile was modified to include a low-level jet, or not.

Assimilation of UMass X-Pol data results in more pronounced changes to the analyses than the addition of a low-level jet, although both changes result in near-surface vortices that are stronger, deeper, and longer-lived than in experiments without. When UMass X-Pol data are assimilated, vortices appear in the analyses that correspond to mode I tornadoes, and the southward-spreading, surface cold pool from the Greensburg storm (which likely results from the use of a relatively simple microphysical parameterization scheme) deflects around the assimilated observations of southerly flow at the UMass X-Pol deployment site. Neither of these features appear when UMass X-Pol data are withheld.

I close by discussing the implications of these results for future avenues of research involving analysis and assimilation of data from mobile Doppler radars, including storm-scale prediction.

Chapter 1 Introduction

1.1 Motivation

Violent tornadoes (those rated F-4 or F-5 on the Fujita scale or EF-4 or EF-5 on the enhanced Fujita scale) are a very rare phenomenon, but cause a disproportionate majority of tornado fatalities and property damage. Grazulis (1993) tabulated that only 2% of all U.S. tornadoes between 1950 and 1991 were violent, but caused 67% of tornado fatalities during that period. More recent examples of such violent tornadoes include the 3 May 1999 Moore / Bridge Creek, Oklahoma F-5 tornado, the 5 May 2007[1] Greensburg, Kansas EF-5 tornado (hereafter "the Greensburg tornado"), and the 25 May 2008 Parkersburg, Iowa EF-5 tornado. The supercell that produced the Greensburg tornado is the focus of this dissertation.

Such violent tornadoes often occur as part of a series of tornadoes produced by a single parent storm. Cyclic tornadogenesis, the process whereby a single storm generates a series of tornadoes (Darkow and Roos 1970; Burgess *et al.* 1982), has been documented numerous times using airborne or ground-based mobile Doppler radars (e.g., Burgess *et al.* 2002; Dowell and Bluestein 2002b, 2002a; Alexander and Wurman 2005; Wurman *et al.* 2007; French *et al.* 2008; MacGorman *et al.* 2008). A cyclic, tornadic supercell (CTS) *may* exhibit multiple, distinct tornado production "modes" with the following general characteristics:

(I) the storm produces a series of relatively weak (e.g., ≤ F3 or EF-3), short-track tornadoes in a cyclic manner at nearly-regular intervals; or

[1] Speaking historically, the date of the Greensburg storm is 4 May 2007, because the tornado struck Greensburg at about 9:45 p.m. local time (21:45 CDT) on that day. For the purposes of this study, however, we will follow meteorological convention and use UTC time hereafter; e.g., 21:45 CDT on 4 May 2007 corresponds to 0245 UTC on 5 May.

(II) the storm produces a long-track, violent[2] (e.g., ≥ F-4 or EF-4) tornado (and possible accompanying satellite tornadoes).

One might characterize tornado production modes as a sliding spectrum, rather than discrete categories. It is primarily because of the vast differences in potential human impact (as denoted by their EF-scale ratings) that I chose to delineate the two modes in this study.

Numerous examples of CTSs exhibiting both mode I and mode II tornado production have been documented (e.g., Fujita 1960; Alberty *et al.* 1980; Dowell and Bluestein 2002b, 2002a; Speheger *et al.* 2002). Additionally, a CTS may transition multiple times between tornado production modes I and II (e.g., Lemon and Umscheid 2008).

A very limited number of mobile Doppler radar data sets exists which document the transition of a CTS from tornado production mode I to mode II (Dowell and Bluestein 2002b, 2002a; Alexander and Wurman 2005). The number of such data sets is necessarily limited by the rare combination of circumstances required for data collection: a mobile Doppler radar must be collecting data in a CTS, at least one violent tornado must be documented, and at least one weaker tornado *preceding* the violent tornado(es) must be documented as well. Successful and safe deployment of a mobile Doppler radar under such circumstances requires a great deal of forecast skill, patience, situational awareness, and sometimes, luck (Bluestein and Wakimoto 2003).

On 5 May 2007, a severe storm research team from the University of Oklahoma, using the University of Massachusetts, mobile, X-band, polarimetric

[2] Although tornado path length is correlated with intensity (Brooks 2004), it is important not to conflate the two qualities.

Doppler radar (UMass X-Pol; Bluestein *et al.* 2007a), collected volumetric Doppler velocity and reflectivity data during the early life cycle of the 5 May 2007 Greensburg, Kansas CTS (hereafter "the Greensburg storm"; Fig. 1). These data were collected for over one hour (0126 – 0236 UTC), sampling velocities in ten tornadoes that produced surface damage during this period, capturing the genesis of an EF-5 tornado, and documenting the transition of the Greensburg storm from tornado production mode I to mode II (which occurred around 0200 UTC). This mobile Doppler radar data set, while far from being the first collected in a CTS, is one of only a handful to document such a transition.

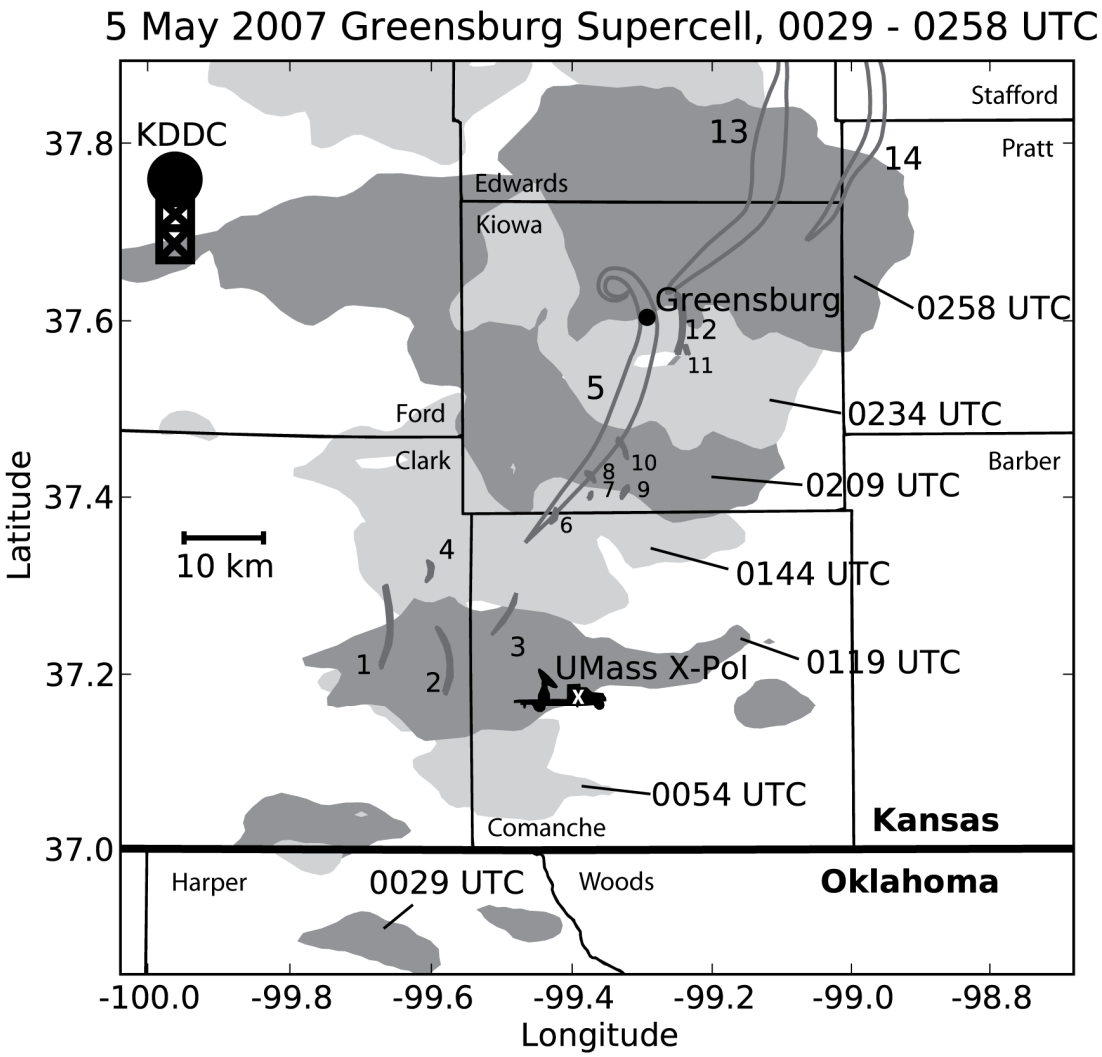


Fig. 1. Objectively analyzed regions of KDDC reflectivity greater than or equal to 35 dBZ at 1.5 km AGL between 0029 and 0258 UTC on 5 May 2007. For clarity, contours for every sixth volume are shown, and shaded in alternating light and dark gray. Surveyed tornado damage tracks are plotted in heavy gray contours and numbered chronologically (following Lemon and Umscheid 2008). The locations of KDDC, UMass X-Pol, and Greensburg, Kansas are marked. Thin black lines denote county boundaries, and the heavy black line denotes the border between Kansas and Oklahoma. Tornado damage tracks are courtesy of J. Hutton of the NWS – Dodge City, Kansas forecast office.

The Greensburg storm was significant in a number of regards:

(1) it produced the first EF-5 rated tornado since the introduction of the Enhanced Fujita Scale (LaDue and Mahoney 2006) by the U.S. National Weather Service (NWS) in early 2007 and the strongest U.S. tornado since the 3 May 1999

Moore / Bridge Creek, Oklahoma F-5 tornado (McCarthy *et al.* 2007; Lemon and Umscheid 2008);

(2) it caused 12 fatalities, 11 of them in the town of Greensburg, Kansas, which was 95% destroyed by the afore-mentioned EF-5 tornado (shown in Fig. 2) (Lemon and Umscheid 2008; Marshall *et al.* 2008);

(3) it had an unusually long period of tornado production, generating at least 22 tornadoes over 6 hours (Lemon and Umscheid 2008); and

(4) it had a complex origin, being the 14th in a sequence of splitting storms, possibly complicating prediction efforts (Bluestein 2009).



Fig. 2. The Greensburg tornado, illuminated by lightning, as seen from 29 km southwest of Greensburg, Kansas at 0234 UTC. At this time, its damage path was at least 1.5 km wide. View is toward the north-northeast. Photograph courtesy of R. Fritchie.

1.2 Statement of hypothesis

The unusual intensity and longevity of the Greensburg tornado makes it an outlier event (Lemon and Umscheid 2008). I hypothesized that either the Great Plains nocturnal low-level jet (LLJ), the cold pool underneath the Greensburg storm, or a combination of both, acted to organize the Greensburg storm such that the horizontal motion of the Greensburg tornado (and associated low-level mesocyclone; mode I) more closely matched that of the updraft than did the motions of previous tornadoes

(mode II). The LLJ could have modified the inflow environment of the Greensburg storm such that the horizontal motions of low-level (0 to 2 km AGL) mesocyclones matched that of the updraft. The cold pool, produced on the rear flank of the Greensburg storm, may have moved the bottom portion of tornado vortices in such a manner as to hasten or hinder their demise. As will be seen, ascertaining the roles of these two processes proved challenging, and more so in the latter case than the former.

Dowell and Bluestein (2002a) observed that, in the 8 June 1995 Kellerville, Texas CTS, "*the cyclic tornadogenesis process was associated with a mismatch between the horizontal motion of successive tornadoes and the horizontal velocity of the main storm-scale updraft and downdraft*" (their emphasis). In the context of this study, this description refers to mode I tornado production. Similar suggestions have been made by Bluestein (2009) with respect to the Greensburg storm and by French *et al.* (2008) with respect to another instance of radar-observed cyclic tornadogenesis. It will be seen that these features were also horizontally "synchronous" in the case of the Greensburg tornado (mode II), and less so in the case of prior tornadoes (mode I), possibly owing to discontinuous propagation of the updraft.

The original goal of this research was to evaluate the conceptual models of cyclic tornadogenesis developed by Dowell and Bluestein (2002b, b) by assimilating the UMass X-Pol data set into a high-resolution, numerical weather prediction (NWP) model, and using the ensemble Kalman filter (EnKF) technique to retrieve unobserved variables. However, as will be discussed, reliable near-surface (< 1.0 km AGL) wind observations in the inflow region of the Greensburg storm, a crucial

component of their conceptual model, could not be inferred with confidence at all times owing to sparse observations in the inflow region, and had to be prescribed based on educated guesses. In addition, the boundary layer wind profile was rapidly evolving during this transition phase owing to the onset of a low-level jet (LLJ), and these changes could not be represented well in the numerical experiment setup. Finally, computational constraints prevented me from producing simulations of the hook region of the Greensburg supercell with adequate horizontal grid spacing ($\leq$ 500 m) to resolve any of the mode I tornadoes reliably. However, the Greensburg tornado, owing to its exceptionally large diameter, was easily simulated on even a relatively coarse (1 km horizontal) grid, and storm-scale features of the Greensburg storm could be simulated and analyzed.

In the process of studying the UMass X-Pol data, I ended up performing a fairly thorough "forensic analysis" of many features of the Greensburg storm. The Greensburg storm proved a prolific producer of vortices (including multiple cyclonic-anticyclonic tornado pairs) and polarimetric tornadic debris signatures. A rear-flank gust front was also documented near UMass X-Pol at the time the mode I-to-mode II transition occurred. It is this observational research that comprises the bulk of this dissertation, with frequent references back to the overarching theme of horizontally synchronous supercell features.

1.3 Overview of dissertation

This dissertation is organized as follows. In Chapter 2, introductory material regarding the LLJ, radar meteorology, and radar data assimilation is presented. In Chapter 3, a meteorological overview of the events surrounding the Greensburg storm

and tornado is provided, and the deployment of the UMass X-Pol radar in the Greensburg storm described. The UMass X-Pol radar data are catalogued and some data quality issues are discussed and addressed in Chapter 4. In Chapter 5, available observations of the transition of the Greensburg storm from tornado production mode I to mode II are documented and analyzed. The UMass X-Pol data are chiefly emphasized, while data from a number of other sources such as the U.S. National Weather Service (NWS) Weather Surveillance Radar – 1988 Doppler (WSR-88D) at Dodge City, Kansas (KDDC), are also used to characterize features of the Greensburg storm related to tornado production (e.g., tornadoes, mesocyclones, and updrafts). In Chapter 6, a set of EnKF analyses are described, the impact of assimilating UMass X-Pol data evaluated, and effects of varying initial environmental low-level wind profiles examined. Principal conclusions are reiterated in Chapter 7.

Several appendices containing supplementary information are also provided. In particular, Appendix E lists expansions of abbreviations and symbols used frequently throughout this document.

Chapter 2 Background

2.1 Cyclic tornadic supercells

The Greensburg storm was, by all accounts, a powerful CTS, producing at least 22 tornadoes. It has been known for over four decades that multiple tornadoes can be produced by the same storm in a periodic or quasi-periodic fashion; studies documenting such cases are reviewed in Davies-Jones *et al.* (2002) and Dowell and Bluestein (2002b). Agee *et al.* (1976) described this phenomenon in the context of repeating, cycloidal tornado damage tracks, and suggested that some storms exhibit combinations of both "series" and "parallel" cyclic tornado modes (Fig. 3).

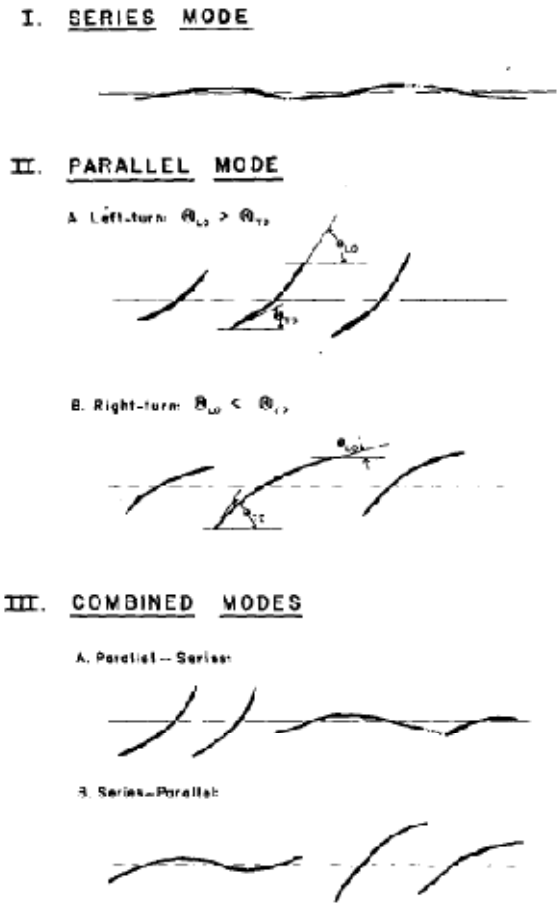


Fig. 3. Conceptual models of (I) "series" and (II) "parallel" tornado damage tracks, and (III) combinations thereof. In this figure, Θ_{TD} (Θ_{LO}) is the angle between the storm and tornado motion vectors at tornado formation (decay). From Agee *et al.* (1976); adapted from Fujita *et al.* (1970).

Cyclic tornadogenesis occurs almost exclusively in supercell thunderstorms (supercells). The reader is referred to reviews by Klemp (1987, b), Bluestein (1993, 2007), Davies-Jones et al. (2002), and Markowski and Richardson (2010) of the physical processes underlying supercells; only a brief review is given here. Supercells, by definition (Glickman 2000), possess at least one persistent, rotating updraft called a mesocyclone (where the prefix "meso-" refers to atmospheric horizontal length scale on the order of 10 – 1000 km; Fujita 1981). Cyclonic rotation at mid-levels (3 – 6 km) occurs as a consequence of ambient vertical wind shear in the environment (Fig. 4). The ambient vertical wind shear is associated with horizontal vorticity, which is then tilted into the vertical by the updraft (Klemp 1987). The area beneath the mesocyclone updraft has been observed to be a favorable location for tornadoes (Davies-Jones 1986). In a mature supercell, a rear-flank downdraft (RFD) may form as a consequence of a downward-directed dynamical pressure gradient associated with a low-level mesocyclone. An RFD may also be enhanced by the effects of evaporative cooling and/or precipitation loading (Bluestein 2007; Markowski and Richardson 2010) and is often manifest visually as a "clear slot" (Lemon and Doswell 1979; Markowski 2002). At low levels, such a mesocyclone consists of a pairing of both an updraft and a downdraft and is called a "divided mesocyclone" (Lemon and Doswell 1979).

The mesocyclone may itself undergo cyclic formation and decay (Davies-Jones *et al.* 2002; French *et al.* 2008) as the less buoyant air in the RFD undercuts (occludes) the source region for the mesocyclone and new updrafts develop as a result of lift above the rear-flank gust front (Fig. 5). Cyclic tornadogenesis may occur as a

result of, or largely separate from, cyclic mesocyclogenesis. Adlerman and Droegemeier (2002, 2005) investigated the sensitivity of cyclic mesocyclogenesis to parameters of an NWP model; their results show tremendous sensitivity to model parameters such as horizontal grid spacing, microphysical parameterization scheme, and numerical diffusion scheme (Stensrud 2007). (Later in this study, when we simulate the Greensburg storm using an NWP model, we adopt a relatively simplified framework and hold it constant through all experiments.)

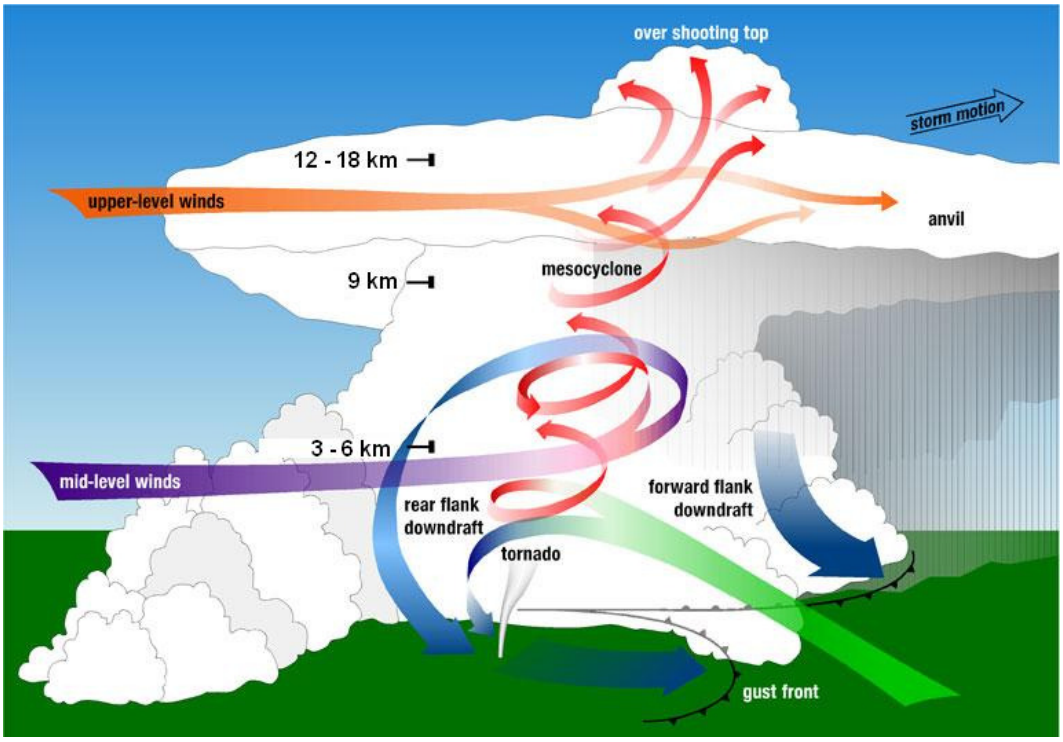


Fig. 4. Schematic diagram of a mature, cyclonic supercell thunderstorm in the Northern Hemisphere as viewed from the south, with common features highlighted. Note the ambient vertical wind shear in the environment, and the locations of the mesocyclone, tornado, forward flank downdraft (FFD), rear flank downdraft (RFD), and surface gust fronts. Courtesy of National Severe Storms Laboratory (NSSL).

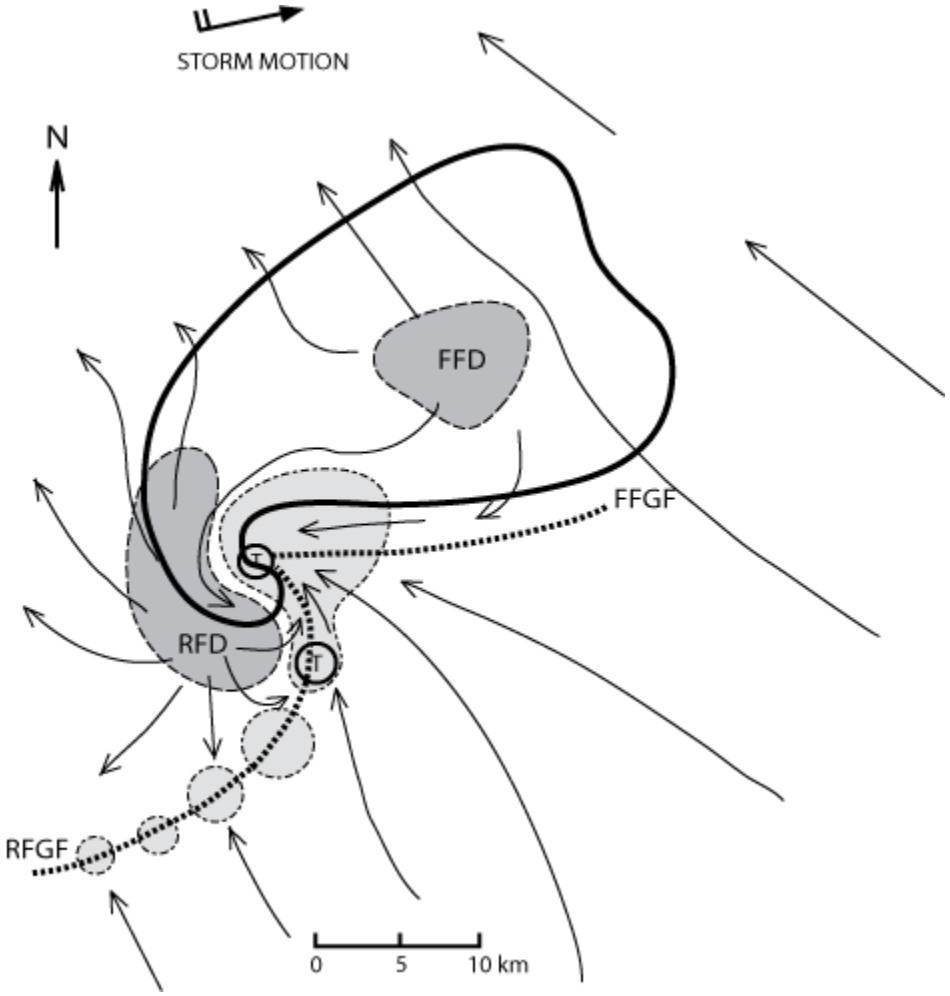


Fig. 5. Plan view diagram of the low-level (i.e., below 2 km AGL) air flow patterns in and around a mature supercell thunderstorm as depicted in Fig. 4. The locations of the FFD and RFD are shaded dark gray; the surface forward flank gust front (FFGF) and rear-flank gust front (RFGF) are denoted by stippled lines. The primary supercell updraft (UD) and smaller updrafts along the RFGF are shaded light gray. The southern "T" represents a favorable location for tornado development and the northern "T" a favorable location for tornado decay. Note that, in this depiction, the storm-relative motion of the tornado is to the left of the overall storm motion. Adapted from Lemon and Doswell (1979) and Davies-Jones (1986).

Davies-Jones *et al.* (2002) posit two distinct mechanisms responsible for cyclic tornado formation and decay: (1) kinematic occlusion of the tornado and parent mesocyclone by cold air and subsequent generation of a new low-level vorticity maximum to the right (with respect to storm motion) of the old one, as described above (e.g., Wurman *et al.* 2007), and (2) rearward advection of the tornado, away from the parent updraft, by low-level front-to-rear storm-relative inflow (e.g., Dowell

and Bluestein 2002a). Knowledge of the air flow at low altitudes (< 1 km AGL) is necessary to distinguish which of the two mechanisms, if either, is responsible for the cyclic tornadic phase of a supercell thunderstorm. The Greensburg storm had a cyclic tornadic phase early in its life cycle, before producing the long-track Greensburg tornado (Fig. 1).

Dowell and Bluestein (2002a) indicated that the horizontal motion of the tornadoes in the 8 June 1995 McLean, Texas supercell was controlled in large part by the near-surface (< 1.0 km AGL) storm-relative inflow. In addition, Esterheld and Guiliano (2008) found that 10 – 500 m bulk shear was a good discriminator between tornadic and non-tornadic environments. A hodograph constructed from the Pratt, Kansas (KPTT) surface observation and velocity-azimuth display (VAD) analyses from the WSR-88D at Vance Air Force Base, Oklahoma (KVNX), thought to represent the environment in the inflow of the Greensburg storm, was included in their study as a prime example.

Limited information exists regarding the near-surface wind fields in and around the Greensburg storm. There is a sparse region in NWS and Kansas mesonet surface observing capability southeast of Dodge City and southwest of Greensburg. The nearest automated surface observing station to Greensburg is KPTT, 50 km to the east, much too far away to sample the inflow in the time frame in question. Some UMass X-Pol data were collected in the inflow sector of the Greensburg storm; these data will be more thoroughly discussed in Chapter 4. Other observations that were not used in this study are listed in Appendix B.

2.2 Radar meteorology

2.2.1 Introduction

The Greensburg storm will be investigated chiefly via analysis of data collected by nearby Doppler radars. Doppler weather radar has proven to be an invaluable tool in severe storm detection, forecasting, and research for the past several decades. In general terms, a Doppler radar emits focused pulses of microwave energy from an antenna, and the returned (backscattered) signal can be used to map precipitation patterns and atmospheric velocities in the path of the beam. Modern pulsed-Doppler radar systems can remotely collect information about thunderstorm structure and evolution over relatively short time scales (on the order of minutes) and large volumes (on the order of thousands of cubic kilometers). The reader is referred to Doviak and Zrnić (1993) and Rinehart (1997) for a comprehensive review of the history of modern Doppler radar, radar theory, hardware, signal processing, and meteorological applications.

While many conventional weather radar systems (such as the WSR-88D) operate from a fixed location, mobile Doppler radar (often mounted on a truck, ship, or airborne platform) can be moved closer to and more intensely sample an area of interest. Bluestein and Wakimoto (2003) discuss the history and development of mobile Doppler radars for studies of severe convective storms. Since their origination in the 1980s, mobile Doppler radars have varied widely in design, from portable, tripod-mounted FMCW Doppler systems that had to be partially assembled prior to data collection (Bluestein and Unruh 1989), to airborne scanning radars used during the Cooperative Oklahoma Profiler Studies program (COPS-91; Hane *et al.* 1993) and

Project VORTEX (Verification of the Origins of Rotation in Tornadoes Experiment; Wakimoto *et al.* 1996), to more recent land-based phased array radars (Bluestein *et al.* 2010).

2.2.2 Radar data

2.2.2.1 Reflectivity and velocity

Doppler radar data consist of reflectivity factor (Z) and Doppler radial velocity (v_r) fields.[3] Is it common for "reflectivity factor" to be shortened to "reflectivity" in meteorological literature, even though reflectivity (η) is actually a slightly different quantity (Doviak and Zrnić 1993). Nonetheless, I will refer to reflectivity factor as "reflectivity" hereafter.

In this context, reflectivity is a measure of average backscattering cross-section per unit volume. "Scatterers" are anything in the path of the radar beam that can absorb and re-radiate microwave energy (precipitation particles, aerosols, insects, birds, and so forth). Z has the strange units of $\text{mm}^6\ \text{m}^{-3}$, a consequence of Z containing a factor of D^6, where D is the diameter of liquid water drops. (Hail and other frozen hydrometeors have different scattering properties which will be discussed in more detail shortly.) In the atmosphere, Z can span many orders of magnitude and is therefore given in the logarithmic units dBZ, where $Z(\text{dbZ}) = 10\log_{10} Z$. Z can range from values of -30 dBZ in clear air to 60 dBZ or higher in heavy precipitation and hail shafts (Doviak and Zrnić 1993).

[3] Spectrum width, the second moment of the radar observation, may also be recorded. While spectrum width can be used to make inferences about the variability of velocities within a radar volume, the interpretation of these data is tricky. Currently, spectrum width data are not commonly assimilated into NWP models.

The backscattered radar signal varies as a function of both wavelength λ and D, creating a number of different scattering "regimes." The two regimes of primary concern to radar meteorologists are Rayleigh scattering, which predominates when $D << \lambda$, and is relatively uniform in terms of forward and backward scattering of electromagnetic radiation, and Mie scattering, which predominates when $D \sim \lambda$, and results in most incident radiation being scattered forward instead of backward (Fig. 6). In general, the backscattered signal decreases as the scatterer diameter approaches the wavelength. Conversely, the same size scatterer will return more of the transmitted signal in the Rayleigh regime (longer λ) than in the Mie regime (shorter λ).

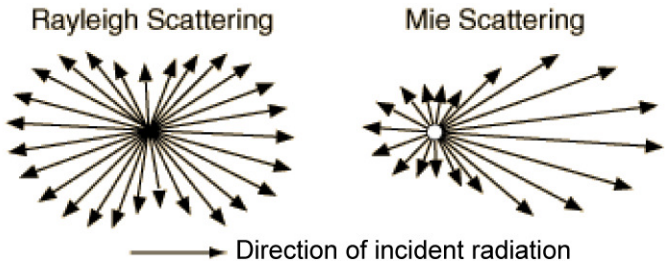


Fig. 6. Illustration of Rayleigh vs. Mie scattering regimes for incident electromagnetic radiation, courtesy Georgia State University.

More energy is scattered out of the radar beam or absorbed by scatterers as the signal traverses longer distances, resulting in a decrease in backscattered signal with distance. This phenomenon is known as attenuation, and it is particularly acute at wavelengths where the Mie scattering regime dominates. The concepts of scattering regimes and attenuation will become important in later discussions in which the WSR-88D and UMass X-Pol radar data collected in the same regions of the Greensburg storm are compared.

Doppler velocity v_r is an estimate of the velocity of scatterers in a volume moving radially away from (positive) or towards (negative) the radar. Generally speaking, values of v_r are more reliable where signal-to-noise ratio (and, often, reflectivity) values are higher. The value of v_r is derived from the predominant frequency shift of the backscattered microwave signal; Doviak and Zrnić (1993) derive the estimators of v_r. Because the incoming data stream is sampled at a finite frequency, the potential for ambiguity (aliasing) of the calculated Doppler velocity exists. Each radar has a characteristic maximum unambiguous velocity value (v_{max}; sometimes called the "Nyquist velocity"); velocity values greater than v_{max} are cyclically aliased to low values of velocity and vice versa (Fig. 7). Velocity aliasing usually appears as sharp discontinuities in the velocity field that can be identified and mitigated (dealiased) by a researcher or by an automated algorithm (Brown and Wood 2007). As will be discussed in the next two subsections, the Doppler velocity data collected in the Greensburg storm by both the KDDC (e.g., Fig. 8) and UMass X-Pol radars exhibited velocity aliasing, and were manually dealiased prior to analysis.

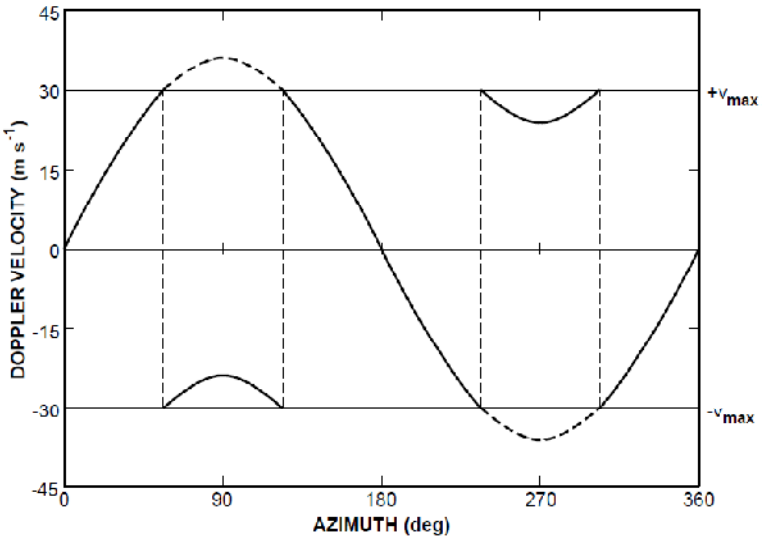


Fig. 7. An example of Doppler velocity aliasing. In this case, a Doppler radar with a v_{max} of 30 m s^{-1} executes a full 360° azimuthal scan at a fixed elevation angle. The winds are westerly (from 270°) at 36 m s^{-1}; expected Doppler velocity measurements are given by the sinusoidal curve. Doppler velocities greater than v_{max} are aliased (solid black curve), resulting in discontinuities in the Doppler velocity measurements (vertical dashed lines). From Brown and Wood (2007).

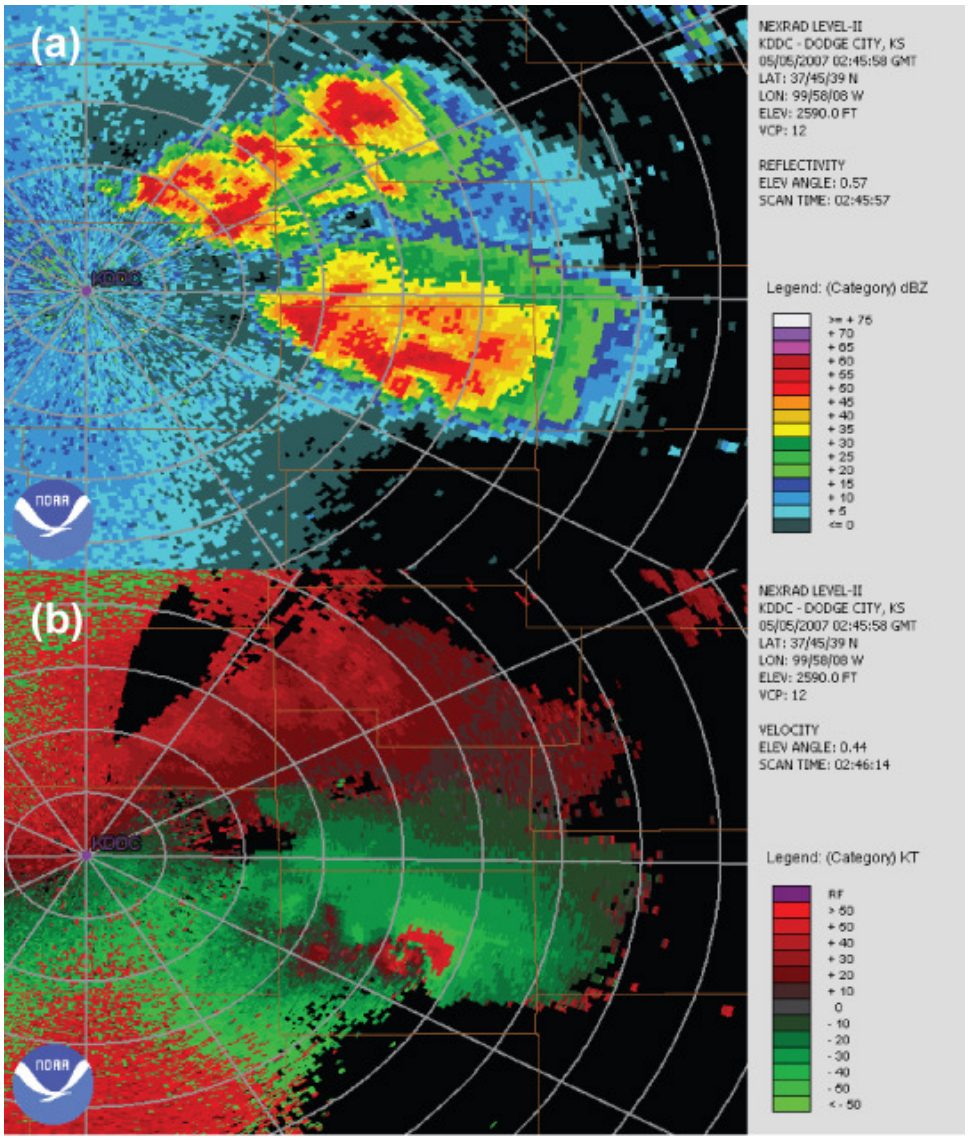


Fig. 8. (a) Reflectivity (in dBZ) and (b) Doppler velocity (in kt) from KDDC at 0246 UTC on 5 May 2007, showing the Greensburg supercell as an EF-5 tornado was severely damaging the town of Greensburg. The elevation angle is 0.5°, the range rings are spaced 15 km apart, and the spokes are 30° apart. Thin brown lines on the map are Kansas county outlines. One knot (kt) is equal to 0.514 m s^{-1}. Note the "hook echo" reflectivity feature associated with the tornadic vortex signature just over 60 km east-southeast of KDDC, and the Doppler velocity aliasing in both the mesocyclone and the clear-air regions north and south of KDDC.

2.2.2.2 Polarimetric variables

In some Doppler radars, the polarization of the transmitted pulses can be controlled and sequenced. A common paradigm, known as dual polarization, involves transmission of specified sequences of horizontal or vertical linearly polarized pulses

(Fig. 9). In this case, additional variables relating to the horizontally and vertically polarized backscattered signal and phase are recorded and information may thereby be inferred regarding the shape and orientation of the scatterers. The interested reader is referred to the introductory chapter of Bringi and Chandrasekar (2001) for more information about this topic. Use of polarimetric radars in meteorological applications is increasingly common; nationwide polarimetric upgrades to the WSR-88D network will occur in the near future (Doviak *et al.* 2000).

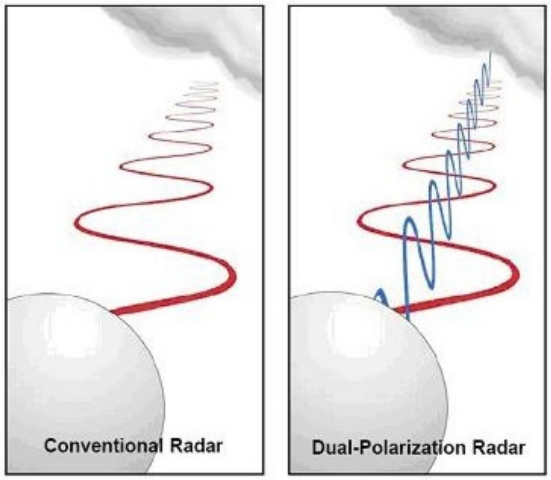


Fig. 9. Illustration of (left) a single, horizontally polarized signal being transmitted from a Doppler radar, compared with a dual (horizontally and vertically) polarized signal. Note that the orthogonally polarized pulses may not be transmitted simultaneously. Image courtesy of NOAA.

Two different reflectivity values are usually reported from a dual polarization radar, one from the received backscattered horizontally polarized signal (Z_{hh}) and the other from the vertically polarized signal (Z_{vv}). These polarimetric reflectivity values may be different for the same volume of air, depending on the shape and orientation of the scattering particles. Z_{hh} and Z_{vv} are proportional to time-averaged backscattering covariance power variables $H = \langle E_h E_h^* \rangle$ and $V = \langle E_v E_v^* \rangle$, respectively (Doviak and Zrnić 1993).

Smaller rain drops (< 2.5 mm) are, in general, spherical, while larger drops (> 2.5 mm) are more oblate (flat), a consequence of deformation resulting from air drag as they fall. Large drops tend to scatter more (less) of the horizontally (vertically) polarized signal back to the radar (i.e., anisotropic scattering), so that Z_{hh} will be greater than Z_{vv} for a volume of air containing predominantly large drops. Small, spherical drops scatter about equal amounts of horizontally and vertically polarized energy back to the radar (i.e., isotropic scattering), so that $Z_{hh} \approx Z_{vv}$ if the same volume of air contains predominantly small drops.

Differential reflectivity (Z_{DR}) is defined as $Z_{DR}(\mathrm{dB}) = 10\log_{10}\left(\frac{Zhh}{Zvv}\right) = 10\log_{10}\left(\frac{\langle E_h E_h^* \rangle}{\langle E_v E_v^* \rangle}\right)$, and is used to obtain a sense of the relative proportions of large and small drops in the radar volume. For large (oblate) drops, Z_{DR} tends to be + 5-10 dB. For small, nearly spherical drops, Z_{DR} is close to zero. Large hail, on the other hand, tumbles as it falls, resulting in near-isotropic scattering; it also generates values of Z_{DR} near zero. However, Z_{hh} from hail will be much higher than it is from small drops, potentially allowing for discrimination between small drops and hail based on combined Z_{hh} and Z_{DR} fields.

Correlation coefficient between *H* and *V* at zero lag ($\rho_{hv}[0] = \frac{|\langle E_h E_v^* \rangle|}{\sqrt{\langle E_h E_h^* \rangle \langle E_v E_v^* \rangle}}$, or simply ρ_{hv}) is predominantly used to discriminate between meteorological and non-meteorological scatterers. In general, meteorological scatters exhibit greater uniformity in size and orientation (and thus, higher ρ_{hv} values) than non-meteorological targets such as debris, vegetation, bioscatterers, and military chaff. Values of ρ_{hv} range from 0.96 - 0.99 for small, nearly-uniform hydrometeors, to 0.85

– 0.95 for hail or wet ice aggregates, to anomalously low values (< 0.85) for non-meteorological targets. Tornadic debris has been observed to have ρ_{hv} values as low as 0.50 (Ryzhkov *et al.* 2005).

Strong attenuation frequently occurs in heavy precipitation cores at X-band. In this case, calculated values of ZDR will be less precise, and ρhv will decorrelate much more quickly than if attenuation were not present.

Other variables related to the differential phase Φ_{DP} between H and V are regularly calculated, and used to infer, for example, the presence of heavy rain. The However, these variables will not be used in this study for reasons to be discussed later. The interested reader is referred to Doviak and Zrnic (1993) for additional information.

2.2.3 Radars used in this study

2.2.3.1 The Dodge City, Kansas WSR-88D (KDDC)

The WSR-88D is an S-band (10 cm wavelength), scanning, pulsed-Doppler radar system that provides volumetric reflectivity, radial velocity, and spectrum width data (Crum and Alberty 1993; Doviak and Zrnić 1993; Research 2008). Some characteristics of the WSR-88D are given in Table 1. The NWS currently operates 150 WSR-88Ds across the continental United States as part of its Next Generation Weather Radar (NEXRAD) program (Rinehart 1997; Crum *et al.* 1998). The nationwide WSR-88D network provides near-continuous radar coverage above 3 km AGL across most of the United States and its territories and is credited, among other things, with reducing the expected number of U.S. tornado fatalities by 45% and increasing the mean tornado warning lead time from 5.3 to 9.5 min (Simmons and

Sutter 2005). Tornado warnings and tornado emergencies issued for the Greensburg storm by forecasters from the NWS forecast office in Dodge City, Kansas were based largely on the storm's presentation on their WSR-88D display (M. Umscheid, personal communication; Fig. 8).

Table 1. A comparison of 2007 characteristics of the WSR-88D and UMass X-Pol radars.

Radar	**WSR-88D**	**UMass X-Pol**
Type	Stationary	Mobile
Wavelength	10 cm	3 cm
Half-power beamwidth	1.0°	1.2°
Peak power	475 kW	25 kW
Max. unambiguous range	231 km	75 km
Max unambiguous velocity	32.5 m s^{-1}	19.2 m s^{-1}
Range gate spacing	1 km (Z), 250 m (v_r)	150 m
Max. azimuthal scan rate	30° s^{-1}	24° s^{-1}
Polarimetry	Single	Dual

WSR-88Ds have a number of different volume coverage patterns (VCPs) available, and forecasters at each office have the option of switching between them depending on what type of observations they wish to collect. For severe convective events, a commonly used coverage pattern is VCP 12, in which the WSR-88D scans 360 degrees in azimuth at 14 different elevation angles (or "tilts", denoted θ_e[4]) ranging from 0.5° to 19.5°. The average time between successive volumes is 4.1 min. Owing to a combination of the earth's curvature and atmospheric refraction, the radar

[4] The symbol θ_e is commonly used in meteorological literature to denote equivalent potential temperature, but in this study, θ_e will be used exclusively to denote elevation angle.

signals do not travel along a straight line with respect to the plane of the earth's surface, but tilt slightly upward (Fig. 10). For example, a storm 60 km from the radar would be sampled at altitudes at and above about 600 m AGL.

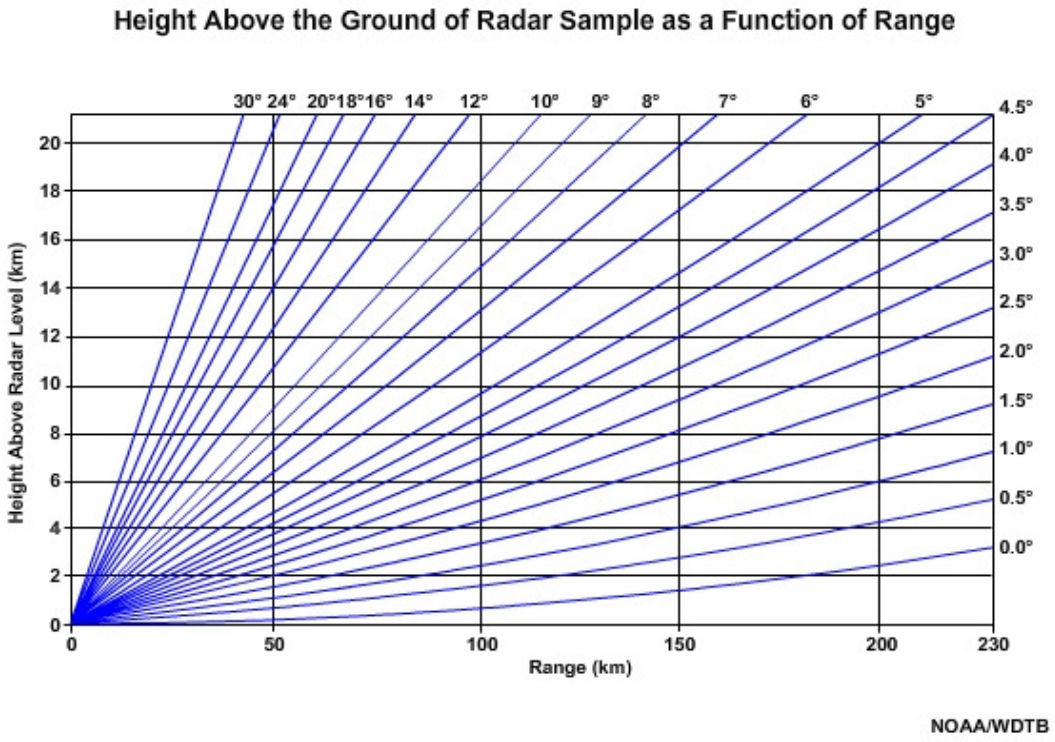


Fig. 10. Illustration of how standard atmospheric refraction modifies the path of a transmitted radar signal with increasing range from the radar, courtesy of NOAA.

2.2.3.2 UMass X-Pol

UMass X-Pol (Bluestein *et al.* 2007a) was built at the Microwave Remote Sensing Laboratory (MIRSL) of the University of Massachusetts – Amherst (UMass) (Juyent 2003). It consists of an X-band (3 cm wavelength)[5], pulsed-Doppler radar

[5] The same hydrometeors scatter signals differently at S- vs. X-band wavelengths. Since the transmitted signal from the UMass X-Pol has a different wavelength (3 cm) than the WSR-88D (10 cm), the reflectivity values recorded by both systems will almost never be identical, even when the two radars are collocated (see Fig. 3.3 of Doviak and Zrnić [1993]). X-band radars such as UMass X-Pol are subject to strong attenuation in heavy precipitation cores (e.g. Wurman et al. 2007), where the Mie scattering regime dominates. The Greensburg storm contained giant hail, and its effects on X-band attenuation were significant. However, all other things being equal, the Doppler velocities collected by S-band and X-band radars *should* be highly similar.

system mounted on a Ford F350 pickup truck (Fig. 11); some basic specifications of this system are given in Table 1. UMass X-Pol was upgraded in 2002 with a dual polarized (horizontal and vertical) pulsing capability in order to provide polarimetric measurements. An onboard deep-cycle marine battery system, recharged via the truck's alternator while the truck was in motion, replaced a gasoline-powered generator as a power source for the radar and computer in early 2007. The switch to battery power imposed limitations on the length of the data collection, and will be discussed later.



Fig. 11. The UMass X-Pol radar truck (in 2008) and its attendant crew members (C. Baldi, H. Bluestein, and J. Snyder). Photograph © R. Tanamachi.

The mobility of the UMass X-Pol makes for some interesting issues not usually associated with stationary radar systems such as the WSR-88D:

(1) When engaged in severe storms research, the UMass X-Pol radar is often hastily deployed in less-than-ideal conditions, and its exact location and

orientation may not be well-documented. This issue has been mitigated by the regular use of global positioning systems (GPS) and the installation of hydraulic levelers on the truck (in 2008) to ensure a level antenna base.

(2) Because the UMass X-Pol antenna is mounted 2 m above the ground for transportability, it experiences beam blockage by trees, hills, buildings, and telephone poles. Ground clutter patterns around the radar change with every deployment. It may be necessary to move the radar mid-deployment in order to maintain a line-of-sight to an area of interest. The clutter sources around the antenna are usually documented via photographs, site surveys, or topographic maps.

For these reasons, greater uncertainty is associated with data collected by UMass X-Pol than with data collected by a WSR-88D. Despite these issues, the UMass X-Pol has been successfully utilized in numerous severe weather studies over the past decade (Bluestein and Wakimoto 2003; Kramar *et al.* 2005; French 2006; French *et al.* 2006; Bluestein *et al.* 2007a; French *et al.* 2008; French *et al.* 2009),.

2.3 The Great Plains nocturnal low-level jet

2.3.1 Past studies

One of the principal environmental changes that occurred prior to the genesis of the Greensburg tornado is the intensification of the LLJ. A LLJ is generally defined as a vertically localized maximum in horizontal velocity occurring at or below an altitude of 2 km AGL (Means 1952; Blackadar 1957; Stensrud 1996; Shapiro and Fedorovich 2009). Although LLJs exist in other parts of the world, I

restrict my discussion of LLJs to the southerly, nocturnal low-level wind maximum over the Great Plains of the central United States (Means 1952; Blackadar 1957; Stensrud 1996) and refer to this phenomenon hereafter in this dissertation as simply "the LLJ" (e.g., Fig. 12).

The reader is referred to Stensrud (1996) for a synthesis of climatological studies of the LLJ (Means 1944; Blackadar 1957; Bonner 1968; Hoxit 1975; Uccellini 1980). From these and subsequent studies (Arritt *et al.* 1997; Whiteman *et al.* 1997; Walters and Winkler 2001; Banta *et al.* 2002; Shapiro and Fedorovich 2009, 2010), it is well-established that the LLJ has the following general characteristics: (1) The LLJ develops after sunset, exhibits peak velocities (of between 12 and 35 m s^{-1}) between sunset and sunrise (typically around 0200 local time), and dissipates near sunrise as the onset of solar heating and turbulent momentum flux re-couple the surface and boundary layers. (2) The maximum winds typically occur at or below 1 km AGL, can be substantially supergeostropic, and the ageostrophic component veers with time. (3) LLJs occur most frequently during the warm season, when solar heating (and associated turbulent momentum flux) are maximized.

It is predominantly accepted that the LLJ results from nocturnal decoupling of the surface layer from the boundary layer (Blackadar 1957; Stull 1988). In the boundary layer, before sunset, air parcels are subject to Coriolis, pressure gradient, and friction forces whose net force drives parcels toward (away from) surface pressure minima (maxima). After sunset, a nocturnal surface inversion forms, and turbulent momentum flux in the boundary layer decreases, reducing the depth over which surface frictional drag affects the winds. As a result, the winds in the upper

boundary layer approach geostrophic balance. Blackadar (1957) hypothesized that subsequent inertial oscillation (veering, or clockwise rotation in the northern hemisphere) of the pre-sunset ageostrophic wind component explained observations of supergeostrophic winds in the LLJ about 6 hr after sunset. However, a companion study (Buajitti and Blackadar 1957), in which Blackadar (1957)'s theoretical wind speeds were calculated for several observed instances of the LLJ, consistently produced an ageostrophic wind component that was smaller than observed. More recent studies have focused on the role played by terrain in increasing the wind speeds beyond what would be predicted by Blackadar (1957)'s theory. In particular, Shapiro and Federovich (2009) argue that the oscillation of the ageostrophic wind component is actually an inertial-gravity oscillation rather than a pure inertial oscillation, because a buoyancy gradient (upslope or downslope) exists in a stratified atmosphere along even gently sloping terrain.[6]

It has been recognized for decades that the LLJ is associated with nocturnal maxima in rainfall and severe thunderstorm activity over the central United States (Means 1944, 1952; Pitchford and London 1962; Bonner 1966; Raymond 1978; Sun and Ogura 1979; Uccellini and Johnson 1979; Maddox and Doswell 1982; Stensrud 1996). The LLJ can transport large amounts of moist air northward into the Great Plains region along a corridor extending roughly from Texas to Minnesota, thereby increasing the CAPE in those areas (Stensrud 1996; Wu and Raman 1998). LLJs frequently occur in advance of extratropical cyclones and associated upper-level jet

[6] Shapiro and Federovich (2009) found an "optimum" range of slopes (0.10 – 0.25°) that maximizes peak LLJ winds in their simplified, one-dimensional model. The slope of the terrain between the longitude of KDDC and UMass X-Pol was 0.17°. Unfortunately, we lack the measurements of the capping inversion strength that would be needed to test their model for this case.

streaks moving east from the Rocky Mountains (Uccellini 1980; Chen and Kpaeyeh 1993; Walters 2001), which create favorable pressure gradients for LLJ development and warm air advection (Maddox and Doswell 1982). In such cases, the LLJ can increase the northward low-level moisture transport already occurring in the warm sector (Means 1944). Quite relevant to the current study, the increase in low-level wind speeds associated with the onset of the LLJ can also increase substantially the storm-relative helicity in the 0 – 3 km layer, creating an environment more favorable for nocturnal tornadoes (Maddox 1993). Depending on the timing and relative position of the LLJ and other features related to deep moist convection, the LLJ may also serve to increase low-level convergence and thereby enhance pre-existing deep moist convection (Pitchford and London 1962; Uccellini and Johnson 1979; Stensrud 1996). Although it has been proposed that uplift may result when an LLJ develops in the vicinity of a surface cold front or dry line (C. Doswell, personal communication), considerable skepticism exists as to whether the LLJ can serve as a direct trigger for convection (Stensrud 1996).

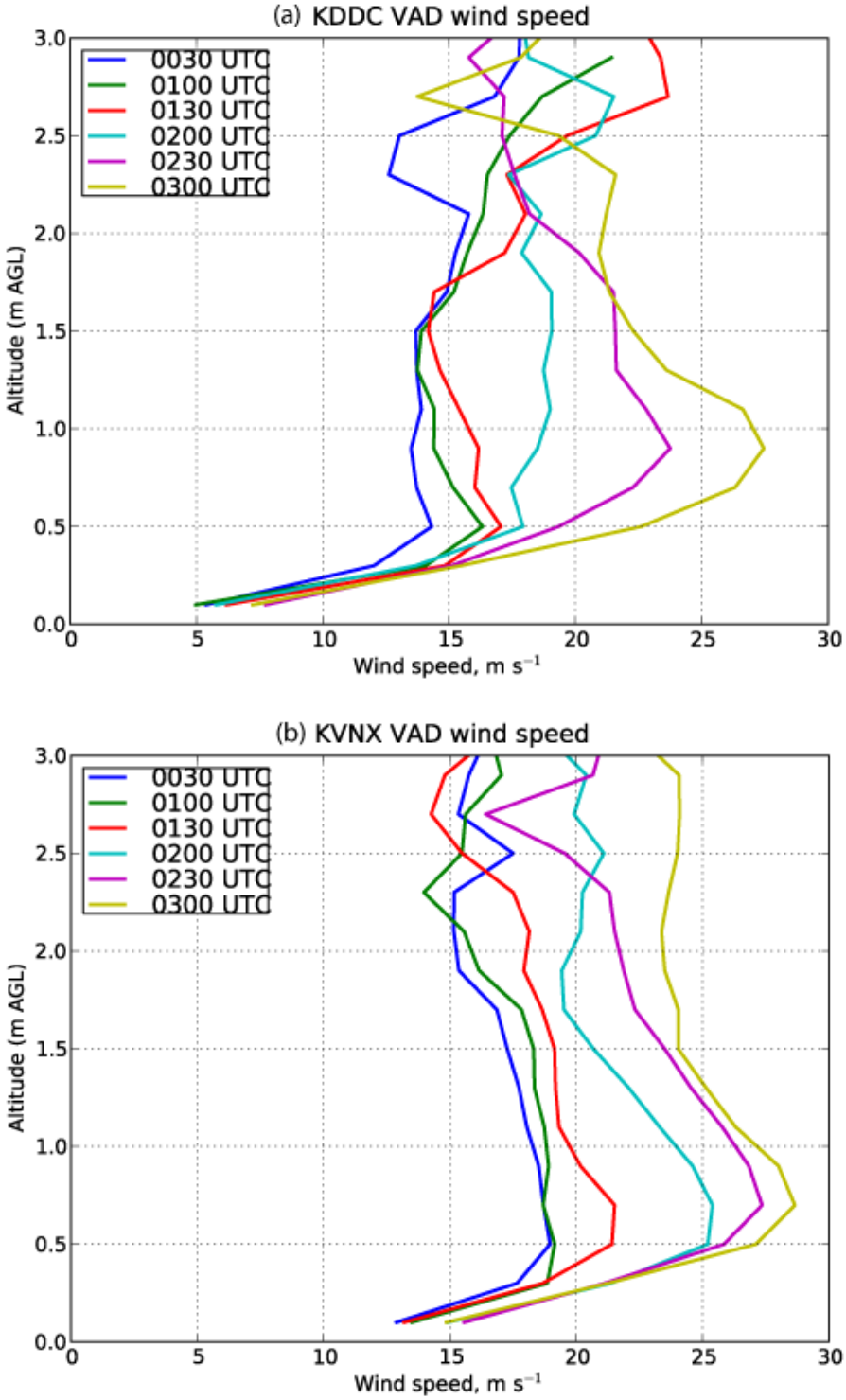


Fig. 12. VAD retrievals of wind speed (in m s^{-1}) vs. altitude (in m AGL) on 5 May 2007 from (a) KDDC and (b) KVNX radial velocity data. The LLJ is the developing "bulge" in wind speeds at 900 m AGL at KDDC and 700 m AGL at KVNX. Velocities aloft also increased, presumably as a result of synoptic-scale forcing, as a 500 mb trough approached from the west.

2.3.2 Issues related to measurement of the LLJ winds

In reviewing past studies of LLJs, I found two significant recurring themes related to detection. The first is that the typical altitude range of the LLJ maximum winds (500 – 1000 m AGL) is ill-represented by many commonly-used wind measurement systems (Stensrud *et al.* 1990). Over the central U.S., this altitude range falls below the 850 mb pressure level but above the surface (both mandatory report levels for rawinsondes), so the LLJ peak velocities will not appear on routinely-generated surface or 850 mb charts. In addition, commonly-used wind profilers such as those in the 404 MHz (74 cm wavelength) NOAA profiler network (Ralph *et al.* 1995, see http://www.profiler.noaa.gov) report their first range gate at an altitude of 500 m AGL owing to their retrieval geometry, transmitter – receiver switch delay, and ground clutter, making it less likely that LLJ peak wind speeds will be sampled. Although the peak winds in LLJs are not consistently measured by these systems, the presence of LLJs can often still be detected, as the LLJ can affect velocities up to 2000 m AGL (e.g., Fig. 12).

The second recurring theme, and one made more prevalent with the advent of radar and other backscatter-based wind profiling systems, is that of bird contamination. For ornithologists, radar reflectivity and velocity patterns generated by birds represent a potential data source for bird migration studies (Gasteren *et al.* 2008; Gauthreaux *et al.* 2008; Schmaljohann *et al.* 2008). For meteorologists, however, birds (and other bioscatterers such as insects) represent unwanted "contamination" by non-meteorological radar targets. Depending on their behavior, such bioscatterers may or may not move with the prevailing atmospheric winds, and

can significantly bias wind measurements if they do not (Wilczak *et al.* 1995; Arritt *et al.* 1997; Daniel *et al.* 1999; Pekour and Coulter 1999; Banta *et al.* 2002; Holleman *et al.* 2008). Complicating matters further, the spring peak bird migration (April and May) partly coincides with climatological maximum in LLJ occurrence. As such, radar- or wind profiler-based climatological studies of the LLJ often contain lengthy caveats or treatments of bird contamination.

Separating radar echo from birds and other targets is not a trivial task. A number of potential automated remedies for this problem have been suggested since the advent of the WSR-88D (e.g., Wilczak *et al.* 1995; Pekour and Coulter 1999; Martin and Shapiro 2007) but, to the best of my knowledge, none particularly effective or widely adopted. One possible future remedy may arrive with the advent of polarimetric data collection by the WSR-88D network. Several studies have already demonstrated the efficacy of polarimetric techniques that discriminate between backscattered signal from hydrometeors and biological targets (Bachmann and Zrnić 2007; Park *et al.* 2009; Snyder *et al.* 2010). However, these techniques could not be applied to the study of the Greensburg storm as KDDC is not yet upgraded to polarimetric measurement capability.

It is very likely that many of the clear-air echoes seen around the KDDC radar, which increase markedly in strength and aerial coverage after sunset (Fig. 8), are birds and/or insects. However, it remains largely unknown what effect(s) these observed non-meteorological targets have on Doppler velocity measurements, and in the following study, no attempt was made to correct for any errors in wind speed measurements thereby introduced.

Chapter 3 The Greensburg storm

3.1 Meteorological overview

As the meteorological background of the Greensburg storm has already been extensively discussed by both Lemon and Umscheid (2008) and Bluestein (2009), only a brief overview and description of the early tornadoes will be given here. The reader is referred to Bluestein (2009) for extended discussion of the prediction aspects of the Greensburg storm, including details of the synoptic setup, the preceding sequence of storms, and a storm "genealogy."

The Greensburg storm was the 14th ("Storm N" in Bluestein [2009]'s genealogy) in a series of splitting and merging storms that started around 2200 UTC on 4 May 2007 near Pampa, Texas. These storms were clustered near an (inferred) confluence between a northward surge of moist surface air from the previous night's LLJ and a surface dryline bulge whose apex was located east of Dodge City, Kansas (Fig. 13). The axis of a 500 mb trough was located west of the longitude of Dodge City on the evening of 5 May 2007 (Fig. 14), and furnished 34 m s^{-1} 0 – 6 km AGL bulk shear, a parameter deemed sufficient for supercells (Lemon and Umscheid 2008).

The onset of the LLJ on the evening of 5 May 2007 was documented by numerous platforms. The two closest WSR-88Ds (KDDC and KVNX) and the NOAA profiler at Haviland, Kansas (HVLK1; see Appendix B) all exhibited a marked increase in southerly low-level flow at and after 0100 UTC. This increased southerly flow can clearly be seen in VAD retrievals of the wind profiles from KDDC and KVNX (Fig. 12). At the UMass X-Pol deployment site, at 0130 UTC, H. Bluestein remarked that low-level clouds were "racing in from the south." Although

no surface velocity measurements were taken at the deployment site, it is the recollection of all present that southerly surface flow persisted from after the passage of the forward flank precipitation shield (around 0140 UTC) to the end of the deployment (0236 UTC).

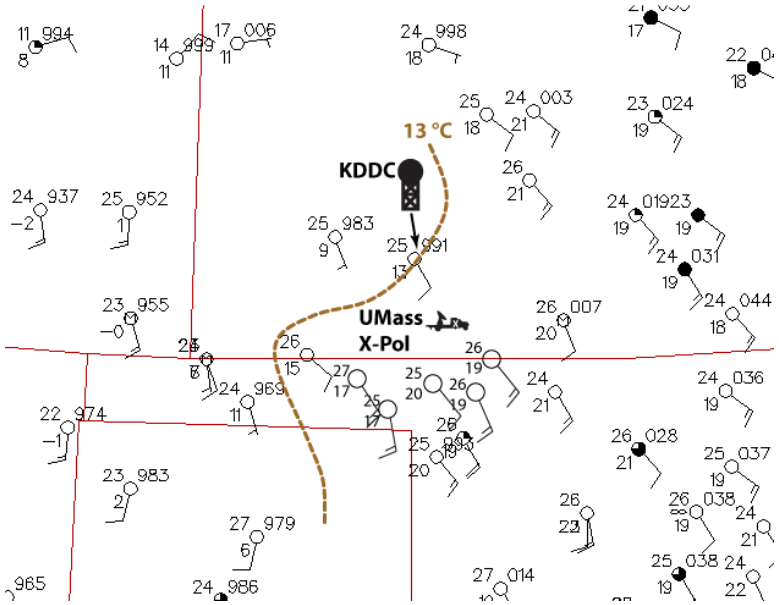


Fig. 13. Surface map from 0100 UTC in western Oklahoma and Kansas. Temperatures and dewpoints are in °C. Full wind barbs are 5 m s^{-1}; half-barbs are 2.5 m s^{-1}. Base map from Plymouth State Weather Center; five Oklahoma Mesonet surface observations from the region upstream of the Greensburg storm have been added. The brown dashed line represents the 13 °C isodrosotherm, used as a proxy for the dryline, which was retreating westward through Dodge City.

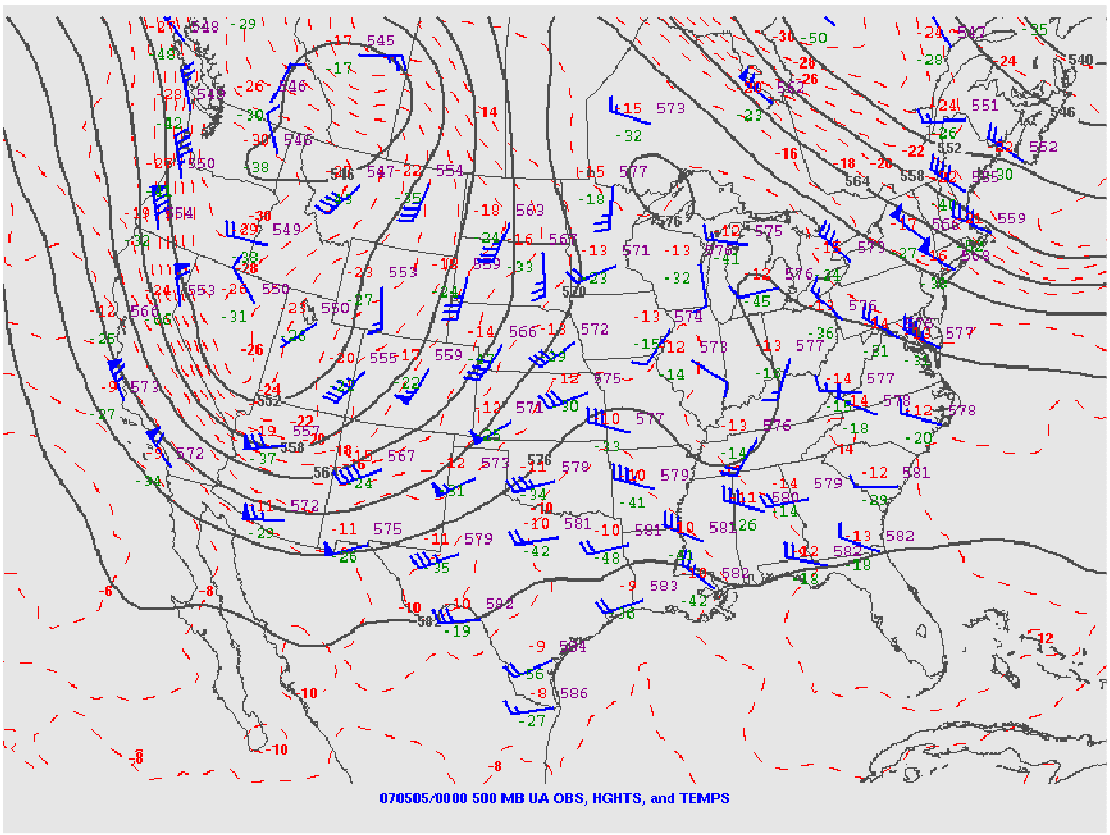


Fig. 14. 500 mb analysis chart from 0000 UTC on 5 May 2007. Solid black contours are the geopotential height in dam; the interval between contours is 6 dam. Dashed red contours and observations printed in red are the temperature in °C; the interval between contours is 2 °C. On the blue wind barbs, flags are 25 m s^{-1}, full wind barbs are 5 m s^{-1}; half-barbs are 2.5 m s^{-1}. From SPC archives (NOAA).

The first radar echo from the Greensburg storm appeared around 0030 UTC on 5 May southwest of a prior storm ("Storm J" in Bluestein [2009]'s genealogy), along its surface outflow boundary. For the duration of its life cycle, the Greensburg storm was and remained the southernmost storm in its cluster. Over a period of 45 – 60 min, the Greensburg storm organized into a supercell as it moved northeastward, first exhibiting a mesocyclone and distinct hook echo (in KDDC observations) around 0100 UTC and rapidly intensifying thereafter. Between 0132 UTC and 0156 UTC, the Greensburg storm produced at least four relatively small (EF-0 or EF-1) tornadoes

(tracks 1-4; Fig. 1) between Sitka and Greensburg, Kansas, one of which came within 8 km of Protection, Kansas and was visible to the UMass X-Pol crew.

A transition from tornado production mode I to mode II occurred around 0155 – 0200 UTC. The Greensburg tornado (track 5; Fig. 1) formed at 0200 UTC, moved generally northeast for most of its mature phase, expanding to a maximum damage path width of 2.7 km, and doing its most severe damage in the city of Greensburg between 0245 and 0250 UTC. The Greensburg tornado dissipated at 0305 UTC, following a narrowing, looping path such that the end of the damage track was located north*west* of Greensburg. During its mature stage, the Greensburg tornado was accompanied by at least five smaller satellite tornadoes (tracks 6-10; Fig. 1). These first 10 tornadoes are summarized in Table 2 (M. Umscheid, personal communication).

Lemon and Umscheid (2008) describe the structure and evolution of the Greensburg storm as inferred from KDDC data and the NWS warning process during this episode (which is widely credited with minimizing the number of fatalities). They also detail the subsequent evolution of the Greensburg storm; twelve additional tornadoes were documented after the Greensburg tornado dissipated (a few of which can be seen in Fig. 1). In the context of this study, a transition from tornado production mode II back to mode I occurred after the dissipation of tornado 15. The Greensburg storm maintained supercell characteristics until about 0800 UTC and a distinct updraft until about 0900 UTC. However, as these events occurred after data collection by UMass X-Pol ended, they will not be further discussed.

Table 2. Chronology and damage survey information concerning the first ten tornadoes produced by the Greensburg storm, courtesy of M. Umscheid, NWS – Dodge City, Kansas office. An asterisk (*) denotes considerable uncertainty in measurements of path length and width owing to overlap with the damage path of the Greensburg tornado (Fig. 1).

Tornado number	**Start time (UTC)**	**End time (UTC)**	**EF-scale rating**	**Damage path length (km)**	**Max. damage path width (m)**	**Comment**
1	0132	0145	0	9.7	68	
2	0134	0139	0	6.8	46	
3	0148	0152	0	4.7	46	
4	0150	0156	1	3.7	68	
5	0200	0305	5	46.4	2730	Greensburg tornado
6	0210	0212	1	2.1	46	Satellite of tornado 5
7	0218	0218	0	0.3*	23*	Anticyclonic satellite of tornado 5
8	0218	0219	0	0.3*	23*	Satellite of tornado 5
9	0225	0226	0	0.5*	36*	Anticyclonic satellite of tornado 5
10	0225	0226	0	0.8*	36*	Satellite of tornado 5

3.2 UMass X-Pol deployment

UMass X-Pol was used for severe storms research by participants from the University of Oklahoma throughout the spring of 2007 (Bluestein *et al.* 2007c). On 5 May 2007, the UMass X-Pol was deployed, somewhat serendipitously[7], 4 km east of Protection, Kansas (Fig. 1; Appendix A) on U.S. Highway 160, to collect data in the approaching Greensburg storm. UMass X-Pol sector scans ("sweeps") were collected between 0115 UTC and 0236 UTC. A wall cloud associated with an early low-level circulation center in the Greensburg storm was located 14 km west-southwest of UMass X-Pol at 0116 UTC, and served as the initial radar target. Once deployed, the crew chose to remain stationary in order to maintain data continuity, apart from one six-minute period (0133 – 0138 UTC) when the truck was moved from the south to the north side of U.S. Highway 160 in order to minimize beam blockage from telephone poles to the west. (As it turned out, parts of the life cycles of tornadoes 1 and 2 fell into this gap.)

As the Greensburg storm moved towards the north-northeast, past the latitude of the UMass X-Pol, the radar operator shifted the target sector clockwise (towards the north), keeping the hook region near the center. Between 0115 and 0125 UTC, 106 single-elevation sector scans were collected at elevation angles of ~3.0 – 4.0°. The radar operator then switched the radar into volume collection mode, wherein sequential sweeps were collected at increasing elevation angles, starting at 3.0°. Initially, the maximum elevation angle was 10°, but as the storm moved away from the radar, this angle increased to 15° at 0216 UTC, and finally, to 20° at 0226 UTC.

[7] The UMass X-Pol crew spent several hours prior to the deployment having a truck tire replaced in Protection, Kansas, which is 48 km south-southwest of Greensburg.

The UMass X-Pol crew visually observed tornadoes 2, 3, 4, and 5 during the deployment. Tornadoes 2 and 3 occurred before sunset and were documented in photographs (Fig. 15; see also Fig. 11 of Bluestein 2009). Intervening precipitation, tree blockage, the onset of darkness, and distance largely prevented visual observation of the other tornadoes. However, tornadoes 4 and 5 were briefly visible to the UMass X-Pol crew, illuminated by lightning (Fig. 16).



Fig. 15. Tornado 2 (22 km WNW) as seen by the UMass X-Pol radar crew at 0138 UTC. The town of Protection, Kansas is located by the grain elevator on the horizon. Note a second lowering (15 km W) in the foreground near the left edge of the frame; this lowering developed into tornado 3 at 0148 UTC. Photograph © R. Tanamachi; contrast enhanced.

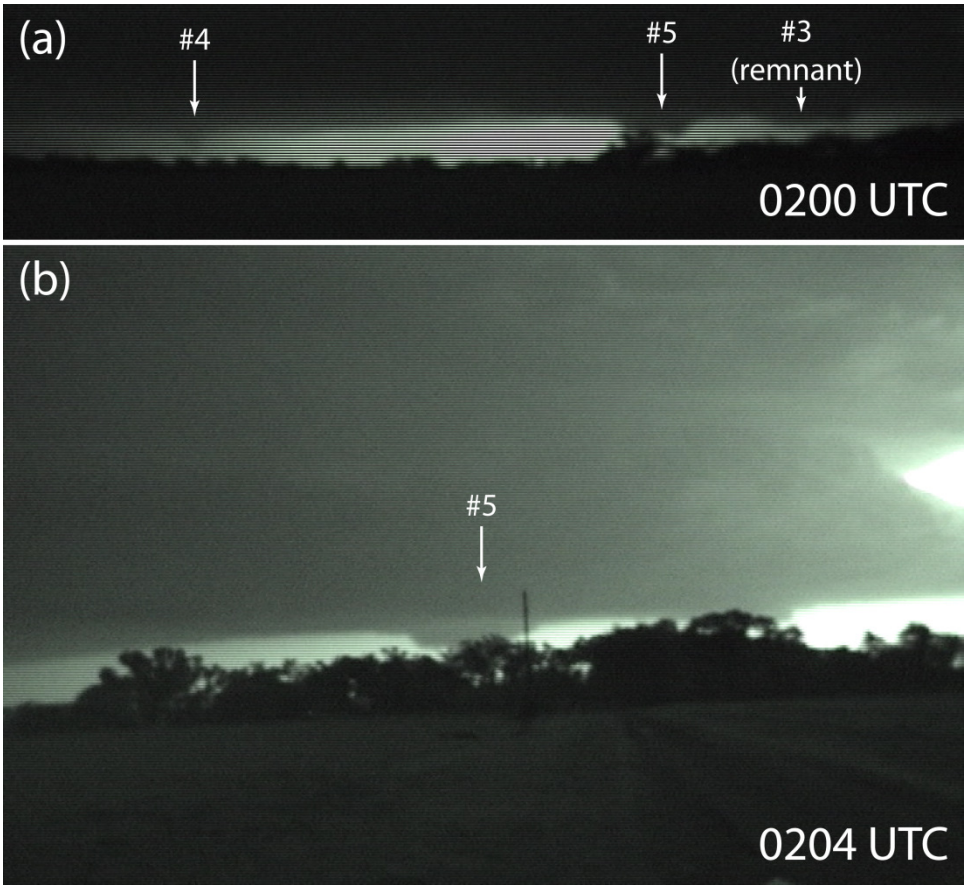


Fig. 16. Video frames taken at (a) 0200 UTC and (b) 0204 UTC, showing tornadoes 4 and 5, as well as the remnants of tornado 3, which had dissipated several minutes earlier. Illumination of the scene comes from lightning. The bell-shaped updraft of the Greensburg storn can be seen in panel (b). View is toward the north-northwest in panel (a), and north in panel (b). Tree blockage along the horizon is apparent. For reference, the tree in front of tornado 5 in panel (a) also appears near the left edge of panel (b). Video © R. Tanamachi.

UMass X-Pol data collection ceased at 0236 UTC owing to depletion of the onboard battery charge. (Recall that the batteries were recharged while the truck was moving, and the truck had been stationary for over an hour by that time.) Therefore, no UMass X-Pol data were collected during the time period (0245 – 0250 UTC) when tornado 5 severely damaged Greensburg. (The crew had no way of knowing that this event was about to occur, and only learned of it while in transit back to Norman, Oklahoma, later that evening.) However, the 5 May 2007 UMass X-Pol data set contains data collected in at least eight of the ten tornadoes reported during the

deployment, including the complete life cycles of at least six tornadoes (3, 4, and 6 through 10), and the genesis through mature stages of the Greensburg tornado (5).

Chapter 4 Radar data

4.1 Description

A radar data collection timeline for the Greensburg storm is shown in Fig. 17. KDDC data coverage during the Greensburg storm was, as per standards of WSR-88D operation, continuous and volumetric. UMass X-Pol, a research radar with a highly adaptable scanning strategy, furnished data with coverage less consistent in terms of update frequency and the volume of the atmosphere sampled. However, its viewing angle toward the Greensburg storm was complementary to that of KDDC, and both radars sampled the Greensburg storm while the tornado that hit Greensburg was forming.

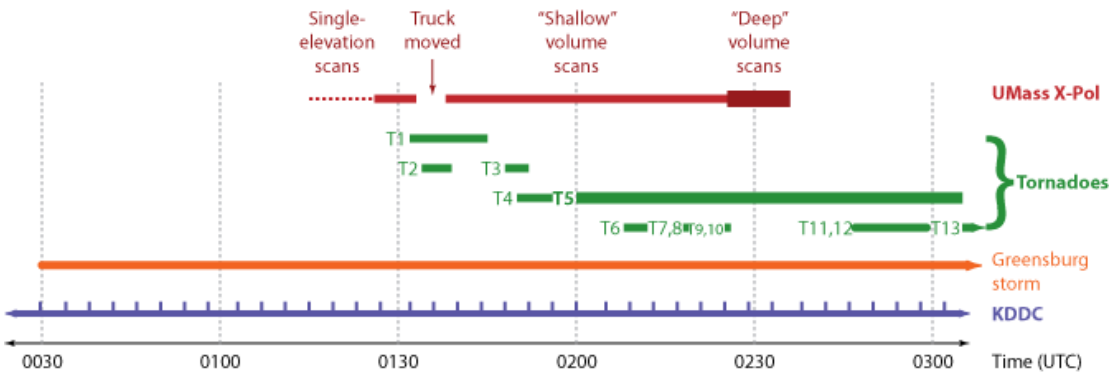


Fig. 17. Timeline of Greensburg storm, tornadoes, and radar data collection. KDDC operated continuously; start times of volume scans are given by tick marks. The life span of the Greensburg storm (starting from first detection by KDDC) is indicated by the orange arrow. Green bars indicate the life spans of tornadoes; numbering is as in Table 2. UMass X-Pol deployment times are indicated by red lines / bars. Dashed lines indicate times when single-elevation scans were collected; the solid red line indicates when "shallow" volume scans were collected, and the thick red bar indicates when "deep" volume scans were collected.

4.1.1 KDDC data

The Greensburg tornado occurred at a range of ~60 km from KDDC (the WSR-88D at the NWS-WFO in Dodge City, Kansas; see Fig. 8). KDDC collected data continuously on 5 May 2007 in VCP 12, encompassing the entire life span of the

Greensburg storm, including its initiation at around 0030 UTC[8]. The KDDC data used in this study consist of 37 volumes collected (at 4.1 minute intervals) from 0029 to 0302 UTC (Fig. 17). Data were obtained from the National Climatic Data Center (NCDC) NEXRAD archive in Level II format, and converted to Doppler Radar Data Exchange (DORADE) format using the "xltrsii" converter included in National Center for Atmospheric Research (NCAR) Solo II radar data editing and visualization software (Oye et al. 1995).

The KDDC radial Doppler velocity data exhibited velocity aliasing in the Greensburg storm (Fig. 8). The maximum unambiguous velocity for WSR-88D data was dependent upon the elevation angle, ranging from 26.23 m s^{-1} at θ_e = 0.5° to 33.20 m s^{-1} at θ_e = 12.5° and above. To make these data more usable for study, I manually dealiased the aliased velocities using Solo II.

4.1.2 UMass X-Pol data

Initially, single-elevation scans were collected (0115 – 0126 UTC), followed by "shallow" volume scans (3 – 10°; 0126 – 0215 UTC), and finally "deep" volume scans (3 – 15° or 3 – 20°; 0215 – 0236 UTC). Between 0125 and 0236 UTC, UMass X-Pol collected 81 volume scans over various azimuthal sectors towards the west and north, for a total of 539 sweeps (Table 3).

The UMass X-Pol data were recorded in a raw binary format during deployment, processed at MIRSL, and received in DORADE format. The data were

[8] The Greensburg storm was also detected by KVNX and the WSR-88D located at the NWS-WFO in Amarillo, Texas (KAMA), among others. The distance between the Greensburg tornado and KVNX was ~130 km; for KAMA this distance was ~330 km. While the KVNX data cover a substantial portion of the Greensburg storm (i.e. above 1 km), KAMA only sampled the upper levels of the Greensburg storm (i.e. above 7 km AGL) at a very coarse spatial resolution. KVNX data were used to a limited extent in this study, while KAMA data were not used at all.

oversampled in range and azimuth such that the radial resolution was 60 m and the azimuthal resolution was 0.8°.

Like the WSR-88D data, the UMass X-Pol Doppler velocity data were also aliased, but around a maximum unambiguous velocity of ±19.2 m s^{-1}, resulting in multiple "folds" (up to three near the center of the mature Greensburg tornado; Fig. 18b). Additionally, areas of ground clutter and range ambiguous reflectivity (second trip echo; see Doviak and Zrnić 1993) from more distant storms were apparent in the data at the lowest few elevation angles. For ease of study, UMass X-Pol Doppler velocity data associated with second trip echo and clutter were manually masked in Solo II, and the remaining Doppler velocities manually dealiased. Some additional editing of low-SNR data was performed in preparation for data assimilation experiments, to be described later.

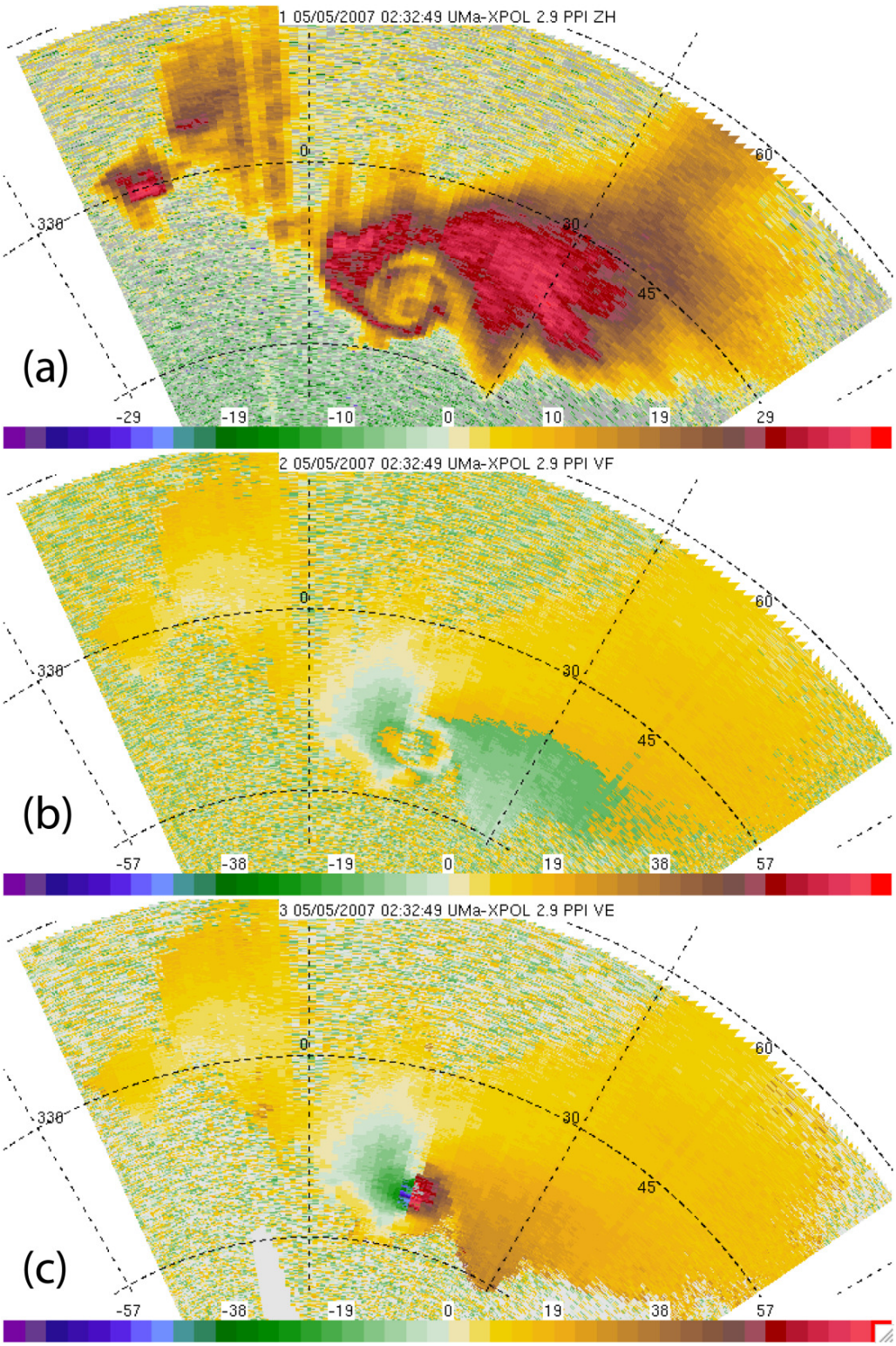


Fig. 18. UMass X-Pol (a) reflectivity (in dBZ_e) and (b) velocity (in m s^{-1}) data collected at 02:32:49 UTC, at an elevation angle of 2.9°. At this time, the damage track of the mature Greensburg tornado was 2.5 km wide. The UMass X-Pol radar is located at the origin (not shown). Panel (c) shows the Doppler velocity data after manual dealiasing and some editing. Range rings are 15 km apart; spokes are 30° apart.

Table 3. UMass X-Pol data collected in the Greensburg storm. Elevation angles are measured relative to the truck bed, while azimuth angles are measured clockwise from north (compass headings).

Time (UTC)	**Volumes / sweeps collected**	**Elevation angle(s) (° ± 0.3°)**	**Max. range (km)**	**Min. az. angle (° ± 3°)**	**Max. az. angle (° ± 3°)**
01:15:00 – 01:16:17	– / 15	3.0	30	187.5	269.0
01:16:54 – 01:20:51	– / 44	3.0	60	185.0	265.0
01:21:30 – 01:23:01	– / 23	3.0	60	230.0	295.0
01:24:02 – 01:25:54	– / 24	4.0	30	226.0	298.0
01:26:28 – 01:32:50	11 / 62	3.7 – 10.0	30	230.0	295.0
01:32:50 – 01:38:17	Truck moved	–	–	–	–
01:38:17 – 01:54:35	25 / 148	3.7 – 10.0	30	272.0	330.0
01:55:10 – 02:05:31	17 / 98	3.0 – 10.0	30	292.0	358.0
02:06:04 – 02:15:02	12 / 72	4.0 – 10.2	30	305.0	25.0
02:15:47 – 02:21:39	5 / 52	3.0 – 15.5	30	305.0	25.0
02:22:10 – 02:26:05	3 / 35	3.0 – 15.5	60	335.0	55.0
02:26:35 – 02:36:18	6 / 72	3.0 – 20.0	60	335.0	55.0

4.2 Issues affecting UMass X-Pol data quality and usability

4.2.1 Reflectivity attenuation and calibration

When reflectivity fields from KDDC and UMass X-Pol are plotted over the same area, regions of attenuated X-band reflectivity were evident on the far side (with respect to UMass X-Pol) of the Greensburg storm core (Fig. 19), owing to the presence of large hail (> 3 cm diameter; NCDC 2007). Such large hail falls into the Mie scattering regime at X-band (3 cm) wavelengths, i.e., more of the incident X-band radiation is scattered away from the radar than back to it, and this attenuating effect increases with increasing range from the radar (Doviak and Zrnić 1993). (Reflectivity observations from S-band radars such as the WSR-88D are not as susceptible to this effect, since scatterer sizes rarely fall into the Mie regime at 10 cm wavelength.) Attenuation in the hail core accounts for some of the differences seen between the observed KDDC reflectivity patterns and those from UMass X-Pol.

However, for this particular deployment, UMass X-Pol reflectivity data were not well calibrated. In most instances, the reflectivity values measured by UMass X-Pol in areas of the Greensburg storm that were not heavily affected by attenuation were ~30 dBZ_e lower than corresponding KDDC observations, and 15-20 dBZ_e lower than measurements taken by UMass X-Pol in comparable parts of other Great Plains tornadic supercells (Bluestein *et al.* 2007a). Consequently, the UMass X-Pol reflectivity data were only used to infer qualitative details about the structure of the Greensburg storm and tornadoes, and were not directly compared to observed reflectivity fields from KDDC or any other radars.

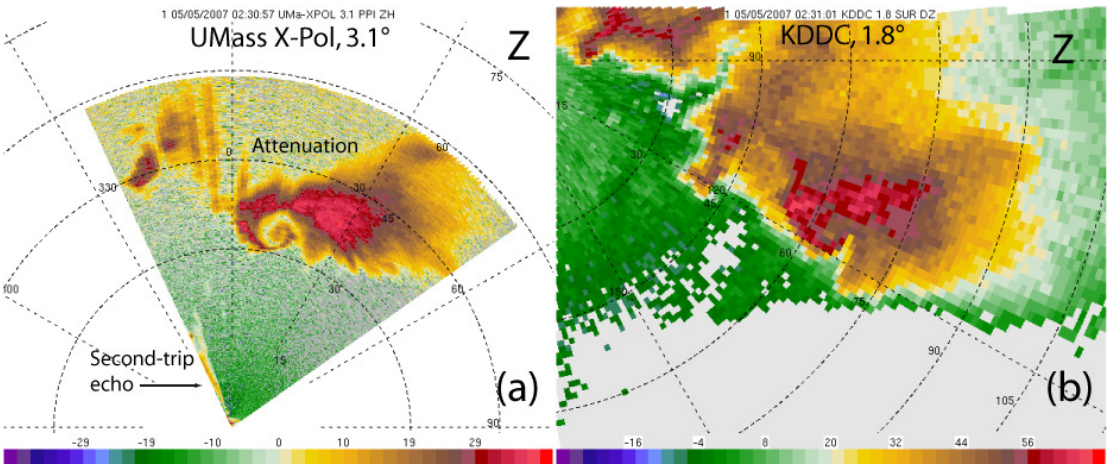


Fig. 19. Comparison of (a) UMass X-Pol equivalent reflectivity factor (in dBZ_e) and (b) KDDC reflectivity (in dBZ) in the Greensburg supercell at about 0231 UTC. Zoom factor is the same in both panels, and elevation angles are chosen so that both radars sample the "core" of the Greensburg storm (with the highest reflectivity values) at an altitude of about 2 km. Range rings are every 15 km, and azimuth spokes every 30°. The radars are located at the origins of their respective polar grids. Note that the color scales differ between the two panels.

4.2.2 Limitations of the polarimetric data

During the UMass X-Pol deployment on the Greensburg storm, the onboard computer was configured in such a way that, while Z_{dr} was correctly calculated and recorded, ρ_{hv} was calculated based on only the real component of the covariance between H and V signals. This "incomplete" correlation coefficient, denoted $\tilde{\rho}_{hv}$, is less than or equal to ρ_{hv}. However, we proceed to interpret $\tilde{\rho}_{hv}$, *qualitatively*, in much the same manner as ρ_{hv}, because its values agree reasonably well with ρ_{hv} values reported in other cases in which X-band, polarimetric data were collected in tornadic supercells (Bluestein *et al.* 2007a). This issue is discussed in greater detail in Appendix C.

Owing to this same issue, UMass X-Pol differential phase (Φ_{DP}) and specific differential phase (K_{DP}) could not be reliably calculated, and recently-developed techniques of Snyder *et al.* (2010), utilizing these quantities to correct in part for the

effects of attenuation of the X-band signal in heavy precipitation, could not be applied.

4.2.3 Radar orientation

Thanks to an onboard GPS receiver, the deployment location of UMass X-Pol in the Greensburg storm is known to within a few tens of meters. However, the exact orientation of the platform is not. UMass X-Pol did not have a hydraulic leveling system in 2007. (This was not installed until 2008.) As mentioned previously, I attempted to align the truck as close to north-south as I could, using the gridded roads as a guide, but estimated that I was likely to have been off by a few degrees.

In this study, the radar data are treated as point observations in the east-north-up (ENU) coordinate system with the radar at the origin (Fig. 20). In ENU coordinates, the positive x-axis points east, the positive y-axis points north, and the positive z-axis points up. The orientation of radar data in this space has three components: pitch (θ_p), roll (Φ_r), and yaw (Ψ). Changes in Φ_r (θ_p) [Ψ] effectively rotate the data points about the x-axis (y-axis) [z-axis].

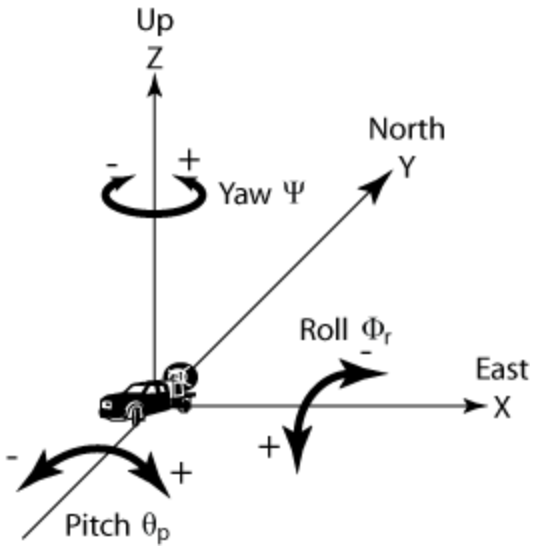


Fig. 20. The ENU coordinate system, showing how changes in pitch, roll, and yaw of the radar affect the orientation of data with respect to the coordinate axes. Note that the radar truck is depicted symbolically; it may have any orientation in space.

I undertook to try to correct the UMass X-Pol data (as best I could) for errors in yaw (azimuth) using highly reflective (i.e. metal-roofed) ground clutter targets near UMass X-Pol as a reference. UMass X-Pol was deployed less than 5 km east of Protection, Kansas. Buildings in and around Protection appeared in UMass X-Pol data as persistent targets with relatively high values of uncalibrated reflectivity and near-zero Doppler velocity. Using the internet mapping service Google Earth (http://earth.google.com), I located a number of these buildings in and around Protection, Kansas in satellite imagery, obtained their latitudes and longitudes, then and calculated the bearing between them and UMass X-Pol. I used this bearing to make corrections to UMass X-Pol azimuth data, on a volume-by-volume basis, in Solo II. These corrections ranged from -0.3° to +3.1° (see Appendix D). (Incidentally, this result affirmed my guess that, in parking the radar, I was off by no more than "a few degrees" from north.) I speculate that the variability in the azimuth corrections resulted from hysteresis of the UMass X-Pol antenna, particularly near the edges of

its sector, and possibly from gusty winds at the deployment site that may have rocked the truck slightly, even while it was parked in place.

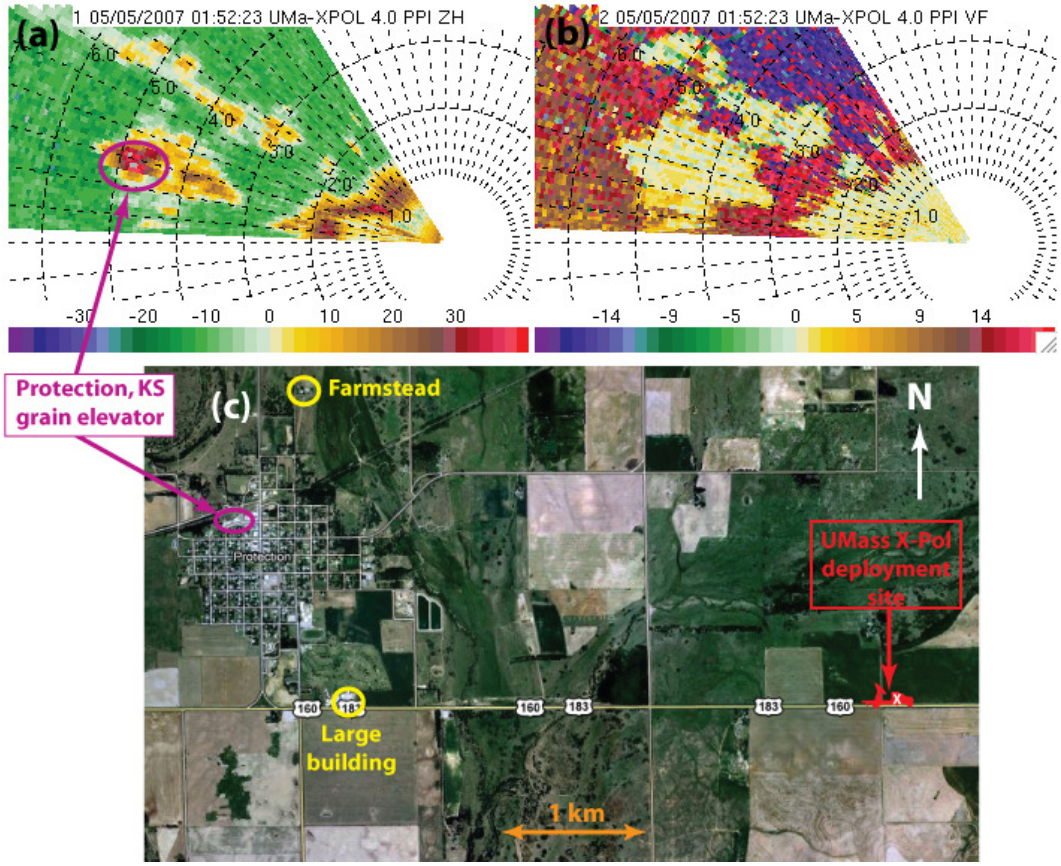


Fig. 21. Example of azimuthal (yaw) correction to UMass X-Pol data based upon location of nearby ground clutter targets. The top two panels are enlarged views of (a) unedited UMass X-Pol uncalibrated reflectivity (in dBZe) and (b) unedited, aliased Doppler velocity (in m s^{-1}) collected at 0152 UTC. Range rings are in km; azimuths are every 5 degrees. Panel (c) is a Google Earth satellite image showing the UMass X-Pol deployment site (red truck symbol) in relation to the town of Protection, Kansas. The Protection, Kansas grain elevator (circled in magenta) was easily identifiable as a clutter target in UMass X-Pol data and was visible from the deployment site (Fig. 15). Based on the Google Earth depiction, the UMass X-Pol data in (a) and (b) were rotated clockwise 1.5 degrees. Two other clutter targets used to correct other UMass X-Pol sweeps are also circled in yellow on panel (c).

Although the deployment surface (a side road) was close to level, it was unpaved, and as such the exact pitch and roll of the UMass X-Pol data are not known. I conducted an informal site survey in November 2008, locating the intersection where UMass X-Pol was deployed (and, in the process, re-confirmed the GPS coordinates). I found that the deployment surface was composed of compacted sandy

soil and contained numerous potholes, making it possible that the surface had changed substantially since the data collection in May 2007. Not knowing exactly where the UMass X-Pol's tires had been placed, I glumly concluded that it was not possible to determine the pitch and roll of the UMass X-Pol with uncertainty less than 5°, using the site survey information.

Nonetheless, I proceeded under the assumption that the pitch and roll angles of the UMass X-Pol were within 1° of zero. As it turned out, I was later able to peform EnKF-based rotation sensitivity tests that solidified this assumption. These sensitivity tests will be described in Chapter 6.

Chapter 5 Radar data analysis

5.1 UMass X-Pol observations of tornadoes

5.1.1 UMass X-Pol vortex signatures and surveyed surface damage

Vortex signatures (small areas of relatively strong inbound and outbound velocities in close proximity) were subjectively located in all UMass X-Pol radial velocity sweeps collected at and after 0132 UTC. Lemon and Umscheid (2008) reported at least 22 separate tornadoes spawned from the Greensburg storm based on surveyed tornado damage tracks. Approximate start and end times for the first 10 of these tornadoes were based on KDDC data and other evidence furnished by eyewitnesses, including reports and videos (Table 2). These times were used to associate UMass X-Pol vortex signatures with tornado damage tracks 1-10.

The structure of the Greensburg supercell's hook region changed considerably during the UMass X-Pol deployment (Fig. 22). Between 0130 and 0200 UTC, numerous circulations formed and dissipated along a roughly northwest-to-southeast axis. Some circulations were associated with tornado damage, but some were not (e.g., Fig. 22a, b). At 0145 UTC, a maximum of four simultaneous circulations were detected by UMass X-Pol (Fig. 22c, d), representing tornadoes 1-3 in various stages of their respective life cycles, as well as at least one weak circulation that was not associated with a surface damage track. The location of the RFGF is initially marked by a wind-shift line (in Doppler velocity; Fig. 22b, d) and "fine line" of slightly elevated reflectivity (Fig. 22c); as the radar viewing angle becomes more parallel to the RFGF, this boundary is marked by a reflectivity feature only (to the south of tornado 3; Fig. 22e, f). After 0200 UTC, a large reflectivity spiral pattern and strong

Doppler velocity couplet (with velocities sometimes exceeding 80 m s^{-1} on the outbound side) are evident (Fig. 22g – j), roughly coinciding with the early portion of the Greensburg tornado (5) damage track. Smaller circulations, occasionally accompanied by reflectivity hooks, appear near the Greensburg tornado at various times between 0208 – 0236 UTC. In general, those to the east of the Greensburg tornado are associated with damage tracks of satellite tornadoes (6 - 10; e.g. Fig. 22i, j), but at least two weaker circulations to the west of the Greensburg tornado are not associated with any tornado damage track.

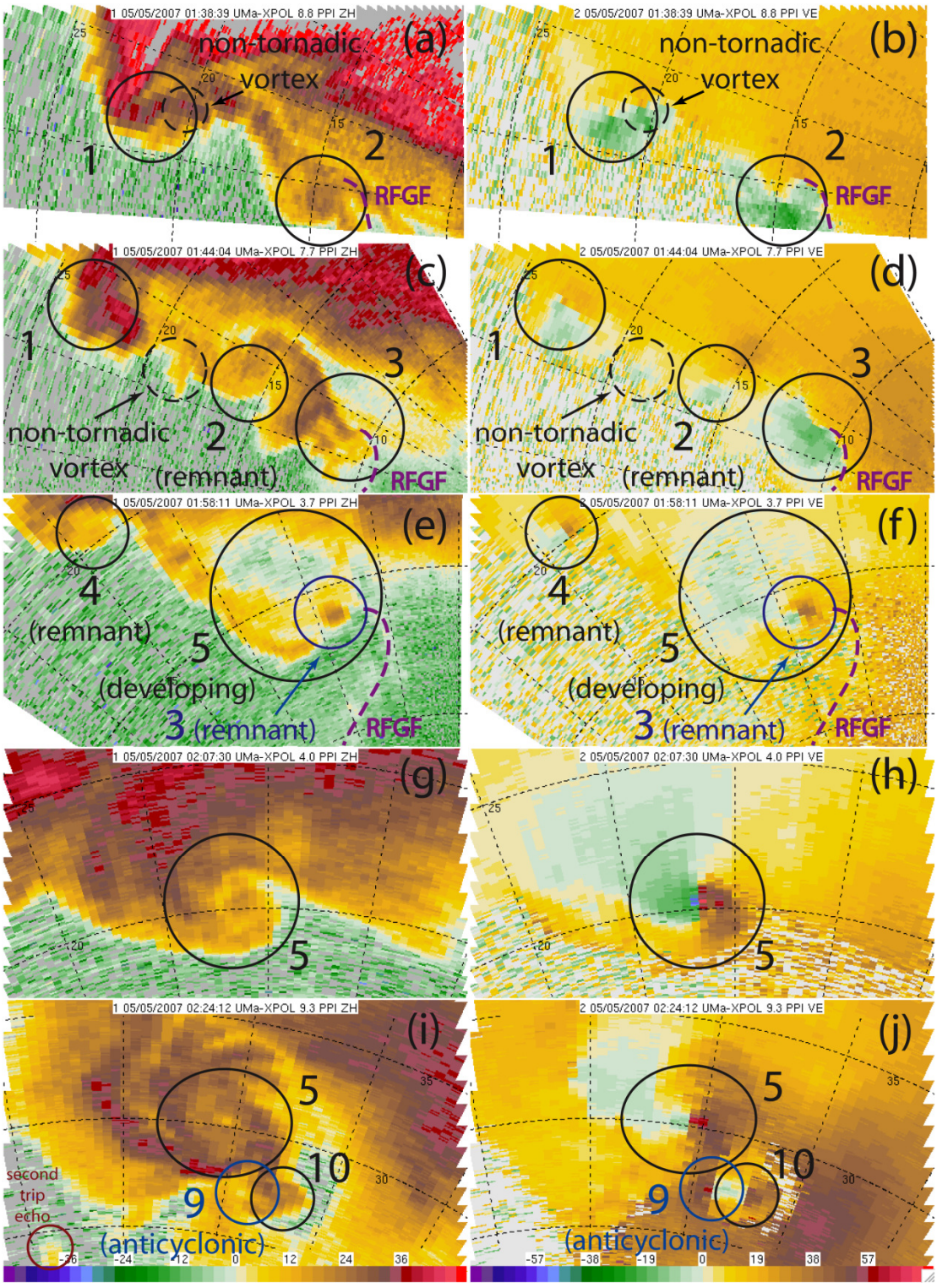


Fig. 22. UMass X-Pol uncalibrated equivalent reflectivity (Z, in dBZ_e, left column) and dealiased Doppler velocity (V_r, in m s^{-1}, right column) in the hook region of the Greensburg supercell at (a, b) 0139 UTC, 8.8°; (c, d) 0144 UTC, 7.7°; (e, f) 0158 UTC, 3.7°; (g, h) 0207 UTC, 4.0°; and (i, j) 0224 UTC, 9.3°. These images represent (a - d) the early tornado production stage with numerous small, short-lived vortices, (c, d) the transition to a single,

long-track tornado production phase, (e, f) the developing phase of the Greensburg tornado, and (g – j) the mature Greensburg tornado with a two satellite tornadoes. Range rings are plotted every 5 km, azimuth spokes every 10°. Vortex signatures associated with tornadoes are numbered according to Fig. 1 and Table 2.

Most of the tornadoes first appeared in the Doppler velocity data as a broad, mid-level (2.0 to 4.0 km AGL) circulations that gradually contracted and intensified over periods on the order of a few minutes. In some cases (tornadoes 2 through 5), these mid-level circulations preceded the start time of associated damage tracks by several minutes, and conversely, some of these mid-level circulations persisted long after the tornado dissipated or ceased doing damage. In particular, the mid-level circulation associated with tornado 4 was distinct as early as 0141 UTC and persisted until 0202 UTC, well outside of the NWS-reported start and end times of the tornado damage track (0150 – 0156 UTC; Table 2). Tornado 4 also had a visible funnel as late as 0200 UTC; see Fig. 16a. UMass X-Pol did not collect data in any of the tornadoes at altitudes below 800 m (or higher as the hook region moved farther away from UMass X-Pol) owing to distance and beam blockage (Fig. 16), so it is conceivable that the vortex signatures aloft and reported times of surface damage do not match perfectly.

Most of the radar-indicated circulations associated with tornadoes 1-5 were located to the west of corresponding surface damage (Fig. 23). The notable exception is tornado 4, whose vortex signatures aloft were east of its surveyed damage track. Tornado 4 tilted with height toward the northeast later in its life cycle, so the westward offset of the surface damage from the UMass X-Pol vortex signatures is not entirely surprising.

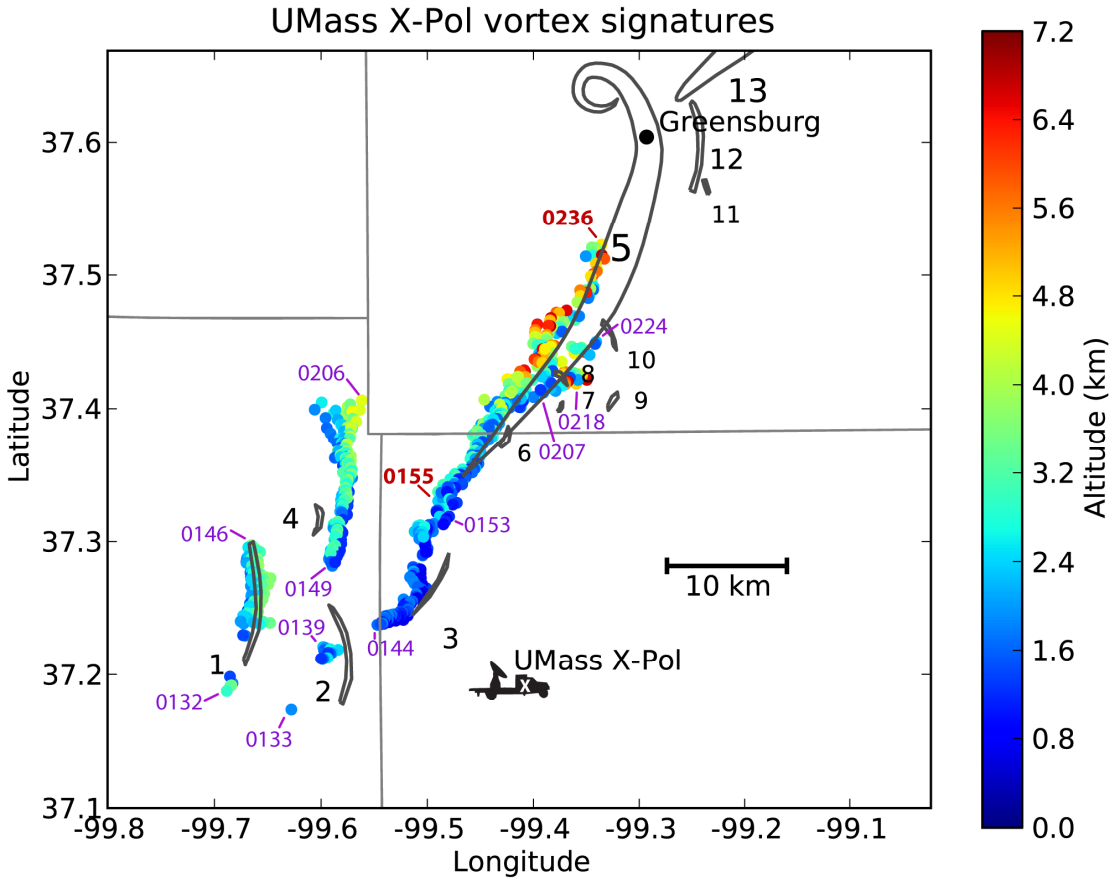


Fig. 23. UMass X-Pol-detected vortex signatures (dots, shaded by altitude in m AGL) associated with tornado damage tracks (Table 2). Times (in UTC) of the first and last vortex signatures for each track are indicated; the times for tornado 5 are in bold red text. A gap in the data from 0133 to 0138 UTC results in breaks in the vortex signature tracks for tornadoes 1 and 2. Data collection ceased at 0236 UTC; Greensburg was struck at 0245 UTC. Recall that "shallow" UMass X-Pol volumes were collected until 0216 UTC and "deep" volumes after, so there is more information about the vortex centers at altitudes above 5 km after that time.

5.1.2 Vortex tilt

Far from being vertically erect, some of the tornadoes exhibited considerable tilt with height, sometimes spanning over 5 km in the horizontal (Fig. 23). Tornadoes 1, 2, 3, and 6 through 10 did not exhibit a consistent tilt in any particular direction. Tornado 4 tilted primarily toward the north with height until the end of its life cycle, when it leaned sharply to the northeast before dissipating (a description evocative of a "rope" tornado, albeit one not verified with visual observations; Fig. 23). Tornado 5

(the Greensburg tornado) did not appear to tilt in any particular direction early in its life cycle, but as it became more mature (around 0220 UTC) it tilted increasingly toward the north with height. However, recall that the depth of the UMass X-Pol volumes increased with time as the Greensburg storm moved farther away from the radar (Table 3). Therefore, there is more information available about the upper-level (> 4.0 km AGL) structure of the later tornadoes (5-10) than the earlier ones (1-4). The earlier tornadoes may have had tilt at altitudes above which they were sampled by the UMass X-Pol, but data collected at these altitudes by KDDC are spatially too coarse to resolve the tilt in a comparable manner.

5.1.3 Tornadoes originating from the same mid-level circulations

The tracks of the UMass X-Pol vortex signatures associated with tornado 2 (3) and tornado 4 (5) are nearly contiguous (Fig. 23). Tornadoes 2 and 4 appear to have originated from the same mid-level circulation, although this circulation became very broad (> 4 km) and diffuse during the interval between the two tornadoes (0139 – 0150 UTC). Similar observations of multiple low-level circulations originating from the same mid-level circulation in the 15 May 2003 Shamrock, Texas tornadic supercell were reported by French *et al.* (2008). The low-level vortex signature associated with tornado 3 moved out of the UMass X-Pol sector between 0153 and 0155 UTC, and when the sector was shifted in a clockwise direction to include it again at 0155 UTC, a dissipating low-level circulation (presumably the remnant of tornado 3) was being absorbed into the east side of the precursor circulation of tornado 5 (Fig. 22e, f).

5.1.4 Cyclonic-anticyclonic satellite tornado pairs

In the surface damage surveys and UMass X-Pol data, tornadoes 7 and 9 were found to be anticyclonic (M. Umscheid and L. Lemon, personal communications). In the UMass X-Pol data and Table 1, tornado 7 (9) was almost simultaneous with tornado 8 (10). Tornadoes 7 (9) and 8 (10) were, in fact, a counter-rotating (i.e., anticyclonic-cyclonic) pair of tornadoes, separated by 3 – 4 km, that occurred south of the Greensburg tornado (Fig. 22i, j; Fig. 24). Curiously, the anticyclonic member of each tornado pair inflicted its surface damage *south* of the cyclonic member (Fig. 23), despite having circulations located *west* of the cyclonic member in the UMass X-Pol data. Lemon and Umscheid (2008) provide photographic evidence (their Fig. 7) that corroborates this perpendicular configuration of tornadoes 9 and 10 (north-south) and corresponding circulations (east-west) in KDDC velocity data. We speculate that the near-surface portions of the anticyclonic tornadoes may have been pushed south and east by surges in the RFGF near the surface. Indeed, such tornado pairs would indicate the presence of arched vortex lines (Markowski *et al.* 2008), possibly caused by lifting of baroclinic horizontal vorticity over a bulge in the RFGF. However, UMass X-Pol did not observe these areas at altitudes below 1.5 km, owing to distance, so the positions of the near-surface portions of tornadoes 4-10 and the RFGF were not observed.

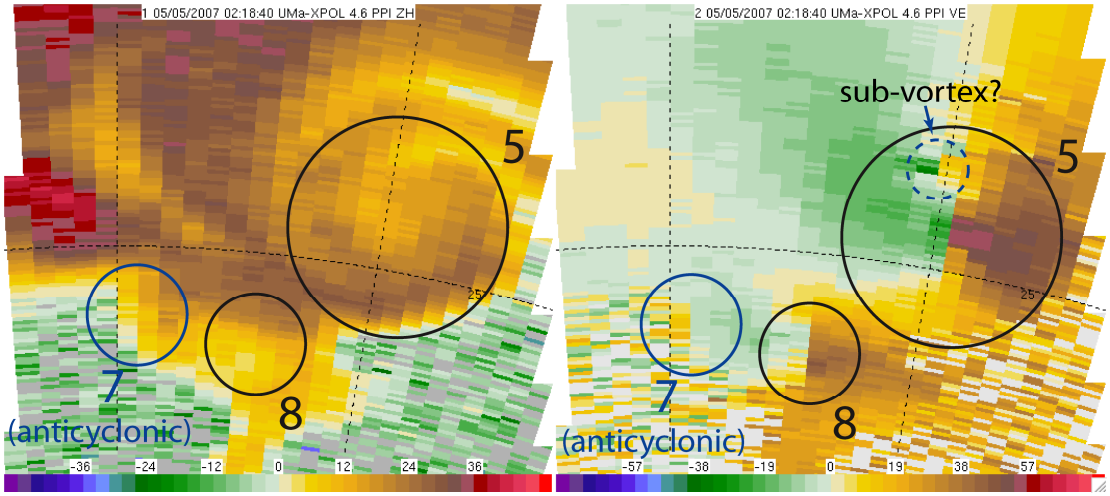


Fig. 24. As in Fig. 22, but for UMass X-Pol data collected at 0219 UTC at an elevation angle of 4.6°. A possible, brief sub-vortex of tornado 5 is indicated; this feature did not appear in the preceding or succeeding volumes.

5.2 Reflectivity features

As previously discussed, UMass X-Pol reflectivity fields were not well calibrated for this deployment. In addition, hydrometeors with diameters on the order of 3 cm (large hail, in the Mie regime at X-band) were documented, so the more appropriate name for the "reflectivity" field in this data set is the "equivalent reflectivity" field (with units of dBZ_e). Most of the following discussion of the equivalent reflectivity fields will be qualitative rather than quantitative, with numerical comparisons only made within the data set.

Most of the vortex signatures in UMass X-Pol velocity data correspond to hooks in equivalent reflectivity fields (although some are embedded within the overall reflectivity structure of the Greensburg storm and difficult to discern). In addition, several of the tornadoes (1, 3, 4, 5, 10; e.g., Fig. 22i, j, Fig. 25) exhibited a weak-echo hole (WEH; Bluestein *et al.* 2007a).

A bounded weak echo region (BWER) with an upper-level echo overhang, indicative of a strongly rotating updraft region or "vault" (Browning and Donaldson

1963) in the Greensburg supercell, is also apparent, wrapping upward and from south to north around the east side of the tornado (Fig. 25). These features are common in radar observations of tornadic supercells (e.g., Bluestein *et al.* 2007b).

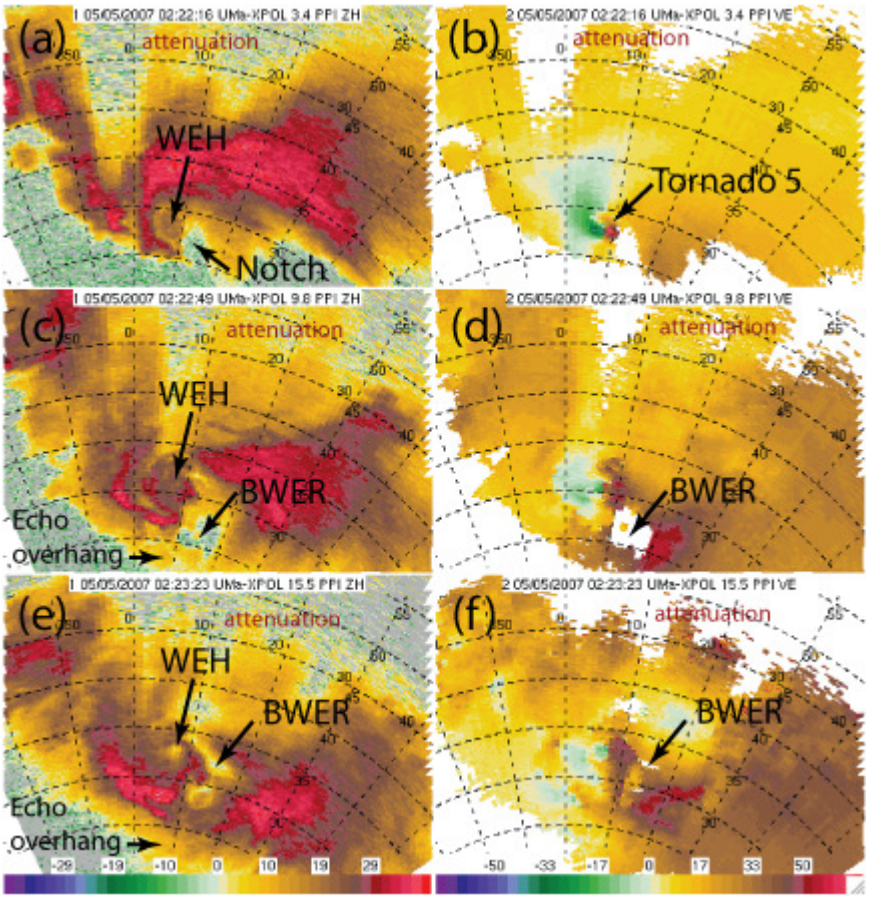


Fig. 25. UMass X-Pol uncalibrated equivalent reflectivity (Z, in dBZ_e, left column) and dealiased Doppler velocity (V_r, in m s^{-1}, right column) in the Greensburg supercell at 0223 UTC at (a, b) 3.4°; (c, d) 9.8°; and (e, f) 15.5°. At this time, the Greensburg tornado was approaching its peak intensity. Location of the weak-echo notch, BWER, and WEH associated with tornado 5 are indicated.

5.2.1 Vertical cross-sections / pseudo-RHIs

I constructed "pseudo-RHIs" for each UMass X-Pol volume by extracting single rays from each sweep that were closest to a chosen azimuth angle (Ψ), and generating a range-height plot (effectively, a vertical cross-section at Ψ). A number of interesting features of the Greensburg storm emerged when Ψ was chosen to pass

through the center of the mature Greensburg tornado. First, the WEH appears a continuous weak-echo column (WEC) extending to altitudes above 10 km AGL (Fig. 26a). (Hereafter, this reflectivity minimum will be called a WEH when it is discussed in the context of a single sweep, and a WEC when discussed over a depth of more than one sweep.) This WEC is similar to those observed in previous radar data sets collected in tornadoes (e.g., Wakimoto *et al.* 1996; Dowell and Bluestein 2002b). Second, a horizontal vortex (Fig. 26b) and partial reflectivity curl (Fig. 26a) appear in the echo overhang. Wakimoto et al. (1996) found similar features in the echo overhangs of supercells sampled by airborne radars during Project VORTEX, which they refer to as "echo curls" (see their Fig. 6) and attribute to recycling of hail embryos into the supercell updraft.

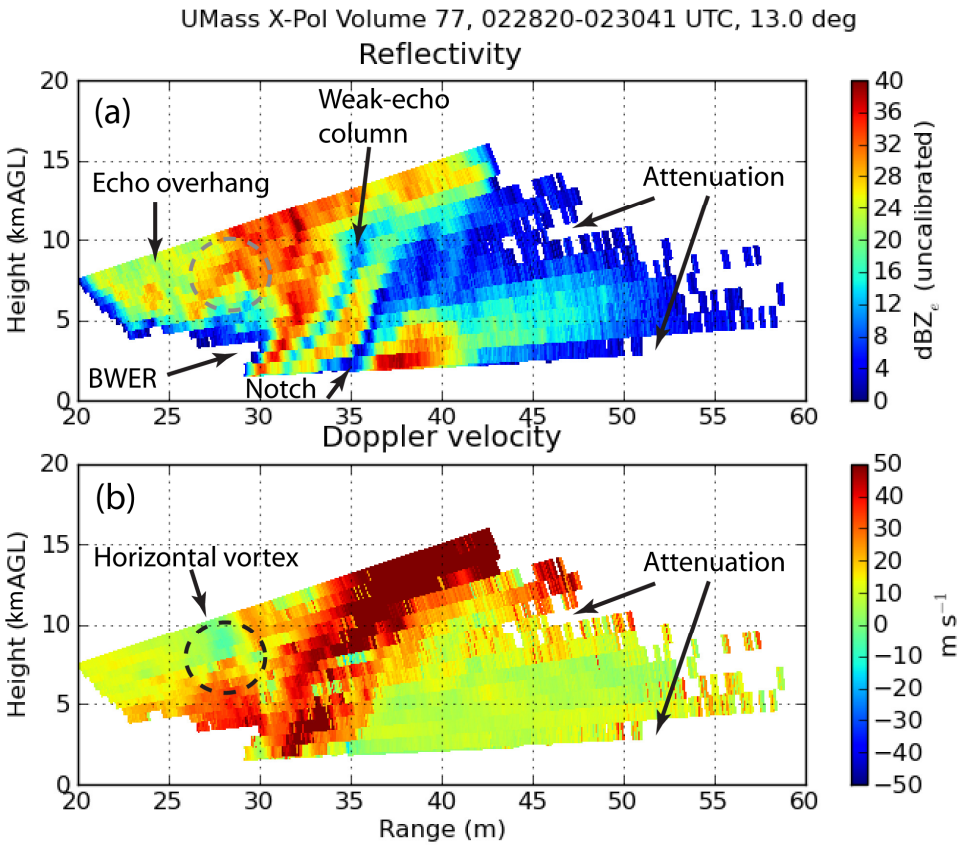


Fig. 26. A pseudo-RHI of UMass X-Pol (a) uncalibrated equivalent reflectivity (in dBZe) and (b) Doppler velocity (in m s^{-1}) at an azimuthal angle of 13.0 degrees (clockwise from north), slicing through the Greensburg tornado during its mature phase at 0228-0230 UTC. Note the northward tilt of the WEC with height, the horizontal vortex / reflectivity curl in the echo overhang (dashed circle), and relatively high reflectivity values near the surface on the far side of the vortex, where large hail was reported.

5.2.2 Weak-echo holes and weak-echo columns

WEHs have been documented in previous radar data sets collected in tornadoes (Wakimoto *et al.* 1996; Wurman and Gill 2000; Burgess *et al.* 2002; e.g., Dowell and Bluestein 2002b; Bluestein *et al.* 2007a; e.g., Bluestein *et al.* 2007b; Tanamachi *et al.* 2007). The earliest example (to the best of my knowledge) of a WEC associated with a tornado is in an RHI documented by Fujita (1963; labeled "eye" in his Fig. 17).

5.2.2.1 Possible causes of the weak-echo column

WEHs and WECs are commonly explained by centrifuging of hydrometeors and debris from the center of a tornado (Dowell *et al.* 2005). It was somewhat surprising to see that the WEC sometimes extended to altitudes above 10 km AGL (Fig. 26). It has been hypothesized that an axial downdraft (i.e., a two-celled vortex structure; Sullivan 1959; Trapp 2000) may also be at least partly responsible for the WEC, particularly in the upper levels (Fig. 27). Vortices may transition between one-celled and two-celled structure, and a vortex may simultaneously exhibit one-celled structure near the surface and and two-celled structure aloft, separated by a region of "vortex breakdown" (Fig. 28).

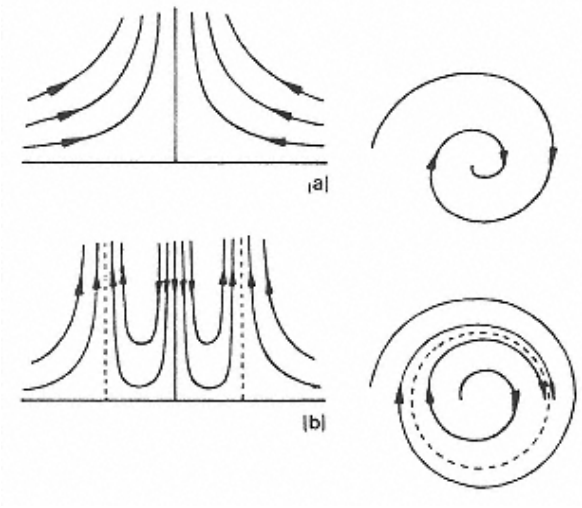


Fig. 27. Illustration from Sullivan (1959) of (a) one-celled and (b) two-celled vortices. The left panels show the flow as seen in a cross-section taken through the center of the vortices; the right panels show the flow as viewed from above. Note that the axial downdraft in the two-celled vortex (bounded by the dotted lines) is associated with divergence.

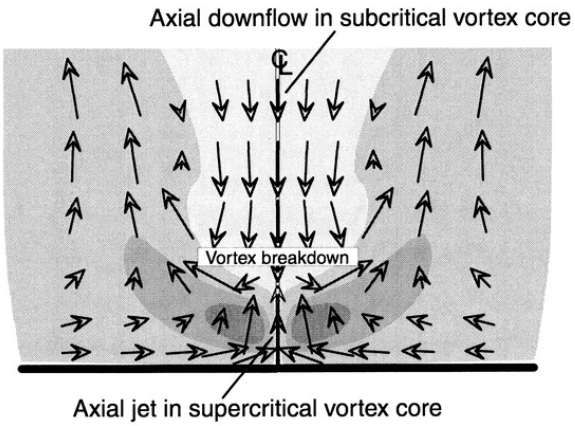


Fig. 28. Illustration from Trapp (2000) of vortex breakdown, in which a vortex (viewed here in cross-section) exhibits one-celled structure close to the surface and two-celled structure aloft. Shading represents tangential motion with respect to the vortex core; darker shadings indicate faster winds.

In Doppler radar data, the signature of a cyclonic, divergent (convergent) vortex would appear like a cyclonic vortex signature (VS) turned slightly counterclockwise (clockwise; Fig. 29). We sought evidence in the UMass X-Pol velocity data that the Greensburg tornado exhibited divergence at upper levels (i.e., above 6 km) during times when "deep" volume scans were collected.

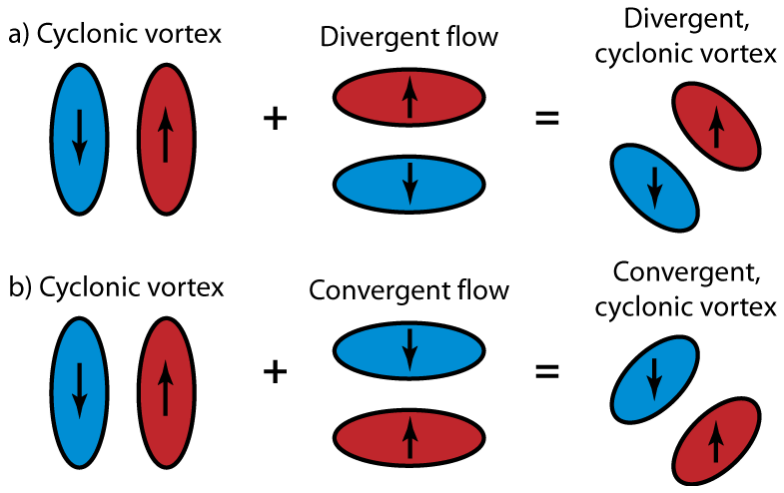


Fig. 29. Schematic illustration of the superposition of (a) divergent flow or (b) convergent flow on a cyclonic vortex signature in Doppler velocity data. Red (blue) shading indicates flow away from (toward) the radar (which is assumed to be located well south of the features). A real Doppler velocity field generated by an axisymmetric vortex would exhibit some distortion from the geometry of the radar scan; see Brown and Wood (2007) for simulated Doppler velocity signatures of an idealized, convergent vortex.

We subtracted the mean storm motion (14 m s^{-1} from 219°) from the Doppler velocity fields), then examined sweeps that intersected the Greensburg tornado at altitudes above 6 km. We made subjective judgments about whether the VSs appeared to be convergent or divergent, and did not seek to tabulate the results. (We may yet perform this step in the future.) We found a mixture of convergent, neutral, and divergent VSs at these altitudes (Fig. 30). Some VSs were noisy and left unclassified. Overall, we found more convergent VSs in these data than neutral or divergent VSs.

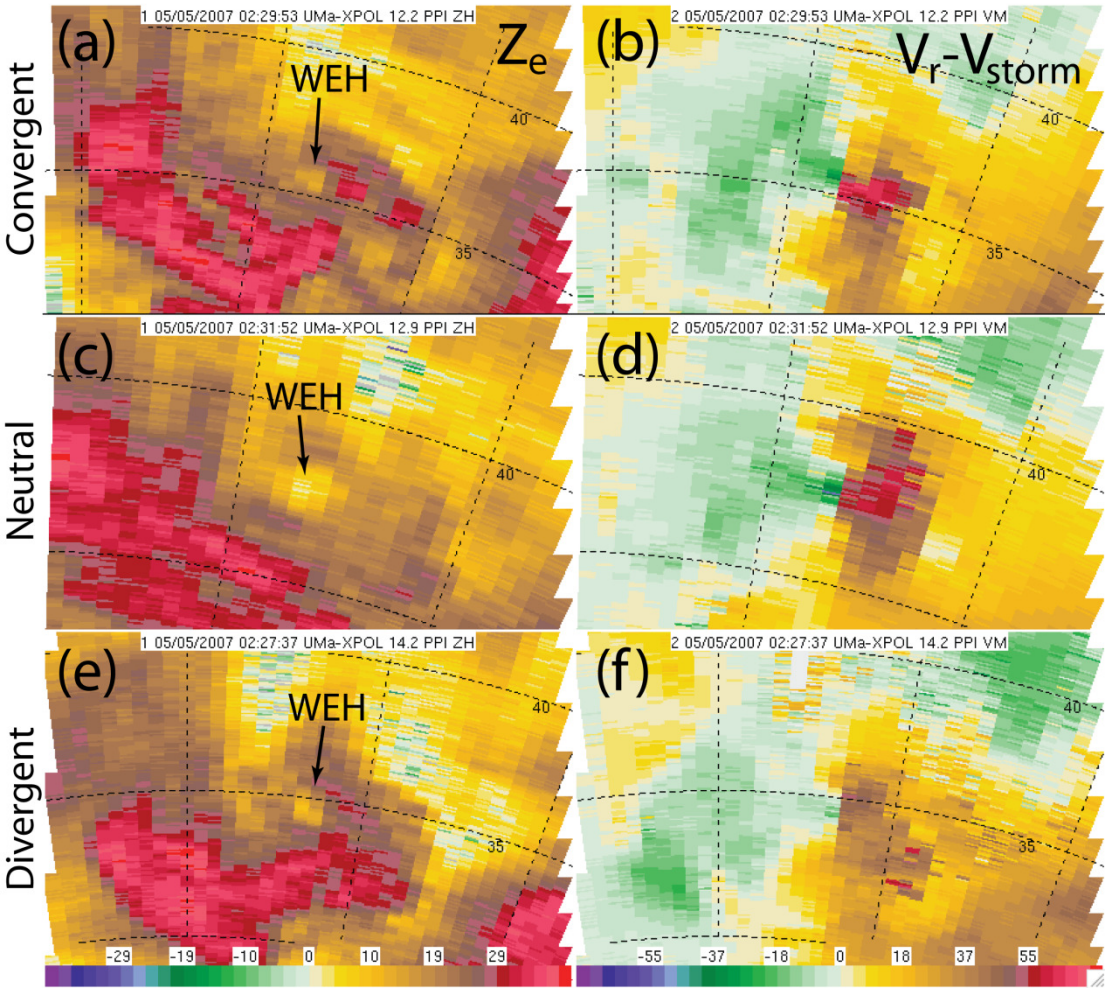


Fig. 30. As in Fig. 22, but for but for UMass X-Pol data collected at (a) 0230 UTC at 12.2°, (b) 0232 UTC at 12.9°, and (c) 0228 UTC at 14.2°. The pairs of panels convey examples of (a, b) a convergent VS, (c, d) a neutral VS, and (e, f) a divergent VS.

In contrast, a more consistent convergence signature was found in the Greensburg tornado at low levels, indicating one-celled vortex structure near the surface. While the lack of a consistent, divergent VS aloft would seem to indicate that an upper-level axial downdraft was not present in the Greensburg tornado, that the vortex was one-celled throughout its depth, and that the WEC occurred primarily as a result of centrifuging throughout the depth of the tornado vortex, we feel that cannot wholly reject the possibility of an axial downdraft for the following reasons:

(1) The azimuthal gate spacing at the range of the Greensburg tornado was on the order of 500 m. If the area of divergence were substantially narrower than the gate spacing, its signal in the Doppler velocity data would have been overwhelmed by the signals from convergent flow outside the downdraft envelope (Fig. 27b). A radar with a much smaller azimuthal gate spacing (such as the UMass W-band radar; Bluestein and Pazmany 2000; Tanamachi *et al.* 2007) would have been necessary to distinguish such a narrow, divergent VS.

(2) An axial downdraft may still have occurred at very high altitudes, above those sampled by UMass X-Pol.

(3) Brief axial downdraft(s) may not have been captured in UMass X-Pol volumes, which were collected ~60 – 90 sec apart.

(4) At such high elevation angles (i.e., above 15°), a substantial component of vertical velocity is present in the Doppler velocity fields, complicating interpretation of VSs. It is difficult to distinguish components of velocity

associated with the vortex, divergence / convergence, and upward / downward motion simply by examining the Doppler velocity fields from a single radar.

5.2.2.2 Locations of weak-echo hole and vortex signature

In previous studies, WEHs sampled by radars have been found (or assumed) to be collocated with the center of the tornado (R. Wakimoto, personal communication). Since the Greensburg tornado had a large and persistent WEC; we sought to verify that the WEHs were indeed collocated with the vortex signature at most times and elevations.

I located a local reflectivity minimum associated with each tornado in as many sweeps as I could, and recorded this as the location (range [r] and Ψ) of the WEH. I then calculated the distance (in m) between the WEH and vortex signatures (VS) discussed in the previous section (e.g. Fig. 31). While a WEH location could be determined to within a single UMass X-Pol gate, the VS required at least two gates to locate (i.e., inbound and outbound). When faced with a choice, I selected the inbound gate and then subtracted 0.4° (half an azimuth space). In addition, sometimes the SNR values (not shown) in the WEH were low, making the velocity fields noisy and adding uncertainty to the location of the VS.

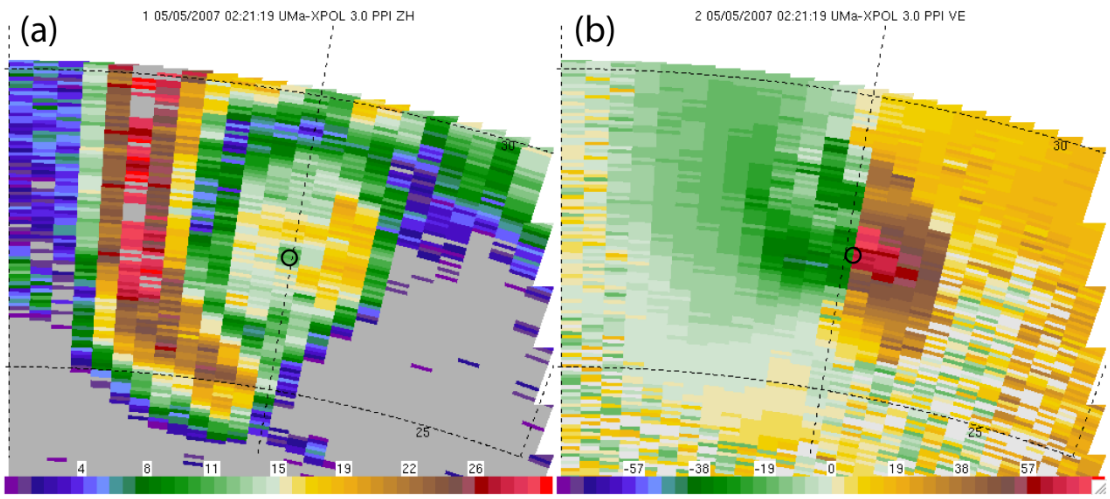


Fig. 31. As in Fig. 22, but for but for UMass X-Pol data collected at 0221 UTC at an elevation angle of 3.0°. Locations of a (a) WEH and (b) vortex signature are indicated by small black circles.

I found that the distance between the WEH and VS was less than or equal to 850 m 85% of the time, with a mean offset of 512 m. However, the discrete, uneven azimuthal spacing of UMass X-Pol gates (which grow farther apart with distance from the radar; Fig. 32) also meant that the calculated distances could not be assumed to be normally distributed, and that standard statistical hypothesis tests (such as the Student's *t*-test) could not be applied to the null hypothesis that the mean of the distribution was 0 m.

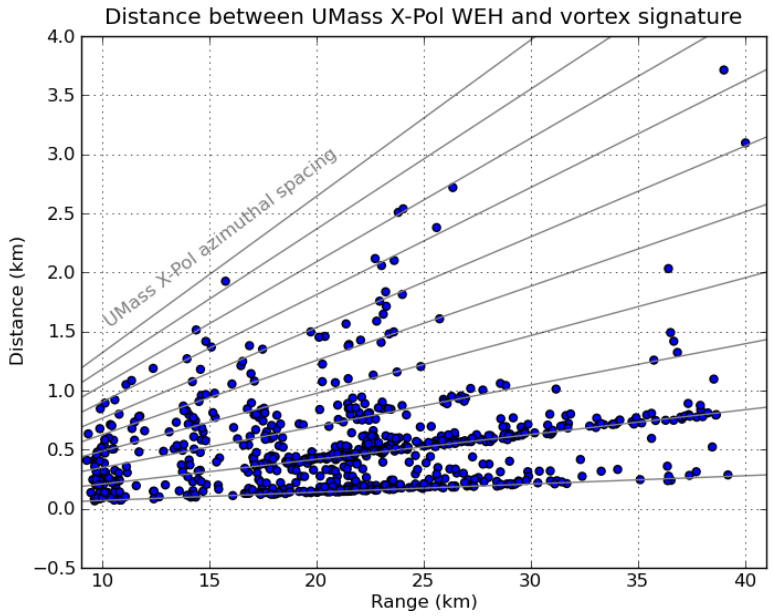


Fig. 32. Distance between UMass X-Pol-detected WEH and vortex signature (in km) as a function of range (of the vortex signature, in km) from the radar. Note that the distances are strongly discretized by the azimuthal spacing of the UMass X-Pol data (gray contours, every 0.8° starting at 0.4°).

I decided instead to look at the range and azimuth offsets separately (Fig. 33), assuming that the offsets $\Delta r = r_{WEH} - r_{VS}$ and $\Delta\Psi = \Psi_{WEH} - \Psi_{VS}$ were both normally distributed. The mean range (azimuthal) offset was +50 m (+0.0°), and the variance was 15 m (1.3°). I first tested the null hypothesis $H_o : \Delta r = 0$ (alternative hypothesis $H_a: \Delta r \neq 0$) using a one-sample, two-tailed Student's t-test with an alpha level of 0.05. I obtained a *t*-statistic of 3.433 and a *p*-value of 0.00, so I rejected the first null hypothesis. I then tested the second null hypothesis $H_o: \Delta\Psi = 0$ (alternative hypothesis $H_a: \Delta\Psi \neq 0$), using the same alpha level of 0.05. I obtained a *t*-statistic of 0.974 and a *p*-value of 0.33, so I could not reject the second null hypothesis. I conclude that, for this deployment, the WEH is indeed collocated with the VS in azimuth, but located slightly farther from the radar in range (by about one range gate). This is the same impression one gets examining histograms of Δr and $\Delta\Psi$ (Fig. 33).

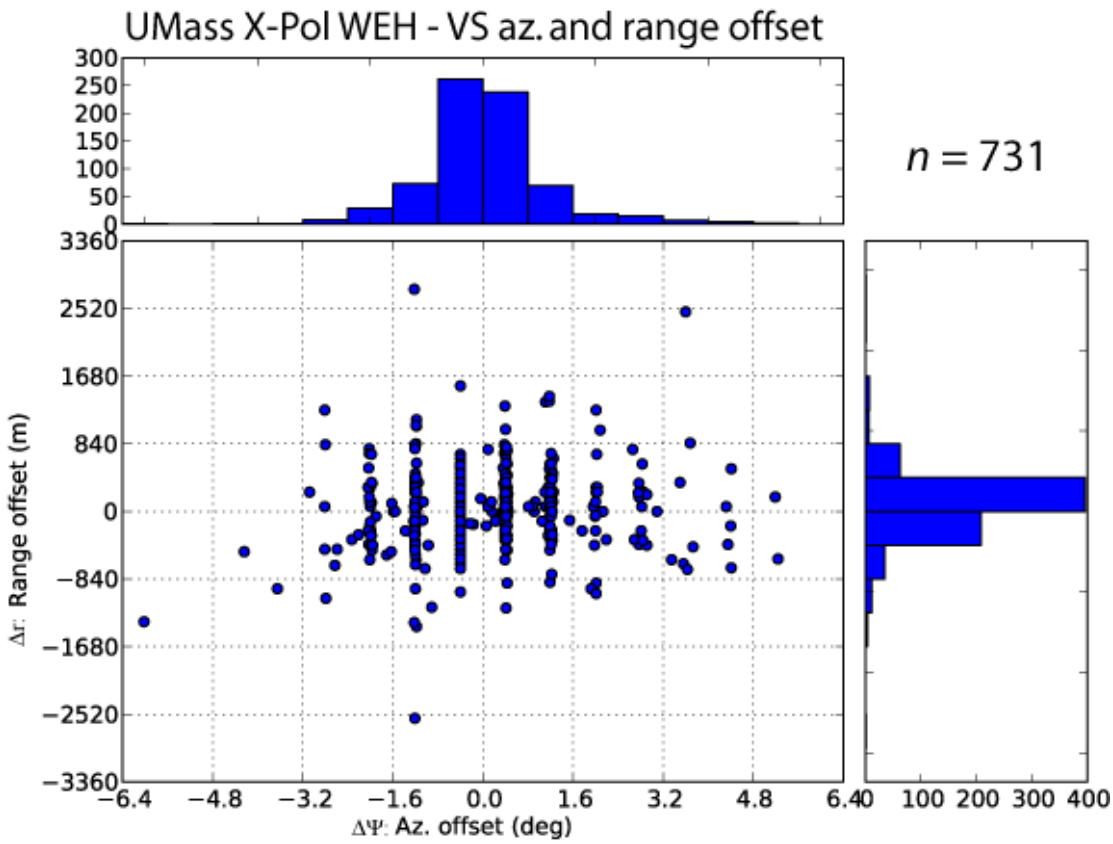


Fig. 33. Scatterplot of WEH minus vortex signature range offset (in m) versus azimuthal offset (in deg). Histograms at the top (right) are for azimuthal (range) offset, with a bin width of 0.8° (420 m).

5.3 Comparison of tornado and updraft motion

Dowell and Bluestein (2002a) observed that cyclic tornadogenesis (i.e., mode I) in the 8 June 1995 McLean, Texas storm resulted from "a mismatch between the horizontal motion of successive tornadoes and the horizontal velocity of the main storm-scale updraft and downdraft." Additionally, long-track tornadoes (i.e., mode II) resulted when the horizontal motion of a tornado closely matched that of its associated updraft and downdraft. To see if this conclusion was also applicable the Greensburg storm, we sought to compare locations of the updraft and tornadoes. We used reflectivity and velocity data from KDDC to subjectively locate the supercell vault (as a proxy for the updraft, in the absence of vertical velocity measurements)

and the VSs from altitudes between 1.5 and 2.0 km from the UMass X-Pol data (as a proxy for the tornadoes), and compared the motions of each.

Because the updraft of a supercell spans a considerable depth (about 1.0 to 8.0 km AGL), and KDDC data had more consistent coverage at altitudes at and above 5 km than UMass X-Pol, particularly during the early tornadoes (1-4), KDDC data were used to locate the updraft. Recall that KDDC collected volumetric reflectivity and Doppler velocity data every 4.1 min in the Greensburg storm. These data were objectively analyzed to a 1 km grid using a two-pass Barnes scheme (Trapp and Doswell 2000; Majcen *et al.* 2008). According to the conceptual model of Browning and Donaldson (1963) – later refined by Lemon and Doswell (1979) - and results of numerical simulations (e.g., Weisman *et al.* 1983), the center of the updraft of a mature, cyclonic supercell is typically located near the highest reflectivity gradients on the north side of the notch at low levels and on the near-hook side of the BWER at upper levels. We assumed that the updraft remained in the same place with respect to these reflectivity features. The latitude and longitude of the updraft were subjectively located (to within ± 2 km) by comparing these objectively analyzed reflectivity fields at 1.5 and 7.5 km AGL (taken to be the altitudes of the low-level hook and upper-level echo overhang, respectively).

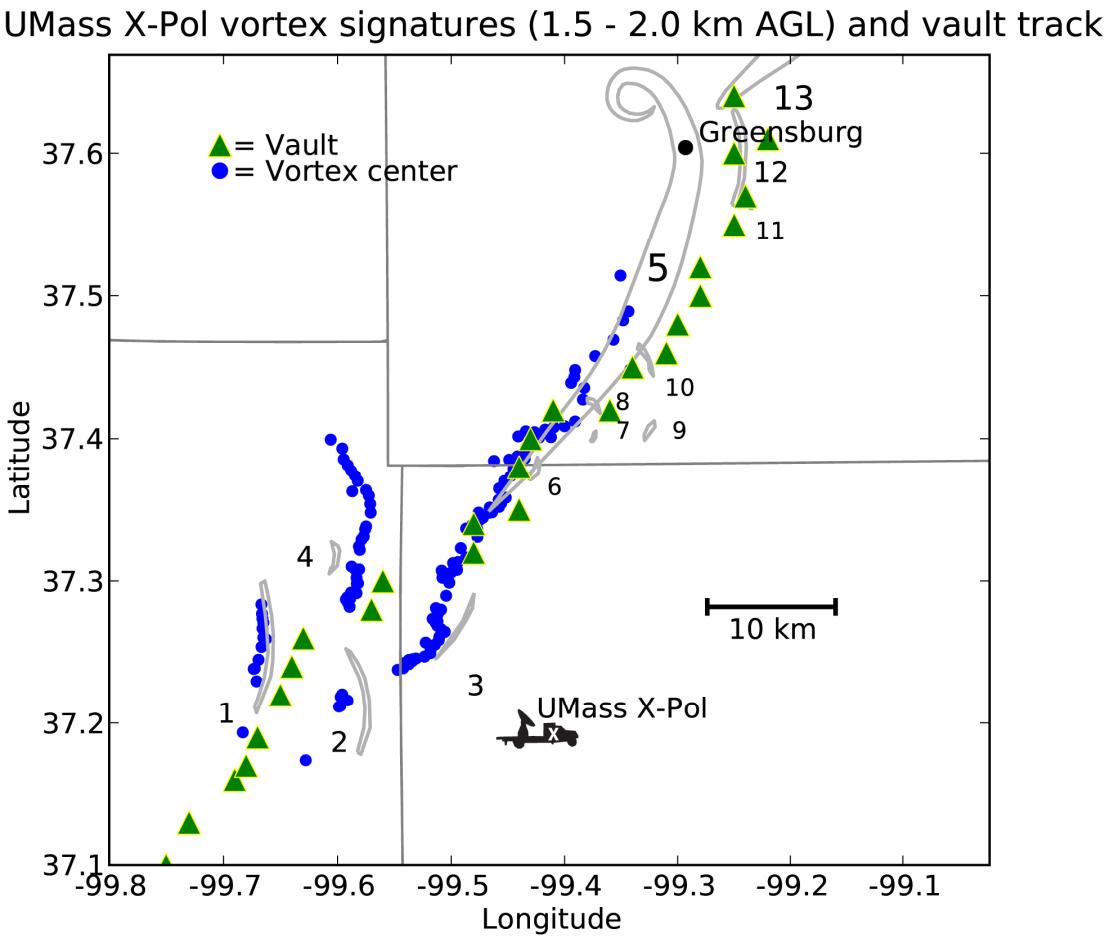


Fig. 34. Tracks of UMass X-Pol vortex signatures between 1.5 and 2.0 km AGL (blue dots) and the updraft of the Greensburg storm (green triangles) overlaid on top of tornado tracks.

The earlier tornado surface damage tracks (1-4) had a component of motion to the *left* of the updraft motion, while the Greensburg tornado tracked more or less *parallel* to the updraft during its mature phase (Fig. 34). However, the surface tornado tracks did not contain information about the horizontal speeds of the tornadoes, so UMass X-Pol data were used to estimate the components of each tornado's motion.

UMass X-Pol VSs falling between 1.5 and 2.0 km AGL (the lowest altitude range over which most of the tornadoes were sampled) were sorted, by tornado, into 4.1 min intervals corresponding to the KDDC volumes. The average velocity of these

VSs were computed and compared to the updraft velocity over the same 4.1 min intervals. The motion of the Greensburg tornado did, indeed, match the motion of the updraft more closely than the other tornadoes, particularly when the Greensburg tornado was approaching its mature phase (0208 – 0236 UTC; Fig. 35). This behavior persisted for at least 20 min, and may have continued after UMass X-Pol data collection ended.

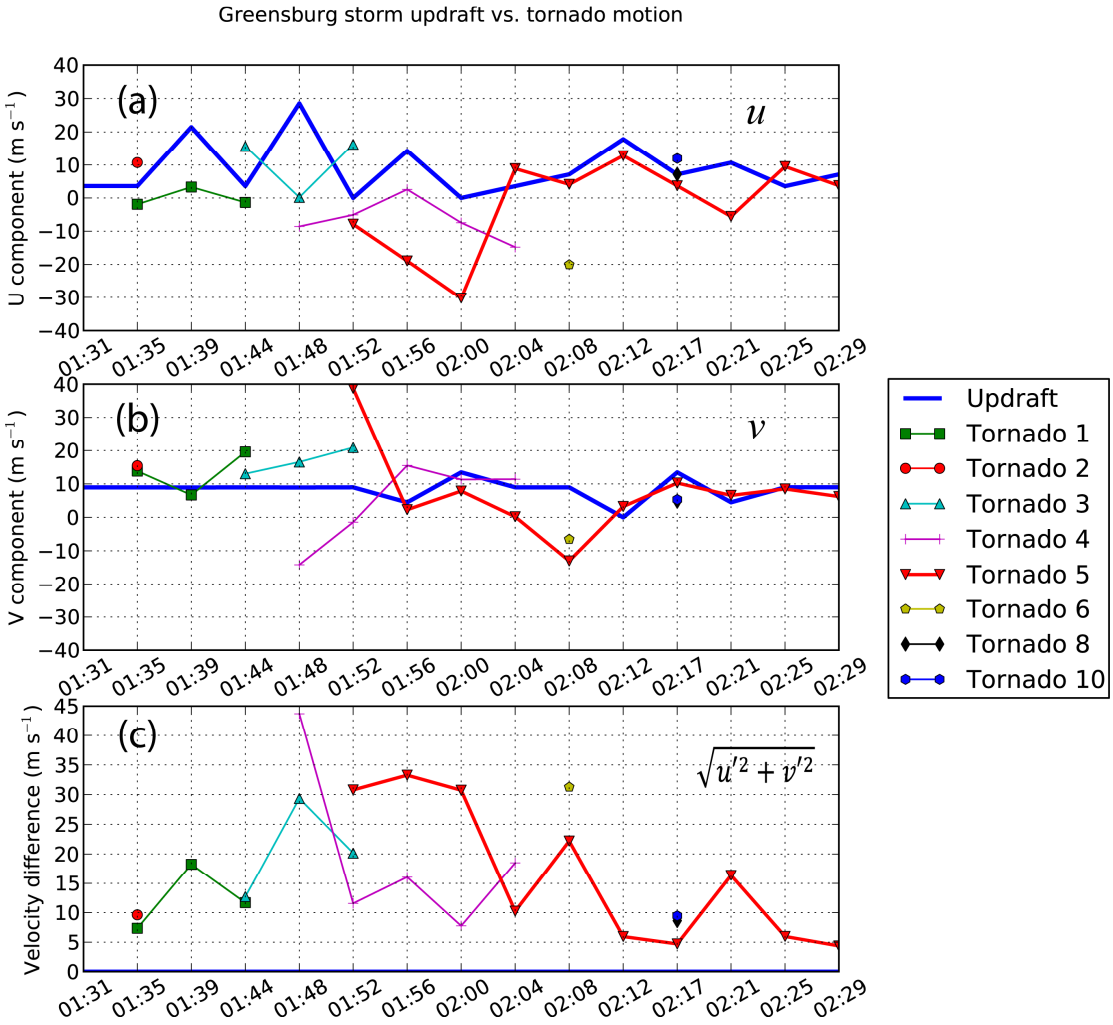


Fig. 35. The (a) *u*- and (b) *v*-components of motion (in m s^{-1}) of the Greensburg storm updraft (solid blue with no markers) and tornadoes (marked lines) as depicted in Fig. 34. The magnitude of the velocity difference between the tornado and the updraft is shown in panel (c). There are no markers for tornadoes 7 and 9 because neither lasted longer than a full UMass X-Pol volume scan, so their velocities could not be computed.

The reader is cautioned against interpreting Fig. 35 in a strictly quantitative sense. I located the updraft and VSs subjectively (albeit to the best of my ability). At some times, it was very difficult to "pin down" the precise location of a VS, particularly when it was broad and / or weak, or other VSs were close by. Recall that the precursor circulation of tornado 5 (which was initially very diffuse) is believed to have ingested the remnant circulation of tornado 3. Therefore, the uncertainty associated with the location of the precursor circulation of tornado 5 was particularly elevated, and may explain, at least in part, the apparent substantial westward component of motion of tornado 5 prior to tornadogenesis (0200 UTC).

5.4 Behavior of rear flank gust front(s)

Surface outflow boundaries were only briefly sampled in the UMass X-Pol data owing to distance and beam blockage (discussed previously). Some information about a RFGF, however, can be inferred from UMass X-Pol data. Any ouflow boundaries would have been located outside the southern edge of the UMass X-Pol sector until 0138 UTC. As the precursor circulation of tornado 3 intensified and moved into the middle (in an azimuthal sense) of the UMass X-Pol sector, a weak reflectivity appendage (Fig. 22e; Fig. 36a) associated with inbound velocities and low values of $\tilde{\rho}_{hv}$ (~0.5; Fig. 36c), which we interpret as lofted dust and insects on the leading edge of a RFGF, appeared on the south side of tornado 3 and wrapped partway around it (Fig. 37). This reflectivity appendage varied greatly in width during the deployment, despite being sampled at almost the same elevation angle. The appendage was relatively slender at some times (Fig. 22e) and "filled in" at other times with predominantly non-meteorological scatterers (perhaps more dust and

insects; Fig. 36a, c). The RFGF surged the farthest eastward with respect to tornado 3 at about 0150 UTC (Fig. 37), about halfway between the NWS-reported start and end times (0148 and 0152 UTC, respectively; Table 2). After 0150 UTC, this RFGF retreated, and tornado 3 turned to the left with respect to the updraft motion (Fig. 23) and weakened. The precursor circulation of tornado 5 absorbed what is presumed to be the remnant circulation from tornado 3 (Fig. 22e, f). The RFGF then trailed tornado 5, but did not wrap around it. After 0206 UTC, this feature was too far away to be detected in the UMass X-Pol reflectivity fields, even at the lowest elevation angles.

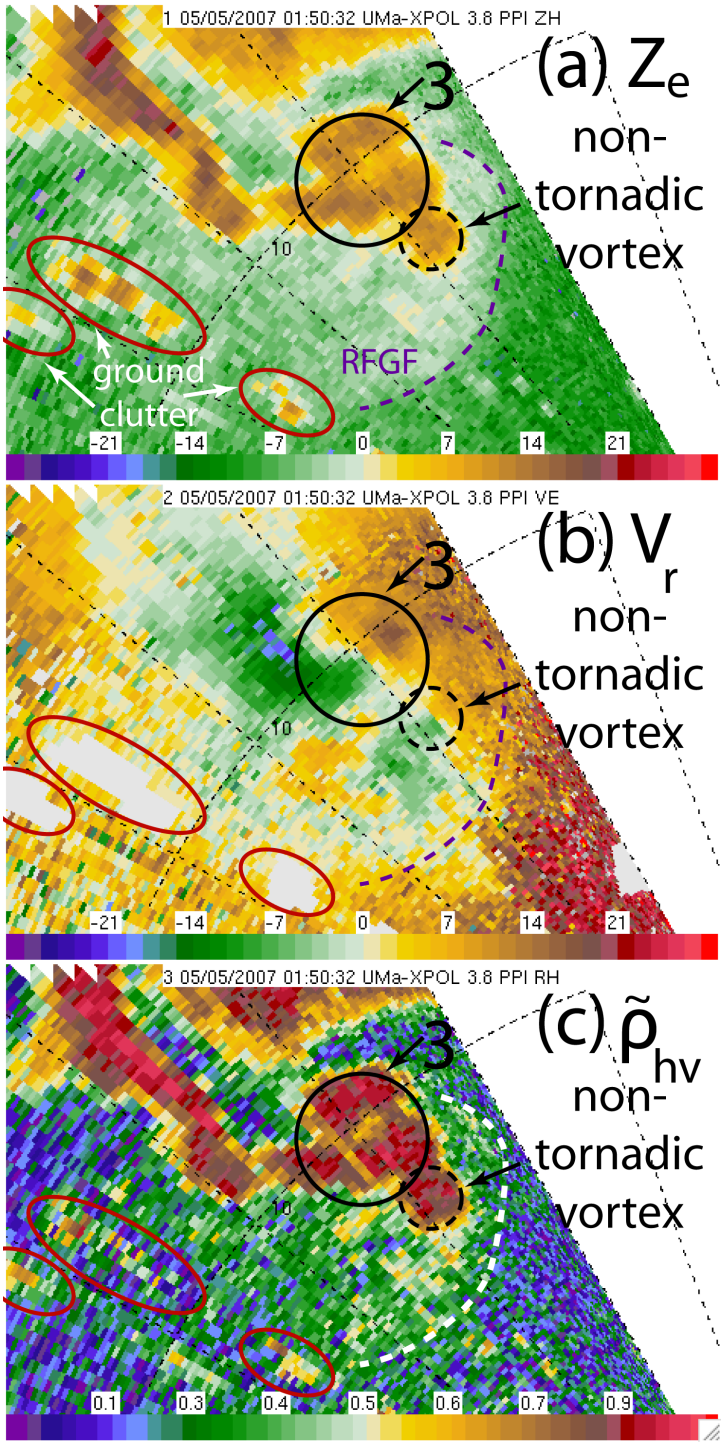


Fig. 36. UMass X-Pol (a) uncalibrated equivalent reflectivity (in dBZ_e), (b) dealiased Doppler velocity (in m s^{-1}), and (c) cross-correlation coefficient (unitless) associated with tornado 3 in Greensburg supercell at 0151 UTC at an elevation angle of 3.8°. Tornado 3 is circled in solid black; the dashed black circle highlights a smaller circulation that was not associated with any surveyed surface damage. Red ovals encircle ground clutter targets; these velocity data have been edited out of panel (b). The dashed purple curve is the inferred leading edge of the rear flank gust front. Range rings are every 5 km; azimuth spokes are every 10°.

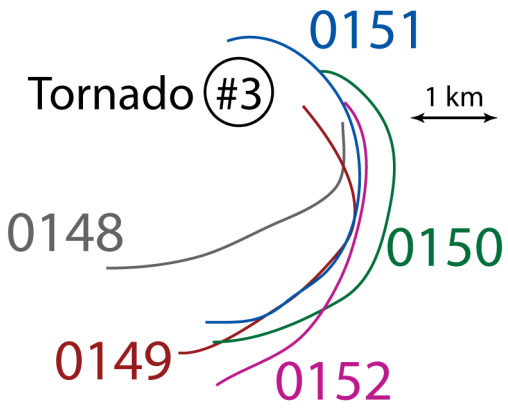


Fig. 37. The position of the RFGF, as inferred from UMass X-Pol equivalent reflectivity and velocity fields, relative to tornado 3 (black circle). Indicated times are UTC on 5 May 2007.

The updraft exhibited fairly steady motion toward the northeast at most of the analysis times, except for three eastward "jumps" in its track that occurred between 0139 – 0156 UTC (Fig. 34, Fig. 35), during the Greensburg storm's mode I tornado production phase (0132 – 0200 UTC). Such eastward jumps could have been caused by discontinuous propagation, as new pulses in updraft at the apex of the RFGF as it wrapped around the hook region of the supercell. The forward surge of the RFGF relative to tornado 3 (0150 UTC) occurred prior to an eastward jump in the updraft position between 0152 and 0156 UTC; however, the KDDC volumes were too coarsely spaced in time to definitively link the two events.

Forward surges in the RFGF might also have served to advect the lower portions of any ongoing tornadoes left and/or rearward with respect to the updraft motion, thereby causing a mismatch in the horizontal velocities of these two features (Dowell and Bluestein 2002a). The tilt (toward the updraft) with height of tornado 4's circulation toward the end if its life cycle may be evidence of the rearward advection of the lower portion of tornado 4. However, no reflectivity appendage that might have

indicated another RFGF was detected by UMass X-Pol in conjunction with tornado 4, presumably because tornado 4 was farther from the radar.

5.5 Polarimetric observations

Patterns of differential reflectivity (Z_{DR}) and partial cross-correlation coefficient ($\tilde{\rho}_{hv}$; Appendix C) variables in the Greensburg supercell indicated a predominance of oblate hydrometeors ($Z_{DR} > 0$ and $\tilde{\rho}_{hv} > 0.9$; probably raindrops or a rain/hail mixture) in the hook echo region. A relatively high-Z_{DR} "ring" surrounded the mature Greensburg tornado up to altitudes of about 5 km. The inner diameter of this ring was about 5 km at low levels at 0230 UTC (Fig. 38g), considerably wider than the maximum 2.7 km surface damage path width reported by Lemon and Umscheid (2008).

5.5.1 Z_{DR} arc

Relatively high values of Z_{DR} (> 5.0 dB) were observed at low levels along the inflow of the forward flank precipitation shield (Fig. 38g). This "Z_{DR} arc" has been reported in numerous other supercells sampled by polarimetric radars at different wavelengths and has been hypothesized to result from size-sorting of precipitation particles in the presence of strong low-level vertical wind shear (Kumjian and Ryzhkov 2009). Specifically, small drops in the forward flank are advected toward the interior of the storm's core by powerful near-surface inflow, while larger, more oblate hydrometeors linger near the edge of the precipitation shield, resulting in enhanced Z_{DR} values in this area. While the Z_{DR} arc was consistently present whenever the forward flank was sampled by UMass X-Pol, the UMass X-Pol sector was selected to focus on the hook echo region of the Greensburg

storm rather than the forward flank, so substantial portions of the Z_{DR} arc often lay outside the sector for long periods of time. Because of this inconsistent sampling, I do not feel comfortable making a definitive statement about any association between the Z_{DR} gradient, for example, and the increase of low-level shear.

5.5.2 Tornadic debris signatures

In the tornadoes produced by the Greesnburg storm, low-Z_{DR} (< 0 dB), low-$\tilde{\rho}_{hv}$ (~ 0 – 0.25) columns, coincident with the WEC, were observed in tornadoes 4, 5 and 10 (Fig. 38c, d, g, h). In tornadoes 4 and 10, the WEC, and low-Z_{DR}, low-$\tilde{\rho}_{hv}$ column were well-defined above about 2.0 km, but not closed below. In the case of tornado 5, the low-Z_{DR}, low-$\tilde{\rho}_{hv}$ columns extended through a considerable depth of the storm, often above and beyond the maximum height sampled by UMass X-Pol when it was collecting "shallow" volumes. At 0229 UTC, it can be seen in polarimetric data collected over a "deep" volume that the low-Z_{DR}, low-$\tilde{\rho}_{hv}$ column was flared out at low levels relative to the diameter of the WEC (Fig. 38e, g, h, and Fig. 39). Values of equivalent reflectivity in the inner spiral bands of the tornado were consistent with those in the outer bands, but values of Z_{DR} and $\tilde{\rho}_{hv}$ were relatively low in the inner bands. We infer that non-meteorological scatterers were present in the tornado at low levels (Bluestein *et al.* 2007a; Kumjian and Ryzhkov 2008). Although very little photographic evidence exists (owing to darkness; see the caption of Fig. 1) that documents the composition of the tornado funnel (raindrops vs. debris) at this time, it is believed that these features are associated with lofted dust and vegetation particles (as the tornado was over open fields) surrounded by a closed curtain of raindrops ($Z_{DR} > 0$, $\tilde{\rho}_{hv} > 0.9$). However, the low values of $\tilde{\rho}_{hv}$ in the upper

portion of the WEC may simply be biased by the low power of the backscattered signal at these elevations (M. Kumjian, personal communication).

Tornado 5 had at least five satellite tornadoes, two of which were anticyclonic, as well as several more accompanying non-tornadic circulations detected by UMass X-Pol. Tornado 10 was the largest and best resolved of the satellite tornadoes (Fig. 22i, j), but still considerably smaller and shorter-lived (2-3 min) than tornado 5. Its low-Z_{DR}, low-$\tilde{\rho}_{hv}$ column never perceptibly exceeded the diameter of its WEC. (However, the azimuthal resolution of the UMass X-Pol data at that range – 30 km – was ~400 m.) We infer that, in contrast to tornado 5, in which the lowest portion of the tornado was contaminated by debris, this column was created almost entirely by centrifuging throughout the depth over which it was sampled. It is possible, however, that debris may have been present at altitudes lower than those sampled by UMass X-Pol.

Observations and interpretations of the polarimetric variables in the Greensburg storm tornadoes are consistent with previous UMass X-Pol polarimetric observations collected in the 12 May 2004 Attica, Kansas tornadoes (Junyent *et al.* 2005; Bluestein *et al.* 2007a), S-band polarimetric observations in tornadic supercells by Van Den Broeke *et al.* (2008), Romine et al. (2008), and Kumjian and Ryzhkov (2009), and the "tornadic debris signature" (TDS) identified in tornadic supercells by Kumjian and Ryzhkov (2008).

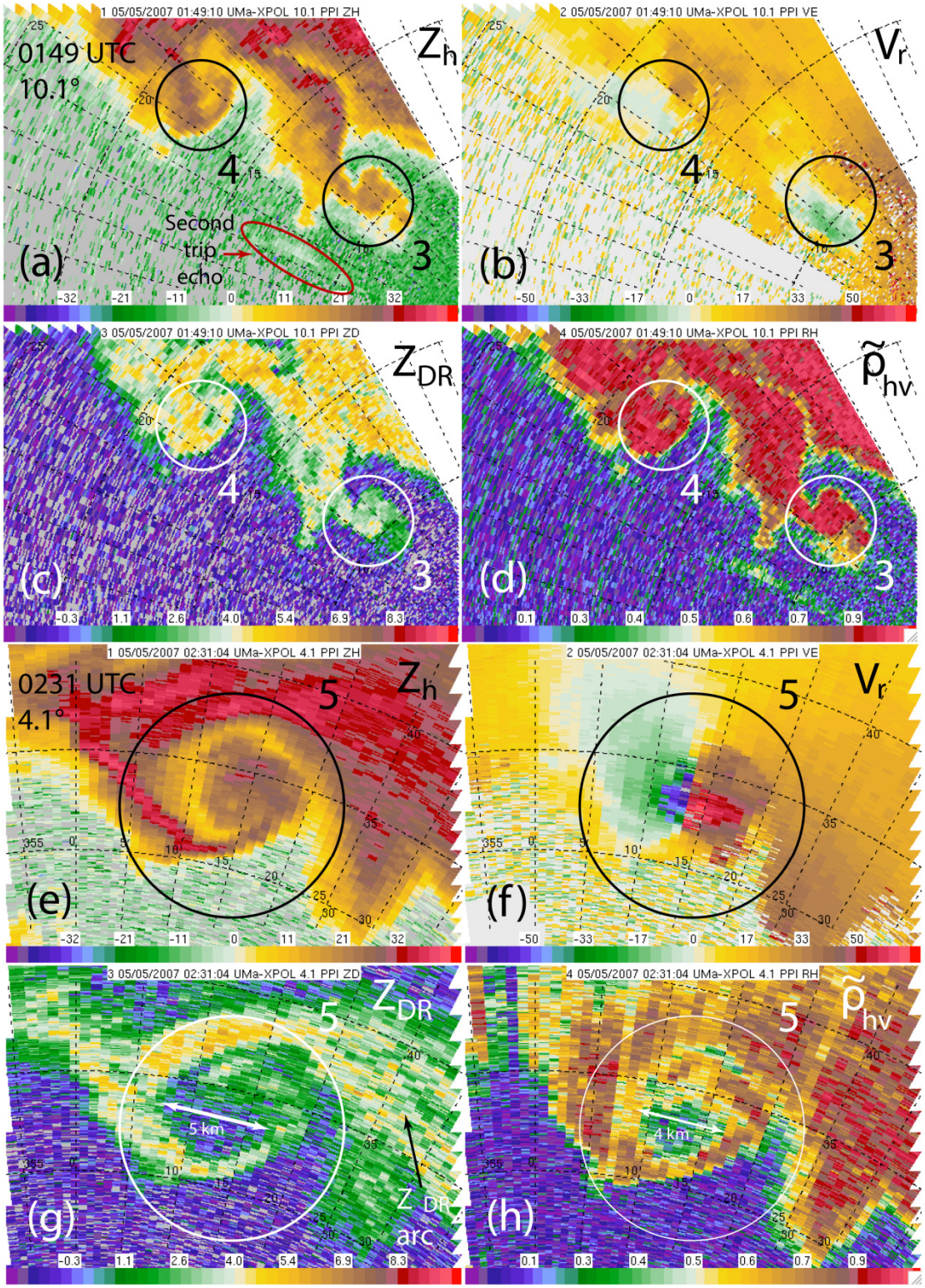


Fig. 38. (a, e) UMass X-Pol uncalibrated equivalent reflectivity (in dBZ_e), (b, f) dealiased Doppler velocity (in m s^{-1}), (c, g) Z_{DR} (in dB), and $\tilde{\rho}_{hv}$ (unitless) in the Greensburg supercell at (a, b, c, d) 0149 UTC, 10.1°; (e, f, g, h) 0231 UTC, 4.1°. Range rings are every 5 km, azimuth spokes every 10°.

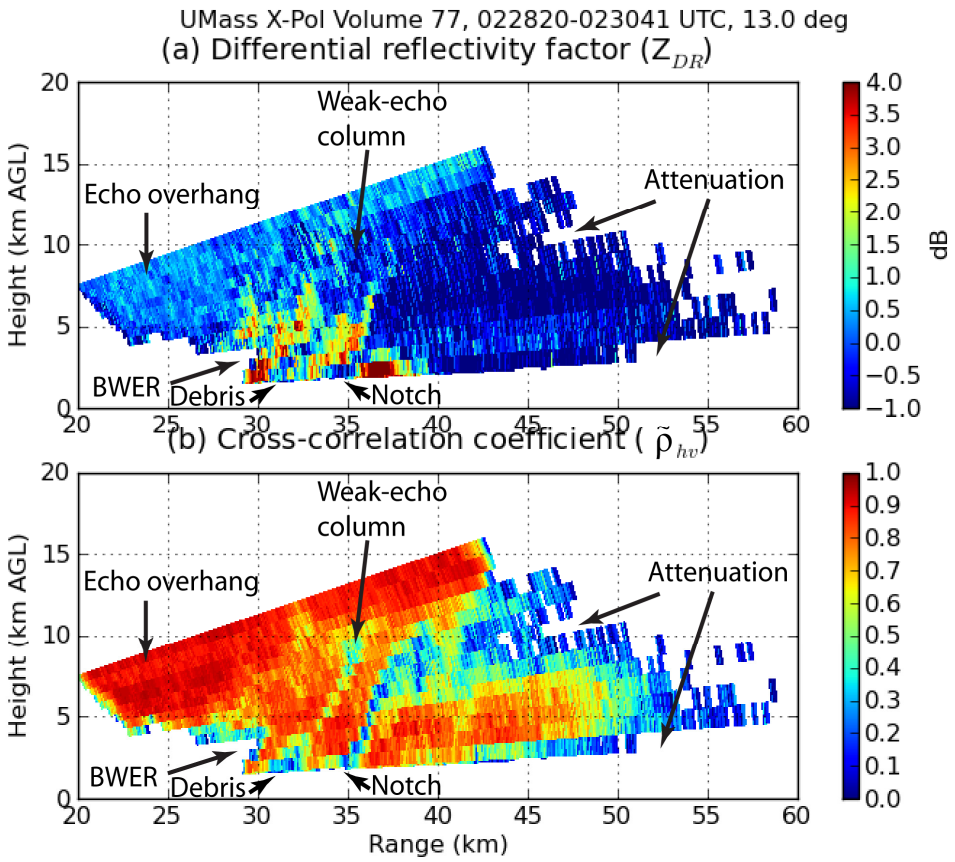


Fig. 39. As in Fig. 26, but for (a) Z_{DR} (in dB) and (b) $\tilde{\rho}_{hv}$ (unitless).

5.6 Comment about clear-air velocity measurements

During the period in which UMass X-Pol was collecting data in the inflow region of the Greensburg storm (i.e., after about 0140 UTC), beam blockage to its northwest and north (Fig. 16) prevented Doppler velocity data collection at angles below 3.0°. In addition, much of the close-range velocity data was contaminated by ground clutter (trees and buildings; Fig. 21), the clear-air data beyond a range of about 10 km from UMass X-Pol was noisy owing to a lack of scatterers. UMass X-Pol collected some uncontaminated (by precipitation, outflow, ground clutter, and second trip echo) Doppler velocity data in the area in the inflow region of the Greensburg storm after 0143 UTC (e.g., Fig. 40), but did not sample inflow over a

sufficiently azimuthally wide sector (i.e. > 90°) to successfully retrieve a near-surface velocity profile using the VAD technique (Browning and Wexler 1968).

Outbound velocities of 29 m s^{-1} were observed 500 m AGL northwest of UMass X-Pol, in the "notch" region of the Greensburg supercell at 0145 UTC, 15 minutes before to the formation of the Greensburg tornado (Fig. 40). This value is consistent with VAD-retrieved low-level wind profiles (Fig. 12) and probably represents the best information available about the inflow environment of the Grensburg storm prior to the mode I-to-mode II transition. The cross-beam component of inflow increased as the Greensburg storm moved away to the northeast.

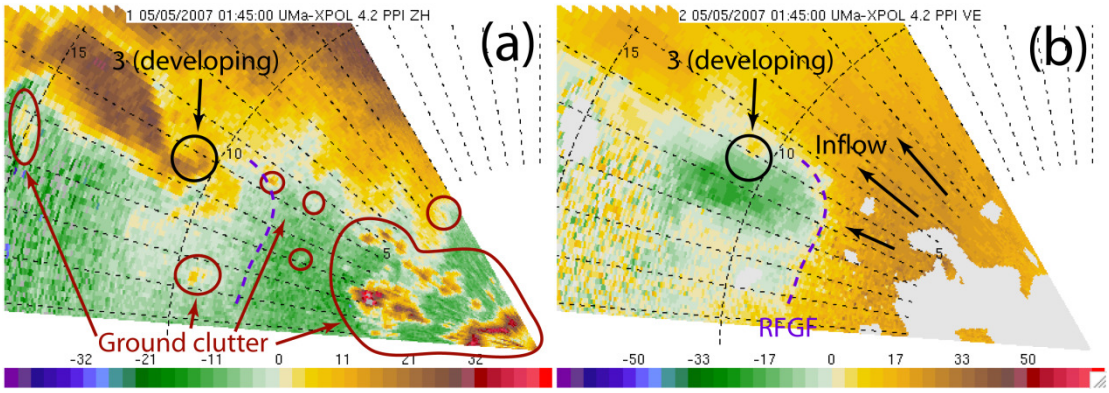


Fig. 40. As in Fig. 22, but for UMass X-Pol data collected at 0145 UTC at an elevation angle of 4.2°. Areas of ground clutter are circled in red on panel (a); associated velocities were edited out of panel (b). The inferred location of the RFGF is denoted by the purple dashed line.

Chapter 6 Ensemble Kalman Filter (EnKF) experiments

Diagnosis of dynamic and kinematic processes in supercells requires more information than can be furnished by radar measurements of reflectivity and Doppler velocity alone. A full, four-dimensional representation of a supercell in an NWP model requires additional variables not observed by radar, such as temperature and moisture. As we will see, the EnKF DA technique provides a potential pathway for retrieval of these unobserved variables.

Because of their relatively dense spatial and temporal coverage, as well as the UMass X-Pol's proximity to the Greensburg storm during its mode I-to-mode II transition, the radar data collected in the Greensburg storm are an attractive candidate for DA via the EnKF technique. The following DA experiments were originally conducted with the intention of illuminating this transition; however, in the course of experimentation, it was found that the transition was partially affected by changes in the cold pool of the Greensburg storm, the extent of which was poorly reproduced in the simulations. This incorrect analysis of cold pool structure may have resulted, in part, from the use of a relatively simplistic microphysical parameterization scheme, inadequate retrieval of cross-beam velocities in the cold pool (French 2006), where only UMass X-Pol data were available for assimilation, or because surface physics (including frictional effects) were not included in the model.

A comprehensive history of the EnKF and its applications is furnished by Evensen (2007). The EnKF was first formulated by Evensen (1994) as a means to reduce the computational cost of assimilating stochastic observational data into dynamic numerical fluid flow models. The following "tutorial" on the EnKF is synthesized from a large number of resources, primarily Evensen (1994, 2003, 2007),

Houtekamer and Mitchell (1998, 2005), Hamill (2000), Kalnay (2003), Snyder and Zhang (2003), Hunt *et al.* (2004), Anderson (2005), Lewis *et al.* (2006), and Tong (2006).

6.1 Basic concepts of data assimilation

NWP is the process whereby estimates of the state of the atmosphere at a future time are computed, usually by integration forward in time of partial differential equations representing physical processes (e.g., fluid flow, thermodynamics). NWP is essentially an initial and/or boundary value problem in discretized partial differential equations. Accurate specification of the initial conditions is necessary in order to achieve accurate and useful forecasts. However, the true state of the atmosphere can never be perfectly known, but only approximated, owing to incomplete observational coverage, instrument error (Kalnay 2003), and the inherently chaotic nature of the atmosphere (Lorenz 1993).

DA is the process whereby observational data are combined, in an "optimal" sense, with a short-range forecast or "background state" (based on previous observations) in order to produce an analysis of the atmospheric state (Kalnay 2003). In this framework, the conditions at a given grid point are a weighted average of nearby observations and a short-range forecast (often based on previously assimilated data). These conditions serve as an initial condition for a subsequent forecast.

Numerous techniques have been developed for assimilation of regularly collected atmospheric observations such as surface thermodynamic and wind measurements, rawinsonde (balloon-borne instrument) measurements, and satellite-measured radiances. As we will see, since radar data are now consistently available in

digital form, radar DA represents an active area of current research. In order of increasing complexity, some DA techniques commonly used in meteorology, all of which are predicated on using least-squares methods to minimize the total (model and observation) error covariance, include:

(1) Optimal interpolation (OI; Eliassen 1954; Gandin 1965), in which the analyzed state is obtained by adding to the background state a weighted (by error covariances) difference between an observation and the background state. A principal assumption of OI is a constant (i.e., not flow-dependent) background error covariance matrix.

(2) 3DVAR, in which the analyzed state is obtained by minimizing a scalar cost functional J relating background and observation states and their respective error covariances. This method is mathematically equivalent to OI (Lorenc 1986), but its implementation does not necessitate error covariance localization often required by OI.

(3) 4DVAR (Talagrand and Courtier 1987), which is a generalization of 3DVAR to observations distributed in time. It requires both forward and backward (adjoint) integration of the model (i.e. a forecast) in order to obtain the initial conditions that best fit the observations within an assimilation interval.

(4) EnKF (Evensen 1994); discussed below.

Excellent overviews of these techniques, the relationships among them, and their comparative advantages are given by Lorenc (1986), Bouttier and Courtier (1999) and Kalnay (2003).

Because of the sheer volume of atmospheric data now available in near real-time and the often relatively short range of forecasts, computational optimization for any DA technique is imperative. Many variations of each of the DA techniques listed above exist; most implementations have been optimized for some specialized application (Kalnay 2003).

6.1.1 The Kalman filter (KF)

The following derivation of the basic Kalman (1960) filter (KF) equations draws heavily from Hamill (2000), Snyder and Zhang (2003), Anderson (2005), and Lewis *et al*. (2006).

Dynamic model: Consider the following linear dynamical system at a given time t_k,:

$$\mathbf{x}_{k+1} = \mathbf{M}_k \mathbf{x}_k + \mathbf{w}_{k+1}, \tag{6.1}$$

where $\mathbf{M}_k$ is a time-varying linear dynamical model, $\mathbf{w}_k \sim N(0, \mathbf{Q}_k)$ is the unbiased model error, and $\mathbf{Q}_k$ is the model error covariance matrix. We assume that the initial state vector $\mathbf{x}_0$ is random with known mean $\mathbf{m}_0$ and known covariance matrix $\mathbf{P}_0$, and that the model error $\mathbf{w}_k$ is not correlated with the initial state vector $\mathbf{x}_0$.

Observations: Consider, at time $t = t_k$, an atmospheric state vector $\mathbf{x}_k$ of length N_x (which may contain fields such as temperature, moisture, or wind speeds at a finite number of locations, e.g., model grid points). As previously mentioned, the *true* state of the system (i.e., true values of temperature, etc. at the grid points) can never be known; at best, we can forecast the probability density function (pdf) $p(\mathbf{x}_k)$.

Suppose we have a prior (or background) forecast of $p(\mathbf{x}_k)$, and a vector of observations $\mathbf{y}^o$ of length N_y.[9] Our objective is to update $p(\mathbf{x}_k)$ using the additional information in $\mathbf{y}^o$, making the new estimate optimal in a least squares sense. Intuitively, the statistical likelihood of the new (posterior or "analysis") estimate $\mathbf{x}_k^a$ (with associated covariance matrix $\mathbf{P}_k^a$) should be greater than that of the prior estimate $p(\mathbf{x}_k)$ or the observations $\mathbf{y}^o$ when either is considered individually (Fig. 41).

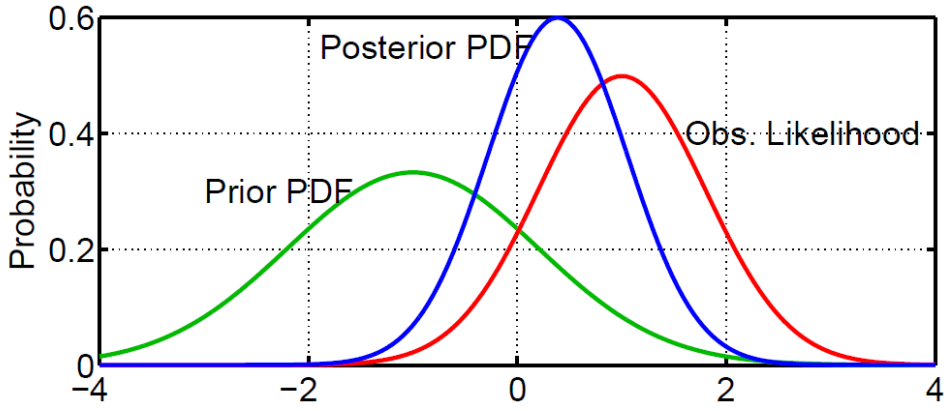


Fig. 41. Conceptual illustration of the improvement in likelihood of $p(x_k^a)$ (blue) when observation(s) (red) are assimilated into the prior $p(x_k)$ (green). From Anderson (2005).

We make the following two assumptions: First, there exists a $N_x \times N_y$ matrix $\mathbf{H}$ such that

$$\mathbf{y}^o = \mathbf{H}\mathbf{x}_k + \mathbf{v}_k, \tag{6.2}$$

that is, $\mathbf{H}$ linearly maps the state vector $\mathbf{x}_k$ to the observations $\mathbf{y}^o$. The error vector $\mathbf{v}_k$ (also of length N_y) contains the instrument errors associated with each of the observations in $\mathbf{y}^o$. Second, both $p(\mathbf{x}_k)$ and $\mathbf{v}_k$ are Gaussian; i.e., $p(\mathbf{x}_k) \sim N(\bar{\mathbf{x}}_k^f, \mathbf{P}_k^f)$, where

$$\mathbf{x}_k^f = \mathbf{M}_{k-1}\mathbf{x}_{k-1}^a, \tag{6.3}$$

[9] It is assumed that all these observations are valid at time t, but this may not always be true. Often the observations are assimilated within a certain "time window" (e.g., Dowell and Wicker 2008). See Hunt et al. (2004) for a four-dimensional formulation of the EnKF that accounts for observations collected at non-assimilation times.

$$\mathbf{P}_{\mathrm{k}}^{\mathrm{f}} = \mathbf{M}_{\mathbf{k-1}}\mathbf{P}_{\mathbf{k-1}}^{\mathbf{a}}\mathbf{M}_{\mathbf{k-1}}^{\mathrm{T}} + \mathbf{Q}_{\mathbf{k}}, \tag{6.4}$$

and $\mathbf{v}_{\mathrm{k}} \sim \mathrm{N}(0, \mathbf{R})$. (Additionally, it is assumed that $\mathbf{v}_{\mathrm{k}}$ is independent of $\mathbf{x}_{\mathrm{k}}$., so that their cross-correlation $\mathbf{v}_{\mathrm{k}}\mathbf{x}_{\mathrm{j}}$ goes to zero in the computation of $\mathbf{P}_{\mathrm{k}}^{\mathrm{f}}$; see Lewis et al. (2006).) Under these assumptions, $p(\mathbf{x}_{\mathrm{k}}|\mathbf{y}^{\mathrm{o}})$ is also Gaussian.

Given that $\mathbf{x}_{\mathrm{k}}$ evolves according to (6.1), and a set of observations $\mathbf{y}^{\mathrm{o}}$ in the form (6.2), the minimum variance (Cohn 1997) estimator $\mathbf{x}_{\mathrm{k}}^{\mathrm{a}}$ of $\mathbf{x}_{\mathrm{k}}$ that minimizes the mean squared error

$$E[(\mathbf{x}_{\mathrm{k}} - \mathbf{x}_{\mathrm{k}}^{\mathrm{a}})^{\mathrm{T}}(\mathbf{x}_{\mathrm{k}} - \mathbf{x}_{\mathrm{k}}^{\mathrm{a}})] = \mathrm{tr}\{E[(\mathbf{x}_{\mathrm{k}} - \mathbf{x}_{\mathrm{k}}^{\mathrm{a}})(\mathbf{x}_{\mathrm{k}} - \mathbf{x}_{\mathrm{k}}^{\mathrm{a}})^{\mathrm{T}}]\} \tag{6.5}$$

is $\mathbf{x}_{\mathrm{k}}^{\mathrm{a}} = E\,[p(\mathbf{x}_{\mathrm{k}}|\mathbf{y}^{\mathrm{o}})]$ and is given, via Bayes' Rule,

$$p(\mathbf{x}_{\mathrm{k}}|\mathbf{y}^{\mathrm{o}}) = \frac{p(\mathbf{y}^{\mathrm{o}}|\mathbf{x}_{\mathrm{k}})p(\mathbf{x}_{\mathrm{k}})}{p(\mathbf{y}^{\mathrm{o}})}, \tag{6.6}$$

and after extensive variational calculus (Lewis *et al.* 2006), by the KF analysis equations

$$\mathbf{x}_{\mathrm{k}}^{\mathrm{a}} = \mathbf{x}_{\mathrm{k}}^{\mathrm{f}} + \mathbf{K}\left[\mathbf{y}^{\mathrm{o}} - \mathbf{H}\mathbf{x}_{\mathrm{k}}^{\mathrm{f}}\right] \tag{6.7}$$

and

$$\mathbf{P}_{\mathrm{k}}^{\mathrm{a}} = [\mathbf{I} - \mathbf{K}\mathbf{H}]\mathbf{P}_{\mathrm{k}}^{\mathrm{f}}, \tag{6.8}$$

where

$$\mathbf{K} = \mathbf{P}_{\mathrm{k}}^{\mathrm{f}}\mathbf{H}^{\mathbf{T}}\left[\mathbf{H}\mathbf{P}_{\mathrm{k}}^{\mathrm{f}}\mathbf{H}^{\mathrm{T}} + \mathbf{R}\right]^{-1} \tag{6.9}$$

is the Kalman gain. (See Lewis *et al*. (2006) for the exhaustive derivation of these equations.) In words, Eqn. (6.7) says that the analyzed (posterior) value is the forecast (prior) value updated by the "innovation" ($\mathbf{y}^{\mathrm{o}} - \mathbf{H}\mathbf{x}_{\mathrm{k}}^{\mathrm{f}}$) of the observations, weighted by the Kalman gain. Note that the formulation of Eqn. (6.8) indicates that the forecast error covariance should be reduced as a result of the assimilation of the observations. The Kalman gain is the covariance between observed and state variables ($\mathbf{P}_{\mathrm{k}}^{\mathrm{f}}\mathbf{H}^{\mathbf{T}}$) divided by total system error covariance (the sum of the forecast error covariance and

observational error covariance, the former of which is transformed into observation space).

6.1.2 The extended Kalman filter (EKF)

Of course, the model with which we are working may not be linear. In this case, a desirable approach is to use an extended Kalman filter (EKF) (Talagrand 1997; Lewis *et al.* 2006), in which the linear mappings $\mathbf{M_k x_k^a}$ in (6.3) and $\mathbf{H x_k^f}$ in (6.7) are replaced by the full nonlinear model $M(\mathbf{x_k^a})$ and the forward observation operator $H(\mathbf{x_k^f})$, respectively, while $\mathbf{M} = \frac{\partial M}{\partial x}$ and $\mathbf{H} = \frac{\partial H}{\partial x}$ are now Jacobians (tangent linear trajectories) elsewhere. The primary advantage of the EKF is that the forecast covariance matrix $\mathbf{P_k^f}$ explicitly accounts for flow-dependent error, whereas simpler schemes (such as OI; see Kalnay (2003)) usually represent the covariances as a constant matrix (which may not be a valid assumption in a rapidly-evolving system such as a convective thunderstorm).

However, as has been exhaustively documented in the literature, the forecast covariance matrix $\mathbf{P_k^f}$ is also the Achilles' heel of the KF and EKF. Computationally speaking, the matrix $\mathbf{P_k^f}$, is an $N_x \times N_x$ matrix and its calculation requires matrix multiplication of two other $N_x \times N_x$ matrices in Eqn. (6.4). It is often the case that $N_x >> N_y$, i.e. that the number of degrees of freedom of the model (which can be ~10^6-10^8 for some models) far exceeds the number of observations assimilated (~10^2 for rawinsonde and ~10^3-10^5 for radar or satellite data). Calculating $\mathbf{P_k^f}$ can be both computationally extremely demanding and require a large amount of storage (Kalnay 2003; Lewis *et al.* 2006).

6.1.3 The ensemble Kalman filter (EnKF)

To ameliorate the computational issues associated with the EKF, Evensen (1994) suggested the novel approach of estimating $\mathbf{P}_k^f$ from an ensemble of forecasts, thereby inventing the EnKF. (Here and after, an "ensemble" refers to multiple forecasts completed in a parallel or quasi-parallel fashion.) The strategy is as follows: By randomly perturbing the observation(s) $\mathbf{y}^o$ K times using its known error statistics (i.e., Monte Carlo method), then evolving an ensemble of K separate forecasts based on assimilation of each perturbed observation, we presumably obtain a "random sample" of $p(\mathbf{x}_k)$, rather than having to obtain $p(\mathbf{x}_k)$ itself (Hamill 2000). Recalling our assumption that $p(\mathbf{x}_k)$ is Gaussian, it can then be used to estimate the true state $\mathbf{x}_k$ and the uncertainty of that estimate (i.e., error covariance statistics; see Fig. 42). This process can be repeated, at user-specified intervals (assimilation cycles), throughout the forecast period.

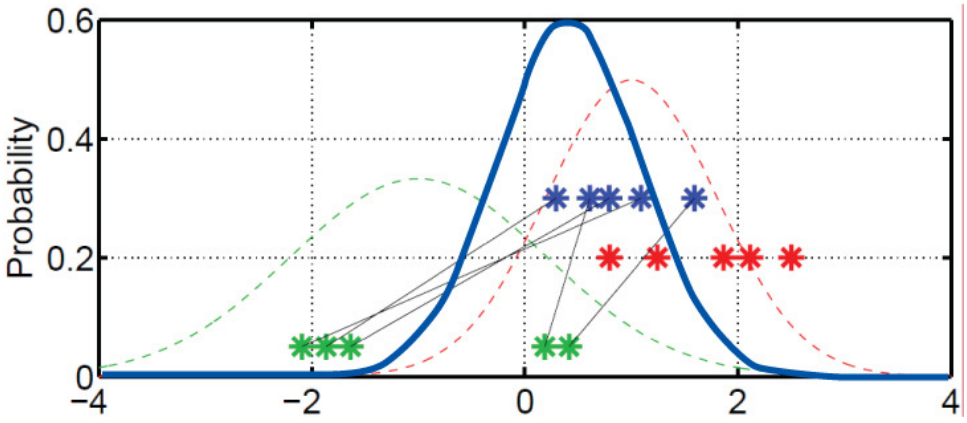


Fig. 42. As in Fig. 41, but conceptually illustrating one algorithmic approach to the EnKF. Each asterisk (*) represents an ensemble member element. Each perturbed observation (*) is associated with a sample randomly drawn from the prior distribution $p(x_k)$ (*), and each pair is then used to generate a new (posterior) value x_n^f (*). If we can assume the posterior distribution to be Gaussian (blue curve), then we can infer basic information about the true atmospheric state x^t_k. From Anderson (2005).

The basic EnKF equations are therefore

$$\hat{\mathbf{x}}_{\mathrm{k}}^{\mathrm{f}} = \frac{1}{K}\sum_{\mathrm{n}=1}^{K}\mathbf{x}_{\mathrm{n}}^{\mathrm{f}}, \tag{6.10}$$

$$\widehat{\mathbf{P}}_{\mathbf{k}}^{\mathbf{f}}\mathbf{H}^{\mathrm{T}} = \frac{1}{K-1}\sum_{\mathrm{n}=1}^{K}\left(\mathbf{x}_{\mathrm{n}}^{\mathrm{f}} - \bar{\mathbf{x}}^{\mathrm{f}}\right)\left(\mathbf{H}\mathbf{x}_{\mathrm{n}}^{\mathrm{f}} - \mathbf{H}\bar{\mathbf{x}}^{\mathrm{f}}\right)^{T} \tag{6.11}$$

and

$$\mathbf{H}\widehat{\mathbf{P}}_{\mathbf{k}}^{\mathbf{f}}\mathbf{H}^{\mathrm{T}} = \frac{1}{K-1}\sum_{\mathrm{n}=1}^{K}\left(\mathbf{H}\mathbf{x}_{\mathrm{n}}^{\mathrm{f}} - \mathbf{H}\bar{\mathbf{x}}^{\mathrm{f}}\right)\left(\mathbf{H}\mathbf{x}_{\mathrm{n}}^{\mathrm{f}} - \mathbf{H}\bar{\mathbf{x}}^{\mathrm{f}}\right)^{T} \tag{6.12}$$

where the "hat" (^) represents an estimate. Note first that the EnKF technique provides an estimate $\widehat{\mathbf{P}}_{\mathbf{k}}^{\mathbf{f}}$ of the computationally demanding $N_x \times N_x$ forecast error covariance term $\mathbf{P}_{\mathrm{k}}^{\mathrm{f}}$. The terms used to calculate the RHS of (6.11) are all of size $N_x \times N_y$ or smaller.

Secondly, note that the term $\widehat{\mathbf{P}}_{\mathbf{k}}^{\mathbf{f}}\mathbf{H}^{\mathrm{T}}$ in (6.11) represents the covariance between state and observed variables. In other words: *The EnKF furnishes information about the relationships between observed and unobserved variables*. This crucial concept is illustrated in Fig. 43 and is worth repeating: *observations can potentially be used to update unobserved state variables*. For example, one could conceive of updating estimates of vertical velocity by assimilating radial velocity, or updating estimates of temperature by assimilating radar reflectivity.

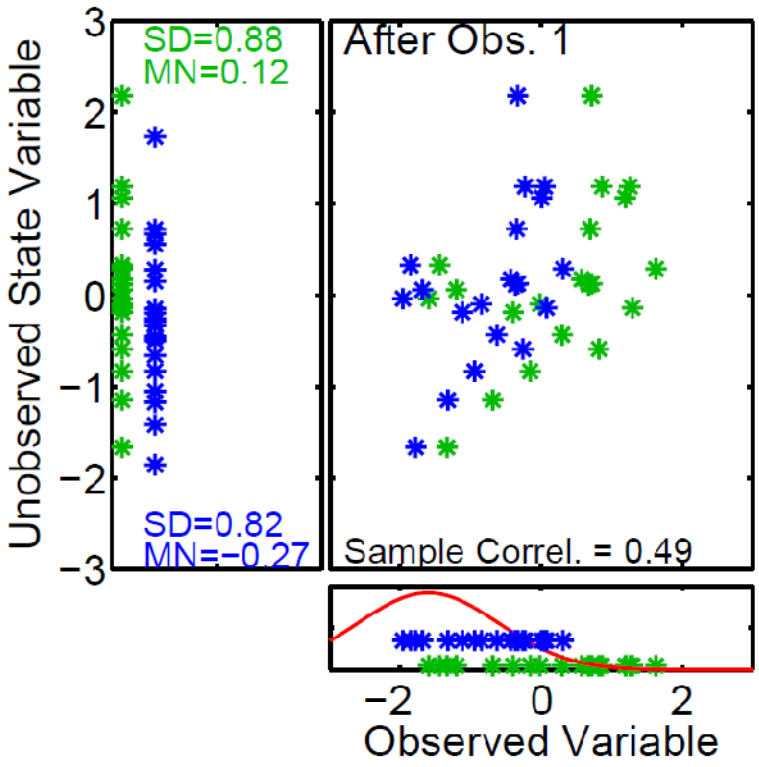


Fig. 43. Conceptual illustration of how assimilation of an observation (red) via EnKF can be used to update prior estimates of unobserved variables. From Anderson (2005), which provides a very clear series of illustrations of how these updates are performed.

A few caveats are in order. First, we assume knowledge of at best a *linear* relationship (least squares fit) between the prior distributions of observed and unobserved variables. If the true relationships between observed and unobserved variables are highly nonlinear, the EnKF will not be as useful (Anderson 2005). Second, many convective storm processes, such as cloud microphysics, may be highly nonlinear and therefore violate the assumption of a Gaussian $p(\mathbf{x}_k)$ (Snyder and Zhang 2003). Nonetheless, EnKF has shown promise as a tool for assimilating data on convective scales, e.g. (Snyder and Zhang 2003; Dowell *et al.* 2004; Tong 2006; Aksoy *et al.* 2009).

The EnKF as formulated in Eqns (6.10 - 6.12) is a stochastic algorithm. (In the present sense, "stochastic" refers to assumed probabilistic error characteristics of

the observing instruments; i.e., measurements will always contain error, but it is assumed that the error characteristics of the instruments are reasonably well-known.) A deterministic formulation of the EnKF, ensemble square root Kalman filter (EnSRF) (Whitaker and Hamill 2002; Tippett *et al.* 2003) exists, and has been used in previous radar DA experiments (e.g., Tong and Xue 2005; Xue *et al.* 2006; Dowell and Wicker 2009). However, the DA tools that I used employed a different but mathematically equivalent formulation of EnKF (discussed in the next subsection). Therefore, the EnSRF will not be further discussed, aside from a brief mention in the next subsection. The interested reader is referred to the dissertation work of M. Tong (2006).

6.1.4 The ensemble adjustment Kalman filter (EAKF)

The EnKF algorithm depicted in Fig. 42 destroys most of the information about the (possibly non-Gaussian) structure of the prior sample of $p(\mathbf{x}_k)$. Anderson (2001) formulated the ensemble adjustment Kalman filter (EAKF) as a potential remedy. In this algorithm, the posterior distribution is computed using the normal EnKF algorithm, and its variance and mean calculated according to

$$\mathbf{P_k^u} = \left[\left(\mathbf{P}_k^f\right)^{-1} + \mathbf{H^T R^{-1} H}\right]^{-1} \tag{6.13}$$

and

$$\bar{\mathbf{x}}_\mathbf{k}^\mathbf{u} = \mathbf{P_k^u}\left[\left(\mathbf{P}_k^f\right)^{-1}\hat{\mathbf{x}}_k^f + \mathbf{H^T R^{-1} y^o}\right]^{-1}, \tag{6.14}$$

respectively, where the superscript *u* indicates an updated (posterior) value. The prior distribution's mean is then shifted and its variance linearly contracted or expanded to match that of the posterior (Fig. 44). This "adjusted" distribution is then taken as the

new posterior distribution, thereby retaining characteristics (e.g., multimodality) of the prior distribution that would have otherwise been erased by the random association in the original formulation of the EnKF. (It should be noted that if the "random sample" of $p(\mathbf{x}_k)$ is not actually representative of $p(\mathbf{x}_k)$, the EAKF will preserve the nonrepresentativeness. However, this effect can be controlled to some extent by increasing the ensemble size.) The EAKF, which is mathematically equivalent to the EnSRF (Anderson 2001), is employed in this study.

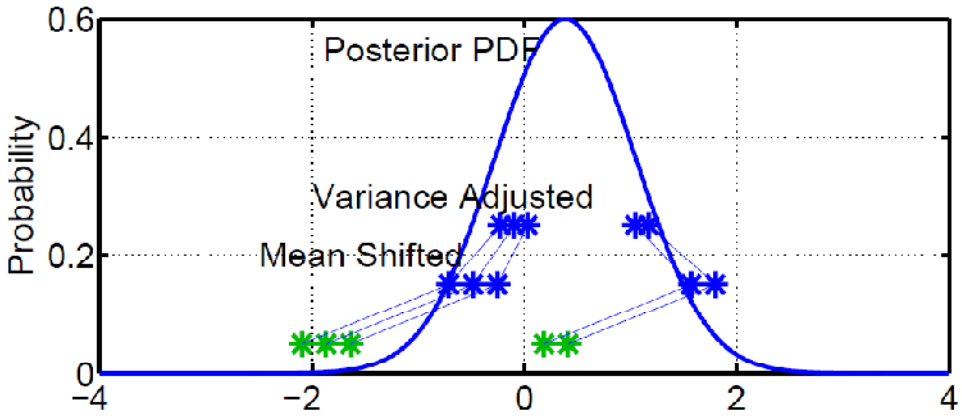


Fig. 44. As in Fig. 41, but illustrating the EAKF concept. In this example, the EAKF preserves the bimodality of the prior distribution. From Anderson (2005).

6.1.5 Comparisons between EnKF and other DA schemes

As previously noted, the EnKF was formulated as a lower-computational cost alternative to the EKF. The terms used to calculate the RHS of (6.11) are all of size $N_x \times N_y$ or smaller. While this computational cost is not trivial, and may be on the order of 10-100 times more demanding than OI or 3DVAR (Kalnay 2003), it is still substantially reduced from that of the EKF. Hybrid EnKF-3DVAR systems have recently been developed by Gao *et al.* (2010).

One additional, substantial advantage of the EnKF is that it does not require the formulation of a tangent linear model $\mathbf{M}_k$ and corresponding adjoint model $\mathbf{M}_k^{-1}$

(Errico 1997), as required by 4DVAR (Kalnay 2003). Caya *et al.* (2005) directly compared 4DVAR and EnKF supercell thunderstorm radar DA experiments with 10-minute assimilation cycles; it was found that 4DVAR furnished better results in early assimilation cycles (0 – 30 min) but that the results from using EnKF were better in later assimilation cycles (30 – 90 min). They speculated that the EnKF better handled nonlinear dynamics of the supercell thunderstorm over the longer forecast period. In light of these results, I was inclined to use EnKF for radar DA experiments on the Greensburg storm, because the anticipated simulation period was on the order of two hours.

6.2 Computing tools

6.2.1 Weather Research and Forecasting (WRF) model

The WRF model (http://www.wrf-model.org/) is an open-source NWP system developed at NCAR for use both as an operational forecasting model and as a community research tool (Skamarock *et al.* 2008). The Advanced Research WRF (WRF-ARW) dynamical core utilizes compressible, non-hydrostatic Euler equations, and is conservative for scalar variables. The model has six main prognostic variables: velocity components u, v, and w, perturbation pressure p', perturbation geopotential height Φ', and perturbation pressure of surface dry air $p'_{sfc_dry_air}$. Scalar variables (e.g., water vapor mixing ratio q, potential temperature θ) are also computed, depending on the model physics packages used; these scalar variables are conserved by the model. The horizontal grid is a staggered Arakawa C-grid (Fig. 45); in the vertical, the model utilizes terrain-following hydrostatic pressure surfaces (η), relaxing towards the top of the model, which is a constant-pressure surface (Fig. 46).

The model employs a 3rd order Runge-Kutta advection scheme with a secondary, shorter time step for acoustic modes (Wicker and Skamarock 2002). Version 3.0.1.1 of the WRF (WRFV3), which became available in late 2008, is used in this study.

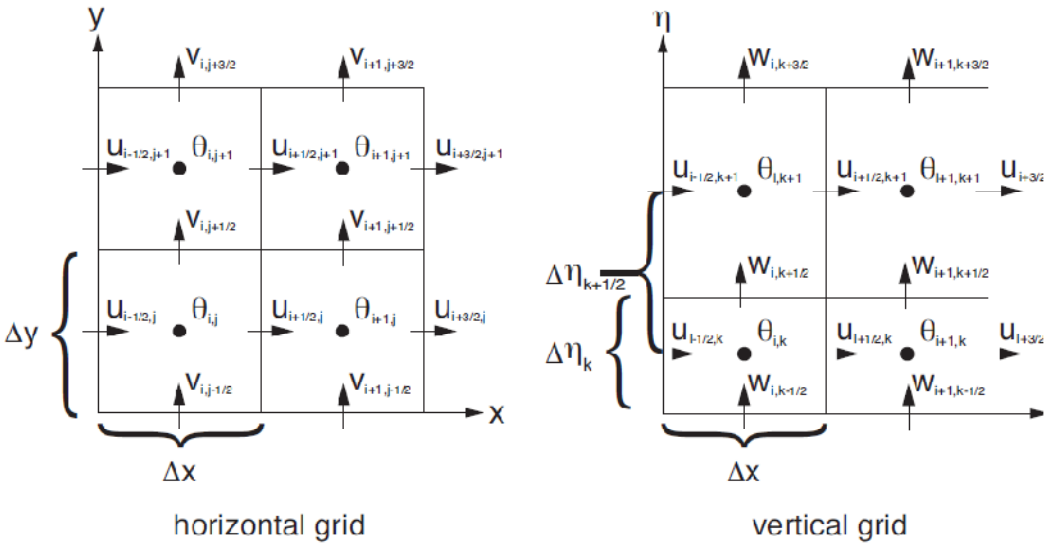


Fig. 45. Horizontal and vertical grids of the WRF-ARW. From Skamarock *et al.* (2008).

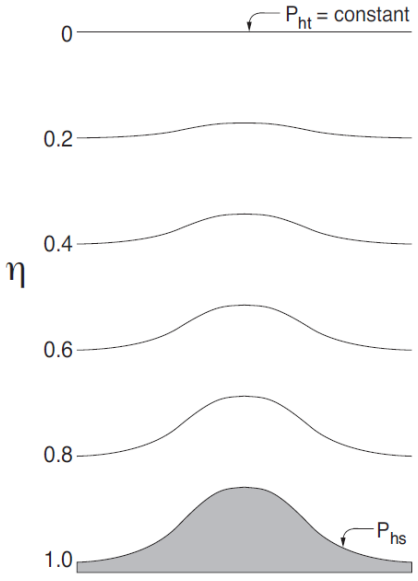


Fig. 46. Vertical coordinate system of the WRF-ARW. From Skamarock et al. (2008).

6.2.2 Data Assimilation Research Testbed (DART)

The Data Assimilation Research Testbed (DART[10], http://www.image.ucar.edu/DAReS/DART/) system, is a versatile computational framework for ensemble DA that is designed for interface with the WRF model (Anderson and Collins 2007; Anderson *et al.* 2009). Like WRF, DART is also open-source. It includes several different "flavors" of the EnKF, including EAKF (which has been favored in some previous radar DA studies; e.g. Aksoy *et al.* [2009]), additional algorithms for covariance localization, and modules (containing observation operators) for most common types of meteorological observations.

DART also includes a radar DA module. Radar observations are treated as point observations with a specified radius of influence (which can be specified differently in the horizontal and vertical). Objective analysis is used to reduce the number of radar gate observations (~10^5 for a single radar sweep) to a manageable quantity prior to assimilation.

6.2.2.1 Observation operator for reflectivity

The following discussion of the DART observation operator for radar reflectivity (factor) is drawn heavily from the appendix Dowell *et al.* (2010), who, in turn, draw on derivations of Smith *et al.* (1975), Smith (1984), Gilmore *et al.* (2004), and Tong and Xue (2005).

When the Lin *et al.* (1983) microphysical parameterization scheme is selected, the WRF model generates, for each of six hydrometeor species *i* (water vapor, cloud

[10] Because it was originally designed for interface with the WRF model, the abbreviation WRF/DART is sometimes used.

droplets, cloud ice, rain, snow, and hail / graupel), mixing ratio fields (q_i, in kg kg^{-1}) at each scalar grid point (Skamarock *et al.* 2008). Based on these model fields, the equivalent radar reflectivity factor (Z_e) that would be measured by a radar operating at S-band (10 cm wavelength) can be calculated. For the observed distributions of hydrometeors within a severe thunderstorm, Rayleigh scattering predominates at S-band. For the purposes of calculating Z_e, the contributions from water vapor, cloud droplets, and cloud ice are assumed to be negligible. The remaining categories (rain, snow, and hail / graupel) each additively contribute to Z_e:

$$Z_e = Z_r + Z_s + Z_{gh} \tag{6.15}$$

where Z_r, Z_s, and Z_{gh} are the reflectivity factors associated with rain, snow, and graupel / hail, respectively.

Assuming Rayleigh scattering, the reflectivity factor for spherical raindrops is

$$Z_r = \int_0^\infty N_r(D) D^6 dD, \tag{6.16}$$

where D is the drop diameter. In the Lin *et al.* (1983) microphysical parameterization scheme, it is assumed that raindrops exhibit an inverse-exponential size distribution N_r:

$$N_r(D) = N_{0r} exp\left[-D\left(\frac{\pi \rho_r N_{0r}}{\rho q_r}\right)^{0.25}\right], \tag{6.17}$$

where N_{0r} is the intercept parameter for rain, ρ_r is the density of liquid water (1000 kg m^{-3}), and ρ is the density of air.

Plugging (6.17) into (6.16) and solving the integral yields

$$Z_r = 7.2 \times 10^{20} N_{0r} \left(\frac{\rho q_r}{\pi \rho_r N_{0r}}\right)^{1.75}. \tag{6.18}$$

For the experiments described herein, in which N_{0r} was 1.0 x 10^5 m^{-4} (L. Wicker, personal communication), (6.18) reduces to

$$Z_r = 9.7 \times 10^{10}(\rho q_r)^{1.75}. \tag{6.19}$$

It is assumed that snowflakes also exhibit an inverse exponential size distribution N_s, analogous to that for N_r (6.17).

$$N_s(D) = N_{0s} exp\left[-D\left(\frac{\pi \rho_s N_{0s}}{\rho q_s}\right)^{0.25}\right], \tag{6.20}$$

Snowflakes are treated as though they have dry (wet) surfaces if the air temperature at that scalar grid point is below (above) freezing, and it is assumed that wet snowflakes scatter like raindrops with the same water mass. Therefore, Z_s is calculated differently depending on whether the air temperature is above or below freezing:

$$Z_s = \begin{cases} \left(\frac{|K_i|^2}{|K_w|^2}\right)\left(\frac{{\rho_s}^2}{{\rho_r}^2}\right) 7.2 \times 10^{20} N_{0s} \left(\frac{\rho q_s}{\pi \rho_s N_{0s}}\right)^{1.75}, & T \leq 0\ ℃ \\ 7.2 \times 10^{20} N_{0s} \left(\frac{\rho q_s}{\pi \rho_s N_{0s}}\right)^{1.75}, & T > 0\ ℃ \end{cases}. \tag{6.21}$$

The factor $\left(\frac{|K_i|^2}{|K_w|^2}\right) = 0.224$ in the formula (6.21a) for dry snowflakes accounts for the different scattering properties of frozen (as opposed to liquid) water; the quantities K_i and K_w are the dielectric constants for ice and water, respectively (Smith 1984; Doviak and Zrnić 1993).

For my experiments, N_{0s} was prescribed as 3.0 x 10^6 m^{-4} (Gunn and Marshall 1958) and ρ_s as 100 kg m^{-3} (Gilmore *et al.* 2004). In this case,

$$Z_s = \begin{cases} 9.6 \times 10^8 (\rho q_s)^{1.75}, & T \leq 0\ ℃ \\ 4.3 \times 10^{11} (\rho q_s)^{1.75}, & T > 0\ ℃ \end{cases}. \tag{6.22}$$

Hail / graupel, on the other hand, is assumed to have a dry surface always. Dowell *et al.* (2010) found that calculated values of Z_{gh} were closer to observations in

simulations of the 8 May 2003 Moore, Oklahoma tornadic supercell when all hail / graupel was treated as dry than when a mixture of wet and dry hail, partitioned by air temperatures above or below freezing (as in the case of snow), was assumed. Tong and Xue (2005) assumed wet hail (following Smith *et al.* 1975) in their EnKF experiments on the 20 May 1977 Del City, Oklahoma supercell. However, Dowell *et al.* (2010) question the validity of that assumption, since freshly-fallen hail from supercells has been observed to have dry surfaces at temperatures well above freezing. I follow the example of Dowell *et al.* (2010) and assume that only dry hail is present. The resulting equivalent reflectivity factor for hail is

$$Z_{gh} = \left(\frac{|K_i|^2}{|K_w|^2}\right)\left(\frac{{\rho_h}^2}{{\rho_r}^2}\right) 7.2 \times 10^{20} N_{0h} \left(\frac{\rho q_h}{\pi \rho_h N_{0h}}\right)^{1.75}. \quad (6.23)$$

In my experiments, I assumed that N_{0h} = 4.0 x 10^5, a "compromise" between the values used by both Dowell and Wicker (2009) and Dowell *et al.* (2010) (4.0 x 10^4 kg m^{-3}), and Aksoy *et al.* (2009) (4.0 x 10^6 kg m^{-3}). The density of graupel / hail was assumed to be ρ_h = 800 kg m^{-3}, the lower bound on the range of values for ρ_h suggested by Lin et al. (1983). Gilmore *et al.* (2004), Dowell and Wicker (2009), and Dowell *et al.* (2010) use 900 kg m^{-3}, but we believe that this higher value of density for graupel / hail particles may cause them to precipitate out of the storm too quickly, resulting in smaller hailstones than those observed at Greensburg (4 cm diameter). Aksoy *et al.* (2009) use the value ρ_h = 400 kg m^{-3}, but do not explain their choice of this relatively low density for graupel / hail. The value of ρ_h = 800 kg m^{-3} was felt to more accurately reflect the graupel / hail mixture believed present in the Greensburg storm. Therefore, the resulting equivalent reflectivity factor due to graupel / hail is:

$$Z_{gh} = 8.2 \times 10^{10} (\rho q_h)^{1.75}. \quad (6.24)$$

After summing together the components Z_r, Z_s, and Z_{gh}, Z_e (which is in linear units) is converted into logarithmic units (dBZ_e) via

$$Z_{dBZ_e} = 10 \log_{10} Z_e. \tag{6.25}$$

Finally, in the special case where q_r, q_s, and q_h are all zero (and $Z_e = 0$), Z_{dBZe} is set to 0 dBZ_e, because it would be undefined otherwise (Tong and Xue 2005; Dowell *et al.* 2010). Z_{dBZe} is also set to 0 dBZ_e in those locations where Z_{dBZe} evaluates to a quantity less than 0 dBZ_e. Thus, a lower reflectivity threshold of 0 dBZ_e is effectively applied throughout the domain:

$$Z_{dBZe} = \begin{cases} \min(0\ \mathrm{dBZ}_e, Z_{dBZ_e}), & Z_e > 0 \\ 0\ \mathrm{dBZ}_e, & \text{otherwise} \end{cases}. \tag{6.26}$$

6.2.2.2 Observation operator for velocity

The observation operator for Doppler radial velocity is

$$v_r = (\sin\alpha \cos\theta_e)u + (\cos\alpha \cos\theta_e)v + (\sin\theta_e)(w - w_t) \tag{6.27}$$

where α and θ_e are the azimuth angle of the radar beam, respectively, and w_t is the fall speed of precipitation particles within the grid volume. The geometry of this equation is illustrated in Fig. 47. Given the radar location and a radial velocity observation, DART then computes the radial velocity that would be measured by the radar given the model velocity field (prior distribution) at the same time, and uses these values to update the model via the EAKF algorithm.

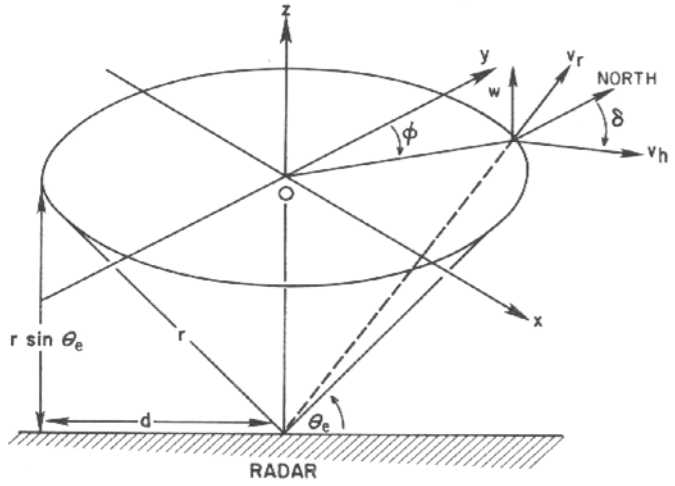


Fig. 47. Geometry of a radar sweep at elevation angle θ_e collected by a ground-based radar at the origin. It can be seen that the radar beam sweeps out a conical surface. From Doviak and Zrnić (1993).

6.2.3 Observation-space diagnostics

A set of observation-space diagnostics for evaluating radar DA experiments are defined by Dowell and Wicker (2009). These diagnostics quantify the change in the model fields as a result of assimilation of radar observations and verify that sufficient spread (comparable to observation errors) is being maintained in the ensemble throughout the assimilation cycles.

For a vector of observations $\mathbf{y}^o$ valid at time t_k, the "innovation" d (or difference between the observation and the ensemble mean model forecast mapped to observation space) is defined as

$$d = \mathbf{y}^o - \overline{H(\mathbf{x}_k^f)}. \tag{6.28}$$

This quantity is averaged over the model volume to furnish the quantity ‹d›. (Angled brackets, ‹›, indicate volume-averaging.) The volume-mean innovation ‹d›, a measure of the overall impact of the assimilation of the observation vector $\mathbf{y}^o$ on the

model state vector $\mathbf{x}_k^f$, can then be used to calculate the root mean square of the innovations (RMSI),

$$\text{RMSI} = \sqrt{\langle [d - \langle d \rangle]^2 \rangle}. \tag{6.29}$$

The "total spread" (a measure of the ensemble spread that includes observation error) is defined as

$$\text{total spread} = \sqrt{\sigma_{vr}^2 + \langle \frac{1}{K-1} \sum_{n=1}^{K} \left[H(\mathbf{x}_\text{n}^\text{f}) - \overline{H(\mathbf{x}^f)} \right]^2 \rangle}. \tag{6.30}$$

This quantity represents rms of the volume-averaged ensemble spread (mapped into observation space) plus observation error σ_{vr}. (We assume a fixed value of σ_{vr} when we populate the initial ensemble.)

Dowell and Wicker (2009) further define a quantity called the "consistency ratio" (CR), which is given by

$$\text{CR} = \frac{(\text{total spread})^2}{\text{RMSI}^2}. \tag{6.31}$$

which should remain close to 1.0 throughout the assimilation cycles (i.e., the ensemble statistics should be similar in magnitude to the observation errors). A value of CR < 1 (> 1) indicates too little (much) model spread; either σ_{vr} may be too small (large) and/or additive noise should be increased (decreased).

6.3 Experiment setup

6.3.1 Introduction and context

The increased availability of current radar data, as well as advances in computing and data transfer, have made it feasible to assimilate radar data into NWP models for the purposes of studying past weather events, or forecasting future ones.

Ongoing research is aimed toward generation of short-term (~1-3 hr) forecasts of convective-scale weather augmented by assimilation of near-real-time radar observations such as those from the WSR-88D (Stensrud *et al.* 2010; Stensrud and Gao 2010; Dawson *et al.* 2011) and the Collaborative Adaptive Sensing of the Atmosphere (CASA) radar testbed (Brotzge *et al.* 2004; Godfrey *et al.* 2005; Schenkman *et al.* 2011; Snook *et al.* 2011).

Currently, data collected by mobile research radars, which are voluminous (in terms of disk storage) and usually collected under adverse conditions in rural areas with limited internet access, are not consistently available in real time.[11] However, as internet connectivity continues to expand and data transfer rates improve, one can forsee these data being made available to forecasters and researchers as convective events unfold. Eventually, it may even be feasible to assimilate mobile radar data into NWP models as part of the operational forecasting process, perhaps within the "Warn-on-Forecast" paradigm (Stensrud *et al.* 2010) currently under development for the NWS.

In the remainder of this chapter, I describe experiments in which I use EnKF to assimilate the UMass X-Pol data collected in the Greensburg storm into an NWP model alongside data from KDDC. While data from mobile Doppler radars has been assimilated into NWP models in previous studies (e.g., French 2006; Marquis *et al.* 2008), these experiments constitute the first instance (to the best of my knowledge) in which data from a mobile Doppler radar and WSR-88D data were assimilated

[11] A stripped-down version of the data from the Shared Mobile Atmospheric Research and Teaching radars (SMART-Rs), processed during deployment to occupy as little bandwidth as possible on the cellular telephone network, was available in near real-time to VORTEX2 project participants during 2009 and 2010.

together. In contrast to some previous studies, *only* radar data are assimilated in the present experiments, not only to limit the complications introduced by the addition of other data sources, but also because so few supplemental data were available.

While in the process of doing the experiments described in this dissertation, I also I collaborated with D. Dawson, L. Wicker, and E. Mansell on a study (Dawson *et al.* 2011) exploring the impact of modifying the initial 0 – 3.5 km AGL wind profile on probabilistic *forecasts* of the Greensburg storm and its associated mesocyclones after assimilation of KDDC data. The primary differences between that study and the experiments covered in this chapter are (1) Dawson *et al.* (2011) used the NSSL Collaborative Model for Multiscale Atmospheric Simulation; I used WRFV3), (2) Dawson *et al.* (2011) assimilated only KDDC data, while I (in some experiments) also assimilated UMass X-Pol velocity data, and (3) Dawson *et al.* (2011)'s study focused on *predictability* (after analysis) of the Greesnburg storm and tornadoes. I focused exclusively on producing *analyses* of the storm, rather than forecasts.

Bluestein (2009) speculated that the intensification of the LLJ (which was recorded by multiple observing systems) may have played a role in the mode I-to-II transition of the Greensburg storm via an increase the magnitude of the low-level vertical wind shear. It was desirable to test this hypothesis in a simulated framework, assimilating Doppler radar data into a likely thermodynamic environment in order to establish the gross features of the Greensburg storm, while allowing the model to produce smaller-scale vortices.

Initialization of the model with a likely thermodynamic and kinematic environment, which was already rapidly changing during the simulation period (0100

– 0300 UTC), proved tricky. Unfortunately, few observations exist of the low-level winds in the inflow region of the Greensburg storm, which moved over a relatively observation-sparse area southeast of Dodge City during most of its early life cycle. While winds were southerly at the UMass X-Pol deployment site from the time that the forward flank passed over (about 0140 UTC) to the end of data collection at 0236 UTC (an observation that became significant in light of the simulation results), UMass X-Pol did not carry equipment to collect *in situ* wind measurements, and in any case the peak LLJ winds would have been located at a height of around 800 m AGL (Fig. 12). (Recall that the closest WSR-88D observations were made from a range of 60 - 75 km by KDDC, sampling the Greensburg storm at altitudes above ~ 600 m AGL.)

My approach was to generate storm-scale analyses of the Greensburg storm in an initially horizontally homogeneous environment, and allow the simulated storm to evolve within the model while periodically assimilating radar data. Since there are no comparable data available for independent verification, the crucial, underlying assumption in these experiments is the following: *I expect the model innovations to have smaller magnitudes when the model environment more closely represents the actual storm inflow environment*.

6.3.2 Experiment nomenclature

Two pairs of EnKF analysis experiments were performed (i.e., four experiments in total). In the first pair of experiments, two slightly different data sets were assimilated. In the first, KDDC reflectivity and Doppler velocity (denoted "kddc_only") were assimilated, while in the second, supplemental UMass X-Pol

Doppler velocity data were also assimilated ("kddc+umass").[12] The value added to the simulations by the additional assimilation of UMass X-Pol Doppler velocity data could therefore be assessed by examining the observation-space error statistics.

In the second pair of experiments, the initial velocity profile was changed over the 0 – 3 km AGL layer using VAD wind profiles retrieved from KDDC data collected at 0100 and 0230 UTC (Fig. 12). The first experiment, an initial velocity profile thought to be representative of the 0 – 3 km AGL inflow environment at 0230 UTC, containing a strengthening LLJ, was used (denoted "vad0230"), while in the second, an initial velocity profile thought to be representative of the environment prior (e.g., at 0100 UTC) to the onset of the LLJ (denoted "vad0100") was used. The thermodynamic profiles used in all four experiments were identical.

The nomenclature for these two pairs of experiments is documented in Table 4.

Table 4. EnKF experiment nomenclature used in this study.

Experiment name	"Stronger LLJ"	"Weaker LLJ"
KDDC $\boldsymbol{Z}$ and $\boldsymbol{V}_r$ data assimilated	kddc_only_vad0230	kddc_only_vad0100
KDDC $\boldsymbol{Z}$ and $\boldsymbol{V}_r$ and UMass $\boldsymbol{V}_r$ data assimilated	kddc+umass_vad0230	kddc+umass_vad0100

[12] UMass X-Pol reflectivity data were not assimilated because (1) they were not well calibrated, and (2) they exhibited substantial attenuation in some areas of the storm resulting from Mie scattering by large hail in the storm core. Assimilating these data would likely have had the undesired effect of suppressing convection in the supercell.

6.3.3 Base state environment

The experimental setup is derived from that used by Aksoy *et al.* (2009), who simulated isolated convective storms in an initially horizontally homogeneous environment. Their 50-member ensemble was populated with slightly perturbed initial temperature and velocity profiles derived from a proximity sounding. The primary differences between my experimental setup and theirs are the choice of horizontal grid spacing (my 1 km vs. their 2 km), the version of WRF used (my v3.0.1.1 vs. their v2.1), and number of ensemble members (my 48 vs. their 50). I elected not to perturb the initial temperature profiles (only the velocity profiles) in order to avoid the inadvertent generation of superadiabatic layers. In this framework, the model environment is homogeneous only at the initial time; forward integration of the model and DA make the model state horizontally inhomogeneous at all subsequent times.

Some discussion about the choice of a horizontally homogeneous initial environment (also known as a "single-sounding environment") is warranted here. Recent results from Stensrud and Gao (2010), who also performed radar DA experiments using the case of the Greensburg storm, demonstrate the apparent need for realistic three-dimensional variability in model initial conditions when practical. They conclude that "knowledge of horizontal environmental variability is important to successful convective-scale ensemble predictions and needs to be included in real-data experiments." In light of these results, Dawson *et al.* (2011) ruminate on the merits of an horizontally homogeneous versus inhomogeneous model initial environment. They argue that the horizontally inhomogeneous initial environment

does confer advantages for prediction, but also introduces additional complexities that make both the model implementation and evaluation of the results of sensitivity studies more difficult. In addition, Stensrud and Gao (2010) focus on prediction, whereas I focused on conducting sensitivity studies on the analyses, an objective more easily accomplished in an initially horizontally homogeneous environment.

Considering that the Greensburg storm developed on an outflow boundary from a previous storm (Bluestein 2009), any assumption of environmental horizontal homogeneity is, admittedly, a poor one. It is accepted that there will be some errors in the analyses resulting from environmental horizontal inhomogeneity that is not accounted for in the experimental setup. Therefore, I focused on developing an initial environment representative of the *inflow* region of the Greensburg storm and trying to inform it with as many observations as I could find.

I chose to exploit the experimental setup of Aksoy *et al.* (2009), who simulated several different types of isolated convective storms on storm-scale domains (i.e., with horizontal dimensions ~ 160 – 200 km). They initialized their simulated storms in model environments initialized using the nearest (in both space and time) available rawinsonde observation (sounding), and populated their initial ensembles by adding sinusoidal perturbations the temperature and wind profiles in these soundings to account for uncertainty in the rawinsonde measurements. In this spirit, I sought to develop a model initial environment based purely on observations collected near the Greensburg storm, rather than on coarser-resolution forecast models such as the Rapid Update Cycle (RUC) or North American Mesoscale (NAM)

models (e.g., Stensrud and Gao 2010). I developed the model initial environment as a collaborator on the study described by Dawson *et al.* (2011).

The nearest available rawinsonde observation (in both space and time) to the Greensburg storm was that collected by NWS at 0000 UTC on 5 May 2007 at Dodge City, Kansas (DDC; Fig. 48). This rawinsonde was launched after the passage of a dryline through the Dodge City area, substantially modifying both the wind and thermodynamic profiles below about 800 mb such that they were certainly not representative of the inflow region of the Greensburg storm. In addition, between 0000 and 0300 UTC, an intensifying LLJ was observed; its temporal variability was not captured by the single DDC rawinsonde. (The next regular rawinsonde launch occurred at 1200 UTC, long after the storms and upper-level trough had moved out of the area.) For these reasons, we chose to retain the DDC thermodynamic and wind profiles aloft, but made modifications to the near-surface layers to account for the temporal and spatial variability of the near-storm environment.

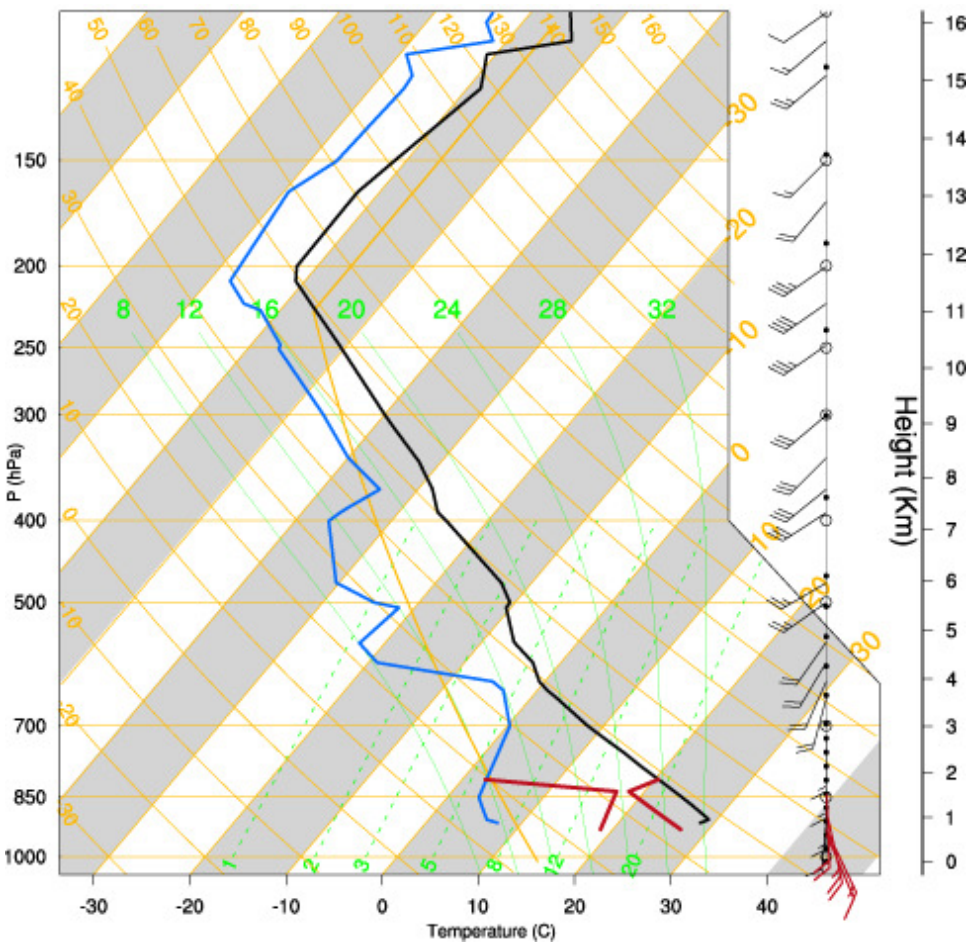


Fig. 48. Skew-T diagram of the 0000 UTC rawinsonde from Dodge City, Kansas (blue and black curves), showing the deep, dry layer below 700 mb following the dryline passage. Modifications to the sounding that were used in the generation of initial conditions for the EnKF experiments are highlighted in red.

The nearest well-calibrated, ASOS site to the Greensburg storm during the 0000 to 0300 UTC time frame is that at Pratt, Kansas (KPTT), 49 km east of Greensburg. The forward flank region of the Greensburg storm passed over KPTT at approximately 0230 UTC. We assumed that the closest prior KPTT observation (taken at 0210 UTC; T = 26.1 °C, T_d = 18.9 °C, u = -5 m s^{-1}, v = 8 m s^{-1}), was representative of the near-surface inflow environment of the Greensburg storm. With no better information available about the thermodynamic characteristics of the boundary layer, we simply inserted a well-mixed (constant θ = 307 K, constant q_v =

15 g kg^{-1}) layer between the surface (650 m ASL) and 1550 m ASL, just below the altitude (1600 m ASL) where a parcel with those characteristics, lifted dry adiabatically, would reach saturation. The presence of such a well-mixed layer near the surface is supported by the sounding taken at Lamont, Oklahoma (180 km east-southeast of the UMass X-Pol deployment site), at 0000 UTC on 5 May 2007 (Appendix B.3), in which a nearly well-mixed layer extended from the surface (317 m ASL) to 1500 m ASL.

For winds between the surface and 3000 m AGL, I used VAD (Browning and Wexler 1968, and D. Dowell, personal communication) wind profiles derived from KDDC Doppler velocity measurements. The KDDC volumes collected closest to 0100 UTC (0230 UTC), denoted "vad0100" ("vad0230"), were chosen to represent the low-level wind profile prior to (during the) the strengthening of the nocturnal LLJ. These two differing low-level wind profiles form the basis of the "weaker LLJ" and "stronger LLJ" experiments discussed below. The lowest useable VAD wind retrieval (at 1090 m ASL, 300 m above KDDC) was simply linearly interpolated to the KPTT surface velocity observation.

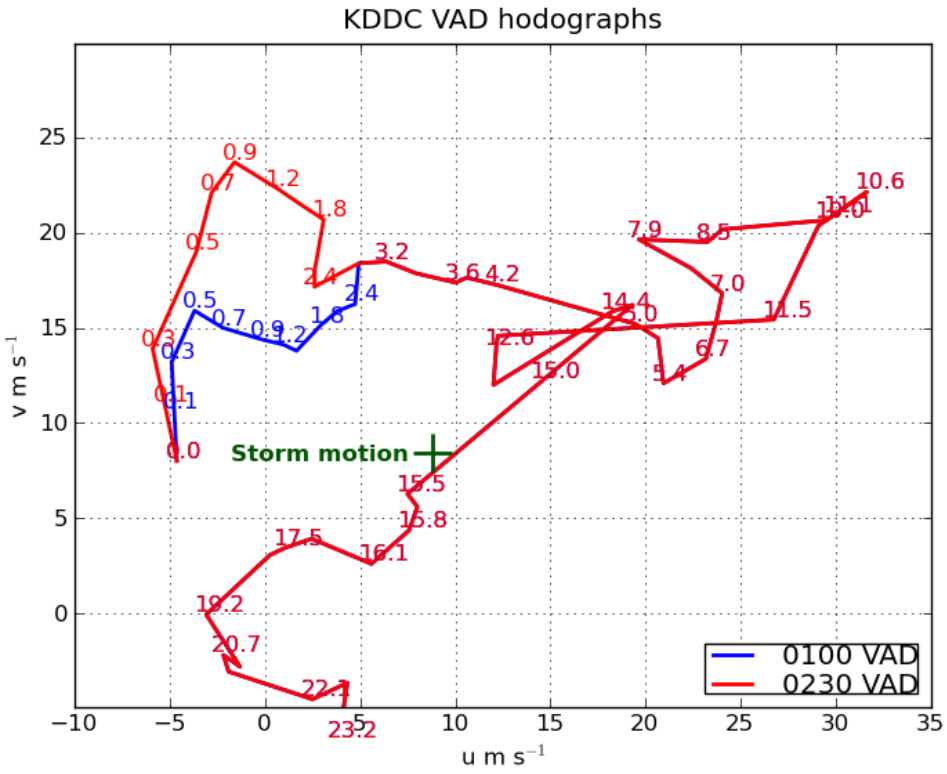


Fig. 49. Hodographs of the model initial environmental wind profiles used in the EnKF experiments. The blue (red) curve represents the "vad0100" ("vad0230") wind profile. Altitude labels are in km AGL. The surface velocity components are from the KPTT observation at 0210 UTC on 5 May 2007, those in the 0.3 – 3.0 km layer are from KDDC VAD retrievals, and the upper-level wind profiles are from the DDC sounding taken at 0000 UTC.

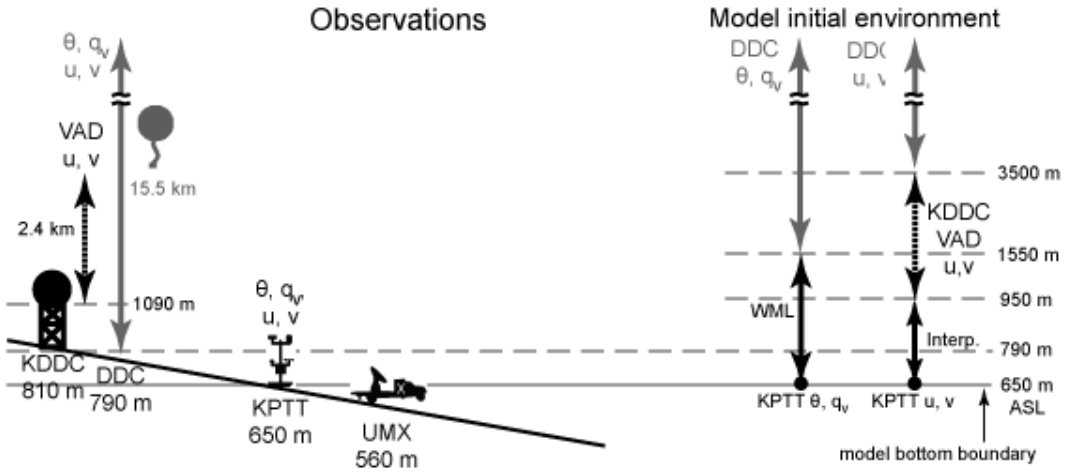


Fig. 50. Observations used in the construction of the model initial environment. Heights and distances between observing platforms are not to scale.

In summary, the model initial environment contained thermodynamic and wind information from the DDC sounding aloft, low-level wind profiles from the KDDC VAD retrievals, and near-surface thermodynamic and wind profiles based on the KPTT surface observations (Fig. 50).[13] These observations were selected and combined because they were thought likeliest to represent the inflow environment of the Greensburg storm out of all the observations available. The resultant initial environment had 4600 J kg^{-1} of CAPE and 26 m s^{-1} (50 kts) of 0 – 6 km bulk shear, which are both consistent with an environment supportive of supercell thunderstorms.

6.3.4 Radar data objective analysis

In order to reduce the volume of observations being assimilated to a manageable size, and to translate the radar observations into the model space, both the KDDC (reflectivity and Doppler velocity) and UMass X-Pol (Doppler velocity only) data from 0030 to 0302 UTC were objectively analyzed to the model domain grid using a Cressman (1959) technique. The radar data were analyzed in such a way that each sweep remained on its original, conical sweep surface while being horizontally interpolated to the grid, as in Aksoy *et al.* (2009), thereby retaining the greater vertical density of data near the radars. Radar data were then treated as a stream of point observations as they were assimilated into WRF.

The KDDC data covered the entire horizontal extent of the objective analysis domain. Areas in which KDDC reflectivity was greater than or equal to (less than) 20 dBZ were analyzed at 1 km (2 km) horizontal grid spacing with a radius of influence

[13] D. Dawson and I refer to such an environmental profile, constructed from various data sources, as a "Frankensounding" in reference to Mary Shelley's character Frankenstein's monster, who was constructed by assembly of body parts from multiple cadavers.

of 1.5 km (3 km; Fig. 51). The lower-reflectivity observations were analyzed at a lower horizontal grid spacing so as to reduce the total number of observations being assimilated (thus reducing the size of the matrices used to calculate the estimate of the forecast error covariance matrix $\widehat{\mathbf{P}}_{\mathbf{k}}^{\mathbf{f}}$), while still retaining enough information in areas of low reflectivity (where, presumably, little to no convection is ongoing) to suppress spurious convection in the model (Caya *et al.* 2005; Aksoy *et al.* 2009).

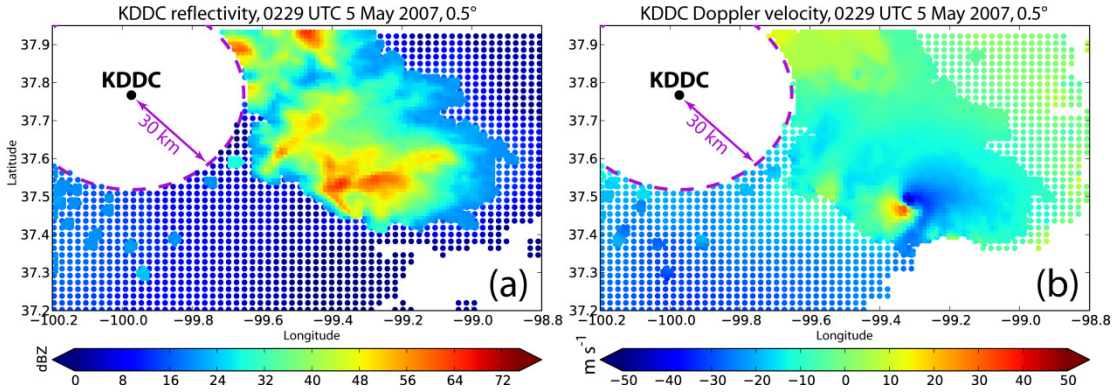


Fig. 51. Objectively analyzed KDDC (a) reflectivity (in dBZ) and (b) Doppler velocity (in m s^{-1}) collected at 0229 UTC at an elevation angle of 0.5°. Observations associated with reflectivity values greater (less) than 20 dBZ were analyzed at (1 km) 2 km grid spacing. The purple dashed circle denotes the 30 km range ring around KDDC; data inside this radius were discarded for the lowest three elevation angles (0.5°, 0.9°, and 1.3°) in each volume in order to avoid assimilation of data associated with ground clutter targets.

Assimilation of KDDC data from non-meteorological targets (buildings, biological targets) was problematic in preliminary versions of these experiments. In some cases, the relatively high reflectivity values associated with clutter targets such as buildings and wind farms were erroneously recast by the EnKF as convective precipitation. To ameliorate this issue, KDDC reflectivity and Doppler velocity data in the lowest three elevation angles (0.5°, 0.9°, and 1.3°) within 30 km of KDDC were omitted from the objective analysis (Fig. 51). This practice had the undesirable effect of removing some observations of actual convective precipitation within 30 km of KDDC, at altitudes at or below 680 m AGL. However, these areas of convective

precipitation (which occurred well away from the Greensburg storm) were not the focus of these experiments, and observations at higher elevation angles of the same convective regions helped to mitigate the effects of these omitted low-altitude data.

Prior to objective analysis, UMass X-Pol data were further edited (beyond the point described in Section 4.1.2). First, Doppler velocity data associated with uncalibrated reflectivity values less than -18 dBZ_e were discarded. Second, Doppler velocity data that appeared to contain primarily noise (low-reflectivity observations, areas of attenuation) were manually discarded.[14] These data would be objectively analyzed as near-zero velocity, when in fact there is simply not enough reliable information about the velocities in those areas. The resulting Doppler velocity field contained only data from the Greensburg storm, and some boundary layer wind observations near the UMass X-Pol (Fig. 52a).

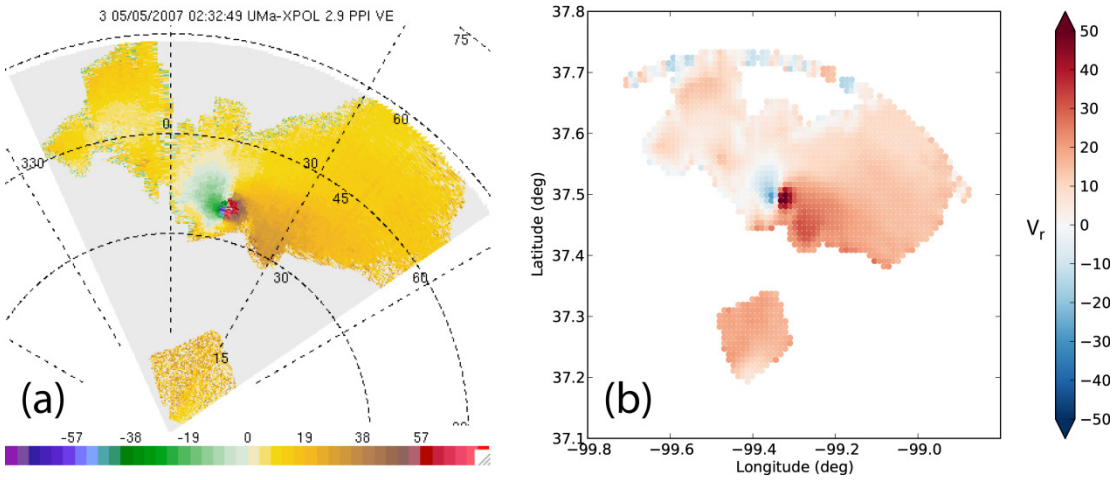


Fig. 52. (a) As in Fig. 18c, But after additional editing to remove noisy UMass X-Pol Doppler velocity data. Note that some gates clear UMass X-Pol are retained and dealiased. (b) Objectively analyzed Doppler velocity field produced from data in panel (a), displayed as a scatterplot. Only a portion of the larger objective analysis domain is shown. The values in the farthest ring of range gates from UMass X-Pol (60 km range) did not appear in the Solo II

[14] I experimented with several reflectivity and SNR thresholds, but found that manual editing was the most reliable way to retain the desired data near UMass X-Pol while discarding undesired data associated with second trip echo clutter, and attenuation.

display (panel a) and could not be edited; their values carry over into the objective analysis (panel b). Range rings in panel (a) are in km; azimuth spokes are every 30°.

The UMass X-Pol Doppler velocity data were analyzed at 1 km horizontal grid spacing with a Cressman radius of influence of 1.5 km (Fig. 52b). The UMass X-Pol reflectivity data, which one might recall were not well calibrated, were not assimilated at all. Calibration issues notwithstanding, the DART forward operator for reflectivity was formulated for S-band, not X-band, reflectivity, so it was not considered advisable to assimilate UMass X-Pol reflectivity data in these experiments anyway.

Finally, just prior to assimilation, the objectively analyzed radar data were "trimmed" such that all observations within 6 km of the edge of the model domain, or outside of the domain entirely, were discarded (Fig. 53). This practice avoided the juxtaposition of sharp gradients in observation availability with the edge of the model domain, a condition that has been associated with the production by the model of spurious convective "bands" originating from the edge(s) of the domain where inflow predominates (L. Wicker, personal communication). Such bands were generated in preliminary versions of these experiments, and nearly eliminated via a combination of this "trimming" of the objective analysis domain and the assimilation of low-reflectivity observations from KDDC to suppress spurious convection.

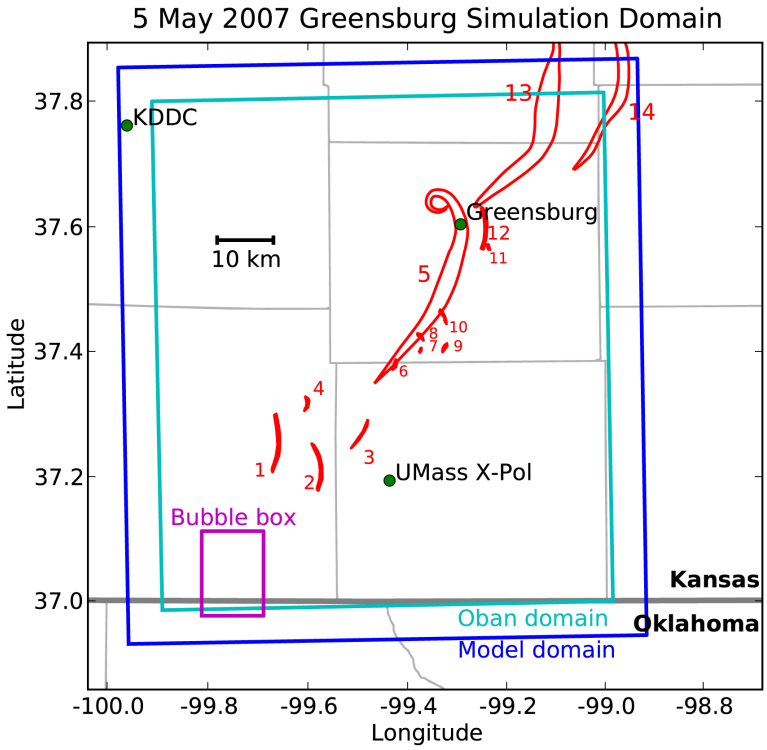


Fig. 53. Computational (blue) and objective analysis (cyan) domain boundaries. The purple box bounds thermal bubbles randomly placed in the initial environment. Tornado damage tracks are plotted in red and numbered according to Table 2.

6.3.5 Experiment parameters

The experiment setup, using WRFV3 and DART, is summarized in Table 5. The domain was centered slightly southwest of Greensburg, Kansas (Fig. 53) and made sufficiently large to contain most of the storm between 0100 and 0300 UTC (the analysis cycle time span). For cloud and precipitation microphysics, the commonly-used Purdue Lin et al. (1983) microphysical scheme in WRFV3 (Skamarock *et al.* 2008) was used. This single-moment scheme uses six hydrometeor classes, including three ice classes (cloud ice, snow, and hail/graupel). Large hail was documented in the Greensburg storm (NCDC 2007; Lemon and Umscheid 2008). Based on conversations with L. Wicker, relatively high hail/graupel density (ρ_h = 800 kg m^{-3}) and slope intercept parameter (N_{0h} = 40000 m^{-4}) were prescribed. It has been

found in previous idealized simulations of supercell thunderstorms that the presence of large numbers of small drops in the hook region can result in stronger cold pools (Snook and Xue 2008; Dawson *et al.* 2010). The presence of large raindrops in the hook region could be inferred from Z_{DR} values (discussed in Section 5.5), so, after some additional consultation with L. Wicker, the intercept parameter for rain N_{0r} was prescribed as 1×10^5 m^{-4}. No surface fluxes, turbulence parameterizations, or radiation physics were employed.

Table 5. Experiment parameters.

Parameter	**Value**
Assimilation period	0100 – 0300 UTC
Assimilation cycle frequency	2 min
Ensemble members	48
Simulation domain	92 km × 102 km × 20 km
Domain size	92 × 102 × 51
Center of domain	37.400 °N, 99.450 °W
Model bottom boundary	650 m ASL
Horizontal grid spacing	1 km
Vertical grid spacing	Stretched, 175 m (bottom) to 1500 m (top)
Cloud microphysical scheme	Lin et al. (1983)
Rain density (ρ_r)	1000 kg m^{-3}
Rain intercept parameter (N_{0r})	1.0×10^5 m^{-4}
Graupel/hail density (ρ_h)	800 kg m^{-3}
Graupel/hail intercept parameter (N_{0h})	4.0×10^5 m^{-4}
Snow density (ρ_s)	100 kg m^{-3}
Snow intercept parameter (N_{0s})	3.0×10^6 m^{-4}
Lateral boundaries	Open
Model time step	3 sec

To populate the initial ensemble of 48 members, and also to account to some extent for instrument error in the DDC sounding and KDDC VADs used to generate the base state environment, vectors of random, normally distributed wind components ~ $N(\bar{v}, \sigma_v^2)$ = N(0 m s^{-1}, [2.0 m s^{-1}]^2) were added to each ensemble member's base

state wind profile. These perturbations are similar to those applied to base-state wind profiles by Aksoy *et al.* (2009) and Dowell et al. (2010). The temperature profile was *not* perturbed so as to avoid the inadvertent generation of superadiabatic layers. These 48 perturbed soundings were then interpolated to the model vertical levels in order to generate the horizontally homogeneous initial model states.

To decrease the model spin-up time, and to account for uncertainty in the convective processes during the organization of the Greensburg storm (Aksoy *et al.* 2009), three thermal bubbles were randomly placed inside a box close to the southwest corner of the domain (Fig. 53). This area ($[x_{min}, x_{max}, y_{min}, y_{max}, z_{min}, z_{max}]$ = [13 km, 24 km, 5 km, 20 km, 0 km, 2.1 km]) was chosen to encompass tightly the location of the developing Greensburg storm at the beginning of the simulation period (0100 UTC). The bubble center locations within the box were randomly chosen for each ensemble member. As in Aksoy *et al.* (2009), the magnitude of the temperature perturbation in each bubble was randomly drawn from a Gaussian distribution ~ $N(\bar{t}, \sigma_t^2)$ = N(5.0 K, 1.0 K^2) and then windowed to the interval (2.5 K, 7.5 K) to exclude extreme outliers. The temperature perturbation in each bubble decayed exponentially to zero at a horizontal (vertical) radius of 7.5 km (1.5 km).

With the ensemble members' initial states thereby populated, the Greensburg storm was analyzed in this framework between 0100 and 0300 UTC. Radar data were assimilated in 2 min cycles; this cycle period was chosen as a compromise between the volume update time of KDDC (4.1 min) and that of UMass X-Pol (~1 min). In contrast to previous data assimilation studies of the Greensburg case (e.g., Gao *et al.*

2008), no observations other than those from the two radars were assimilated. (Indeed, very few were available.)

An additive noise scheme (Caya *et al.* 2005; Dowell and Wicker 2009) was used to maintain ensemble spread throughout the assimilation period. In this scheme, random noise was added to the model temperature (T), dewpoint (T_d), and horizontal velocity (u, v) fields every 5 min in areas where KDDC reflectivity was greater than 25 dBZ during the preceding 5 min. The standard deviations of the noise added to the T, T_d, u, and v field (before smoothing) were prescribed as 0.5 K, 0.5 K, 1.0 m s^{-1}, and 1.0 m s^{-1}, respectively, and the horizontal (vertical) length scale for the perturbations was 4 km (2 km). These values were selected based on results from preliminary versions of these experiments.

6.4 Results

Some selected model ensemble mean fields are plotted as 2 x 2 panels (Fig. 55 - Fig. 61), time-height plots (Fig. 62, Fig. 63), and observation-space diagnostics (Fig. 64, Fig. 65). In all four experiments, the model analyzed a supercell that generally followed the same track as the Greensburg storm, indicating that the assimilation of KDDC data succeeded in establishing the rotating updraft (Fig. 61) and forward flank precipitation region of the Greensburg storm (Fig. 55). The assimilation of thinned low-reflectivity observations (Fig. 51) served to suppress spurious convection in the southern and western portions of the domain (Fig. 55). In addition, a near-surface vorticity maximum closely followed the track of the Greensburg tornado (Fig. 57). The simulated Greensburg storm generated a large cold pool (regions of relatively low θ), primarily in two large "pulses" whose timing varied slightly between

experiments (Fig. 59); these pulses were found to be manifestations of the RFD. The kddc+umass_0230vad experiment (Fig. 59d), in particular, produced a very intense cold downdraft that is not seen in any of the other experiments, southwest of the vortex corresponding to the Greensburg tornado; however, it is believed that this very cold downdraft may be a numerical artifact, since it was not seen in any earlier versions of the same experiment.

Ensemble mean maximum vertical vorticity ($\overline{\zeta_{max}}$) generally increased with time (Fig. 62), attaining a maximum when the Greensburg tornado was mature (0215 – 0245 UTC) and detectable by KDDC. The maximum vertical velocities generally occur in an early burst within the first 45 minutes of the experiment (Fig. 63), and are presumably related to the use of the initial thermal bubbles; updrafts of comparable strength and longevity are not sustained by the model.[15] Assimilation of UMass X-Pol data did have a noticeable impact on updraft strength toward the end of the simulation period (Fig. 61c, d). The 1 km horizontal grid spacing resolves an updraft 4 – 6 km in diameter (inferred from UMass X-Pol observations of the BWER; Fig. 25). Presumably, the *w*-fields are being updated through rather weak covariances with the variables being assimilated (reflectivity and radial velocity), subject to mass conservation constraints. Because of the shallow radar elevation angles (< 20°) used, the Doppler velocity observations only sampled a small component of *w*, and then only over a small area around each radar. One could surmise that assimilation of more direct measurements of vertical velocity in the supercell updraft (e.g., from vertically

[15] I ran tests on a few members (not shown) in which I did not assimilate any data at all. In all of these so-called "bubble tests", the simulated Greensburg storm decayed about 1 hr into the simulation. Similar results were obtained by Dawson *et al.* (2011).

pointing radar(s), or sounding(s) launched directly into the storm updraft) would help to sustain stronger updrafts in the simulation.

The RMSI values remained close to 3.0 m s^{-1} (the assumed observation error for v_r) near the surface throughout most of the assimilation period (Fig. 64). However, these values exceeded 3.0 m s^{-1} at mid-levels and increased beyond 4.0 m s^{-1} during the last hour of the assimilation period (Fig. 65), indicating too much ensemble spread at those altitudes. Results at upper levels (above 6.0 km) were even worse, with RMSI values approaching 8.0 m s^{-1} during the last hour of the assimilation period. As the assimilation cycles progressed, the base state environment (based on the 0000 UTC DDC sounding) became less and less representative of the actual storm environment. In particular, the 500 mb trough that had been located west of DDC at 0000 UTC (Fig. 14) continued to progress east; velocities aloft would have increased in magnitude and assumed more of a southerly component during the assimilation period. In the model, the base state velocity profile was maintained along the southern (inflow) edge of the domain, because no convection occurred there and no additional observations were assimilated that might have modified velocities in that region. As a result, this increasingly outdated wind profile was continually "replenished" in the interior of the domain from its southern edge, and would have increasingly conflicted with Doppler velocity observations in the anvil region of the Greensburg storm that reflected the evolving upper tropospheric wind profile. In addition, the anvil region of the Greensburg storm moved out of the model domain with time, so that fewer observations reflecting the changes in the upper tropospheric winds were being assimilated overall.

Layer-averaged innovation values ($\bar{d}$) generally remained near zero throughout most of the experiment, drifting away from zero toward the end of the assimilation period (Fig. 64, Fig. 65). Again, it is believed that this behavior results from the movement of portions of the Greensburg storm out of the model domain.

The storm's internal behavior varies, sometimes substantially, among the four experiments; discussion follows.

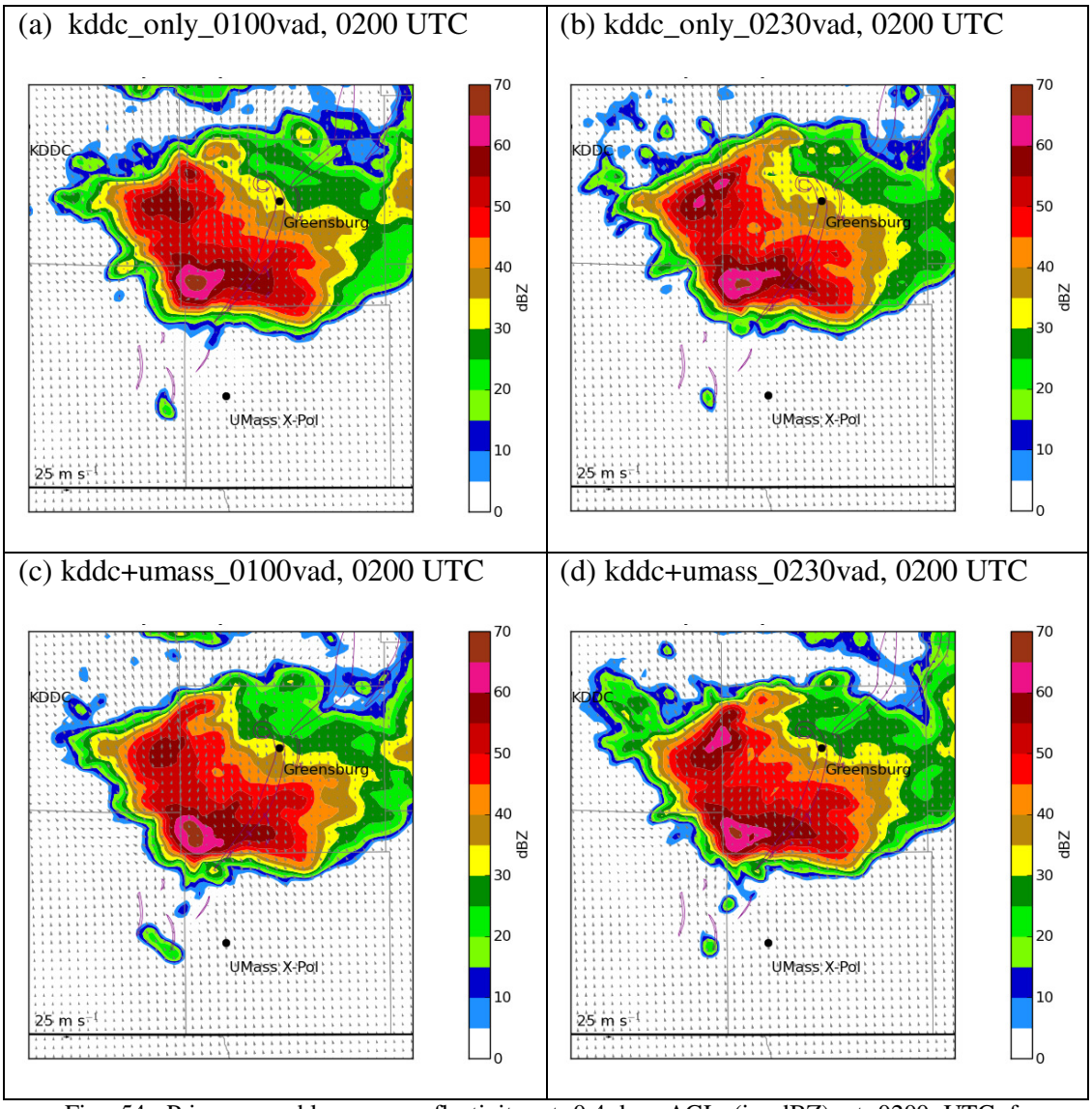


Fig. 54. Prior ensemble mean reflectivity at 0.4 km AGL (in dBZ) at 0200 UTC for experiments (a) kddc_only_0100vad, (b) kddc_only_0230vad, (c) kddc+umass_0100vad, and (d) kddc+umass_0230vad.

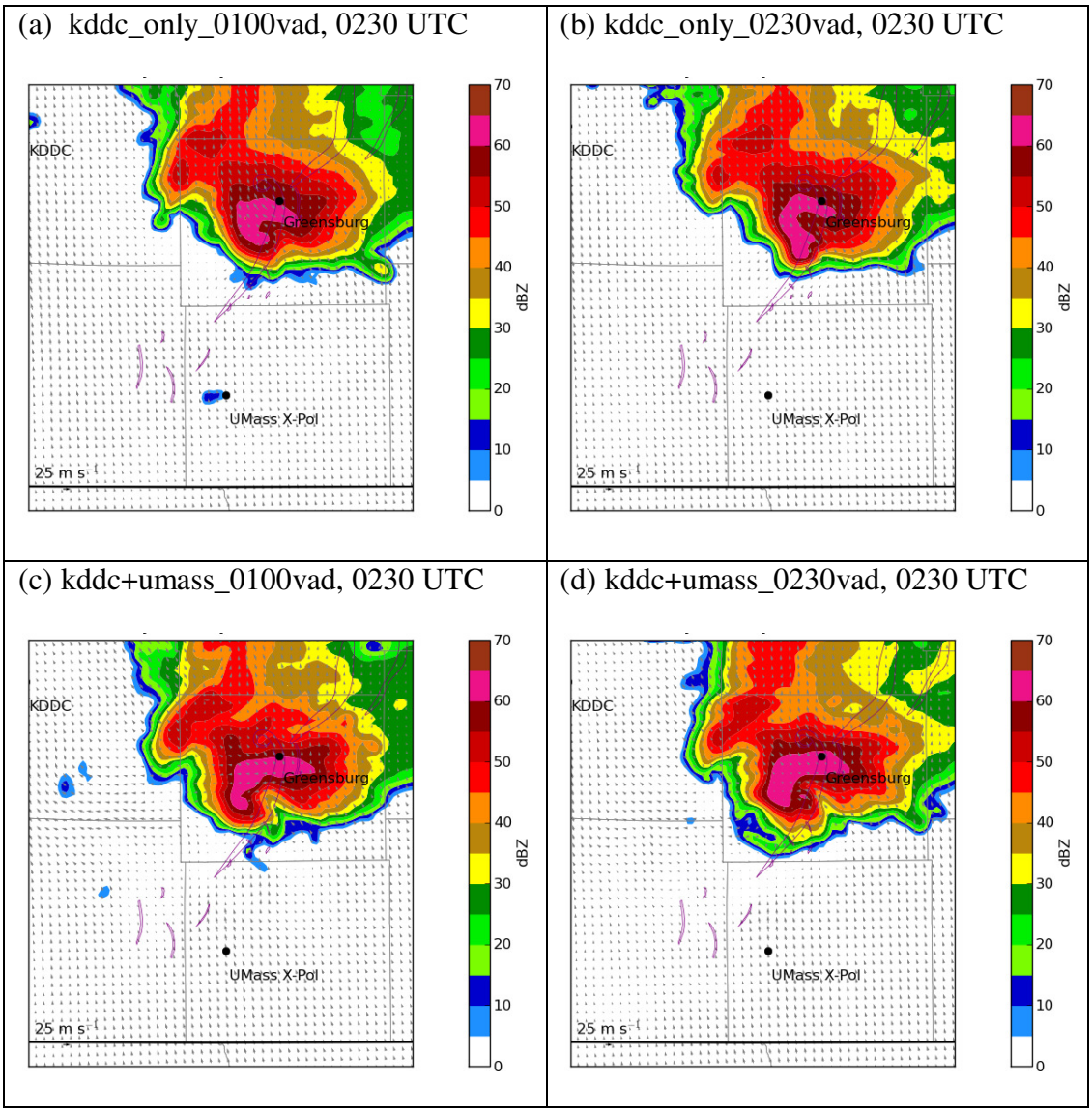


Fig. 55. As in Fig. 54, but for analyses at 0230 UTC.

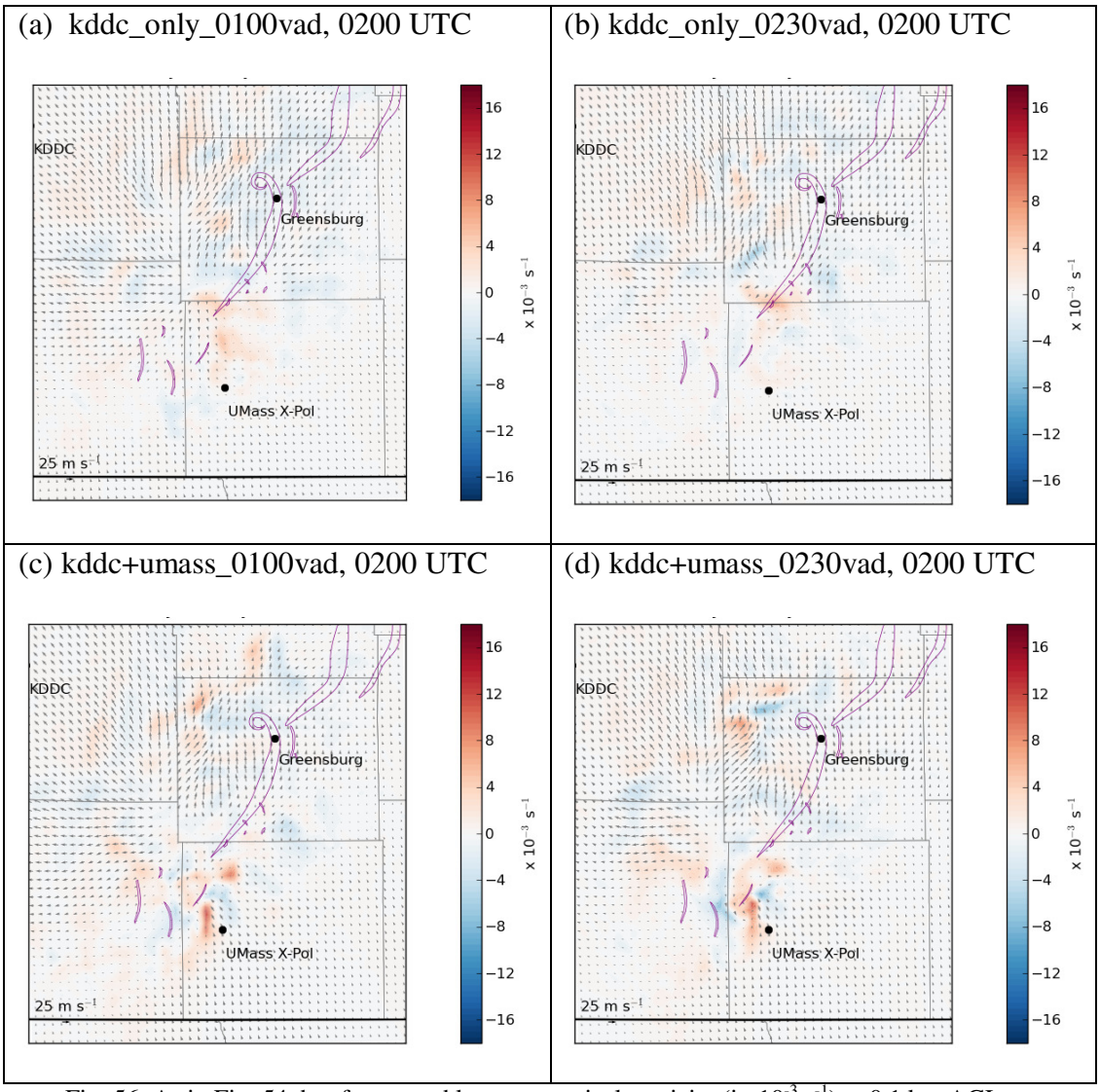


Fig. 56. As in Fig. 54, but for ensemble mean vertical vorticity (in 10^{-3} s^{-1}) at 0.1 km AGL.

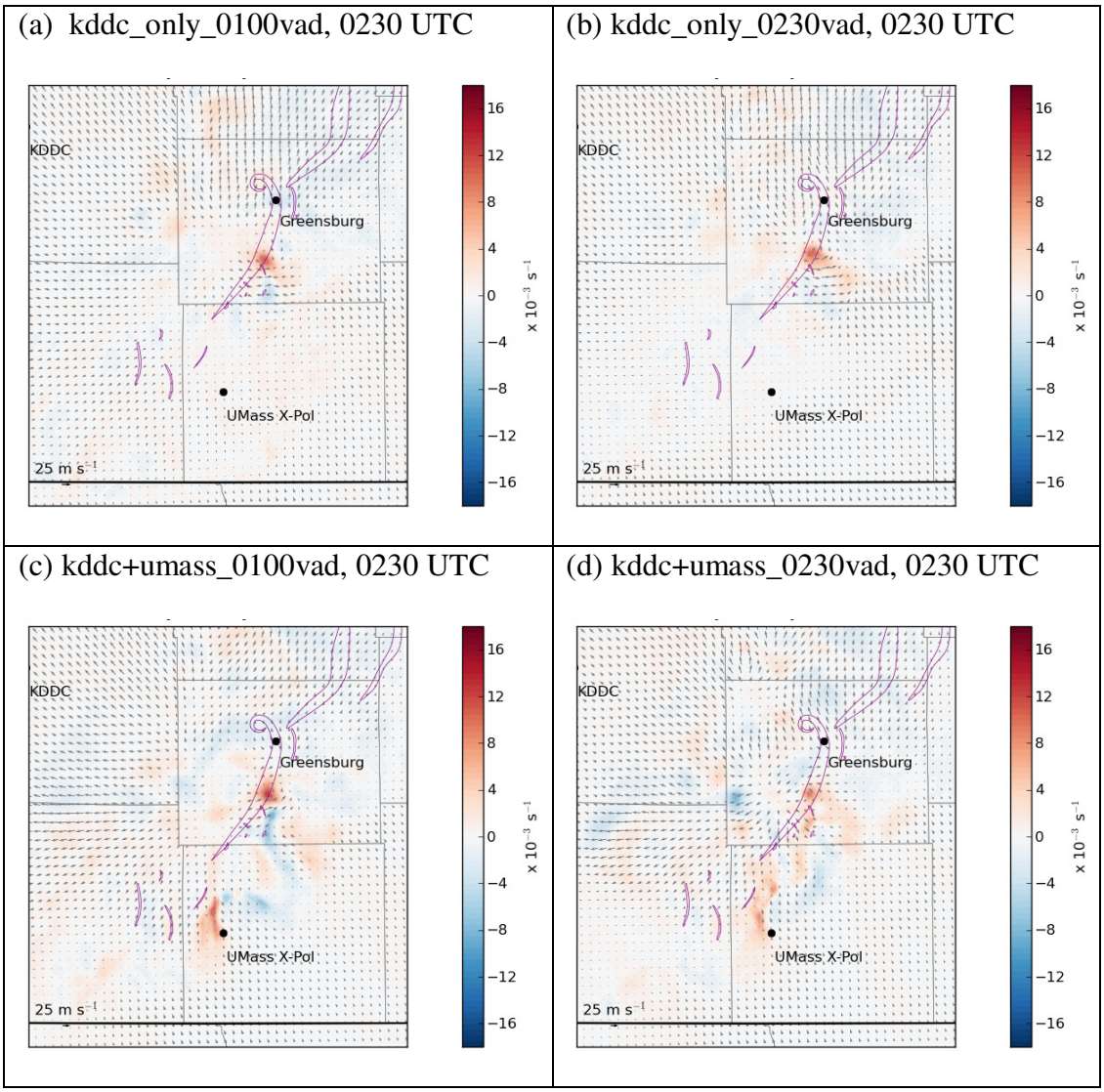


Fig. 57. As in Fig. 56, but for analyses at 0230 UTC.

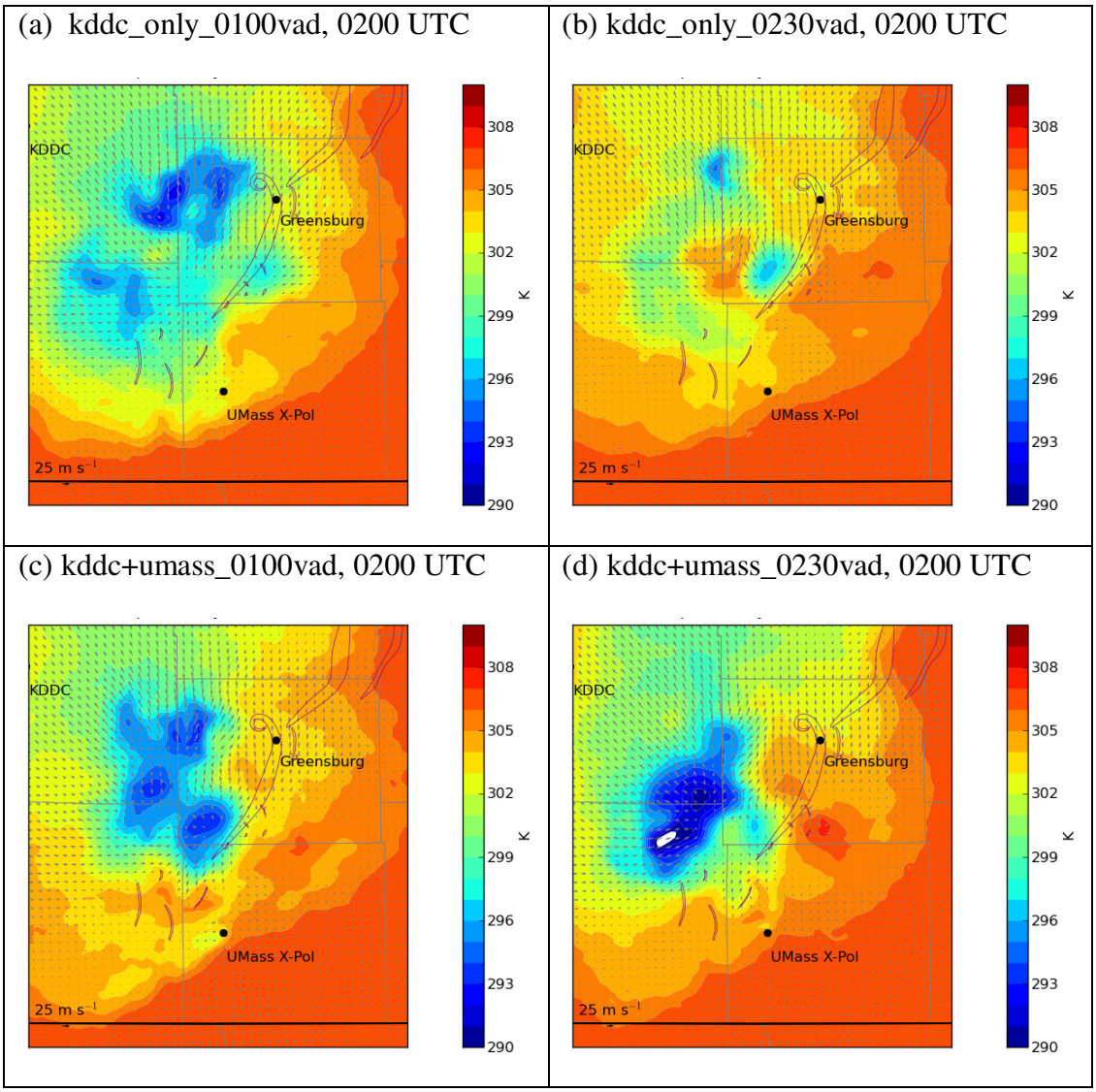


Fig. 58. As in Fig. 54, but for ensemble mean potential temperature (in K) at 0.1 km AGL (the scalar model level closest to the surface).

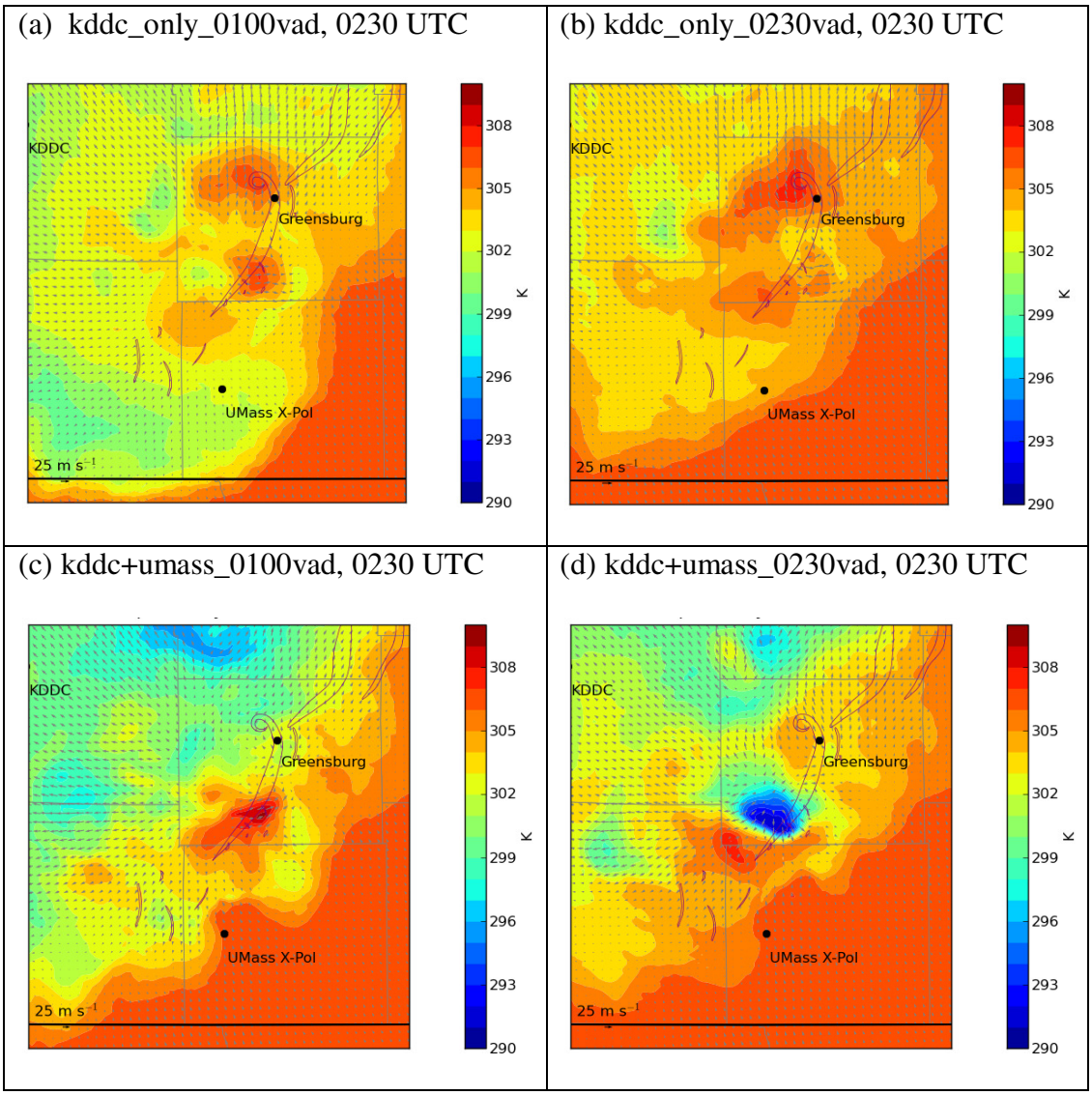


Fig. 59. As in Fig. 62, but for analyses at 0230 UTC.

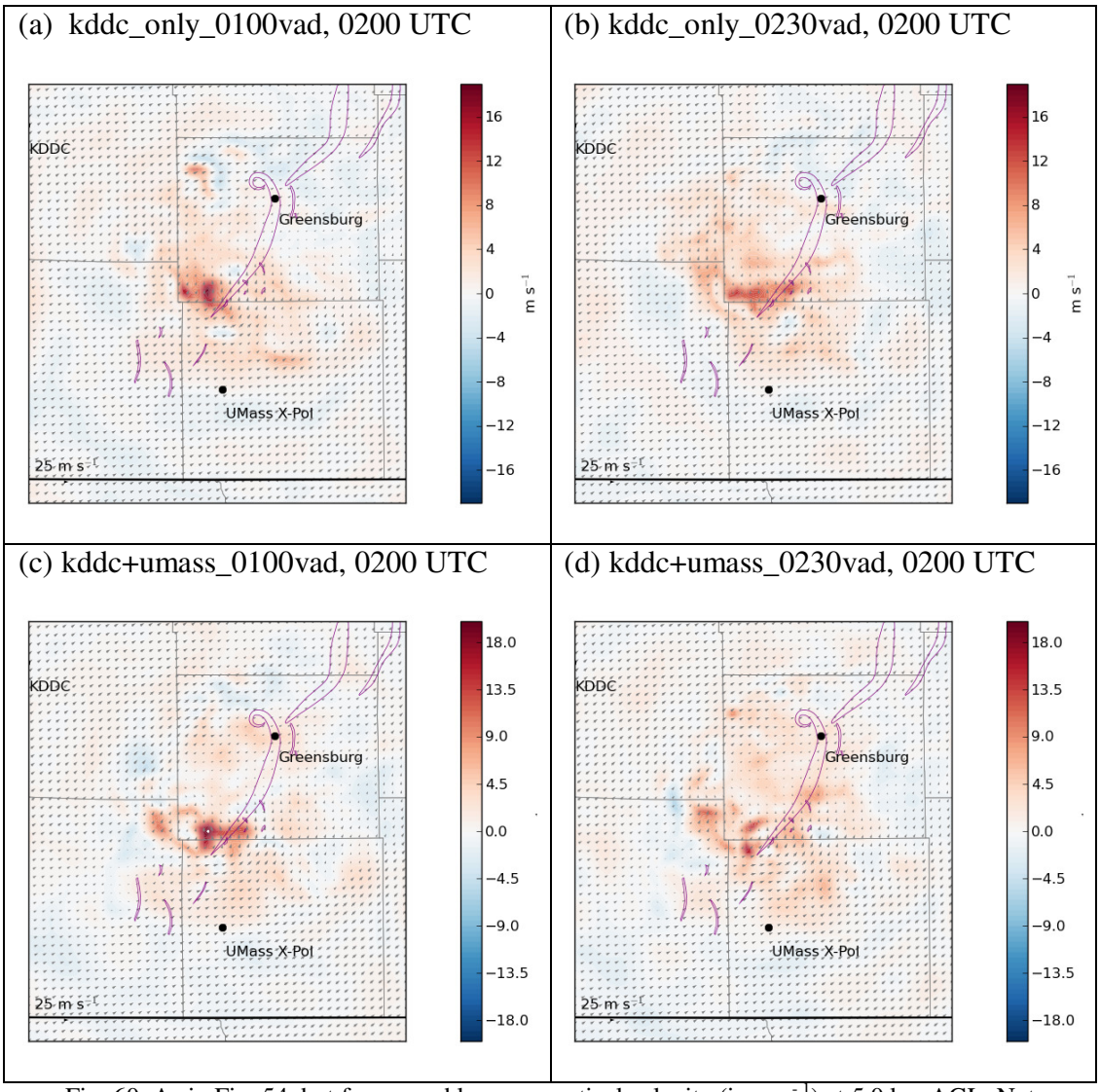


Fig. 60. As in Fig. 54, but for ensemble mean vertical velocity (in m s^{-1}) at 5.0 km AGL. Note that the color scales differ slightly between panels.

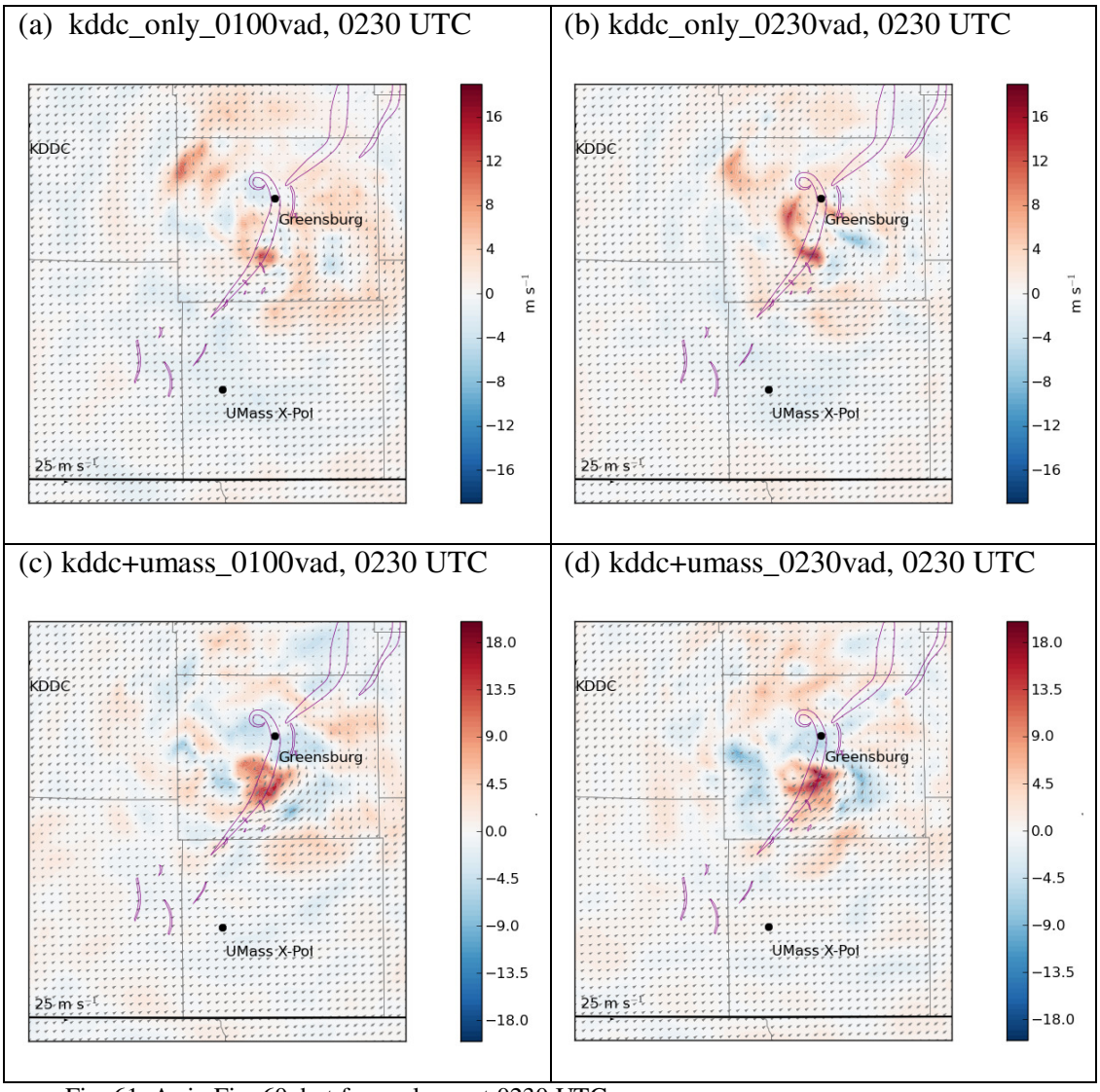


Fig. 61. As in Fig. 60, but for analyses at 0230 UTC.

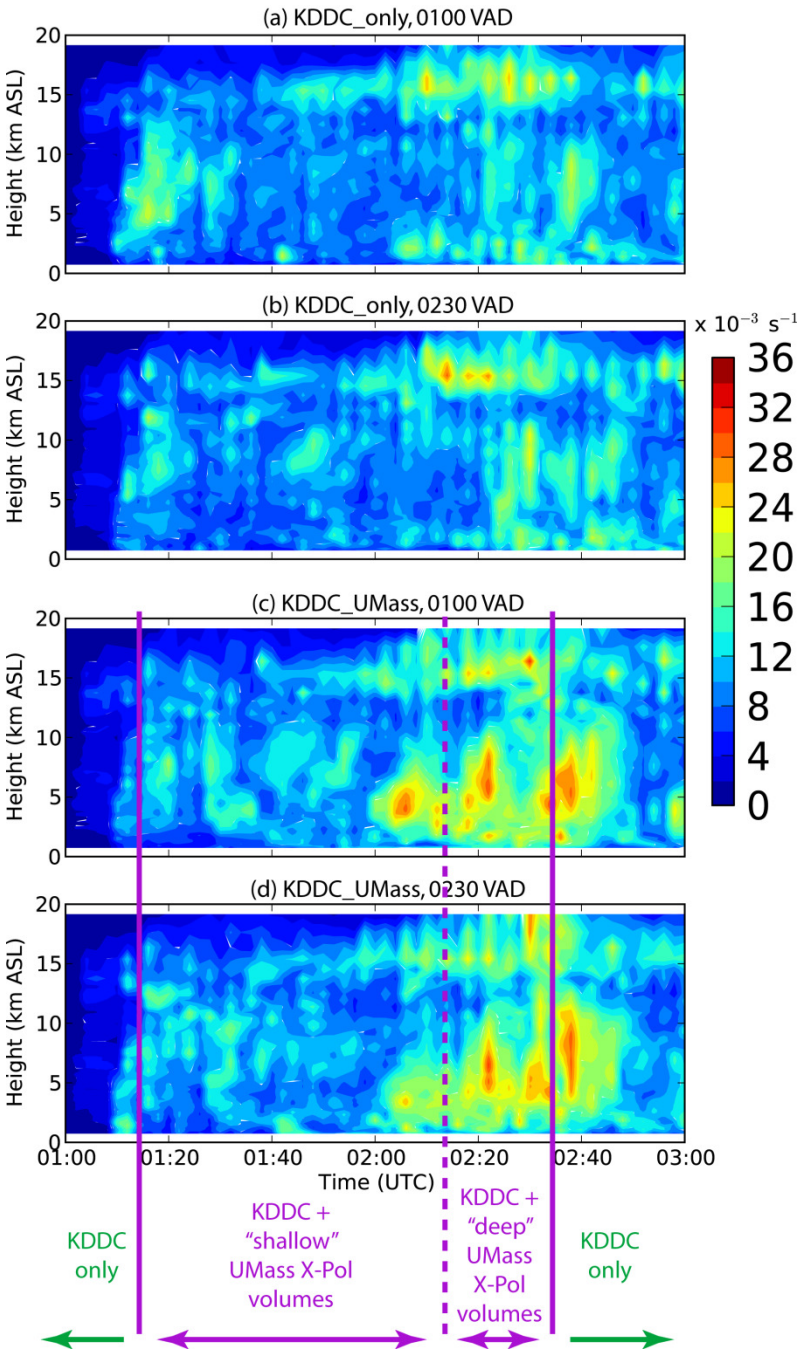


Fig. 62. Time-height plot of ensemble mean maximum vertical vorticity for experiments (a) kddc_only_0100vad, (b) kddc_only_0230vad, (c) kddc+umass_0100vad, and (d) kddc+umass_0230vad. Times for which UMass X-Pol "shallow" and "deep" volumetric Doppler velocity were assimilated in addition to KDDC reflectivity and Doppler velocity data are delineated in purple.

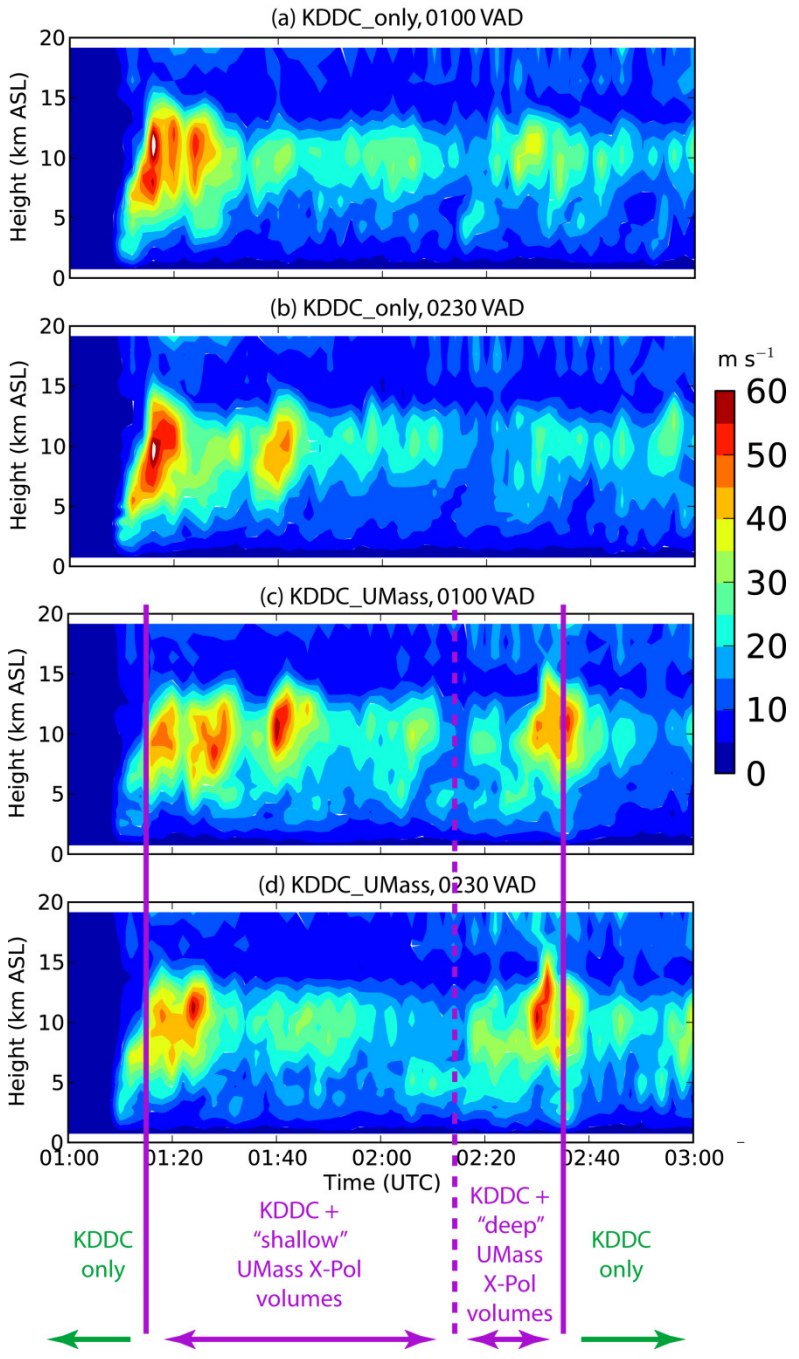


Fig. 63. As in Fig. 62, but for ensemble mean maximum vertical velocity.

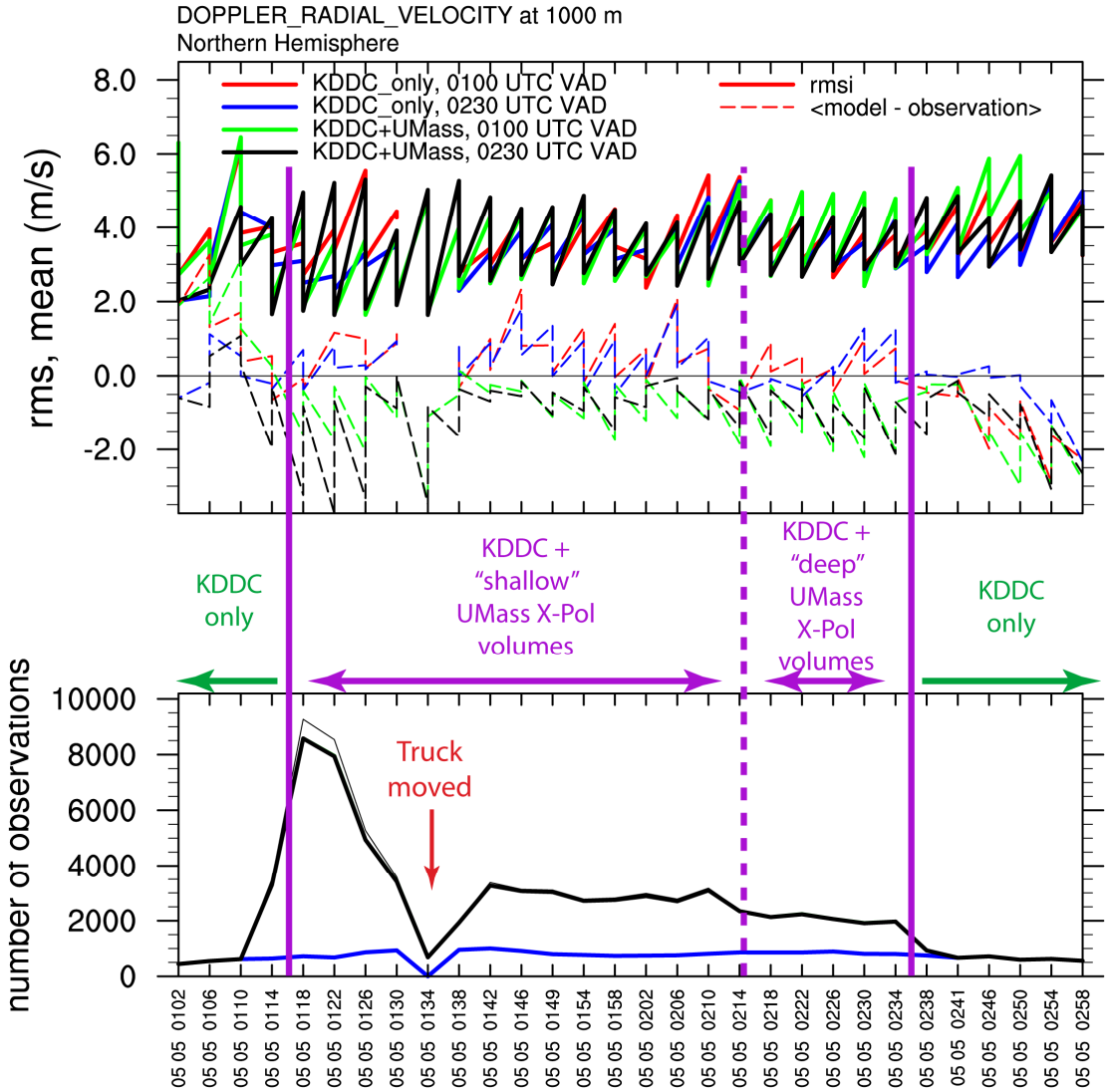


Fig. 64. (Top) Observation-space diagnostics for Doppler velocity, over 4-minute intervals, for kddc_only_0100vad (red curves), kddc_only_0230vad (blue curves), kddc+umass_0100vad (green curves) and kddc+umass_0230vad (black curves), for the 0 – 1 km AGL layer of the model. The quantities plotted are (solid curves) RMSI and (dashed curve) layer-averaged innovation (model minus observation). Both the prior and posterior diagnostic quantities are plotted; hence the "sawtooth" pattern. (Bottom) The number of objectively analyzed Doppler velocity observations, binned in 4-minute intervals. Thin lines indicate the number of available Doppler velocity observations; the thick lines indicate the number of observations that were actually assimilated into the model. Note that there are many more observations assimilated over this layer from 0115 to 0126 UTC, when UMass X-Pol was collecting single-elevation scans at 3.0° - 4.0°.

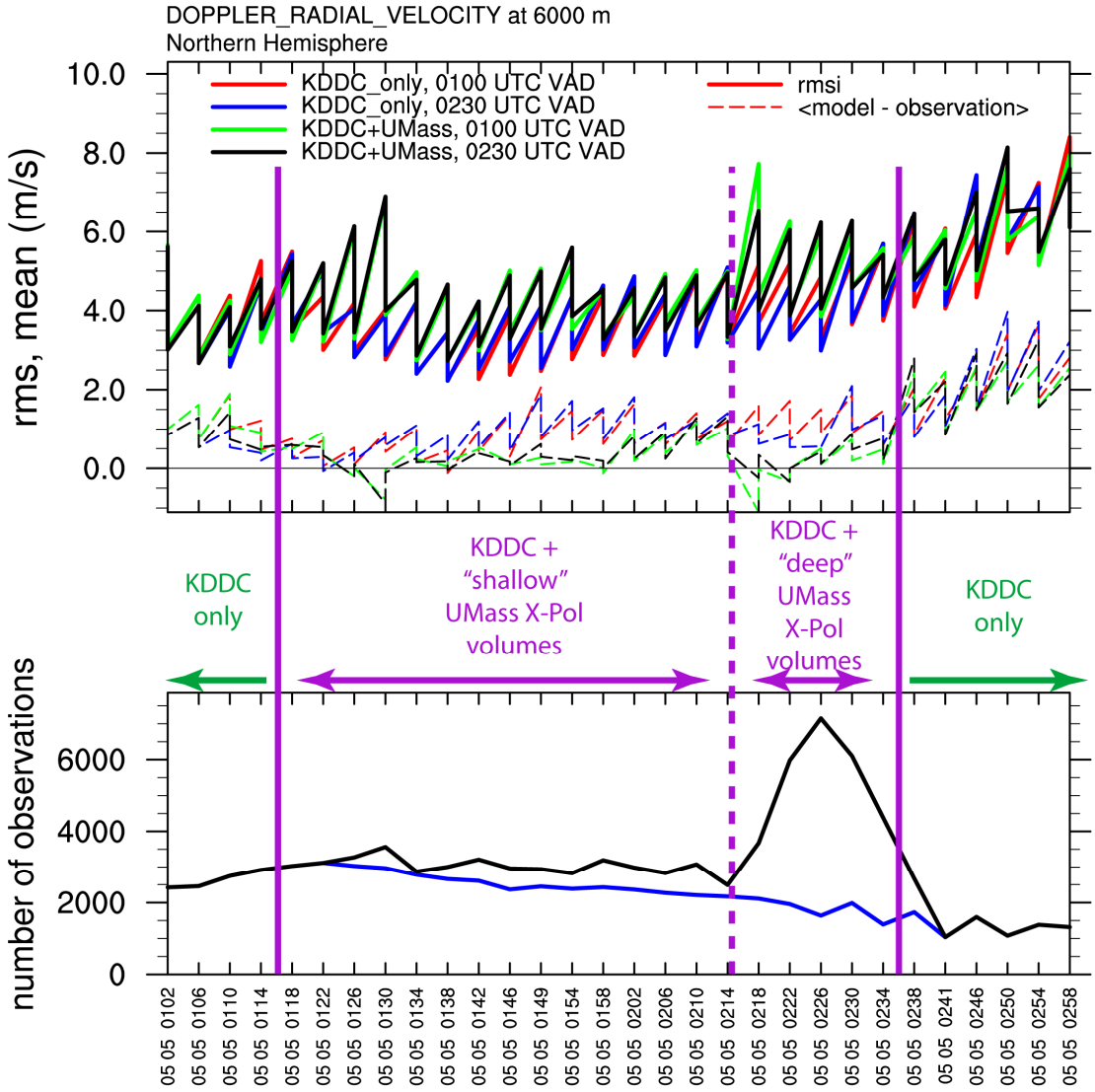


Fig. 65. Same as Fig. 64, but for the 5 – 6 km AGL layer of the model. Note that there are many more observations assimilated over this layer between 0215 and 0236 UTC, when "deep" UMass X-Pol volumes were being collected.

6.4.1 Inclusion of UMass X-Pol Doppler velocities (kddc_only versus kddc+umass)

The experiments in which UMass X-Pol Doppler velocity data are assimilated produce vortices that are, stronger, deeper, and more persistent than corresponding experiments in which UMass X-Pol data are withheld, particularly at the mid- and upper levels (Fig. 57, Fig. 62). In particular, a strong, low-level vortex maximum,

corresponding to the Greensburg tornado, developed shortly after 0200 UTC (the actual start time of the Greensburg tornado). This vortex was deeper and stronger in kddc+umass experiments when "deep" UMass X-Pol volumes are assimilated (0215 – 0236 UTC) when compared with corresponding kddc_only experiments, presumably because more information about the strength of mid-to-upper level mesocyclone(s) was being assimilated. In addition, the model would have assimilated UMass X-Pol velocity observations of the mesocyclones and tornadoes at lower elevations than KDDC. We have seen that low-level convergence was likely present in these tornadoes (Section 5.2.2.1), and could have served to concentrate cyclonic vorticity, intensifying the modeled vortices (Gaudet and Cotton 2006; Gaudet *et al.* 2006).

Some weaker vortices (not shown) appear between 0130 and 0145 UTC in the kddc+umass experiments, and appear to correspond to tornadoes 1, 3 and 4, although they are not present in all ensemble members. Only for tornadoes 1 and 4 can a one-to-one correspondence with a vortex in some ensemble members be established. In Fig. 56, a weak vortex can be seen in the ensemble mean, just north of UMass X-Pol, that corresponds with tornado 3. Recall that tornadoes 1 through 4 were much smaller in scale (~ 1-2 km) and shorter-lived (~ 4 -13 min) than tornado 5; these vortices would have been barely resolvable at 1 km horizontal grid spacing. I could not distinguish vortices corresponding to tornadoes 6 through 10 in any of the ensemble members. Recall that tornadoes 6 through 10 were very brief (Table 2), with none lasting longer than 2 min (the length of the assimilation cycle).

Interestingly, kddc+umass experiments produce stronger cold pools than corresponding kddc_only experiments (Fig. 59). The reason for this difference is still unclear to me, and in fact it contradicts results from preliminary versions of these experiments (presented at my general examination). I used a relatively simple, single-moment microphysical parameterization scheme (Lin *et al.* 1983), albeit one that does include ice species. Cold pool strength is often strongly tied to the choice of microphysical parameterization scheme (e.g., single- versus multi-moment, inclusion versus exclusion of ice species) used, and non-linear feedback processes sometimes lead to vastly different cold pool structures, even when the same scheme is used with slightly different parameter values (Gilmore *et al.* 2004; Snook and Xue 2008; Dawson *et al.* 2010). The appearance of a very cold downdraft in the kddc+umass_0230vad experiment (only) may have resulted from such a feedback process; it did not appear in preliminary versions of these experiments in which less near-surface UMass X-Pol velocity data were assimilated.

The southward spread of the cold pool was clearly affected by assimilation of near-surface UMass X-Pol velocity data (Fig. 59c, d), which had a strong southerly component of velocity (~ 30 m s^{-1}) just above the surface (Figs. Fig. 40, Fig. 52). Regions of spurious, positive near-surface vorticity can be seen just northwest of UMass X-Pol (Fig. 57c, d), where the edge of the UMass X-Pol sector (containing measurements of southerly flow) sit adjacent to northerly flow in the simulated cold pool.

Assimilation of "deep" UMass X-Pol volumes corresponded with an increase in updraft strength (velocities ~ 60 m s^{-1}), particularly in upper levels of the

Greensburg storm (Fig. 63), whereas updraft strength in corresponding kddc_only experiments did not exceed 40 m s^{-1} after the effect of the initial thermal bubbles wore off. The additional assimilation of upper-level UMass X-Pol Doppler velocity appears to have strengthened the updraft in the simulated Greensburg storm.

6.4.2 Variation of the initial low-level environmental velocity profile (0100vad versus 0230vad)

There was little appreciable difference in the positions and strengths of mid-level updrafts (Figs. Fig. 61a, b, Fig. 63) in the simulated Greensburg storm and near-surface vortices corresponding to the Greensburg tornado in the two kddc_only experiments (Fig. 57a, b, Fig. 62). However, the Greensburg tornado vortex was, in the ensemble mean, stronger in the kddc+umass_0100vad experiment than in the kddc+umass_0230vad experiments (Fig. 55, Fig. 62). The very low-θ downdraft air being ingested into the Greensburg tornado vortex (Fig. 59d) weakened the vortex (Fig. 57d); assimilation of the Doppler velocity data re-established the strong Greensburg tornado vortex with each assimilation cycle.[16] Posterior vorticity fields (not shown) support this statement. I suspect that the Greensburg tornado vortex would have been stronger were it not for the presence of this very low-θ downdraft air near the surface.

Overall, cold pool structures were similar between corresponding pairs of 0100vad and 0230vad experiments (Fig. 59). The intensities of the cold pools,

[16] An earlier version of the kddc_umass_0230vad experiment, in which more of the near-surface, clear-air UMass X-Pol Doppler velocity data were withheld from assimilation (not shown), did not produce the very low-θ downdraft that can be seen in Fig. 59d. In that earlier experiment, the Greensburg tornado vortex was stronger (0.030 s^{-1} versus 0.015 s^{-1}) than in the corresponding kddc_umass_0100vad experiment.

however, were different, with lower values of θ analyzed in 0100vad experiments than in 0230vad experiments (excluding the very cold downdraft near the center of the domain in the kddc+umass_0230vad experiment). Without surface measurements to independently corroborate the exact θ values, little can be said with confidence about which cold pool intensity was more realistic, and the mechanism(s) by which low-level shear impact(s) cold pool intensity is still an open area of research (D. Dawson and L. Wicker, personal communications).

I revisit my underlying supposition that innovations would have a smaller magnitude when the model environment more closely matched the inflow environment. I *believed* that the 0100vad (0230vad) wind profile more closely represented the Greensburg storm inflow environment early (later) in the assimilation period. Consequently, I expected the innovations to have smaller magnitudes at those times. However, in my opinion, the innovations do not bear out the veracity of that supposition; at best, the results are mixed. I have difficulty distinguishing a consistent link between innovation magnitude and the initial wind profile used, and suspect that the coverage of the UMass X-Pol radar data actually has a stronger impact on these values. Indeed, UMass X-Pol data have the greatest impact in areas of the domain where wind fields have strong spatial gradients and are rapidly evolving. In future versions of the experiments, I may need to revise the above supposition, or evaluate it more thoroughly in an idealized framework.

6.4.3 Pitch/roll sensitivity experiments

Recall that the pitch and roll angles of UMass X-Pol are not known, because the truck did not have a leveling system. Until now, I have assumed that the pitch and

roll of the UMass X-Pol data are correct as recorded, to within 1°. An error of 1° in either pitch or roll would correspond to an error in altitude of 523 m at a distance of 30 km from UMass X-Pol. Near the surface, this would correspond to an error of several model levels.

The data assimilation experiment setup provided an opportunity to manipulate the orientation of the UMass X-Pol data in a novel way. I designed a small module that, given a prescribed change the orientation (θ_p, Φ_r, and/or Ψ; see Fig. 20) of the objectively analyzed UMass X-Pol observations, would rotate those observations in space around UMass X-Pol via a rotation matrix, effectively simulating a change in pitch, roll, or yaw of UMass X-Pol. I then assimilated these rotated UMass X-Pol observations, just as I had assimilated the unrotated ones, in an experimental setup that was otherwise identical to kddc+umass_0230vad. I hypothesized that rotating the UMass X-Pol data away from their true orientation would result in poorer performance of the EnKF, manifesting as higher values of RMSI and innovation.

Since I felt confident in the azimuthal orientation (yaw) of the UMass X-Pol data (based on ground-clutter-based adjustments discussed in Section 4.2.3), I only tested the effects of changing the pitch or roll of the UMass X-Pol data by 1° in either the positive (clockwise) or negative (counterclockwise) direction. Observation-space diagnostic quantities for the 0 – 1 km layer (where the greatest number of observations would be rotated into or out of the layer) are shown in Fig. 66 and Fig. 67. It can be seen that adjustments of 1° result in significant increases in the RMSI and innovation values, indicating increased disagreement between the model and the assimilated observations. I repeated these experiments for changes in pitch or roll of

±2°; this change resulted in even larger values of RMSI (not shown). Based on these results, I concluded that UMass X-Pol was level to within 1°.

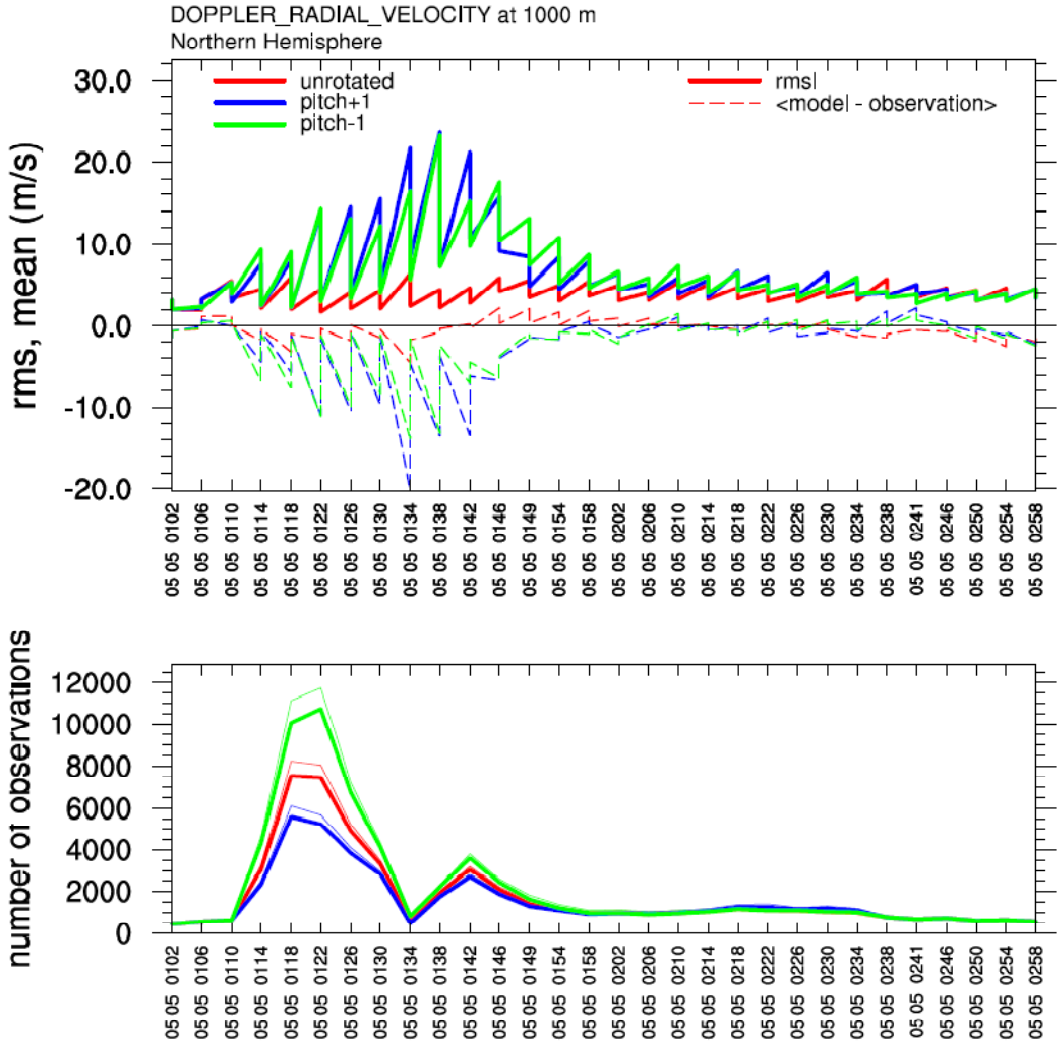


Fig. 66. Effects of pitch adjustments of +1° (blue) and -1° (green) on RMSI (solid curves) and layer-averaged-model innovations (dashed curves) for the 0 – 1 km AGL layer in the kddc+umass_0230vad experiments (red).

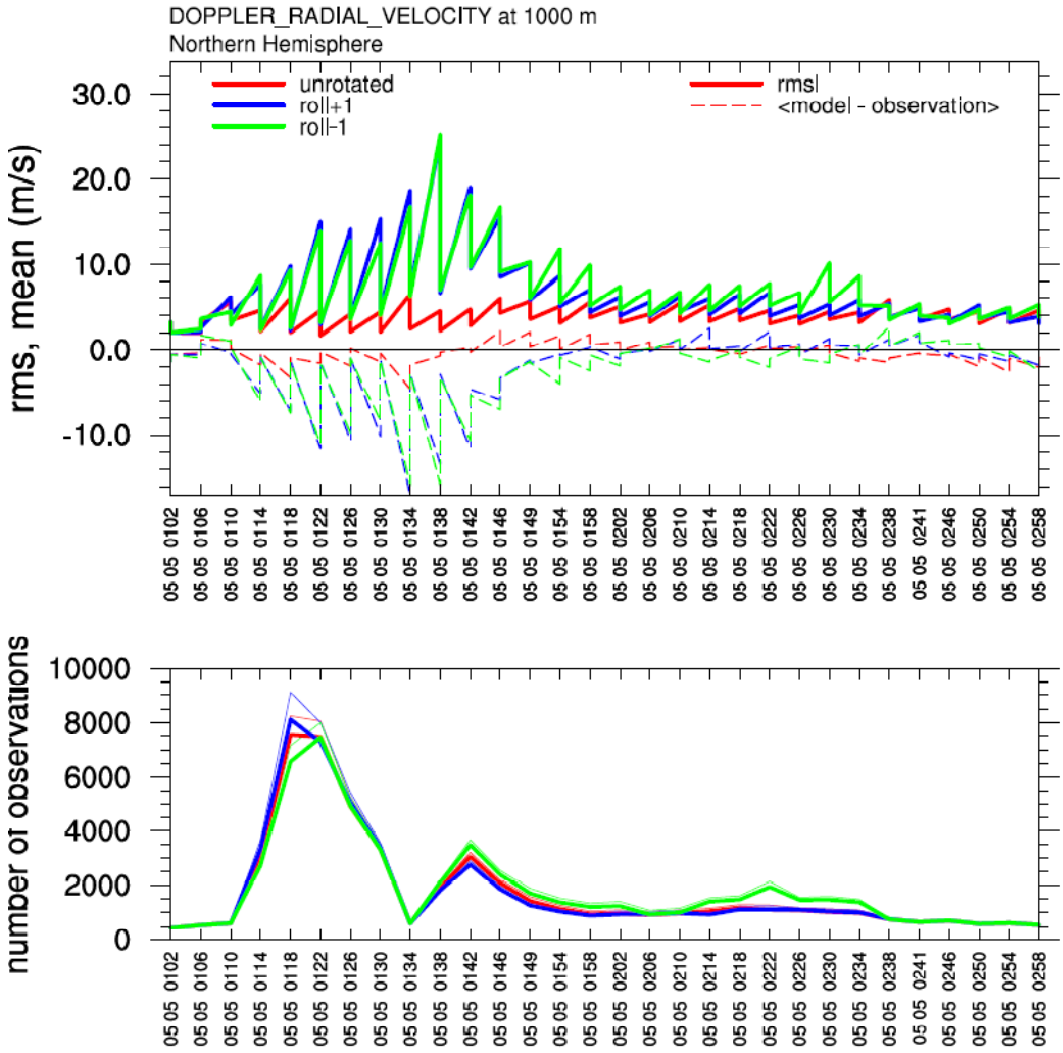


Fig. 67. As in Fig. 66, but for roll adjustments of +1° (blue) and -1° (green).

6.4.4 Closing comments

Overall, the modification to the low-level wind profile had less impact on the analyses than did the assimilation of mobile Doppler radar data. This trend is reflected in the ensemble mean analysis fields (Fig. 55 - Fig. 61), time-height cross-sections of domain-wide maximum ζ and w (Fig. 62 and Fig. 63), and observation-space diagnostics (Fig. 64 and Fig. 65). While this result is not entirely surprising, it underscores the relative importance of assimilation of data from multiple, independent platforms as opposed to "tweaking" the model initial environment.

Based on the results described above and those from previous DA studies of convective thunderstorms (e.g., Jung *et al.* 2008; Dowell and Wicker 2009; Dowell *et al.* 2010; Stensrud and Gao 2010; Yussouf and Stensrud 2010; Dawson *et al.* 2011), it seems appropriate to remark that any future forecasting strategy that incorporates data from mobile observing systems must make accurate recording of exact data collection times, locations, and orientations of instruments paramount.

Chapter 7 Conclusions

The UMass X-Pol data collected in the 5 May 2007 Greensburg, Kansas storm were unusual in their coverage and continuous depiction of a violent tornado and the evolution of the storm that produced it. In the preceding chapters, I have used these data to document and analyze the Greensburg storm in the hour leading up to this historic event. In submitting this dissertation, my intention is to make these results available to the forecasting and research communities for whatever insights they may offer.

The Greensburg storm exhibited two tornado cyclic production modes, which I referred to as "mode I" (short-track, relatively weak tornadoes), and "mode II" (a single, large, violent tornado and satellites). The UMass X-Pol radar collected data in the hook region of the Greensburg storm during the transition from mode I to mode II, which occurred at around 0155 – 0200 UTC. Using these data, I attempted to explore the mechanisms (if any) by which the changing low-level wind profile (owing to the onset of the LLJ), or the expansion of the storm's cold pool, or a combination of both, were related to the mode I-to-mode II transition. To this end, I was only partially successful. I was able to characterize the relationships but not fully explain their causative mechanism(s), primarily because observations of the surface and near-surface winds in the inflow region of the Greensburg storm are spatially sparse and/or infrequent. Below, I briefly summarize the primary findings of the observational study and the EnKF experiments, and close with some points for future exploration.

7.1 Radar data analysis

- The Greensburg storm was found to be a prolific producer of vortices during the period in which it was sampled by the UMass X-Pol radar (0115 – 0236 UTC). It produced at least 10 NWS-documented tornadoes during this period (Lemon and Umscheid 2008), as well as numerous other vortices detected by UMass X-Pol that were not associated with surface damage tracks.
- Tornadoes 2 and 4 appear to have originated from the same mid-level circulation(s), although those circulations became broad and diffuse during the period between the two tornadoes. In addition, the remnant circulation of tornado 4 persisted at mid-levels at least 10 minutes beyond its "official" demise.
- The remnant circulation of tornado 3 appears to have been absorbed into tornado 5 (i.e., the Greensburg tornado).
- Tornadoes 7 (9) and 8 (10) were brief, concurrent cyclonic-anticyclonic pairs of satellite tornadoes of tornado 5, separated by a small mid-level jet pointing *into* the inflow region, away from tornado 5 and the main storm updraft. We speculate that these cyclonic-anticyclonic pairs of tornadoes resulted from upward arching of vortex lines (Markowski *et al.* 2008) over surges in the RFGF.
- It was found that tornadoes 1-4 exhibited motion to the *left* with respect to the updraft, while the Greensburg tornado (5) *paralleled* the updraft closely during its mature phase. In addition, the difference between the

horizontal motion of the tornadoes and the horizontal motion of the updraft diminished as the Greensburg tornado became more mature. I speculate that the updraft and tornado became "synchronized" in a configuration that allowed for the Greensburg tornado's unusual longevity and intensity, a finding consistent with previous studies of CTSs (Dowell and Bluestein 2002a). The updraft, in particular, exhibited at least three eastward "jumps" in its track (i.e., discontinuous propagation) as it produced tornadoes in mode I. The updraft of the Greensburg storm appears have slowed its eastward motion while tornado 3 was in progress, then jumped eastward after tornado 3 ended and before tornado 5 developed. Its motion towards the northeast steadied as the Greensburg tornado developed, and remained steady as the Greensburg tornado matured.

- Tornado 3 was the only tornado for which an accompanying RFGF was consistently detected throughout its life span. Interestingly, the RFGF surged forward with respect to tornado 3 until about halfway through the tornado's life cycle, retreated back as tornado 3 decayed, and then may have surged forward again as tornado 5 absorbed tornado 3.
- A WEC, likely resulting from centrifuging of hydrometeors and debris (Dowell *et al.* 2005), was found in tornadoes 4, 5, and 10. The position of the WEH in each sweep was compared to the location of the VS, and found, in the aggregate, to be collocated in azimuth but biased slightly away from the radar in range (by slightly less than one range gate).

- Z_{DR} measurements in the Greensburg storm consistently indicated the presence of oblate hydrometeors in the hook region during both mode I and mode II tornado production, as well as a relatively high Z_{DR} ring (i.e., raindrops) surrounding the WEH in the mature Greensburg tornado.
- The presence of strong low-level shear in the inflow region of the Greensburg storm is corroborated by the presence of a "Z_{DR} arc" at low-to-mid levels, along the inflow edge of the forward flank. However, this Z_{DR} arc was not consistently sampled until the Greensburg tornado was mature.
- Tornadoes 4, 5, and 10 all exhibited a low-Z_{DR}, low-$\tilde{\rho}_{hv}$ column in conjunction with their WECs, likely caused by centrifuging of hydrometeors. A 5 km wide, polarimetric "tornadic debris signature" (Kumjian and Ryzhkov 2008) was present in tornado 5 at 2 km AGL at 0230 UTC, when the tornado was mature and width of the damage track was around 2.5 km.

These results are only applicable for the case of the 5 May 2007 Greensburg storm, and are listed to provide possible starting points for future research. They should not be generalized beyond the context of this study.

7.2 EnKF experiments

In an attempt to diagnose the kinematic and thermodynamic processes the Greensburg storm during the mode I-to-mode II transition, the data from UMass X-Pol and KDDC were assimilated, via the EnKF technique, into the WRF NWP model using the DART radar data assimilation module (as in Aksoy *et al.* 2009). A highly

simplified, horizontally homogeneous initial environment was constructed, with horizontal grid spacing of 1 km and a stretched vertical grid, and data were assimilated every 2 min. Two sets of experiments were performed, one in which UMass X-Pol data were either assimilated or withheld, and in the other, the 0 to 3 km AGL wind profile was modified to reflect the onset of the LLJ. In all experiments, analysis cycles started at 0100 UTC and ended at 0300 UTC.

- The impacts of assimilating UMass X-Pol velocity data were more pronounced than the impacts of modifying the initial low-level wind profile. The additional information imparted by the UMass X-Pol data caused significant modifications to the analyzed updraft strength, vortex location and strength, and cold pool structure.
- Overall, the locations of the updraft of the Greensburg storm and low-level vortex corresponding to the Greensburg tornado matched the observations well, often to within a few km. In some ensemble members, UMass X-Pol data collected in much smaller tornadoes 1, 3, and 4 produced distinct vortices in the analyzed velocity fields; these vortices were absent when UMass X-Pol data were withheld.
- Likely as a consequence of the single-moment microphysical scheme used, the WRF model produced too large and expansive a cold pool in all cases. This simulated cold pool spread over the location of UMass X-Pol, resulting in near-surface northerly flow where UMass X-Pol measured southerly flow. As a result, the analyzed cold pool spread farther south when UMass X-Pol data were withheld rather than assimilated.

- Effects on observation-space diagnostics of adding UMass X-Pol data, however, were mixed. In all cases, slightly too much ensemble spread (RMSI > 3.0 m s^{-1}) was present, particularly at higher altitudes and toward the end of the analysis period (0300 UTC). I speculate that the initial wind profile, which was based on the 0000 UTC DDC sounding and continually replenished from the southern edge of the domain, became increasingly obsolete and increasingly conflicted with assimilated radar data toward the end of the assimilation cycles, resulting in higher RMSI values. In contrast, layer-averaged innovations were closer to zero at those times and altitudes when UMass X-Pol data (particularly "deep" volumes) were assimilated.
- Modifying the initial environmental wind profile to include a stronger LLJ led to slightly stronger near-surface vortices corresponding to the Greensburg tornado in the kddc_only experiments, but not in the kddc+umass experiments. I am dubious about the latter result because of the presence of a very cold RFD pulse that was not analyzed earlier versions of the same experiment. I believe that this cold RFD pulse may be a numerical artifact and that the analyzed vortex would have been stronger had it not been present.

I had originally intended to perform EnKF experiments at much higher horizontal grid spacing (500 m and 250 m) and with more frequent DA cycles, in order to exploit more fully the spatial and temporal resolution of the UMass X-Pol data, but was unable to complete those experiments owing to limited computational

resources. I may yet perform these experiments in the future, using the analyses to diagnose and forecast the motions of vortices, updrafts, and downdrafts, with the aim of better prediction of storms that may undergo tornado production mode I-to-mode II transition. One could envision using the model fields to diagnose vertical perturbation pressure gradients in the Greensburg storm and thereby assess and / or predict the motions of vortices, updrafts, and downdrafts (Rotunno and Klemp 1985; Klemp 1987; Davies-Jones 2002), looking for signs of the impending synchronous motion that seems to be characteristic of large tornadoes produced via mode II.

The radar data analyses and EnKF analyses discussed in this dissertation, which were only for a single case, took several years' work to produce. Currently, I do not see any feasible way to assimilate mobile Doppler radar data in a real time in an automated fashion into NWP models for short-range prediction of severe convective storms, chiefly because of the inconsistent conditions under which these data are collected (e.g., clutter patterns that change with every deployment). However, a large body of radar data were recently collected in both tornadic and non-tornadic supercells during Project VORTEX2 (Wurman *et al.* 2010). In addition, ongoing efforts to assimilate data from novel radar systems, such as polarimetric, phased-array, and / or short-range, stationary, X-band radars, are beginning to bear fruit (Jung *et al.* 2008; Brewster *et al.* 2010; Yussouf and Stensrud 2010). It is my hope that subsequent analysis and assimilation of these and other future data will furnish the first few stepping stones toward fuller exploitation of a greatly expanded and diversified collection of radar systems in a "Warn-on-Forecast"-style paradigm.

References

Adlerman, E. J., and K. K. Droegemeier, 2002: The sensitivity of numerically simulated cyclic mesocyclogenesis to variations in model physical and computational parameters. *Mon. Wea. Rev.*, **130,** 2671-2691.

——, 2005: The dependence of numerically simulated cyclic mesocyclogenesis upon environmental vertical wind shear. *Mon. Wea. Rev.*, **133,** 3595-3623.

Agee, E. M., J. T. Snow, and P. R. Clare, 1976: Multiple vortex features in the tornado cyclone and the occurrence of tornado families. *Mon. Wea. Rev.*, **104,** 552-563.

Aksoy, A., D. C. Dowell, and C. Snyder, 2009: A multicase comparative assessment of the ensemble Kalman filter for assimilation of radar observations. Part I: Storm-scale analyses. *Mon. Wea. Rev.*, **137,** 1805-1824.

Alberty, R. L., D. B. Burgess, and T. Fujita, 1980: Severe weather events of 10 April 1979. *Bull. Amer. Meteor. Soc.*, **61,** 1033-1034.

Alexander, C. R., and J. Wurman, 2005: The 30 May 1998 Spencer, South Dakota, storm. Part I: The structural evolution and environment of the tornadoes. *Mon. Wea. Rev.*, **133,** 72-97.

Anderson, J., T. Hoar, K. Raeder, H. Liu, N. Collins, R. Torn, and A. Avellano, 2009: The Data Assimilation Research Testbed: A community facility. *Bull. Amer. Meteor. Soc.*, **90,** 1283-1296.

Anderson, J. L., 2001: An ensemble adjustment Kalman filter for data assimilation. *Mon. Wea. Rev.*, **129,** 2884-2903.

——, 2005: Ensemble Filters for Geophysical Data Assimilation: A Tutorial. http://www.image.ucar.edu/DAReS/DART/tut1.pdf.

Anderson, J. L., and N. Collins, 2007: Scalable implementations of ensemble filter algorithms for data assimilation. *J. Atmos. Oceanic Technol.*, **24,** 1452-1463.

Arritt, R. W., T. D. Rink, M. Segal, D. P. Todey, C. A. Clark, M. J. Mitchell, and K. M. Labas, 1997: The Great Plains low-level jet during the warm season of 1993. *Mon. Wea. Rev.*, **125,** 2176-2192.

Bachmann, S., and D. Zrnić, 2007: Spectral density of polarimetric variables separating biological scatterers in the VAD display. *J. Atmos. Oceanic Technol.*, **24,** 1186-1198.

Banta, R. M., R. K. Newsom, J. K. Lundquist, Y. L. Pichugina, R. L. Coulter, and L. Mahrt, 2002: Nocturnal low-level jet characteristics over Kansas during CASES-99. *Bound.-Layer Meteor.*, **105,** 221-252.

Blackadar, A. K., 1957: Boundary layer wind maxima and their significance for the growth of nocturnal inversions. *Bull. Amer. Meteor. Soc.*, **38,** 283-290.

Bluestein, H. B., 1993: *Synoptic-Dynamic Meteorology in Midlatitudes. Volume II: Observations and Theory of Weather Systems.* Vol. 2, Oxford University Press, 594 pp.

——, 2007: Advances in applications of the physics of fluids to severe weather systems. *Reports on Progress in Physics*, **70,** 1259-1323.

——, 2009: The formation and early evolution of the Greensburg, Kansas, tornadic supercell on 4 May 2007. *Wea. Forecasting*, **24,** 899-920.

Bluestein, H. B., and W. P. Unruh, 1989: Observations of the wind field in tornadoes, funnel clouds, and wall clouds with a portable Doppler radar. *Bull. Amer. Meteor. Soc.*, **70,** 1514-1525.

Bluestein, H. B., and A. L. Pazmany, 2000: Observations of tornadoes and other convective phenomena with a mobile, 3–mm wavelength, Doppler radar: The spring 1999 field experiment. *Bull. Amer. Meteor. Soc.*, **81,** 2939-2951.

Bluestein, H. B., and R. M. Wakimoto, 2003: Mobile Radar Observations of Severe Convective Storms. *Meteor. Monogr.*, Vol. 30, American Meteorological Society, 105 pp.

Bluestein, H. B., M. M. French, I. PopStefanija, R. T. Bluth, and J. B. Knorr, 2010: A mobile, phased-array Doppler radar for the study of severe convective storms. *Bull. Amer. Meteor. Soc.*, **91,** 579-600.

Bluestein, H. B., M. M. French, R. L. Tanamachi, S. Frasier, K. Hardwick, F. Junyent, and A. L. Pazmany, 2007a: Close-range observations of tornadoes in supercells made with a dual-polarization, X-band, mobile Doppler radar. *Mon. Wea. Rev.*, **135,** 1522-1543.

Bluestein, H. B., C. C. Weiss, M. M. French, E. M. Holthaus, R. L. Tanamachi, S. Frasier, and A. L. Pazmany, 2007b: The structure of tornadoes near Attica, Kansas, on 12 May 2004: High-resolution, mobile, Doppler radar observations. *Mon. Wea. Rev.*, **135,** 475-506.

Bluestein, H. B., and Coauthors, 2007c: Preliminary results from the fielding of a disparate triad of mobile Doppler radars to study severe convective storms. *33rd International Conference on Radar Meteorology*, Cairns, Australia, American Meteorological Society, 13A.12.

Bonner, W. D., 1966: Case study of thunderstorm activity in relation to the low-level jet. *Mon. Wea. Rev.*, **94,** 167-178.

——, 1968: Climatology of the low level jet. *Mon. Wea. Rev.*, **96,** 833-850.

Bouttier, F., and P. Courtier, 1999: Data assimilation concepts and methods. *Meteorological Training Course Lecture Series*, ECMWF, http://www.ecmwf.int/newsevents/training/rcourse_notes/pdf_files/Assim_concepts.pdf.

Brewster, K., K. W. Thomas, J. Gao, J. Brotzge, M. Xue, and Y. Wang, 2010: A nowcasting system using full physics numerical weather prediction initialized with CASA and NEXRAD radar data. *25th Conference on Severe Local Storms*, Denver, Colorado, American Meteorological Society, 9.4.

Bringi, V. N., and V. Chandrasekar, 2001: *Polarimetric Doppler Weather Radar: Principles and Applications.* Cambridge University Press, 636 pp.

Brotzge, J., and Coauthors, 2004: Distributed collaborative adaptive sensing for hazardous weather detection, tracking, and predicting. *Computational Science - ICCS 2004*, Vol. 3038, M. Bubak, G. D. v. Albada, P. M. A. Sloot, and J. J. Dongarra, Eds., Springer Berlin / Heidelberg, 670-677.

Brown, R. A., and V. T. Wood, 2007: *A Guide for Interpreting Doppler Velocity Patterns: Northern Hemisphere Edition.* 2 ed. National Severe Storms Laboratory, 61 pp.

Browning, K. A., and R. J. Donaldson, 1963: Airflow and structure of a tornadic storm. *J. Atmos. Sci.*, **20,** 533-545.

Browning, K. A., and R. Wexler, 1968: The determination of kinematic properties of a wind field using Doppler radar. *J. Appl. Meteor.*, **7,** 105-113.

Buajitti, K., and A. K. Blackadar, 1957: Theoretical studies of diurnal wind-structure variations in the planetary boundary layer. *Quart. J. Roy. Meteor. Soc.*, **83,** 486-500.

Burgess, D. B., V. T. Wood, and R. A. Brown, 1982: Mesocyclone evolution statistics. *12th Conference on Severe Local Storms*, San Antonio, Texas, American Meteorological Society, 422–424.

Burgess, D. W., M. A. Magsig, J. Wurman, D. C. Dowell, and Y. Richardson, 2002: Radar observations of the 3 May 1999 Oklahoma City tornado. *Wea. Forecasting*, **17,** 456-471.

Caya, A., J. Sun, and C. Snyder, 2005: A comparison between the 4DVAR and the ensemble Kalman filter techniques for radar data assimilation. *Mon. Wea. Rev.*, **133,** 3081-3094.

Chen, T.-C., and J. A. Kpaeyeh, 1993: The synoptic-scale environment associated with the low-level jet of the Great Plains. *Mon. Wea. Rev.*, **121,** 416-420.

Cohn, S. E., 1997: An introduction to estimation theory. *J. Meteor. Soc. Japan*, **75,** 257-288.

Cressman, G. P., 1959: An operational objective analysis system. *Mon. Wea. Rev.*, **87,** 367–374.

Crum, T. D., and R. L. Alberty, 1993: The WSR-88D and the WSR-88D Operational Support Facility. *Bull. Amer. Meteor. Soc.*, **74,** 1669-1687.

Crum, T. D., R. E. Saffle, and J. W. Wilson, 1998: An update on the NEXRAD program and future WSR-88D support to operations. *Wea. Forecasting*, **13,** 253-262.

Daniel, C. J., R. W. Arritt, and C. J. Anderson, 1999: Accuracy of 404-MHz radar profilers for detection of low-level jets over the central United States. *J. Appl. Meteor.*, **38,** 1391-1396.

Darkow, G. L., and J. C. Roos, 1970: Multiple tornado producing thunderstorms and their apparent cyclic variations in intensity. *14th Conference on Radar Meteorology*, Tuscon, Arizona, American Meteorological Society, 305-309.

Davies-Jones, R., 1986: Tornado Dynamics. *Thunderstorm Morphology and Dynamics*, 2 ed., E. Kessler, Ed., University of Oklahoma Press, 197-236.

——, 2002: Linear and nonlinear propagation of supercell storms. *J. Atmos. Sci.*, **59,** 3178-3205.

Davies-Jones, R., R. J. Trapp, and H. B. Bluestein, 2002: Tornadoes and Tornadic Storms. *Severe Convective Storms*, Vol. 28, C. A. Doswell, Ed., American Meteorological Society, 167-222.

Dawson, D. T., M. Xue, J. A. Milbrandt, and M. K. Yau, 2010: Comparison of evaporation and cold pool development between single-moment and multimoment bulk microphysics schemes in idealized simulations of tornadic thunderstorms. *Mon. Wea. Rev.*, **138,** 1152-1171.

Dawson, D. T., L. J. Wicker, E. R. Mansell, and R. L. Tanamachi, 2011: Impact of the environmental low-level wind profile on ensemble forecasts of the 5 May 2007 Greensburg, Kansas tornadic storm and associated mesocyclones. *Mon. Wea. Rev.***,** conditionally accepted.

Doviak, R. J., and D. S. Zrnić, 1993: *Doppler Weather Radar and Observations.* 2 ed. Academic Press, 562 pp.

Doviak, R. J., V. Bringi, A. Ryzhkov, A. Zahrai, and D. Zrnić, 2000: Considerations for polarimetric upgrades to operational WSR-88D radars. *J. Atmos. Oceanic Technol.*, **17,** 257-278.

Dowell, D. C., and H. B. Bluestein, 2002a: The 8 June 1995 McLean, Texas, storm. Part II: Cyclic tornado formation, maintenance, and dissipation. *Mon. Wea. Rev.*, **130,** 2649-2670.

——, 2002b: The 8 June 1995 McLean, Texas, storm. Part I: Observations of cyclic tornadogenesis. *Mon. Wea. Rev.*, **130,** 2626-2648.

Dowell, D. C., and L. J. Wicker, 2009: Additive noise for storm-scale ensemble data assimilation. *J. Atmos. Oceanic Technol.*, **26,** 911-927.

Dowell, D. C., L. J. Wicker, and C. Snyder, 2010: Ensemble Kalman filter assimilation of radar observations of the 8 May 2003 Oklahoma City supercell: Influences of reflectivity observations on storm-scale analyses. *Mon. Wea. Rev.***,** accepted.

Dowell, D. C., C. R. Alexander, J. M. Wurman, and L. J. Wicker, 2005: Centrifuging of hydrometeors and debris in tornadoes: Radar-reflectivity patterns and wind-measurement errors. *Mon. Wea. Rev.*, **133,** 1501-1524.

Dowell, D. C., F. Zhang, L. J. Wicker, C. Snyder, and N. A. Crook, 2004: Wind and temperature retrievals in the 17 May 1981 Arcadia, Oklahoma, supercell: Ensemble Kalman filter experiments. *Mon. Wea. Rev.*, **132,** 1982-2005.

Eliassen, A., 1954: Provisional report on calculation of spatial covariance and autocorrelation of the pressure field. *Dynamic Meteorology: Data*

Assimilation Methods, L. Bengtsson, M. Ghil, and E. Källen, Eds., Spinger-Verlag, 319-330.

Errico, R. M., 1997: What is an adjoint model? *Bull. Amer. Meteor. Soc.*, **78,** 2577-2591.

Esterheld, J. M., and D. J. Giuliano, 2008: Discriminating between tornadic and non-tornadic supercells: A new hodograph technique. *E-J. Severe Storms Meteor.*, **3,** 1-50.

Evensen, G., 1994: Sequential data assimilation with a nonlinear quasi-geostrophic model using Monte Carlo methods to forecast error statistics. *J. Geophys. Res.*, **99,** 10143–10162.

——, 2003: The Ensemble Kalman Filter: theoretical formulation and practical implementation. *Ocean Dynamics*, **53,** 343-367.

——, 2007: *Data Assimilation: The Ensemble Kalman Filter.* Springer-Verlag, 279 pp.

French, M. M., 2006: The 15 May 2003 Shamrock, Texas, supercell : A dual-Doppler analysis and EnKF data assimilation experiment. M.S. Thesis, School of Meteorology, University of Oklahoma, 145 pp.

French, M. M., H. B. Bluestein, L. J. Wicker, D. C. Dowell, and M. R. Kramar, 2009: An example of the use of mobile, Doppler radar data for tornado verification. *Wea. Forecasting*, **24,** 884-891.

French, M. M., H. B. Bluestein, D. C. Dowell, L. J. Wicker, M. R. Kramar, and A. L. Pazmany, 2006: The 15 May 2003 Shamrock, Texas, supercell: A dual-Doppler analysis and EnKF data-assimilation experiment. *23rd Conference on*

Severe Local Storms, St. Louis, Missouri, American Meteorological Society, 14.16A.

——, 2008: High-resolution, mobile Doppler radar observations of cyclic mesocyclogenesis in a supercell. *Mon. Wea. Rev.*, **136,** 4997-5016.

Fujita, T., 1960: A Detailed Analysis of the Fargo Tornadoes of June 20, 1957. Research Paper No. 42, U.S. Weather Bureau, Washington, D.C., 67 pp.

——, 1963: Analytical Mesometeorology: A Review. *Meteor. Monogr.*, Vol. 5, American Meteorological Society, 77-125.

Fujita, T. T., 1981: Tornadoes and downbursts in the context of generalized planetary scales. *J. Atmos. Sci.*, **38,** 1511-1534.

Fujita, T. T., D. L. Bradbury, and C. F. V. Thullenar, 1970: Palm Sunday tornadoes of April 11, 1965. *Mon. Wea. Rev.*, **98,** 29-69.

Gandin, L. S., 1965: *Objective Analysis of Meteorological Fields.* Israel Program for Scientific Translations, 242 pp.

Gao, J., D. J. Stensrud, and M. Xue, 2008: Importance of environmental variability to storm-scale radar data assimilation. *24th Conference on Severe Local Storms*, Savannah, Georgia, American Meteorological Society, 9B.2.

Gao, J., M. Xue, and D. J. Stensrud, 2010: The development of a hybrid 3DVAR-EnKF algorithm for storm-scale data assimilation. *25th Conference on Severe Local Storms*, Denver, Colorado, American Meteorological Society, P7.4.

Gasteren, H. V., I. Holleman, W. Bouten, E. V. Loon, and J. Shamoun-Baranes, 2008: Extracting bird migration information from C-band Doppler weather radars. *Ibis*, **150,** 674-686.

Gaudet, B. J., and W. R. Cotton, 2006: Low-level mesocyclonic concentration by nonaxisymmetric transport. Part I: Supercell and mesocyclone evolution. *J. Atmos. Sci.*, **63,** 1113-1133.

Gaudet, B. J., W. R. Cotton, and M. T. Montgomery, 2006: Low-level mesocyclonic concentration by nonaxisymmetric transport. Part II: Vorticity dynamics. *J. Atmos. Sci.*, **63,** 1134-1150.

Gauthreaux, S. A., J. W. Livingston, and C. G. Belser, 2008: Detection and discrimination of fauna in the aerosphere using Doppler weather surveillance radar. *Int. Comp. Bio.*, **48,** 12-23.

Gilmore, M. S., J. M. Straka, and E. N. Rasmussen, 2004: Precipitation and evolution sensitivity in simulated deep convective storms: Comparisons between liquid-only and simple ice and liquid phase microphysics. *Mon. Wea. Rev.*, **132,** 1897-1916.

Glickman, T. S., 2000: *Glossary of Meteorology.* 2nd ed. American Meteorological Society, 855 pp.

Godfrey, E. S., M. Tong, M. Xue, and K. K. Droegemeier, 2005: Assimilation of simulated CASA radar data and prediction of varied convective storm types using an ensemble square-root Kalman Filter. *32nd Conference on Radar Meteorology*, Albuquerque, New Mexico, American Meteorological Society, JP1J.16.

Grazulis, T. P., 1993: *Significant Tornadoes: 1680 - 1991.* Environmental Films, 1326 pp.

Gunn, K. L. S., and J. S. Marshall, 1958: The distribution with size of aggregate snowflakes. *J. Meteor.*, **15,** 452-461.

Hamill, T. M., 2000: An overview of ensemble forecasting. American Meteorological Society, 6.1.

Hane, C. E., C. L. Ziegler, and H. B. Bluestein, 1993: Investigation of the dryline and convective storms initiated along the dryline: Field experiments during COPS–91. *Bull. Amer. Meteor. Soc.*, **74,** 2133-2145.

Holleman, I., H. van Gasteren, and W. Bouten, 2008: Quality assessment of weather radar wind profiles during bird migration. *J. Atmos. Oceanic Technol.*, **25,** 2188-2198.

Houtekamer, P. L., and H. L. Mitchell, 1998: Data assimilation using an ensemble Kalman filter technique. *Mon. Wea. Rev.*, **126,** 796-811.

——, 2005: Ensemble Kalman filtering. *Quart. J. Roy. Meteor. Soc.*, **131,** 3269-3289.

Hoxit, L., 1975: Diurnal variations in planetary boundary-layer winds over land. *Bound.-Layer Meteor.*, **8,** 21-38.

Hunt, B. R., and Coauthors, 2004: Four-dimensional ensemble Kalman filtering. *Tellus*, **56A,** 273 - 277.

Jung, Y., M. Xue, G. Zhang, and J. M. Straka, 2008: Assimilation of simulated polarimetric radar data for a convective storm using the ensemble Kalman filter. Part II: Impact of polarimetric data on storm analysis. *Mon. Wea. Rev.*, **136,** 2246-2260.

Junyent, F., S. Frasier, D. J. McLaughlin, V. Chandrasekar, H. Bluestein, and M. French, 2005: High resolution dual-polarization radar observation of tornados:

implications for radar development and tornado detection. *Geoscience and Remote Sensing Symposium, 2005. IGARSS '05. Proceedings. 2005 IEEE International*, 2034-2037.

Juyent, F., 2003: Design, development and initial field deployment of an X band polarimetric, Doppler radar. M.S.E.E. thesis, Department of Electrical and Computer Engineering, University of Massachusetts - Amherst, 121 pp.

Kalman, R. E., 1960: A new approach to linear filtering and prediction problems. *Transactions of the American Society of Mechanical Engineering - Journal of Basic Engineering*, **82D,** 35-45.

Kalnay, E., 2003: *Atmospheric Modeling, Data Assimilation, and Predictability.* Cambridge University Press, 341 pp.

Klemp, J. B., 1987: Dynamics of tornadic storms. *Ann. Rev. Fluid Mech.*, **19,** 369-402.

Kramar, M. R., H. B. Bluestein, A. L. Pazmany, and J. D. Tuttle, 2005: The "owl horn" radar signature in developing southern Plains supercells. *Mon. Wea. Rev.*, **133,** 2608-2634.

Kumjian, M. R., and A. V. Ryzhkov, 2008: Polarimetric signatures in supercell thunderstorms. *J. Climate Appl. Meteor.*, **47,** 1940-1961.

——, 2009: Storm-relative helicity revealed from polarimetric radar measurements. *J. Atmos. Sci.*, **66,** 667-685.

LaDue, J. G., and E. A. Mahoney, 2006: Implementing the new Enhanced Fujita scale within the NWS. *23rd Conference on Severe Local Storms*, St. Louis, Missouri, American Meteorological Society, 5.5.

Lemon, L. R., and C. A. Doswell, 1979: Severe thunderstorm evolution and mesocyclone structure as related to tornadogenesis. *Mon. Wea. Rev.*, **107,** 1184-1197.

Lemon, L. R., and M. Umscheid, 2008: The Greensburg, KS tornadic storm: a storm of extremes. *24th Conference on Severe Local Storms*, Savannah, Georgia, American Meteorological Society, 2.4.

Lewis, J. M., S. Lakshmivarahan, and S. K. Dhall, 2006: *Dynamic Data Assimilation: A Least Squares Approach.* Vol. 104, Cambridge University Press.

Lin, Y.-L., R. D. Farley, and H. D. Orville, 1983: Bulk parameterization of the snow field in a cloud model. *J. Appl. Meteor.*, **22,** 1065-1092.

Lorenc, A. C., 1986: Analysis methods for numerical weather prediction. *Quart. J. Roy. Meteor. Soc.*, **112,** 1177-1194.

Lorenz, E. N., 1993: *The Essence of Chaos.* University of Washington Press, 227 pp.

MacGorman, D. R., and Coauthors, 2008: TELEX: The Thunderstorm Electrification and Lightning Experiment. *Bull. Amer. Meteor. Soc.*, **89,** 997-1013.

Maddox, R. A., 1993: Diurnal low-level wind oscillation and storm-relative helicity. *The Tornado: Its Structure, Dynamics, Prediction, and Hazards*, C. R. Church, D. B. Burgess, C. A. Doswell Iii, and R. Davies-Jones, Eds., American Geophysical Union, 591 - 598.

Maddox, R. A., and C. A. Doswell, 1982: An examination of jet stream configurations, 500 mb vorticity advection and low-level thermal advection patterns during extended periods of intense convection. *Mon. Wea. Rev.*, **110,** 184-197.

Majcen, M., P. Markowski, Y. Richardson, D. Dowell, and J. Wurman, 2008: Multipass objective analyses of Doppler radar data. *J. Atmos. Oceanic Technol.*, **25,** 1845-1858.

Markowski, P., and Y. Richardson, 2010: *Mesoscale Meteorology in Midlatitudes.* Wiley-Blackwell, 407 pp.

Markowski, P., E. Rasmussen, J. Straka, R. Davies-Jones, Y. Richardson, and R. J. Trapp, 2008: Vortex lines within low-level mesocyclones obtained from pseudo-dual-Doppler radar observations. *Mon. Wea. Rev.*, **136,** 3513-3535.

Markowski, P. M., 2002: Hook echoes and rear-flank downdrafts: A review. *Mon. Wea. Rev.*, **130,** 852-876.

Marquis, J., Y. Richardson, J. Wurman, P. Markowski, and D. C. Dowell, 2008: Mobile radar observations of tornadic supercells with multiple rear-flank gust fronts. *24th Conference on Severe Local Storms*, Savannah, Georgia, American Meteorological Society, 19.13.

Marshall, T. P., D. McCarthy, J. G. LaDue, J. Wurman, C. Alexander, P. Robinson, and K. Kosiba, 2008: Damage survey and deduction of vortex structure of the Greensburg, KS tornado. *24th Conference on Severe Local Storms*, Savannah, Georgia, American Meteorological Society, 8B.3.

Martin, W. J., and A. Shapiro, 2007: Discrimination of bird and insect radar echoes in clear air using high-resolution radars. *J. Atmos. Oceanic Technol.*, **24,** 1215-1230.

McCarthy, D., L. Ruthi, and J. Hutton, 2007: The Greensburg, KS tornado. *22nd Conference on Weather Analysis and Forecasting*, Park City, Utah, American Meteorological Society, J2.4.

Means, L. L., 1944: The nocturnal maximum occurrence of thunderstorms in the midwestern states. Misc. Report No. 16, Cloud Physics Laboratory, The University of Chicago, 38 pp.

——, 1952: On thunderstorm forecasting in the central United States. *Mon. Wea. Rev.*, **80,** 165-189.

NCDC, 2007: Storm Events Database. http://www4.ncdc.noaa.gov/cgi-win/wwcgi.dll?wwEvent~Storms, retrieved on 12 January 2009.

Oye, R., C. Mueller, and S. Smith, 1995: Software for radar translation, visualization, editing, and interpolation. *27th Conf. on Radar Meteorology*, Vail, Colorado, American Meteorological Society, 359 - 361.

Park, H. S., A. V. Ryzhkov, D. S. Zrnić, and K.-E. Kim, 2009: The hydrometeor classification algorithm for the polarimetric WSR-88D: Description and application to an MCS. *Wea. Forecasting*, **24,** 730-748.

Pekour, M. S., and R. L. Coulter, 1999: A technique for removing the effect of migrating birds in 915-MHz wind profiler data. *J. Atmos. Oceanic Technol.*, **16,** 1941-1948.

Pitchford, K. L., and J. London, 1962: The low-level jet as related to nocturnal thunderstorms over Midwest United States. *J. Appl. Meteor.*, **1,** 43-47.

Ralph, F. M., P. J. Neiman, D. W. van de Kamp, and D. C. Law, 1995: Using spectral moment data from NOAA's 404-MHz radar wind profilers to observe precipitation. *Bull. Amer. Meteor. Soc.*, **76,** 1717-1739.

Raymond, D. J., 1978: Instability of the low-level jet and severe storm formation. *J. Atmos. Sci.*, **35,** 2274-2280.

Research, F. C. f. M. S. a. S., 2008: Federal Meteorological Handbook No. 11, Part A: System Concepts, Responsibilities, and Procedures, Office of the Federal Coordinator for Meteorological Services and Supporting Research. U.S. Department of Commerce, 53 pp.

Rinehart, R. E., 1997: *Radar for Meteorologists.* 3 ed. Rinehart Publications, 428 pp.

Romine, G. S., D. W. Burgess, and R. B. Wilhelmson, 2008: A dual-polarization-radar-based assessment of the 8 May 2003 Oklahoma City area tornadic supercell. *Mon. Wea. Rev.*, **136,** 2849-2870.

Rotunno, R., and J. Klemp, 1985: On the rotation and propagation of simulated supercell thunderstorms. *J. Atmos. Sci.*, **42,** 271-292.

Ryzhkov, A. V., T. J. Schuur, D. W. Burgess, and D. S. Zrnic, 2005: Polarimetric tornado detection. *J. Appl. Meteor.*, **44,** 557-570.

Schenkman, A. D., M. Xue, A. Shapiro, K. Brewster, and J. Gao, 2011: The analysis and prediction of the 8–9 May 2007 Oklahoma tornadic mesoscale convective system by assimilating WSR-88D and CASA radar data using 3DVAR. *Mon. Wea. Rev.*, **139,** 224-246.

Schmaljohann, H., F. Liechti, E. BÄChler, T. Steuri, and B. Bruderer, 2008: Quantification of bird migration by radar – a detection probability problem. *Ibis*, **150,** 342-355.

Shapiro, A., and E. Fedorovich, 2009: Nocturnal low-level jet over a shallow slope. *Acta Geophysica*, **57,** 950-980.

——, 2010: Analytical description of a nocturnal low-level jet. *Quart. J. Roy. Meteor. Soc.*, **136,** 1255-1262.

Simmons, K. M., and D. Sutter, 2005: WSR-88D radar, tornado warnings, and tornado casualties. *Wea. Forecasting*, **20,** 301-310.

Skamarock, W. C., and Coauthors, 2008: A description of the Advanced Research WRF Version 3. 113 pp.

Smith, P. L., 1984: Equivalent radar reflectivity factors for snow and ice particles. *J. Climate Appl. Meteor.*, **23,** 1258-1260.

Smith, P. L., C. G. Myers, and H. D. Orville, 1975: Radar reflectivity factor calculations in numerical cloud models using bulk parameterization of precipitation. *J. Appl. Meteor.*, **14,** 1156-1165.

Snook, N. A., and M. Xue, 2008: Effects of microphysical drop size distribution on tornadogenesis in supercell thunderstorms. *Geophys. Res. Lett.*, **35,** L28403.

Snook, N. A., M. Xue, and Y. Jung, 2011: Analysis of a tornadic meoscale convective vortex assimilating CASA X-band and WSR-88D radar data using an ensemble Kalman filter. *Mon. Wea. Rev.***,** accepted.

Snyder, C., and F. Zhang, 2003: Assimilation of simulated Doppler radar observations with an ensemble Kalman filter. *Mon. Wea. Rev.*, **131,** 1663-1677.

Snyder, J. C., H. B. Bluestein, G. Zhang, and S. J. Frasier, 2010: Attenuation correction and hydrometeor classification of high-resolution, X-band, dual-polarized mobile radar measurements in severe convective storms. *J. Atmos. Oceanic Technol.*, **27,** 1979-2001.

Speheger, D. A., C. A. Doswell, and G. J. Stumpf, 2002: The tornadoes of 3 May 1999: Event verification in central Oklahoma and related issues. *Wea. Forecasting*, **17,** 362-381.

Stensrud, D. J., 1996: Importance of low-level jets to climate: A review. *J. Climate*, **9,** 1698-1711.

——, 2007: *Parameterization Schemes: Keys to Understanding Numerical Weather Prediction Models.* Cambridge University Press, 478 pp.

Stensrud, D. J., and J. Gao, 2010: Importance of horizontally inhomogeneous environmental initial conditions to ensemble storm-scale radar data assimilation and very short-range forecasts. *Mon. Wea. Rev.*, **138,** 1250-1272.

Stensrud, D. J., M. H. Jain, K. W. Howard, and R. A. Maddox, 1990: Operational systems for observing the lower atmosphere: Importance of data sampling and archival procedures. *J. Atmos. Oceanic Technol.*, **7,** 930-937.

Stensrud, D. J., and Coauthors, 2010: Convective-scale Warn-on-Forecast: The Severe Weather Forecast Improvements Project Plan. Norman, Oklahoma, National Severe Storms Laboratory, 23 pp., available from

http://www.nssl.noaa.gov/projects/wof/documents/WoF_Project_Plan_2010.pdf.

Stull, R. B., 1988: *An Introduction to Boundary Layer Meteorology.* Kluwer Academic Publishers, 670 pp.

Sullivan, R. D., 1959: A two-cell vortex solution of the Navier-Stokes equations. *J. Aerospace Sci.*, **26,** 767–768.

Sun, W.-Y., and Y. Ogura, 1979: Boundary-layer forcing as a possible trigger to a squall-line formation. *J. Atmos. Sci.*, **36,** 235-254.

Talagrand, O., 1997: Assimilation of observations: An introduction. *J. Meteor. Soc. Japan*, **75,** 191-209.

Talagrand, O., and P. Courtier, 1987: Variational assimilation of meteorological observations with the adjoint vorticity equation. I: Theory. *Quart. J. Roy. Meteor. Soc.*, **113,** 1311-1328.

Tanamachi, R. L., H. B. Bluestein, W.-C. Lee, M. Bell, and A. Pazmany, 2007: Ground-Based Velocity Track Display (GBVTD) analysis of W-Band Doppler radar data in a tornado near Stockton, Kansas, on 15 May 1999. *Mon. Wea. Rev.*, **135,** 783-800.

Tippett, M. K., J. L. Anderson, C. H. Bishop, T. M. Hamill, and J. S. Whitaker, 2003: Ensemble square root filters. *Mon. Wea. Rev.*, **131,** 1485-1490.

Tong, M., 2006: Ensemble Kalman Filter Assimilation of Doppler Radar Data for the Initialization and Prediction of Convective Storms. Ph.D. dissertation, School of Meteorology, University of Oklahoma, 264 pp.

Tong, M., and M. Xue, 2005: Ensemble Kalman filter assimilation of Doppler radar data with a compressible nonhydrostatic model: OSS experiments. *Mon. Wea. Rev.*, **133,** 1789-1807.

Trapp, R. J., 2000: A clarification of vortex breakdown and tornadogenesis. *Mon. Wea. Rev.*, **128,** 888-895.

Trapp, R. J., and C. A. Doswell, 2000: Radar data objective analysis. *J. Atmos. Oceanic Technol.*, **17,** 105-120.

Uccellini, L. W., 1980: On the role of upper tropospheric jet streaks and leeside cyclogenesis in the development of low-level jets in the Great Plains. *Mon. Wea. Rev.*, **108,** 1689-1696.

Uccellini, L. W., and D. R. Johnson, 1979: The coupling of upper and lower tropospheric jet dtreaks and implications for the development of severe convective storms. *Mon. Wea. Rev.*, **107,** 682-703.

Van Den Broeke, M. S., J. M. Straka, and E. N. Rasmussen, 2008: Polarimetric radar observations at low levels during tornado life cycles in a small sample of classic Southern Plains supercells. *J. Climate Appl. Meteor.*, **47,** 1232-1247.

Wakimoto, R. M., W.-C. Lee, H. B. Bluestein, C.-H. Liu, and P. H. Hildebrand, 1996: ELDORA observations during VORTEX 95. *Bull. Amer. Meteor. Soc.*, **77,** 1465-1481.

Walters, C. K., 2001: Airflow configurations of warm season southerly low-level wind maxima in the Great Plains. Part II: The synoptic and subsynoptic-scale environment. *Wea. Forecasting*, **16,** 531-551.

Walters, C. K., and J. A. Winkler, 2001: Airflow configurations of warm season southerly low-level wind maxima in the Great Plains. Part I: Spatial and temporal characteristics and relationship to convection. *Wea. Forecasting*, **16,** 513-530.

Weisman, M. L., J. B. Klemp, and J. W. Wilson, 1983: Dynamic interpretation of notches, WERs, and mesocyclones simulated in a numerical cloud model. *21st Conf. on Radar Meteorology*, Edmonton, Alberta, Canada, American Meteorological Society, 39 - 43.

Whitaker, J. S., and T. M. Hamill, 2002: Ensemble data assimilation without perturbed observations. *Mon. Wea. Rev.*, **130,** 1913-1924.

Whiteman, C. D., X. Bian, and S. Zhong, 1997: Low-level jet climatology from enhanced rawinsonde observations at a site in the Southern Great Plains. *J. Appl. Meteor.*, **36,** 1363-1376.

Wicker, L. J., and W. C. Skamarock, 2002: Time-splitting methods for elastic models using forward time schemes. *Mon. Wea. Rev.*, **130,** 2088-2097.

Wilczak, J. M., and Coauthors, 1995: Contamination of wind profiler data by migrating birds: Characteristics of corrupted data and potential solutions. *J. Atmos. Oceanic Technol.*, **12,** 449-467.

Wu, Y., and S. Raman, 1998: The summertime Great Plains low level jet and the effect of its origin on moisture transport. *Bound.-Layer Meteor.*, **88,** 445-466.

Wurman, J., and S. Gill, 2000: Finescale radar observations of the Dimmitt, Texas (2 June 1995), tornado. *Mon. Wea. Rev.*, **128,** 2135-2164.

Wurman, J., Y. Richardson, C. Alexander, S. Weygandt, and P. F. Zhang, 2007: Dual-Doppler and single-Doppler analysis of a tornadic storm undergoing mergers and repeated tornadogenesis. *Mon. Wea. Rev.*, **135,** 736-758.

Wurman, J., and Coauthors, 2010: An overview of the VORTEX2 field campaign. *25th Conference on Severe Local Storms*, Denver, CO, American Meteorological Society, 5.1.

Xue, M., M. Tong, and K. K. Droegemeier, 2006: An OSSE framework based on the ensemble square root Kalman filter for evaluating the impact of data from radar networks on thunderstorm analysis and forecasting. *J. Atmos. Oceanic Technol.*, **23,** 46-66.

Yussouf, N., and D. J. Stensrud, 2010: Impact of phased-array radar observations over a short assimilation period: Observing system simulation experiments using an ensemble Kalman filter. *Mon. Wea. Rev.*, **138,** 517-538.

Appendix A. Geographic information

Table 6. Latitudes, longitudes, and altitudes of some locations relevant to this study.

Location	Latitude	Longitude	Altitude (ASL)
Dodge City, Kansas WSR-88D site (KDDC)	37.760 °N	99.968 °W	809 m
Dodge City, Kansas (town)	37.759 °N	100.019 °W	777 m
Greensburg, Kansas (town)	37.602 °N	99.292 °W	681 m
Pratt, Kansas ASOS site (KPTT)	37.703 °N	99.747 °W	651 m
Protection, Kansas (town)	37.201 °N	99.483 °W	564 m
UMass X-Pol radar deployment site	37.193 °N	99.436 °W	564 m

Appendix B. Additional observations not used in this study

B.1 Haviland, Kansas wind profiler

The Haviland, Kansas 404 MHz NOAA Profiler Network (NPN; Ralph *et al.* 1995, see also http://www.profiler.noaa.gov) station (HVLK1) is located at Haviland, Kansas, approximately 16 km east-northeast of Greensburg, Kansas, at an altitude of 648 m ASL. The profiler consists of a coaxial-collinear antenna that generates three nearly-vertically-pointing radar beams. The profiler collects data in two altitude bins, known as "low" (0.5 – 9.25 km AGL) and "high" (7.5 – 16.25 km AGL), and reports wind speed and direction in 500 m increments, starting from 500 m AGL. Wind profiles recorded every 6 min are available in graphical format (Fig. 68). Hourly profiles are available as rawinsonde observation (RAOB)-formatted text (plotted Fig. 69). Try though I might, I was unable to obtain these RAOB-formatted text files at more frequent intervals, even though 6 min profiles are available in graphical format.

These HVLK1 data collected on 5 May 2007 were of very limited use in this study. First, many wind data were not reported after 0100 UTC, evidenced by large gaps in data coverage on Fig. 68. These data did not pass continuity requirements in the NPN quality control protocol, possibly due to contamination of velocities by falling precipitation particles (Fig. 70), and cannot be retrieved. Second, data collected between 500 and 1500 m AGL from 0200 to 0220 UTC (when the Greensburg tornado was ongoing 25-30 km to the southwest) were flagged by the NPN automated quality control algorithm as bird-contaminated (Fig. 68).

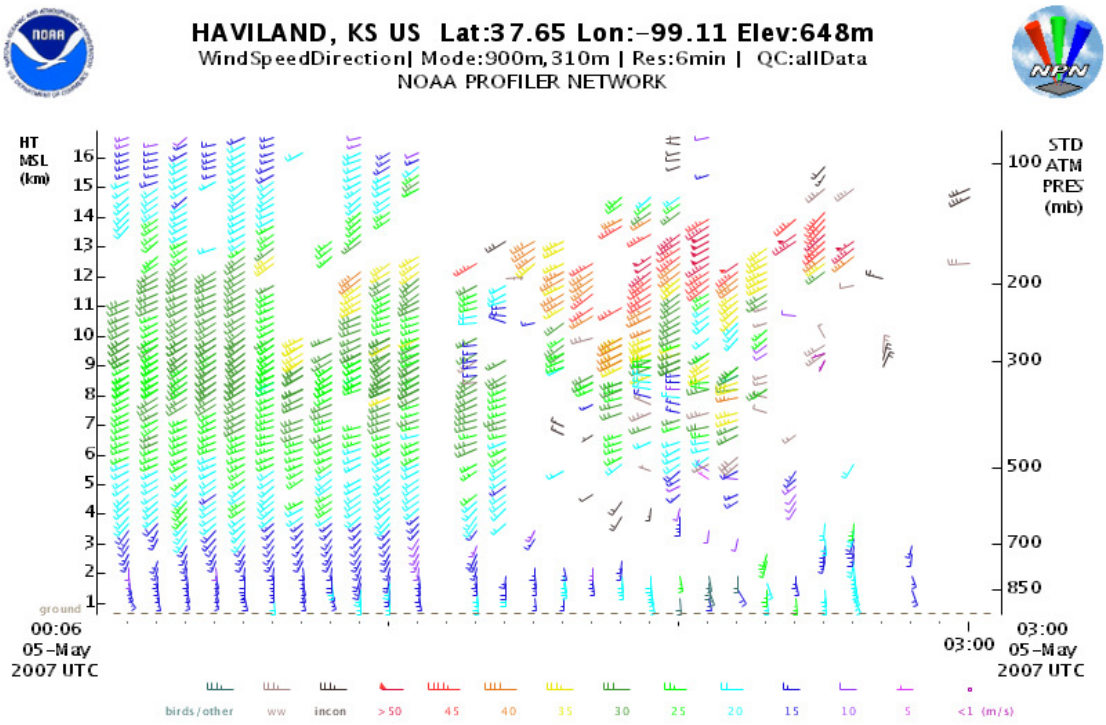


Fig. 68. 6-minute wind profiles from the HVLK1, from 2300 UTC on 4 May 2007 to 0300 UTC on 5 May 2007. The direction in which the barb points indicates wind direction, following meteorological convention. Flags are 50 m s^{-1}, full barbs are 10 m s^{-1}, and half-barbs are 5 m s^{-1}. White areas on this plot indicate data that did not pass continuity requirements for quality control. Note that winds below 2 km reach 30 m s^{-1}around 0200 UTC. Courtesy of NOAA.

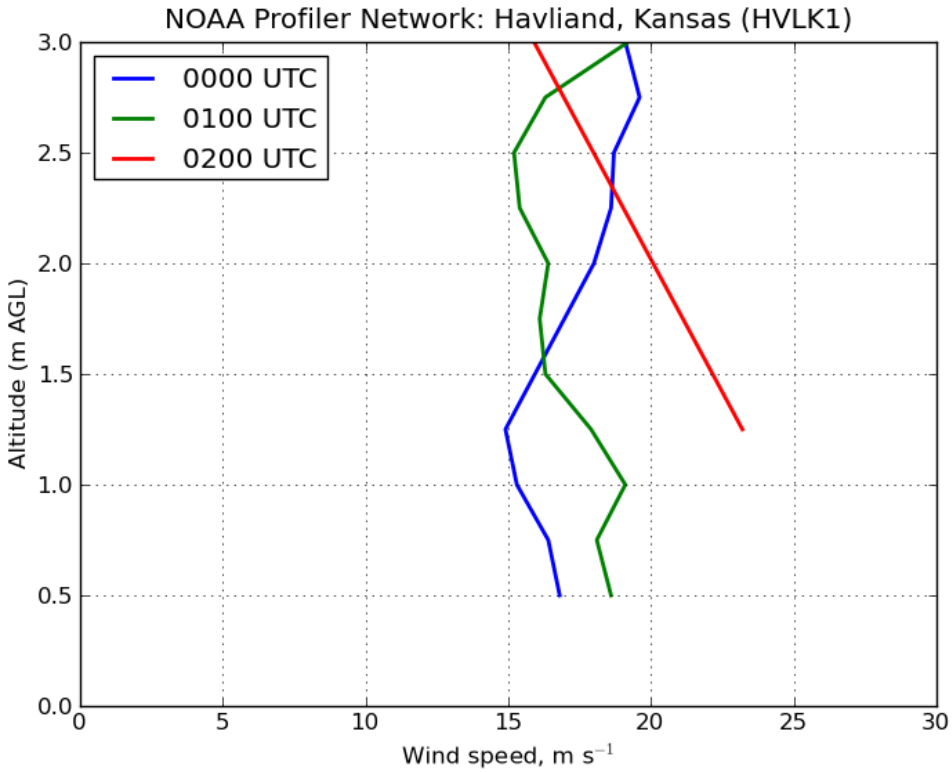


Fig. 69. Velocity profiles from 500 m to 3000 m AGL as measured by HVLK1 at 0000 UTC 0100, and 0200 UTC. No data were reported at 0300 UTC. An LLJ appears to be developing at 0100 UTC; however, by 0200 UTC, the profiler data contain too many gaps in the vertical to infer the presence of the LLJ (Fig. 68).

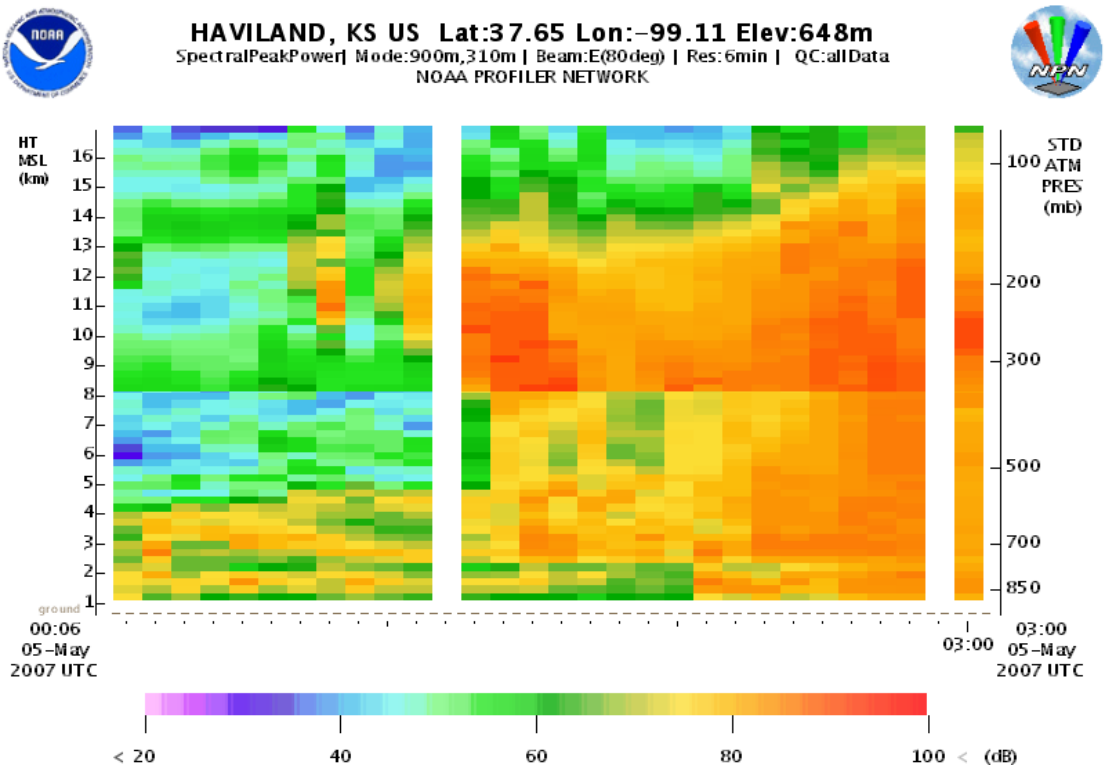


Fig. 70. Signal power (in dB) corresponding to the velocity profiles in Fig. 68. Larger values typically indicate the presence of cloud or precipitation particles, but cannot be interpreted in the same way that "reflectivity" would be. The discontinuity at 8 km ASL results from the juxtaposition of profiler data collected in "low" and "high" mode.

B.2 Groundwater Management District No. 5 surface data

Big Bend Groundwater Management District 5 (GMD5; http://www.gmd5.org/) maintains a small network of ten "weather" stations in south-central Kansas, including one (Station #1) located nominally at Greensburg, Kansas (Fig. 71). This station was not directly impacted by the Greensburg tornado and continued to record data after the Greensburg storm had passed. I obtained the GMD5 data from 4 May 2007 (0000 – 2400 local time) directly from the coordinator of GMD5 (S. Falk, 2009, personal communication).

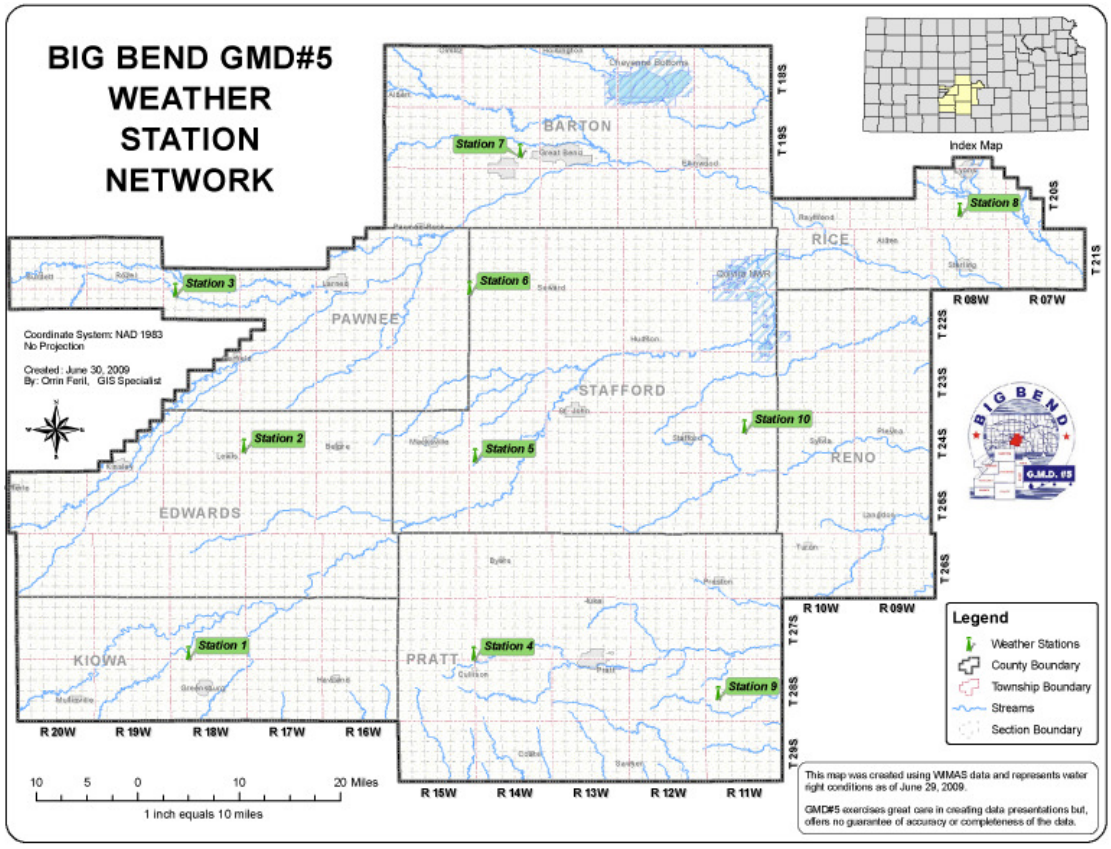


Fig. 71. Map of GMD5 in south central Kansas (see inset at upper right). Locations of weather stations are marked in green; Station #1 (the southwesternmost station) is located just north of the city of Greensburg.

Unfortunately for the purposes of this study, the GMD5 stations are located at and northeast of Greensburg, and therefore did not collect data in the inflow region of the Greensburg storm until well after UMass X-Pol data collection had ceased and after the mode I to mode II transition occurred.

The format of these data also made their usefulness in this study very limited. Because the GMD5 weather stations are designed to collect data pertinent to evapotranspiration studies, they do not report some meteorological variables (such as pressure) that are customarily recorded by NWS ASOS/AWOS observing stations. Perhaps the greatest drawback of all is that the meteorological data from these

stations is reported as hourly averages (e.g., Table 7). It is impossible to infer with temporal precision of less than 1 hour the passage of surface boundaries or storms.

Table 7. GMD5 Station #1 (Greensburg) data from 4 May 2007 (local time), in the format in which they were received (S. Falk, personal communication). Data from the other nine stations are excluded for brevity.

Weather Station #1 Greensburg Hourly Data 2007

Julian Day	Hour (local time)	Avg. Air Temp. (°F)	Relative Hum. (%)	Avg. Vapor Pressure (kPa)	Avg. Solar Rad. (kW m^{-2})	Eto (in hr^{-1})	Avg. Wind Speed (mph)	Avg. Wind Direction (°)	Std. Dev. of Wind Direct. (°)
124	100	60.39	97.9	1.751	0	0	10.34	147.4	10.96
124	200	60.18	98	1.742	0	0	9.86	145.3	11.6
124	300	59.64	98.2	1.712	0	0	9.48	141.4	9.57
124	400	58.99	98.3	1.663	0	0	9.26	136.2	9.57
124	500	58.45	98.5	1.647	0	0	10.78	140.1	9.84
124	600	58.37	96.9	1.632	0.004	0	10.68	147	9.86
124	700	59.72	97.7	1.705	0.03	0	15.02	153.4	11.12
124	800	61.35	95	1.791	0.097	0.002	12.83	159.4	12.7
124	900	63.78	89.9	1.868	0.229	0.004	12.55	159.3	12.71
124	1000	67.31	79.5	1.905	0.416	0.009	11.16	165.3	16.14
124	1100	71.2	74	1.915	0.603	0.014	11.43	171.5	15.43
124	1200	75.6	56.58	1.93	0.83	0.02	12.64	179.4	14.82
124	1300	79.4	48.71	1.843	0.938	0.025	13.28	176.8	16.73
124	1400	82.2	42.02	1.666	0.909	0.026	13.28	185.7	15.71
124	1500	83.4	37.63	1.52	0.745	0.024	12.27	176.6	14.38
124	1600	85.3	30.8	1.369	0.719	0.025	12.06	174.9	13.53
124	1700	85.5	41.68	1.522	0.532	0.02	13.26	164.8	14.34
124	1800	82.8	51.06	1.67	0.223	0.012	14.94	153.2	11.12
124	1900	79.2	58.74	1.911	0.069	0.006	15.07	152.5	11.66
124	2000	76.3	76.8	2.128	0.014	0.002	13.18	146.1	11.35
124	2100	72.3	97.7	2.315	0	0	19.29	122.5	38.73
124	2200	69.13	89.9	2.138	0	0	19.99	228.8	78
124	2300	71.6	93.1	2.433	0	0	14.03	167.4	12.44
124	2400	71.5	91.9	2.439	0	0	19.92	163.4	10.33

Even with these limitations, some interesting observations can be gleaned from these data. Surface winds at Greensburg backed from southerly (180°) in the afternoon to southeasterly (123°) just before the passage of the Greensburg storm, before veering sharply back to southwesterly (229°) immediately after (Fig. 72). During the hour in which the Greensburg storm passed over GMD5 Station #1 (02:00

– 03:00 UTC), hourly average wind speed increased to 9 m s^{-1}, and the standard deviation of the wind speed increased to 78°, indicating great variability in the wind direction. These observations are consistent with the wind speed increase and rapid change in wind direction that would have accompanied the passage of the hook region of the Greensburg storm. During the same period hourly average surface temperature decreased slightly, from 22.4 °C to 20.6°C, possibly capturing the overspread of the Greensburg storm's cold pool.

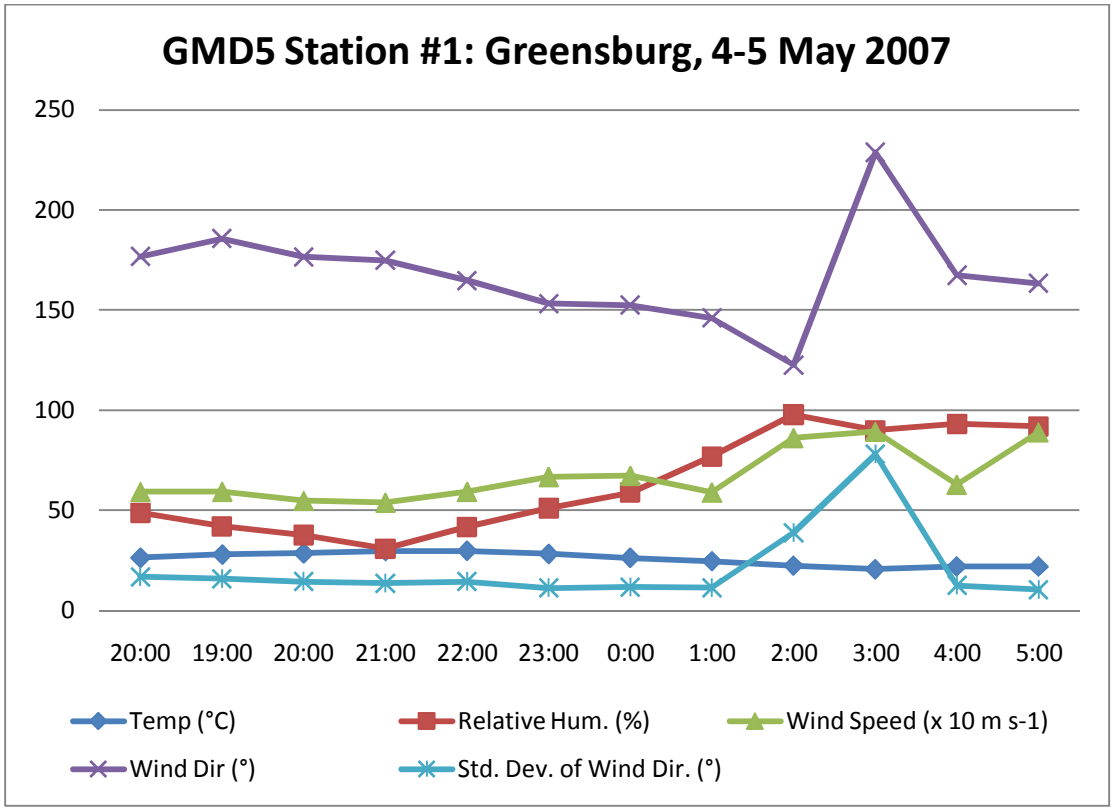


Fig. 72. Selected data from GMD5 Station #1 (located just north of Greensburg, Kansas) from 4-5 May 2007. Times are in UTC. Averages are calculated and reported at the *end* of each hour; thus the values shown at, e.g., data at 0300 UTC are averages for 0200 – 0300 UTC. Note that wind speeds are scaled by a factor of 10 for visibility.

B.3 Lamont, Oklahoma rawinsonde

A standard rawinsonde launch occurred at the Southern Great Plains site of the Atmospheric Radiation Measurement (ARM) program, located near Lamont,

Oklahoma (180 km east-southeast of the UMass X-Pol deployment site) at 0000 UTC on 5 May 2007. This sounding (Fig. 73), denoted LMN, shows the presence of a nearly well-mixed layer between the surface (967 mb) and 850 mb. This sounding was launched at a considerably greater distance from the Greensburg storm from a much lower altitude than the DDC sounding. The DDC sounding was used as the basis for the model initial environment, while the LMN sounding was used to inform the insertion of a well-mixed layer (constant θ and q) with surface characteristics at low levels into that environment.

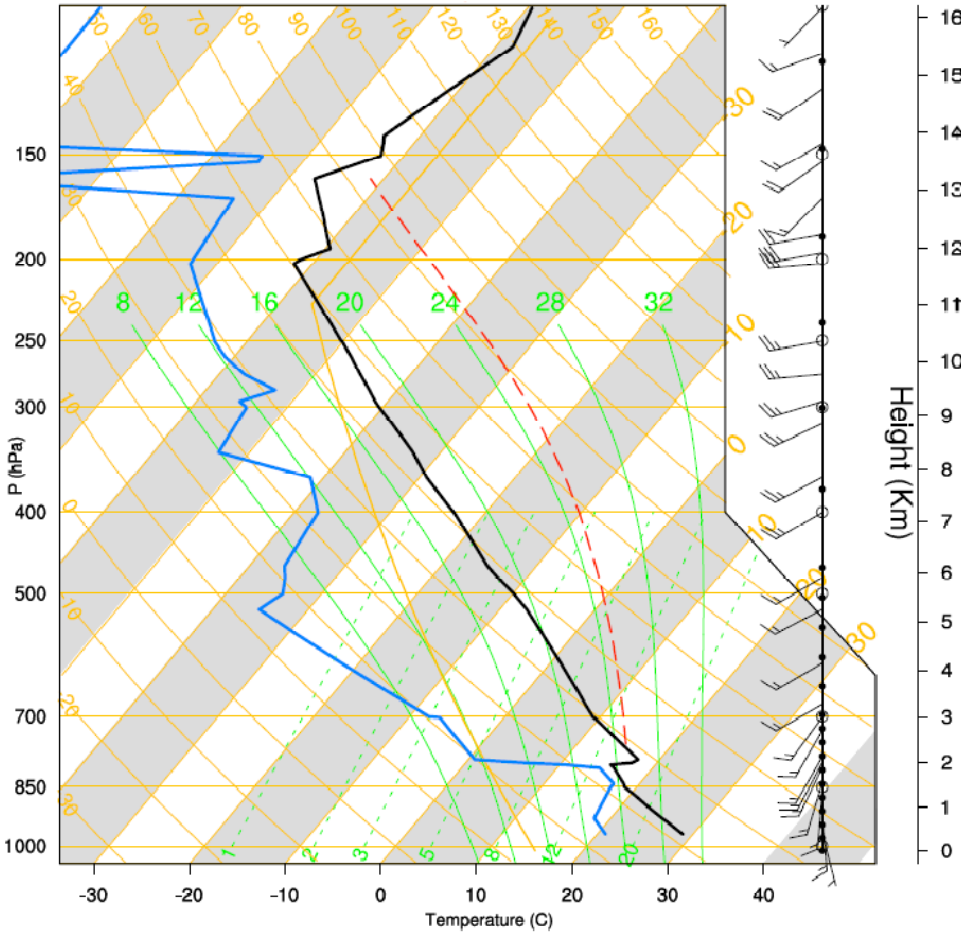


Fig. 73. As in Fig. 48, but for the sounding taken at Lamont, Oklahoma at 0000 UTC on 5 May 2007.

Appendix C. Caveat regarding the UMass X-Pol polarimetric fields

UMass X-Pol, like many radar systems, is configured such that raw in-phase ($I[\tau]$) and quadrature phase ($Q[\tau]$) components of the complex signals are sampled and processed during data collection, and only derived values are actually recorded. This configuration greatly reduces the amount of storage required. Since the UMass X-Pol has orthogonal (horizontal and vertical) polarization diversity, two complex voltages are sampled at a given time τ:

$$E_h(\tau) = I_h(\tau) + jQ_h(\tau)$$

$$E_v(\tau) = I_v(\tau) + jQ_v(\tau)$$

where $j = \sqrt{-1}$. Two power variables are computed:

$$H = \langle E_h E_h^* \rangle$$

$$V = \langle E_v E_v^* \rangle$$

where an asterisk (*) denotes a complex conjugate and angled brackets $\langle x \rangle = \frac{\sum_n x_n}{n}$ denote averages over n = 33 pulses. Note that the time subscript (τ) is hereafter dropped for brevity. Hence,

$$H = \langle (I_h + jQ_h)(I_h - jQ_h) \rangle = \langle I_h^2 + Q_h^2 \rangle$$

$$V = \langle (I_v + jQ_v)(I_v - jQ_v) \rangle = \langle I_v^2 + Q_v^2 \rangle$$

Variables calculated from these quantities that are used in this study include:

1) Reflectivity at horizontal polarization:

$$Z_h = \left(\frac{4\lambda^4}{\pi^4 |K_w|^2} \right) H$$

where λ = 3 cm and $|K_w|^2$=0.93 (Doviak and Zrnić 1993), and

2) Differential reflectivity:

$$Z_{DR} = 10\log_{10}\left(\frac{H}{V}\right)$$

To calculate the correlation coefficient at zero lag ρ_{hv}, we first define a variable C:

$$C = \langle E_h E_v^* \rangle$$

$$C = \langle (I_h + jQ_h)(I_v - jQ_v) \rangle$$

$$C = \langle I_h I_v + Q_h Q_v + j(I_v Q_h - I_h Q_v) \rangle$$

$$C = \langle I_h I_v + Q_h Q_v \rangle + j\langle I_v Q_h - I_h Q_v \rangle$$

During UMass X-Pol data collection, C is calculated and stored. Then, ρ_{hv} is calculated according to

$$\rho_{hv} = \frac{|C|}{\sqrt{HV}}$$

$$\rho_{hv} = \frac{|\langle E_h E_v^* \rangle|}{\sqrt{\langle E_h E_h^* \rangle \langle E_v E_v^* \rangle}}$$

$$\rho_{hv} = \frac{\sqrt{\langle I_h I_v + Q_h Q_v \rangle^2 + \langle I_v Q_h - I_h Q_v \rangle^2}}{\sqrt{\langle I_h^2 + Q_h^2 \rangle \langle I_v^2 + Q_v^2 \rangle}}$$

During the Greensburg deployment, the UMass X-Pol's onboard computer was configured such that C was inadvertently declared as a floating point variable rather than a complex variable. As a result, the imaginary part of C was not recorded.[17] In this case, we deal with an alternative variable:

$$\tilde{C} = Re[C] = \langle I_h I_v + Q_h Q_v \rangle$$

(Note that the imaginary part of C has been omitted.) The corresponding alternative form for ρ_{hv} is

$$\tilde{\rho}_{hv} = \frac{|\tilde{C}|}{\sqrt{HV}}$$

[17] This issue was corrected in subsequent 2007 deployments and seasons thereafter.

$$\tilde{\rho}_{hv} = \frac{\sqrt{\langle I_h I_v + Q_h Q_v \rangle^2}}{\sqrt{\langle I_h^2 + Q_h^2 \rangle \langle I_v^2 + Q_v^2 \rangle}}$$

In the Greensburg data, it is $\tilde{\rho}_{hv}$ that is contained in the UMass X-Pol field RH (S. Frasier, personal communication). Note that $\tilde{\rho}_{hv} \leq \rho_{hv}$. However, values and spatial patterns of $\tilde{\rho}_{hv}$ turned out to agree reasonably well with ρ_{hv} values reported by Bluestein et al. (2007a) in two other tornadic supercells sampled by UMass X-Pol, when both the real and imaginary parts of *C* were recorded. It is therefore assumed that $|Re[C]| \gg |Im[C]|$ (and, consequently, that Φ_{DP} is close to π). We proceed to interpret the $\tilde{\rho}_{hv}$ fields in much the same manner as we would ρ_{hv}, but will repeat the above caveat a few times during the discussion.

Appendix D. Azimuth adjustments to UMass X-Pol data

This appendix summarizes the adjustments made to UMass X-Pol azimuth information collected in the Greensburg, Kansas tornadic supercell on 5 May 2007.

The azimuth (yaw) adjustments listed below were applied to UMass X-Pol data prior to analysis. Shifts in the azimuthal location of ground clutter targets appeared even though neither the truck moved nor the orientation changed during the two segments of the deployment. I do not have a satisfactory explanation for this issue, but I speculate that it may have resulted from one or a combination of the following:

(1) positioner error owing to antenna hysteresis, an issue which has been documented in other UMass radar systems (e.g., Tanamachi *et al.* 2007) (I actually believe this issue is minor, if it is an issue at all, because the sign of the corrections doesn't seem to be related to the direction of antenna motion as in previous studies);

(2) the motion of the antenna during data collection may have caused the truck to shift slightly in place; or

(3) gusty winds at the deployment site may have moved the antenna slightly.

Sweeps were collected in contiguous volumes, and I applied the same azimuthal correction to all the sweeps in a volume, even though the clutter targets may appear in only the lowest one or two tilts.

Table 8. Azimuthal adjustments to UMass X-Pol volumes based upon clutter targets.

Start time (UTC)	End time (UTC)	Volume number	Clutter target	Latitude (°N)	Longitude (°W)	Az. Correction (+ is CW, - is CCW)
011500	011611	0 (single-elevation scans)	Rectangular building on N side of U.S. Hwy 160, about 400 m east of the Broadway Ave. entrance/exit.	37.192869	-99.477725	+1.6°
011617	012051	0 (single-elevation scans)	Small hilltop building (house?), 4.6 km at bearing 239° from the center of Protection, Kansas as depicted on Google Earth.	37.1796	-99.527957	-0.1°
012130	012549	0 (single-elevation scans)	Protection, Kansas grain elevator	37.204116	-99.48633	0.0°
012554	012652	1	None available	N/A	N/A	None applied
012659	012729	2	Protection, Kansas grain elevator	37.204116	-99.48633	-0.1°
012736	012807	3	Protection, Kansas grain elevator	37.204116	-99.48633	+0.3°
012814	012845	4	Protection, Kansas grain elevator	37.204116	-99.48633	-0.3°
012852	012923	5	Protection, Kansas grain elevator	37.204116	-99.48633	-0.1°
012930	013001	6	Protection, Kansas grain elevator	37.204116	-99.48633	-0.2°
013008	013039	7	Protection,	37.204116	-99.48633	-1.7°

			Kansas grain elevator			
013046	013117	8	Protection, Kansas grain elevator	37.204116	-99.48633	-1.7
013123	013154	9	Protection, Kansas grain elevator	37.204116	-99.48633	-1.6°
013201	013232	10	Protection, Kansas grain elevator	37.204116	-99.48633	-1.8°
013238	013250	11	Protection, Kansas grain elevator	37.204116	-99.48633	-1.4°
013251	*013816*	*Truck moved from S to N side of U.S. Hwy. 160*	*N/A*	*N/A*	*N/A*	*N/A*
013817	013845	12	Protection, Kansas grain elevator	37.204116	-99.48633	+1.9°
013853	013922	13	Protection, Kansas grain elevator	37.204116	-99.48633	+2.1°
013930	013958	14	Protection, Kansas grain elevator	37.204116	-99.48633	+1.8°
014007	014035	15	Protection, Kansas grain elevator	37.204116	-99.48633	+2.2°
014043	014111	16	Protection, Kansas grain elevator	37.204116	-99.48633	+1.5°
014120	014149	17	Protection, Kansas grain elevator	37.204116	-99.48633	+2.0°
014157	014225	18	Protection, Kansas grain elevator	37.204116	-99.48633	+1.8°
014234	014302	19	Protection, Kansas grain elevator	37.204116	-99.48633	+1.6°
014310	014338	20	Protection, Kansas grain elevator	37.204116	-99.48633	+1.9°
014346	014415	21	Protection, Kansas grain elevator	37.204116	-99.48633	+1.6°
014423	014452	22	Protection, Kansas grain	37.204116	-99.48633	+1.7°

			elevator			
014500	014529	23	Protection, Kansas grain elevator	37.204116	-99.48633	+2.2°
014537	014606	24	Protection, Kansas grain elevator	37.204116	-99.48633	+1.5°
014614	014643	25	Protection, Kansas grain elevator	37.204116	-99.48633	+1.8°
014651	014719	26	Protection, Kansas grain elevator	37.204116	-99.48633	+2.1°
014727	014756	27	Protection, Kansas grain elevator	37.204116	-99.48633	+1.9°
014804	014833	28	Protection, Kansas grain elevator	37.204116	-99.48633	+1.7°
014842	014910	29	Protection, Kansas grain elevator	37.204116	-99.48633	+1.8°
014918	014947	30	Protection, Kansas grain elevator	37.204116	-99.48633	+1.4°
014955	015024	31	Protection, Kansas grain elevator	37.204116	-99.48633	+2.0°
015032	015101	32	Protection, Kansas grain elevator	37.204116	-99.48633	+2.0°
015109	015138	33	Protection, Kansas grain elevator	37.204116	-99.48633	+1.4°
015146	015214	34	Protection, Kansas grain elevator	37.204116	-99.48633	+1.6°
015223	015251	35	Protection, Kansas grain elevator	37.204116	-99.48633	+1.5°
015300	015328	36	Protection, Kansas grain elevator	37.204116	-99.48633	+2.1°
015336	015405	37	Protection, Kansas grain elevator	37.204116	-99.48633	+1.6°
015413	015435	38	Protection, Kansas grain elevator	37.204116	-99.48633	-0.1°
015510	015538	39	Farmstead	37.22182	-99.455559	+2.2°
015546	015614	40	Farmstead	37.22182	-99.455559	+2.3°

015622	015650	41	Farmstead	37.22182	-99.455559	+2.6°
015658	015726	42	Farmstead	37.22182	-99.455559	+2.1°
015735	015803	43	Farmstead	37.22182	-99.455559	+2.2°
015811	015840	44	Farmstead	37.22182	-99.455559	+2.6°
015848	015916	45	Farmstead	37.22182	-99.455559	+2.2°
015925	015953	46	Farmstead	37.22182	-99.455559	+2.4°
020001	020030	47	Farmstead	37.22182	-99.455559	+2.6°
020038	020112	48	Farmstead	37.22182	-99.455559	+2.4°
020119	020153	49	Farmstead	37.22182	-99.455559	+1.7°
020201	020229	50	Farmstead	37.22182	-99.455559	+2.9°
020237	020306	51	Farmstead	37.22182	-99.455559	+2.9°
020314	020342	52	Farmstead	37.22182	-99.455559	+2.9°
020350	020418	53	Farmstead	37.22182	-99.455559	+3.1°
020426	020455	54	Farmstead	37.22182	-99.455559	+3.1°
020503	020531	55	Farmstead	37.22182	-99.455559	+3.0°
020604	020637	56	Farmstead	37.22182	-99.455559	+1.8°
020646	020720	57	Farmstead	37.22182	-99.455559	+2.1°
020730	020804	58	Farmstead	37.22182	-99.455559	+2.1°
020813	020846	59	Farmstead	37.22182	-99.455559	+2.6°
020855	020928	60	Farmstead	37.22182	-99.455559	+2.2°
020937	021011	61	Farmstead	37.22182	-99.455559	+2.5°
021020	021054	62	Farmstead	37.22182	-99.455559	+2.2°
021103	021143	63	Farmstead	37.22182	-99.455559	+2.7°
021150	021231	64	Farmstead	37.22182	-99.455559	+1.6°
021240	021253	65	Farmstead	37.22182	-99.455559	+2.4°
021341	021427	66	Farmstead	37.22182	-99.455559	+1.7°
021435	021502	67	Farmstead	37.22182	-99.455559	+2.4°
021547	021655	68	Farmstead	37.22182	-99.455559	+2.0°
021704	021818	69	Farmstead	37.22182	-99.455559	+2.5°
021826	021941	70	Farmstead	37.22182	-99.455559	+2.4°
021950	022105	71	Farmstead	37.22182	-99.455559	+1.9°
022112	022139	72	Farmstead	37.22182	-99.455559	+1.7°
022210	022323	73	Farmstead	37.221136	-99.428759	-0.3°
022331	022447	74	Farmstead	37.221136	-99.428759	+0.6°
022455	022605	75	Farmstead	37.221136	-99.428759	-0.3°
022635	022811	76	Farmstead	37.221136	-99.428759	-3.9°
022820	022811	77	None available	N/A	N/A	N/A
023050	*023233*	*78 (bad volume)*	*None available*	*N/A*	*N/A*	*N/A*
023242	023425	79	Farmstead	37.221136	-99.428759	+0.7°
023450	023510	80	None available	N/A	N/A	N/A
023559	023618	81	None available	N/A	N/A	N/A

Appendix E. List of abbreviations

This appendix exists to serve as a quick reference for abbreviations, acronyms, and some variables used in this dissertation. Unless otherwise indicated, SI units are used throughout this dissertation, considered commonly known, and not defined here.

Table 9. Expansions of abbreviations, acronyms, and some variables used in this dissertation.

Abbreviation	Definition
3DVAR	Three dimensional variational assimilation
4DVAR	Four dimensional variational assimilation
AGL	Above ground level
ASL	Above sea level
ASOS	Automated Surface Observing System
BWER	Bounded weak echo region
CAPE	Convective available potential energy
CR	Consistency ratio
CT	Cyclic tornadogenesis
CTS	Cyclic tornadic supercell
d	Innovation (observation minus model)
D	Diameter (of hydrometeor)
DA	Data assimilation
DART	Data Assimilation Research Testbed (software package)
dBZ	Logarithmic units of Z
DDC	Dodge City, Kansas NWS office / rawinsonde
DORADE	Doppler Radar Data Exchange (format)
EAKF	Ensemble adjustment Kalman filter (technique)

EF	Enhanced Fujita (scale)
EKF	Extended Kalman filter (technique)
EnKF	Ensemble Kalman filter (technique)
EnSRF	Ensemble square root Kalman filter (technique)
ENU	"East – north – up" (coordinate system)
FFD	Forward-flank downdraft
GMD5	Kansas Groundwater Management District No. 5
GPS	Global Positioning System
HVLK1	Haviland, Kansas wind profiler
KAMA	The Amarillo, Texas WSR-88D
KDDC	The Dodge City, Kansas WSR-88D
KF	Kalman filter
KPTT	The Pratt, Kansas ASOS site
KVNX	The Vance Air Force Base, Oklahoma WSR-88D
LLJ	Low-level jet; specifically, the southerly, nocturnal low-level wind maximum over the Great Plains of the central U.S.
low-level	0.0 to 2.0 km AGL
mid-level	2.0 to 6.0 km AGL
MIRSL	Microwave Remote Sensing Laboratory (UMass)
N(x,y)	Normal (Gaussian) distribution about a mean x with variance y
near-surface	0.0 to 1.0 km AGL
NCAR	National Center for Atmospheric Research
NCDC	National Climatic Data Center
NEXRAD	Next Generation Weather Radar (program)
NOAA	National Oceanic and Atmospheric Administration

NWP	Numerical weather prediction
NWS	U.S. National Weather Service
OI	Optimal interpolation
OSCER	Oklahoma Supercomputing Center for Education and Research
OU	University of Oklahoma
p	Atmopsheric pressure
pdf	Probability density function
q	Water vapor mixing ratio
r	Range (from radar)
RFD	Rear-flank downdraft
RFGF	Rear-flank gust front
RMSI	Root mean square of innovation
S-band	10 cm wavelength
T	Temperature
T_d	Dew point temperature
u	Zonal (east-west or x-) component of velocity
UMass	University of Massachusetts – Amherst
UMass X-Pol	UMass mobile, X-band, polarimetric Doppler radar
upper-level	6.0 km AGL and above
UTC	Coordinated Universal Time
v	Meridional (north-south or y-) component of velocity
VAD	Velocity-azimuth display (technique)
VCP	Volume Coverage Pattern (for WSR-88Ds)
VORTEX	Verification of the Origin of Rotation in Tornadoes Experiment (1994 – 1995)

VORTEX2	Second Verification of the Origin of Rotation in Tornadoes Experiment (2009 – 2010)
v_{max}	Maximum unambiguous Doppler velocity, or Nyquist velocity
v_r	Radial Doppler velocity
VS	Vortex signature
w	Vertical (up-down or z-) component of velocity
WEC	Weak-echo column
WEH	Weak-echo hole
WRF	Weather Research and Forecasting model
WRF-ARW	Advanced Research WRF core
WRFV3	WRF version 3.0.1.1
WSR-88D	Weather Surveillance Radar 1988 Doppler
X-band	3 cm wavelength
Z	Radar reflectivity factor
Z_{DR}	Differential radar reflectivity factor
Z_{dBZe}	Equivalent radar reflectivity factor (logarithmic units)
Z_e	Equivalent radar reflectivity factor (linear units)
Z_g	Equivalent radar reflectivity factor due to graupel
Z_r	Equivalent radar reflectivity factor due to rain
Z_s	Equivalent radar reflectivity factor due to snow
ζ	Vertical component of vorticity
θ	Potential temperature
θ_p	Pitch angle (of radar antenna)
θ_e	Elevation angle (of radar antenna)
λ	Wavelength

ρ_{hv}	Cross-correlation coefficient at zero lag
Φ	Geopotential height
Φ_r	Roll angle (of radar antenna)
Ψ	Yaw / azimuth angle (of radar antenna)